

**Multi-view and three-dimensional (3D) images in
Wear debris analysis (WDA)**

**A thesis submitted to the University of Manchester for the degree of
Doctor of Philosophy in the Faculty of Engineering and Physical
Sciences**

2013

Reduan Mat Dan

School of Mechanical, Aerospace and Civil Engineering

LIST OF CONTENTS

List of contents.....	2
List of figures.....	6
List of tables.....	10
Abstract.....	13
Declaration.....	14
Copyright statement.....	15
Acknowledgement.....	16
Publications and patents.....	17

Chapter 1 Research identification and significance

1.1 Introduction.....	18
1.2 Research background.....	19
1.3 Research objectives.....	20
1.4 The structure of the thesis.....	20

Chapter 2 Literature review

2.1 Wear debris analysis.....	21
2.2 Wear debris generation.....	21
2.3 Gear flank stress causing wear debris generation.....	25
2.4 Gear wear phenomena.....	29
2.5 Wear debris classification.....	32
2.5.1 Particles morphology.....	32
2.5.1.1 Particle size.....	33
2.5.1.2 Shape.....	34
2.5.1.3 Quantitative basic shape analysis.....	36
2.5.1.4 Colour.....	40
2.5.1.5 Surface texture.....	40
2.6 Types of wear debris particles.....	41
2.7 Techniques of wear debris analysis.....	42
2.8 Wear debris analysis sensors.....	44
2.9 Computer aided software, artificial intelligence and algorithms on wear debris analysis.....	48

2.10	General sampling techniques in wear debris analysis.....	54
2.11	Sampling equipment.....	55
2.12	Image capturing and processing in wear debris analysis.....	57
2.13	Three-dimensional (3D) approaches in wear debris analysis....	63
2.14	Constructing 3D images from 2D images.....	65
2.15	Critical analysis of literature review.....	67
2.16	Conclusions.....	68

Chapter 3 Research methodology and direction

3.1	Introduction.....	69
3.2	Research methodology.....	69
3.3	Conclusions.....	74

Chapter 4 Preliminary experimental result

4.1	Introduction.....	75
4.2	Objectives of preliminary experiment.....	75
4.3	Experiments methodology.....	75
4.4	Selection of machine and experimental setup.....	76
	4.4.1 The lubricant system.....	78
	4.4.1 Gear installation.....	79
	4.4.2 Gear selection.....	80
	4.4.3 Loading setup.....	80
	4.4.4 Calculation of theoretical life.....	81
4.5	Sampling and inspection procedures.....	82
	4.5.1 Visual inspection and image capturing.....	82
	4.5.2 Bottle sampling.....	82
	4.5.3 Magnetic plug sampling.....	82
4.6	Testing	
	4.6.1 Portable oil diagnostic system (PODS).....	85
	4.6.2 Off-line particle counting procedure.....	87
	4.6.3 Image capturing equipment.....	88
	4.6.3.1 Preliminary design of flow cell.....	89
	4.6.3.2 Microscope.....	91
	4.6.3.3 Peristaltic pump.....	91

4.6.3.4	Colour CCD camera.....	92
4.6.4	Software.....	93
4.6.5	Calculation of shape descriptor.....	93
4.7	Preliminary results	
4.7.1	Analysis of data.....	94
4.7.2	Assumption in the analysis.....	95
4.7.3	Particle count and trends.....	95
4.7.3.1	Result scuffing test.....	96
4.7.3.2	Result of pitting test.....	104
4.7.4	Image capturing and analysis.....	110
4.7.5	Quantitative measurement of wear debris particle.....	114
4.7.6	Preliminary 3D image reconstruction.....	115
4.7.7	Volume estimation.....	119
4.7.8	Issues on camera and supply tube of online particles count and image capturing.....	119
4.8	Lessons and observation from the preliminary experiment.....	121
4.9	Conclusions.....	123

Chapter 5 Final and validation experiment results

5.1	Introduction.....	124
5.2	Hardware modification and experimental setup.....	124
5.3	Image processing.....	129
5.3.1	Dynamic of wear debris particle motion	133
5.3.2	Conversion of video images to multi-frame still images.....	133
5.3.3	Tracing the boundary of particle.....	135
5.3.4	3D algorithm.....	138
5.3.5	Analysis of volume of standard shapes.....	142
5.3.6	Quantitative analysis-volume particle estimation.....	144
5.4	Result of experiments.....	145
5.4.1	Result of test 1.....	149
5.4.2	Result of test 2.....	155
5.4.3	Result of test 3.....	160

5.4.4	Summary of results.....	165
5.5	Shape analysis of wear debris particle.....	165
5.6	Conclusions.....	170

Chapter 6 Discussions

6.1	Introduction.....	171
6.2	Contributions.....	171
6.3	Discussion on preliminary result.....	173
6.4	Discussion on final and validation experiment result.....	174
6.5	Critical appraisal of experimental setup.....	175
6.6	Outcome of the research.....	177
6.7	Conclusions.....	177

Chapter 7 Conclusions and future works

7.1	Introductions.....	178
7.2	Aimed objectives and their achievements.....	178
7.3	Future work.....	182

References..... 185

Appendices

Appendix I.....	192
Appendix II.....	198
Appendix III.....	204
Appendix IV.....	206
Appendix V.....	208
Appendix VI.....	223
Appendix VII.....	224
Appendix VIII.....	225

LIST OF FIGURES

Figure 2-1:	Possible quantity features trend in machine component operation	22
Figure 2-2:	Real case of wear progression of a spur gear.....	23
Figure 2-3:	Real case of wear progression of a compress.....	24
Figure 2-4:	Wear particles size distribution versus machinery condition..	25
Figure 2-5:	Gear mesh contact points	26
Figure 2-6:	Flank load of two meshing gears,,,	26
Figure 2-7:	Relationship between wear characteristics and wear particle....	33
Figure 2-8:	Original profile of a particle obtained during severe sliding wear.....	38
Figure 2-9:	Harmonic plot of profile shown on figure 2-8.....	38
Figure 2-10:	Technique of edge detail.....	39
Figure 2-11:	Types of surface textures.....	40
Figure 2-12:	Types of wear debris particles images.....	42
Figure 2-13:	SYCLOPS classifier.....	49
Figure 2-14:	Images of wear debris particles.....	50
Figure 2-15:	The components of the integrated intelligence package for wear debris analysis.....	52
Figure 2-16:	Strategy of Knowledge Based Wear Particles Analysis.....	53
Figure 2-17:	Types of wear debris sampling.....	54
Figure 2-18:	Example of magnetic chip collector and magnetic plug used in the experiment. Wear debris particle stick on the magnetic plug in white circle.....	55
Figure 2-19:	Bottle sampling techniques.....	56
Figure 2-20:	Sampling valve.....	56
Figure 2-21:	Differences between magnification and resolution.....	58
Figure 2-22:	Scanning electron microscopy (SEM) and images.....	59
Figure 2-23:	Transfer Electron Microscopy (TEM)	60
Figure 2-24:	TEM image of wear debris on film (image taken in the TEM laboratory at The Univ. of Manchester.....	61
Figure 2-25:	Wear debris images taken using LSCM.....	61

Figure 2-26: Laser scanning Confocal microscopy.....	62
Figure 2-27: (a) Original image particles taken by LSCM (b) Edge detection using transmission channel LSCM (c) Applying the boundary from (b) to original image.....	63
Figure 2-28: Encoding SEM images surface elevation data into range images.....	64
Figure 2-29: Line intersection method and Hull cylindrical intersection.....	65
Figure 2-30: 3D reconstruction	66
Figure 2-31: Reconstructing the 3D tumour (red) images in a grey tube from two views.	66
Figure 3-1: Research methodology approach.....	70
Figure 3-2: Difference of mass of metal removed from two different gears mesh surfaces although particles have same length	71
Figure 3-3: Wear debris sample flow route during experiment.....	72
Figure 4-1: Test gear rig setup.....	77
Figure 4-2: Schematic test gear rig.....	77
Figure 4-3: Installation of the testing gears.....	79
Figure 4-4: Applying load to the gears.....	81
Figure 4-5: Location of magnetic plug inside the oil sump.....	83
Figure 4-6: (a) Magnetic plug (b) socket of magnetic plug –self closing valve close the socket way (c) magnetic plug inserted in the socket where the self closing valve is pushed upward revealing the head of the magnetic plug.....	83
Figure 4-7: Transferring the wear debris into fresh gear oil in a bottle for further analysis.....	85
Figure 4-8: PODS (Portable Oil Diagnostic System).....	86
Figure 4-9: Particle counting procedures (a) Check sufficient pressure (around 6-7 bar) (b) shake the sample (c) place the sample in container (d) load the container into the PODS	87
Figure 4-10: Offline setup of image capturing equipment.....	88
Figure 4-11: Schematic diagram of the image capturing facilities.....	88
Figure 4-12: Borosilicate flat tube and development of flow cell.....	90
Figure 4-13: Construction of flow cell (flat tube inside the casing).....	90
Figure 4-14: New flow cell.....	91

Figure 4-15: Illustration of perimeter calculation.....	93
Figure 4-16: Particle counts for scuffing test, Valve sampling Normalization Method.....	97
Figure 4-17: Particle counts for scuffing test, Side Magnetic sampling Normalization Method.....	98
Figure 4-18: Particle counts for scuffing test, Base Magnetic sampling Normalization Method.....	99
Figure 4-19: Particle counts for scuffing test, all types of sampling LD Particles Normalization Method.....	100
Figure 4-20: Particle counts for scuffing test, all types of sampling MD Particles Normalization Method.....	101
Figure 4-21: Particle counts for scuffing test, all types of sampling SD Particles Normalization Method.....	102
Figure 4-22: Particle counts for pitting test, Valve sampling all sizes.....	104
Figure 4-23: Particle counts for pitting test, Side magnetic sampling all sizes.....	105
Figure 4-24: Particle counts for pitting test, Base magnetic sampling all sizes.....	106
Figure 4-25: Particle counts for pitting test, all types of sampling LD Particles Normalization Method.....	107
Figure 4-26: Particle counts for pitting test, all types of sampling MD Particles Normalization Method.....	108
Figure 4-27: Particle counts for pitting test, all types of sampling SD Particles Normalization Method.....	109
Figure 4-28: Particle image view at XZ plane.....	117
Figure 4-29: Particle image view at YZ plane.....	117
Figure 4-30: Two images crossed on a single axis.....	118
Figure 4-31: Lines connecting the four edges to reconstruct three dimensional images.....	118
Figure 4-32: Estimated volume calculation.....	119
Figure 4-33: Cross sectional area of internal volume of flow cell.....	120
Figure 4-34: Actual size of image window under microscope.....	121
Figure 5-1: PODs window display software.....	125
Figure 5-2: Flow cell	126

Figure 5-3:	Schematic diagram of flow cell	127
Figure 5-4:	Final setup of experiments.....	127
Figure 5-5:	Schematic diagram of final setup showing the flow of Sample and data.....	128
Figure 5-6:	Degree of freedom of wear debris particles motions.....	130
Figure 5-7:	Result of the percentage of motions according to six degree of freedoms.....	131
Figure 5-8:	Graph of speed of rotation versus size of particles.....	132
Figure 5-9:	Distribution of the shape of particles.....	132
Figure 5-10:	Step by step image trace boundary.....	137
Figure 5-11:	Front view and side view of a particle.....	138
Figure 5-12:	Epipolar view of the particle.....	139
Figure 5-13:	Superimposition of two images.....	140
Figure 5-14:	Pseudo 3D - two boundary coordinates intersect each other.....	141
Figure 5-15:	Pseudo 3d images of particle views at different angles.....	141
Figure 5-16:	The rectangle area equivalent volume estimation.....	144
Figure 5-17:	Volume calculation of a single particle.....	145
Figure 5-18:	Volume calculation of a single particle.....	146
Figure 5-19:	Particle thickness versus size	147
Figure 5-20:	Estimated volume of particles	148
Figure 5-21:	Raw data wear rate versus time – test 1.....	149
Figure 5-22:	Wear rate of mass particles versus time – test 1.....	150
Figure 5-23:	Total wear rate mass of particles versus time – test 1	152
Figure 5-24:	Pitting progress on gears - test 1.....	154
Figure 5-25:	Raw data wear rate – test 2 (particle counts / minutes)	155
Figure 5-26:	Wear rate mass of particles versus time – test 2	156
Figure 5-27:	Total wear rate mass of particles versus time – test 2 (microgram/minutes)	157
Figure 5-28:	Pitting progress on gears - test 2.....	159
Figure 5-29:	Raw data wear rate – test 3 (particle counts / minutes)	161
Figure 5-30:	Wear rate mass of particles versus time – test 3 (microgram/minutes)	161
Figure 5-31:	Total wear rate mass of particles versus time – test 3 (microgram/minutes)	162

Figure 5-32: Pitting progress on gears - test 3.....	164
Figure 5-33: Shape results of the particle analysis	166
Figure 5-34: Shape distribution of the of sample particles-test 1.....	167
Figure 5-35: Shape distribution of the of sample particles-test 3.....	167
Figure 5-36: Ratio size/thickness test 1.....	168
Figure 5-37: Ratio size/thickness test 2.....	169
Figure 5-38: Ratio size/thickness test 3.....	169
Figure 6-1: Flow pattern of oil around a particle.....	172
Figure 6-2: Flow pattern (side view) of oil around a particle when the direction of flow is reversed.....	173
Figure 6-3: Gear setup	175

LIST OF TABLES

Table 2-1:	Gear wear process and mechanism.....	30
Table 2-2:	Relationship between types of particles and size.....	34
Table 2-3:	Platelets and flakes sizes and appearance.....	35
Table 2-4:	Shape of the wear debris.....	36
Table 2-5:	Wear particle shape and size descriptors.....	37
Table 2-6:	Shape parameters.....	39
Table 2-7:	On line / in-line /off-line sensors for condition monitoring of lubricants.....	45
Table 2-8:	The relational grades of the test particles shown in fig. 2- 11 to six types of wear debris.....	51
Table 2-9:	Three dimensional analysis results of particles.....	52
Table 2-10:	Data for the particle in figure 2-2.....	62
Table 4-1:	Gear selection.....	80
Table 4-2:	List of equipment for the image capturing setup.....	92
Table 4-3:	Figures of gear damage and particles images from scuffing test.....	111
Table 4-4:	Figures of gear damage and particles images from pitting test.....	113
Table 4-5:	Measurement of the particles area , perimeter, roundness and Size.....	114
Table 4-7:	Images of same particles undergoing filtration.....	116
Table 5-1:	RS232 Command codes- peristaltic pump Watson Marlow....	124
Table 5-2:	Frames of still images of a rotating particles.....	134
Table 5-3:	Estimated calculation of volume, area and errors of various Shapes	142
Table 5-4:	Volume and mass of particles on selected sizes test 1,2,3.....	148
Table 5-5:	Summary of results.....	165
Table App I-1:	Symbol of parameters.....	192
Table App I-2:	Pre-selected experimental parameters.....	193
Table App II-1:	Particle counts for scuffing test, valve sampling - preliminary experiment	198
Table App II-2:	Particle counts for scuffing test, base magnetic sampling	

preliminary experiment.....	199
Table App II-3: Particle counts for scuffing test, side magnetic sampling preliminary experiment.....	200
Table App II-4: Particle counts for pitting test, valve sampling preliminary experiment.....	201
Table App II-5: Particle counts for pitting test, base magnetic sampling preliminary experiment.....	202
Table App II-6: Particle counts for pitting test, side magnetic sampling preliminary experiment.....	203
Table App V-1: Sample of Command codes sent to peristaltic pump and the associated time of every task.....	223
Table App VII-1:Estimated cost of current setup of the proposed system.....	224
Table App VIII-1:Images of wear debris dynamic study.....	225
Table APP VIII-2 Result of the study of wear debris particles dynamic.....	226

Total words counts – 40434

Abstract

Wear debris found in gear lubricating oil provides extremely valuable information on the nature and severity of gear faults as well as remaining gear life. The conventional off-line process of taking samples of oil for testing of wear debris is a hindrance because it is laborious, expensive, delays information collection, and is expert oriented. In view of these limitations, the development of automating wear debris particle analysis using various approaches has been ongoing for years. However, existing online technology does not encourage widespread use of wear debris analysis (WDA) in the industry. High costs coupled with expert and labour requirements have led users to use other types of condition-based maintenance, such as vibration. There is a need to develop a WDA technique that is relatively cheap, online, requires little expertise to handle, and provides more information for maintenance decision-making. This PhD thesis proposes a WDA technique which uses image processing and three-dimensional image reconstruction to diagnose the health of machinery. Its emphasis is on using the thickness and volume of the particles generated over time to predict the onset of gearbox failure, so that maintenance action can be taken before gears reach catastrophic failure.

Declaration

The author hereby declares that no portion of the work referred to in the thesis has been submitted in support of an application for another degree or qualification for this or any other university or other institute of learning.

Copyright statement

- I.** The author of this thesis (including any appendices and/or schedules to this thesis) owns any copyright in it (the “Copyright”) and he has given The University of Manchester the right to use such Copyright for any administrative, promotional, educational and/or teaching purposes.
- II.** Copies of this thesis, either in full or in extracts, may be made **only** in accordance with the regulations of the John Rylands University Library of Manchester. Details of these regulations may be obtained from the Librarian. This page must form part of any such copies made.
- III.** The ownership of any patents, designs, trademarks and any and all other intellectual property rights except for the Copyright (the “Intellectual Property Rights”) and any reproductions of copyright works, for example graphs and tables (“Reproductions”), which may be described in this thesis, may not be owned by the author and may be owned by third parties. Such Intellectual Property Rights and Reproductions cannot and must not be made available for use without the prior written permission of the owner(s) of the relevant Intellectual Property Rights and/or Reproductions.
- IV.** Further information on the conditions under which disclosure, publication and exploitation of this thesis, the Copyright and any Intellectual Property Rights and/or Reproductions described in it may take place is available from the Head of School of Mechanical, Aerospace and Civil Engineering.

Acknowledgement

First and foremost, I would like to thank Almighty Allah for granting me confidence and determination to pursue this work to its conclusion.

I am especially grateful to my beloved wife and children for their sacrifice, patience and support while I complete my work.

I would like to highly praise my supervisor Dr. Moray Kidd, Mr. Dennis Cooper and my advisor Prof Dr. Andrew Starr for their sound guidance, thorough advice, constant support and encouragement during the course of my research.

I would like to thank the staff of the University of Manchester for their assistance and support during the experiment.

Last but not least, I would like to acknowledge the financial support given by my sponsor, University Teknikal Malaysia Melaka (UTeM), and the government of Malaysia.

Publications and patents

Extract from Thesis:

1. Mat Dan R., Cooper D., Khan M.A., Starr A.G. Pseudo-3D images reconstruction in online wear debris particles analysis. First AAM 2008 conference, New Orleans, Louisiana, USA. (17-20 June 2008).
2. Mat Dan R., Cooper D., Khan M.A., Starr A.G. The development of online wear debris analysis sensor using pseudo 3D images of particles and flow control. BINDT conference in Edinburgh (17-20 July 2008)
3. Khan M.A., Cooper D., Mat Dan R., Starr A.G., Wear debris basic shape classification using fuzzy logic. BNDT conference in Edinburgh (17-20 July 2008)
4. Mat Dan R., Cooper D., Khan M.A., Starr A.G. Pseudo-3D images reconstruction from multi-view images in online wear debris analysis. 3rd WCEAM 2008 conference Beijing China (27-30 Oct 2008)
5. Khan M.A., Cooper D., Mat Dan R., Starr A.G., Wear debris size distribution features for helical gear pitting failure diagnosis, First AAM 2008 conference (17-20 June 2008)
6. UK patent application 0811160.1. Apparatus and method for wear debris analysis. 3D application. Inventors: Mat Dan R., Cooper D., Khan M.A., Starr A.G.(patent pending)
7. UK patent application 0811165.0. Apparatus and method for wear debris analysis. 2D application, colour, Shape, edge. Inventors: Khan M.A., Mat Dan R., Cooper D., Starr A.G.(patent pending)

Chapter 1.0 Research identification and significance

1.1 Introduction

Condition based maintenance (CBM) uses parameters that allow gathering of information indicative of a machine's condition [1]. The parameters collected assist in machinery maintenance decisions. The potential benefits and savings generated through the implementation of various techniques of condition health monitoring are well documented; these techniques may reduce maintenance costs, limit damage to machinery and avoid production loss [1]. Various condition-monitoring techniques on the market include vibration analysis, wear debris analysis, thermography, corrosion, acoustic emission with ultrasound, oil analysis and machine performance. However, all of these techniques have individual limitations, while others are laborious and do not meet the current industry requirements. No single technique has been able to resolve all condition-based maintenance requirements. Indeed, selecting a CBM technique depends on the requirement of the plant. Many users of CBM techniques have recognised wear debris analysis (WDA) as one of the most effective means of machine condition monitoring [2]. The morphology and features of wear debris is closely related to the loading, lubrication and wear processes involved in the machine. The development of the WDA technique has been extensively explored and developed in terms of wear debris size, size distribution, shape and material composition [2; 3]. End users of WDA use these features in their entirety or in part when detecting and diagnosing the deterioration of the machine components [4]. However, the technique has not been widely applied in the industry because it is time consuming and expensive due to lack of automation [4]. Despite these limitations, WDA is fast becoming an attractive condition-based maintenance strategy for assessing and predicting machine conditions. In fact, tremendous economic benefits can result from these condition-based maintenance practices when gear fault detection is paramount [5].

1.2 Research background

Limitations of current offline techniques have driven further development and need to automate the techniques. Previous attempts to integrate automatic features have not entirely been successful in meeting the needs of the industry. On-line automation of wear debris analysis (WDA) techniques will benefit the industry and encourage greater use than offline techniques. Offline sampling is laborious, because manpower must be allocated for a repetitive task that could be replaced with an automated approach. Automation will certainly reduce the need for manpower or expertise [6; 7]. Offline sampling has a risk of contamination due to the sample transfer between different containers for further analysis. On-line sampling will reduce the risk of contamination, as the sample is not exposed to any potential external source of contamination, whereas offline sampling also requires expert evaluation to provide an accurate diagnosis of the machine's condition. In fact, consistency between two expert interpreters is always uncertain. Automation has the potential to maintain consistency and standards in the analysis by minimizing human intervention.

Offline sampling delays the result of the analysis where the component may have the potential to fail by the time the results are generated. An oil sample is taken from machinery in a container such as a bottle to be delivered to the laboratory for analysis. Sometimes the sample needs to be stored before analysis can be conducted, so in practice the time between sample collection and sample analysis may be a few days. Offline sampling is frequently not desirable as most results show that the component is in satisfactory condition; this will waste time and incur unnecessary expense. In contrast, online sampling does not trigger any action until required.

However, off-line sampling allows determination of wear debris composition, which the on-line method is still unable to totally achieve. In addition, due to expert labour requirements, off-line sampling can provide a wider analysis compared to computerised analysis, which normally has preset conditions and only measures certain parameters. In short, while offline sampling techniques using laboratory equipment can provide more information about particles generated, the cost, complexity of services and the duration of analysis make the migration from offline to online the way forward [8].

Most current image processing techniques use 2D image construction to analyze wear debris. This limits analysis of only one part of the particle. The three-dimensional (3D) approach in this project provides the advantages of showing more views of the particles. If one has a full view of a particle, one can see whether the particle has more than one shape. More information from the particle can be obtained and a more accurate diagnosis can be derived from the machine's condition; simultaneously, the thickness of the particle can be measured which enables the volume of the particle to be estimated.

1.3 Research Objectives

This research tries to achieve the following objectives.

Objective one – Identify areas of novelty in wear debris analysis.

Objective two – Develop a methodology that can minimize human intervention in the wear debris analysis.

Objective three – Implement multi-view images and pseudo three- dimensional methodology to extract information from generated particles.

Objective four – Use the extracted information to predict the onset of failure and to assist in maintenance decision making.

1.4 The structure of the thesis

This thesis will adhere to the following structure: literature review, research methodology, preliminary results, validation experiment results, discussion, conclusions, and future works. First, the literature review will briefly discuss wear characteristics, wear debris analysis (WDA) technology, sampling methods, gear types, image capturing in WDA, and three-dimensional imaging. Second, the chapter on research methodology will describe approaches planned to reach the objectives. The preliminary results chapter will present the results of the two experiments and their correlation with a theoretical approach. Subsequently, the validation experiment chapter will discuss the latest findings and the method of the experiment. Then the discussion chapter will highlight the results and the outcome of the work, key areas in the literature review, and critical appraisal of the experimental work. The thesis will end by highlighting the achievement of the objectives and proposing some possible future works.

Chapter 2.0 Literature review

2.1 Wear debris analysis

This chapter will elaborate on the generation and classification of wear debris, gear flank stress and wear phenomena, and the types of wear debris. It will also identify how knowledge of wear debris features such as size, size distribution, and shape can be used for gear diagnostics, and will describe current technologies in WDA and also the opportunity for three-dimensional techniques.

2.2 Wear debris generation

Wear debris is generated when machine components such as gears and bearings undergo a sliding, rubbing or rolling action between their solid surfaces, which contain areas of roughness that are distributed over the surface. Under a microscope, the real contact area of the two surfaces is distributed in terms of several microscopic asperity contact zones or junctions, substantially different from the contact area seen with the naked eye [9]. Therefore, the real area of contact is actually the sum of asperity contact zones proportional to the external load. As load increases, new contact zones are created and as a result of a continuous load, contact zones deform plastically and initiate the degradation of the surface (wear), potentially leading to material loss [10]. There are few possible wear generation trends in the life of machinery, and all machinery will normally experience wear processes in three different periods, which are the running-in, useful working life, and a failure zone periods. Fig 2-1 illustrates the trend lines for different types of wear particle generation over time.

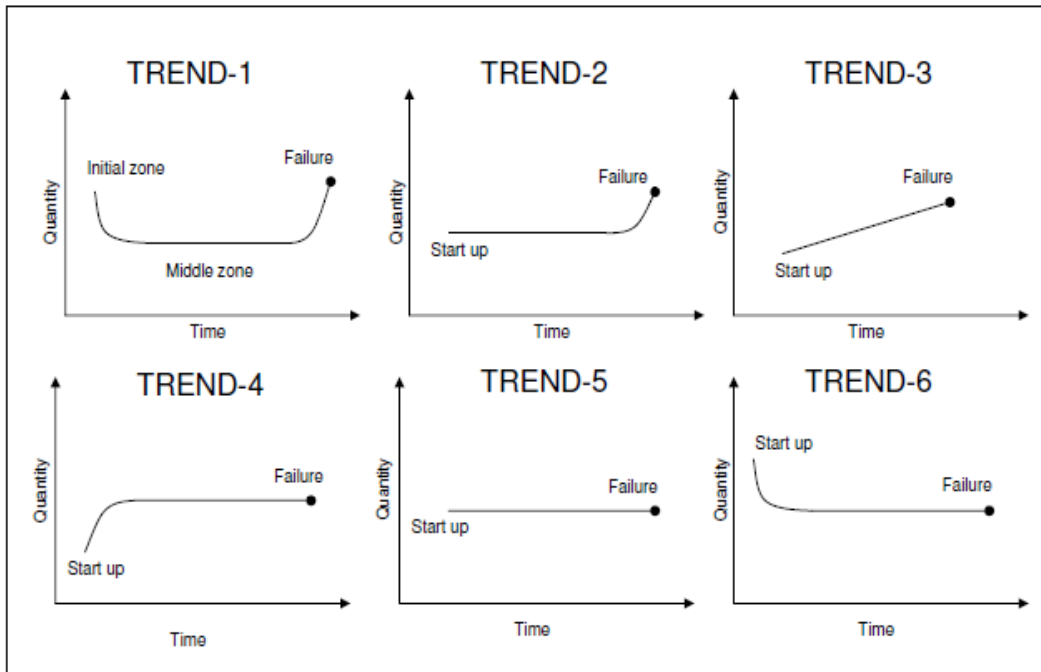


Figure 2-1: Possible quantity features trend in machine component operation [7; 9; 10; 11]

Trend-1 is called a ‘bath tub’ trend, in which at the beginning of the operation the machinery will experience a running-in process where all of the asperities in the case of gears will be knocked down. In the initial stage of graph trend-1, the line shows a downward trend, indicating a reduction in the wear rate over time, and then gradually changes to a useful working life zone which is the longest period, where a horizontal, straight line indicates that the wear rate is constant. Finally, at the end of this zone, the line will start increasing, indicating an ‘onset of failure’; in the failure zone, the wear rate is higher and larger particles are generated. This trend is an ideal trend, but in real life wear progression of a gear mesh very rarely follows this trend. According to Moubray [12], only 4 % of failures follow this type of trend. In fact, in the experiments conducted for this research, none of the trends produced follow this trend except during the running-in period.

Trend-2 in Fig 2-1 shows that the wear particle generation is constant from the beginning of the machine’s life. In this trend, it is difficult to differentiate between the period of running-in and the useful working life zone, as the wear rate in both zones is the same. However, once the failure begins and the condition of the machine deteriorates, an upward trend in the graph shows more wear

particles in terms of quantity and also sizes are generated. Moubray predicts that only 2% of failure trends will follow this shape. Trend-3 suggests that wear generation consistently increases over time and 5% of equipment failure resembles this trend. Trend-4 shows an increased rate in wear generation during the running-in time, but the wear rate stays the same throughout the remaining life. Moubray suggests that about 7% of equipment failure follows trend 4. Trend-5 suggests the wear generation is at a constant rate from the beginning until the end of life and Moubray suggests about 14% of equipment failure rates follow this pattern. Lastly, in Trend-6, the wear particle generation is reduced during the running-in time but then stays at a constant rate until failure [11]. The most common trend in wear particle generation is Trend-6; about 68% of failure rates follow this shape. It is difficult to determine the onset of failure if the trends stay constant towards the end of the gear's life.

Figure 2-2 shows a real example of wear progression of a spur gear which was tested at NASA [13]. The graph is reproduced from the real data of wear debris analysis, which shows the trend of the wear collected over 250 hours. In this graph, the wear rate reaches about 0.5 mg/minutes before stabilizing at a very low wear rate until hour 200, when the wear rates increase tremendously to indicate that the gear has reached failure zones.

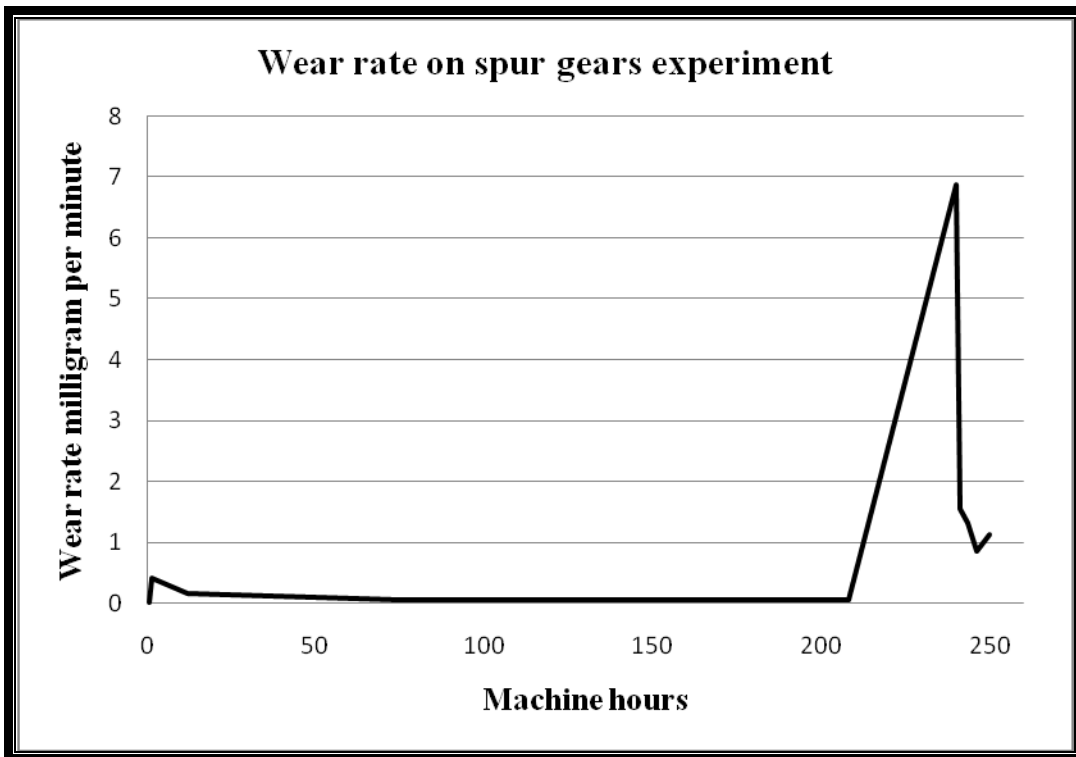


Figure 2-2 real wear progression of a spur gear [13]

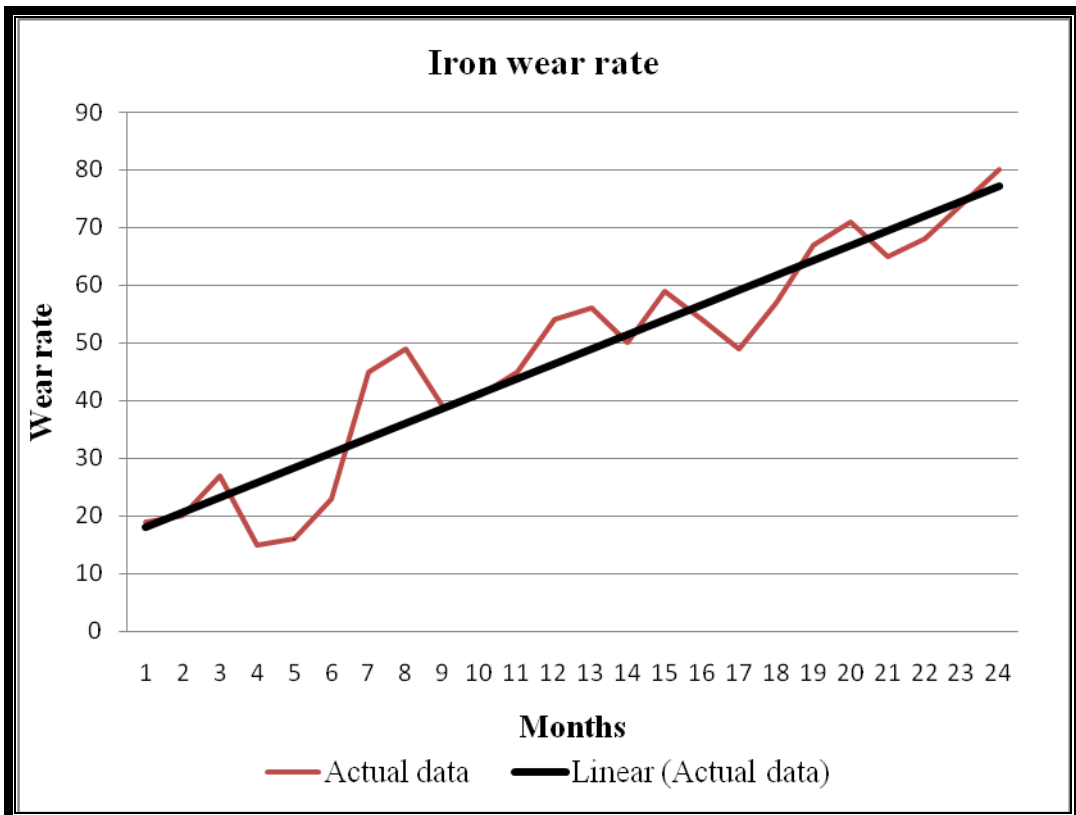


Figure 2-3 : Real wear progression of a compressor [14]

Another real example of wear trends is shown in Figure 2-3 in which 24 months of data were collected from a compressor sump [14]. The trend is quite similar to the trend 3 in that the wear rate continues to increases over time. It is quite difficult to see a downtrend towards the end of life because the parts that wear off would be replaced once the wear reaches a certain level as decided by the maintenance personnel. This strategy tries to avoid catastrophic failure that might affect other components in the system and increase maintenance cost.

Fig 2-4 shows how the size of debris generated becomes larger over the lifetime of machinery, and how the trends of the wear debris generated is used to indicate the onset of failure. As the failure zone approaches, larger particles are generated. The graph also shows the efficiency of the method according to the size of particles. The figure shows the efficiency of spectroscopy for wear debris sizes between 0 to 10 μm , with a higher efficiency for particle size of 5 μm . The ferrography method can be used for particle sizes from 5 μm to 100 μm , with the highest efficiency being at 50 μm . Magnetic debris collection is efficient for the wear debris size of 90 to 1000 μm , with highest efficiency at about 500 μm . This shows that selecting the correct technique for certain sizes of wear particle

analysis is important. However, in the preliminary experiment for this research, the magnetic plug technique was successfully in attracting of particles of less than 100 μm .

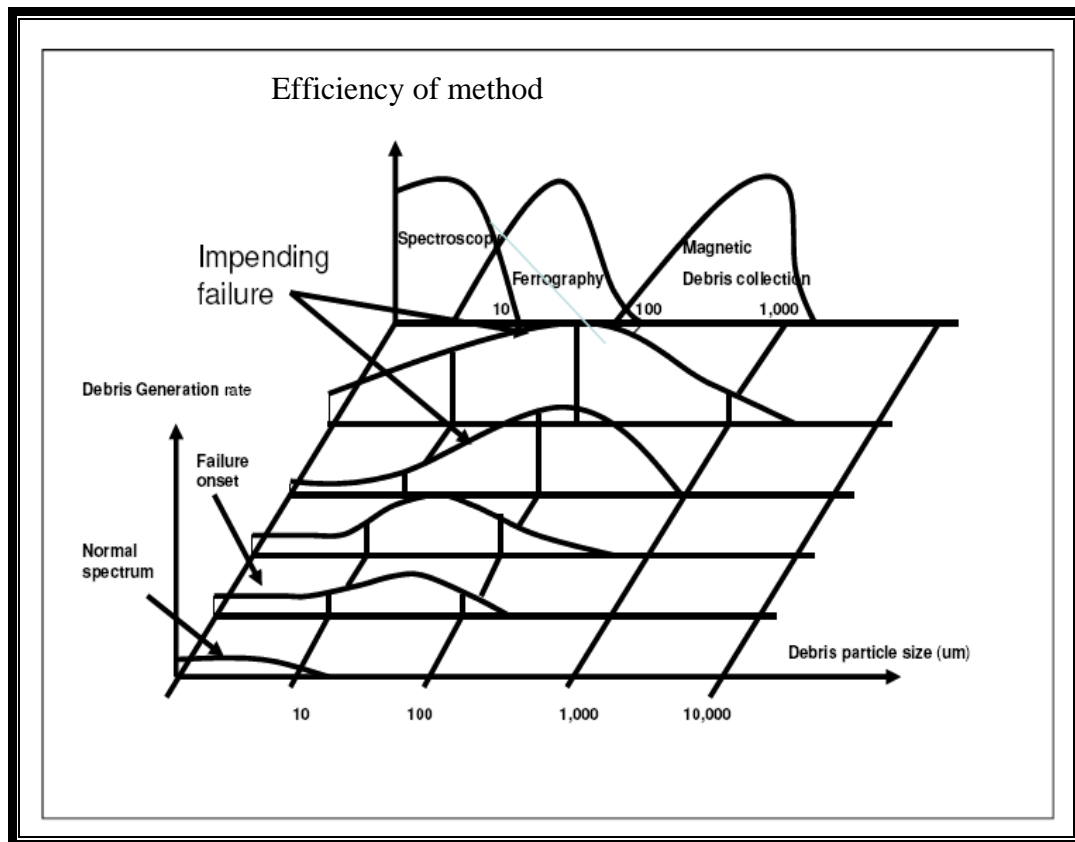


Figure 2-4: Wear particles size distribution versus machinery condition

[8; 9; 10; 11; 17; 20]

2.3 Gear flank stress causing wear debris generation [19].

In order to clearly describe the generation of wear debris from the sliding and rolling action when gears mesh, information on how the meshing mechanism works is essential. A load is applied to the region of the contact point of the two meshing gears and is caused by the sliding and rolling action between them. The contact point becomes flattened elastically when the forces are transmitted. The greatest pressure is at the centre of the flattened area. Fig 2-5 shows the contact points when gears mesh.

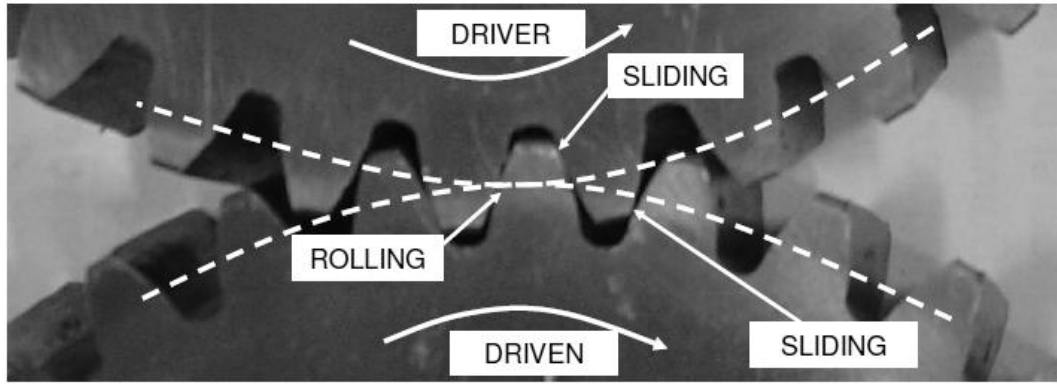


Figure 2-5: Gear mesh contact points [16].

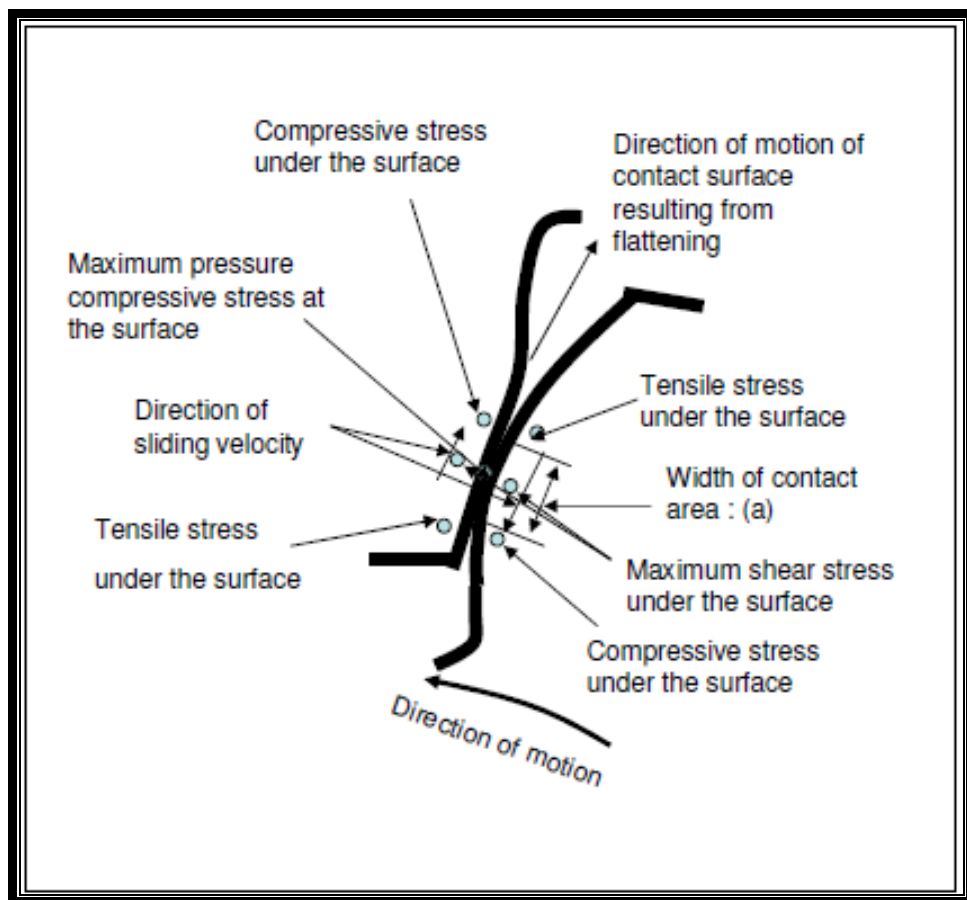


Figure 2-6: Flank load of two meshing gears [19]

Fig 2-6 indicates areas of stress caused by the rolling and sliding action of the gear teeth. The greatest shear stress occurs at a distance of $0.78(a)$, where (a) is a semi width of flattened area. During the rolling process, shear stress increases from zero to 0.3 of maximum surface pressure [19]. In addition, sliding friction components cause further surface stresses, including compressive stress forming before the contact zone and tensile stress just after it. During the rolling process,

the resultant shear stress reaches maximum values of ± 0.25 maximum surface pressure at a depth of 0.5(a) [19]. The area will then experience an alternating stress on each contact, which will lead to surface cracks and plastic deformation. At the same time, the internal shear stress causes cracks under the surface.

2.4 Gear wear phenomena

The most common types of gear wear are pitting, scuffing and scoring [21]:

- **Pitting** wear is caused by surface failure of the material due to continuous stresses that exceeded the endurance (fatigue) limit of the material. High shear stress resulting from rolling contact causes cracks under the gear surface, while tangential stresses originating from sliding effects initiate cracks on the surface. Small metal chunks break off when microscopic cracks propagate and gear teeth frequently fail due to pitting.

Some researchers (Dempsey and Dudley) limit the term “micropitting” or “initial pitting” to pits which are less than 0.396 mm or 1/64 inches and cover a surface area of less than 25 percent of the tooth surface. “Destructive pitting” refers to pits which are larger than 0.396 mm and cover more than 25 percent of the tooth surface. Sizes and area coverage of pits differentiate are the difference between micropitting and destructive pitting. This rule normally covers any gear size, as area coverage is important for determining the stage of the deterioration. The surface area of a gear tooth, which is continuously exposed to stresses exceeding the endurance limit of the material, suffers from destructive pitting which can cause catastrophic failure of the tooth [13, 23].

Factors that contribute or influence the pitting process are material, surface treatment, surface quality, tooth type and shape, operating conditions and lubricant. In the case of material, case-hardened gear teeth better resist pitting in comparison to nitride material and tempered material. The smoother the surface quality such as the one which is manufactured through Electropolishing process, the higher the ability against pitting. On the other hand, the coarser surface gears that are manufactured through sand blasting, the gear tooth surface has lower ability against pitting. Tooth geometry such as tooth shape, meshing angle, helix angle and contact ratio also plays an important role in the pitting process [23]. The bigger the meshing angle, the higher the gear resistance to pitting; similarly,

a higher helix angle improves the load bearing capacity of the gears. The increase in contact ratio between the mating gears will provide stronger ability against pitting. For lubricants, higher viscosity oil provides better oil film thicknesses which reduces the risk of pitting while synthetic oil provides much higher protection against pitting than mineral oil. The velocity of lubricant application is also vital in reducing the risk of pitting; the higher the velocity of the lubricant, the more protection it provides against pitting.

Considering the factors above, the risk of pitting can be reduced by giving attention to the following areas: [23, 24]

- Geometry – optimizing the gear geometry.
- Load – decreasing contact stresses through load reduction.
- Fabrication – making surface gear teeth smooth through proper honing and grinding.
- Materials - using high-hardness material which is properly heat-treated using a carburizing process.
- Lubrication – using the right amount of lubricant, both cool and clean and with required viscosity.
- **Scuffing** results from the rubbing process through small surface irregularities as the gear teeth engage during operation. It is not a fatigue phenomenon and may happen during the early life of gears. In this case, the gear teeth have not had enough operating time to produce smooth surfaces [25]. The phenomenon occurs when gears are subjected to highly loaded conditions with high sliding velocities. In the absence of lubrication, metal-to-metal contact removes the protective oxide layer on the gear metal, while extra heat due to friction welds the surfaces at the contact points. When the gears disengage, metal is torn and transferred between the surfaces. The continuation of engagement and disengagement of the gear mesh will cause the process of welding and tearing of the tooth surface from one tooth flank to another. The scuffing wear is influenced by the critical scuffing temperature, which is the summation of gear bulk temperature and flash temperature as shown in equation 1.

$$T_c = T_b + T_f \dots \dots \dots \text{eq. 1}$$

Where

T_c : Critical temperature

T_b : bulk temperature is the equilibrium temperature of gears before meshing

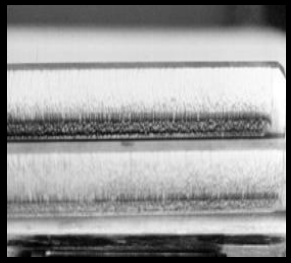
T_f : instantaneous temperature rise caused by local frictional heat at gear teeth meshing point [26].

In order to reduce the risk of scuffing, either T_b or T_f need to be lowered by implementing one or more of the below practices [27] :

- Fabrication - Smoothing tooth surfaces by careful grinding and honing to provide smooth surface which reduces friction during gear meshing.
- Lubrication - Cool the teeth of gears by supplying sufficient cool lubricant which goes through a heat exchanger in its circulation which will reduce the risk of exceeding the critical temperature. Choose high viscosity lubricants blended with antiscuff additives such as sulfur, phosphorus and borate. High viscosity provides a thick film layer which reduces frictional heat and results in a lower flash temperature. In addition, antiscuff additives will react chemically with protected metal gear surfaces to form a very strong solid film to prevent metal contact under extreme pressure and temperature.
- Geometry - Optimize the gear tooth geometry by using small teeth, addendum modification, and profile modification this will lower the bulk temperature.
- Materials - use nitride steels for maximum scuffing resistance. Avoid using stainless steel and aluminium if there is a risk of scuffing.
- Loading - ensure uniform loading throughout the surface of the teeth.
- Operation - use accurate gear teeth, rigid gear mountings and good helix alignment which will reduce friction and flash temperature.
- **Scoring** is caused mainly by failure of lubricant film due to overheating of the mesh area. However, it can also be caused by the misalignment, deflection, and uneven temperature or loads.

Table 2-1 describes the process of different types of gear wear and mechanisms or causes.

Table 2-1: Gear wears process and mechanism [21; 29]

Wear modes	Wear failure
Polishing wear	<p>Process- Slow process of wear - Metals direct contact creates a polished surface on the gear teeth.</p> <p>Mechanism / causes - insufficient lubricant or the gears or operate with a minimum lubricant.</p>
Moderate wear	<p>Process- Wear process occurs where the metal has been removed from the addendum and dedendum of the tooth surface, but still maintaining the operating pitch line as a continuous line.</p> <p>Mechanism / causes - Lubricant contamination. Gears operate near boundary lubrication conditions.</p>
Extreme wear	<p>Process- Uniform removal of relatively large material from the gear tooth surfaces, coupled with the presence of pitting at the pitch line.</p> <p>Mechanism / causes- Insufficient lubricant for the tooth load, presence of fine abrasive particles or contamination in the lubrication system.</p>
Abrasive wear	<p>Process- Appears as a combination of a lapped surface, radial scratches and grooves on the tooth contact points. Mechanism / causes- Particles in the lubricating system consisting of metal particles originates from the gears and bearings, weld spatter, scale or rust; and sand, dirt or other environmental contaminants.</p> 
Corrosive wear	<p>Process- Visible as surface deterioration - chemical action of active ingredients in the lubricant</p> <p>Mechanism/causes- Wear process caused by oil break down and intrusion of corrosive elements in the</p>

	<p>lubricant that “attack” the gear contact surfaces. This process affects the grain boundaries which led to the formation of fine, evenly distributed pitting.</p>
<p>Surface fatigue failure</p>	
Pitting 	<p>Process- Pitting tends to redistribute the load by gradually leveling "high contact" spots and terminates the process once the load has been redistributed. The process eventually causes burnishing to the pitted surface and improves its appearance.</p> <p>Mechanism / causes- Occurs at the gear teeth that are over-stressed.</p>
Destructive pitting 	<p>Process- Appears as much bigger pits than initial pitting</p> <p>Mechanism /causes- More severe overload conditions that cannot be contained by the formation of initial pitting. This is a result of continuous stress cycles building up, which support the pitting wear process that deteriorates and eventually destroys the tooth profile</p>
Spalling 	<p>Process- Similar to destructive pitting with the exception that the pits are larger, relatively shallow and irregularly shaped. Large and irregular voids will be created due to rapid breakages of the edges of the pit. These large voids will eventually join to create even bigger pits.</p> <p>Mechanism / causes- Excessively high contact stress levels.</p>
Case crushing	<p>Process- Longitudinal cracks on the surface of a single or two teeth, and later spread to a break away of a long piece of the tooth surface.</p>



Mechanism / causes- When the case is significantly harder than the core, subsurface fatigue failure will occur. This wear process can also happen as the surface contact stress at high cycle levels surpasses the material's endurance limit.

2.5 Wear debris classification

Wear debris carries with it information about its origin and the health conditions of the machine component. This information is required to be systematically and effectively analyzed to yield an appropriate action to be taken on the machinery. One of the ways to make the information gathered become meaningful is by classifying the particles into different types that can be used as a reference. Wear debris can be classified into morphological and compositional attributes. Sections 2.5.1 and 2.5.2 will briefly explain both attributes.

2.5.1 Particle morphology

Recent developments in WDA suggest that wear particles can be classified into at least six morphological attributes, such as a particle size, shape, edge details, colour, thickness ratio and surface texture [30]. Theoretically, the size would indicate the severity, the wear rate and the wear mode. The other morphologies could be used to identify the source of the wear, the wear mode and the severity of the wear. The amount and concentration of wear would also assist in determining the wear rate and wear severity [30; 31]. Figure 2-7 simplifies how morphology can be used to diagnose the wear of machine components.

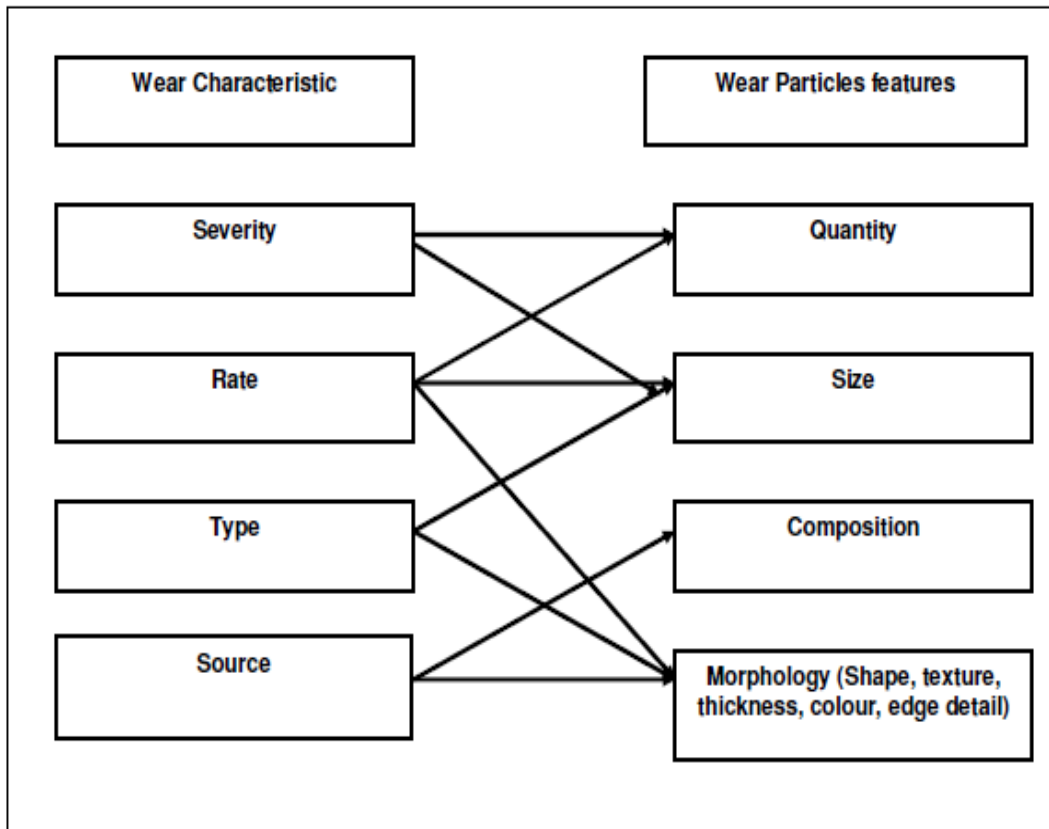


Figure 2-7: Relationship between wear characteristics and wear particles

[30]

Here, the morphology of the wear debris particles is detailed.

2.5.1.1 Particle's size

Previous studies have linked particle size and wear type [19]. The following table explains the connection between the sizes and the possible wear types:

Table 2-2: Relationship between type of particles and size [6; 19].

	Wear type	Wear debris size trend
1	Rubbing wear / break in wear	0.5-1.0 μm or less in major dimensions and may increase to 20 μm
2	Cutting wear	2 - 5 μm wide and 25-100 μm long
3	Rolling fatigue <ul style="list-style-type: none"> • Spall particles • Spherical particles • Laminar particles 	10-100 μm with a major dimension to thickness ratio of 10:1. 3 - 10 μm 20-50 μm with major dimension to thickness ratio 30:1
4	Combined rolling and sliding	2 - 20 μm with major dimensions to thickness ratio between 4:1 to 10:1.
5	Severe sliding and rolling	> 15 μm with major dimension to thickness ratio of 10:1

2.5.1.2 Shape

The following are the shapes of wear debris as suggested by Roylance & Hunt [10; 30; 32].

- **Sphere** – a three-dimensional uniform particle. Debris typically found during the running-in period. Usually spherical particles begin to appear around 60% through the life of the bearing. At 80% – 90% through the life of bearing, these particles are generated in large quantities and are increased rapidly towards failure.
- **Distorted smooth ovoid** – egg-shaped particles. Distorted smooth ovoid (pebbles or granular) usually appear in the following three forms: black granular particles, orange or red granular particles, and atmospheric particles. Black and orange granular particles are mostly due to oxidative wear and are commonly caused by excessive component operating temperatures and/or inadequate lubrication. Atmospheric particles enter into the machine system due to poor sealing and may intensify the wear process or cause blockages in lubricant paths.

- **Chunks and slabs** – chunks are rough, well-proportioned lumps, with width, breadth and length not too dissimilar in dimension, and are usually metallic. Slabs are thick, flattish pieces of metal with rough edges. Fatigue spall, coupled with pitting and break up, produce chunks of sharp rough metals, while rough slabs are generated by sliding action or by fatigue involving extremely high temperatures or inadequate lubrication.
- **Platelets and flakes** – platelets imply flat and smooth whereas flakes are thin but may be slightly twisted. Platelets come from running-in and normal wear. Platelets and flakes usually appear in the following five forms:

Table 2-3 Platelets and flakes' sizes and appearance [11; 33]

Size	Period of appearance	Indication
Very large metal flakes often above 1 mm in length	Rapid failure zone	Total failure is imminent
Large metal flakes about 1 mm in length	Rapid failure zone	Surface fatigue
Medium sized flakes of 150 µm to 1 mm in length	Catastrophic sliding wear occurs	Complete breakdown of component surface
Lesser medium sized flakes of 15 µm to 1 mm in length	This indicates that soft material such as aluminium under wear	Local adhesion caused particle to be larger and higher wear rate
Small sized flakes of 1 µm to 15 µm in length, 1 µm or less in thickness	Running in wear zone	Normal wear

- **Curls, spirals and slivers** – mainly produced due to temperature differences across the debris, causing the particles to distort.
- **Rolls** – a spiral and a platelet. Typically starts like a platelet, and then is either rolled to produce a curve effect, or changes shape due to temperature effects. A roll is a combination of spiral and platelet shape particles, and their generation and behaviour in the wear process is the same as platelets.
- **Strands and fibres** – look like needles and strings. An increase in long-thin particles indicates an increase in metal deterioration. Thin foreign particles can cause an increase in the severity of wear, especially in manufacturing machine systems, by acting like contaminants. Long thin particles usually appear

in five forms, which are Large splinters (>1 mm), small splinters, tiny short hair-like metal strands, miniature spirals, loops and bent metal wires, and rolling pins of polymeric materials.

Table 2-4: Shape of the wear debris [10; 11; 33]

7. Sphere 	1. Distorted smooth ovoid 
2. Chunks and slabs 	3. Platelet and flakes 
4. Curls, spirals and slivers 	5. Rolls 
6. Long thin particles 	

2.5.1.2 Quantitative basic shape analysis

In quantifying and distinguishing the shapes of the particles, the researchers used numerical values as descriptors for different types of particles [29]. Some of the methods applied were form factor in determining roundness factor (RF) and aspect ratio (AR), Fourier analysis in determining the deviation of particles from roundness, curvature analysis in determining the edge detail using standard deviation, skewness and kurtosis, fractal analysis in determining edge detail and profile and size analysis using the Weill bull parameter [16]. Table 2-5

lists the mathematical formulae used to calculate the descriptors of the particle's shape.

Table 2-5: Wear particle shape and size descriptors [30].

Method	Descriptor	Definition
Form factor	Aspect ratio (AR) Roundness factor (RF)	Length / breadth $(\text{Perimeter})^2/4\pi(\text{Area})$
Fourier analysis (Profile & Edge detail)	$1^{\text{st}}, 2^{\text{nd}} \dots,$ harmonics	$C_n = \sqrt{C_{X_n}^2 + C_n^2}$
Curvature analysis (Edge detail)	Standard deviation (R_q) Skewness (R_{sk}) Kurtosis (R_{ku})	$R_q = \sqrt{\frac{\sum_{i=1}^n (X_i - \bar{X})^2}{n-1}}$ $R_{sk} = \frac{\sum_{i=1}^n (X_i - \bar{X})^3}{n R_q^3}$ $R_{ku} = \frac{\sum_{i=1}^n (X_i - \bar{X})^4}{n R_q^4}$
Size analysis	Weibull parameter $\alpha \beta$	$P(\chi) = 1 - \exp \left\{ - \left(\frac{\chi - \chi'}{\alpha} \right)^{\beta} \right\}$

The ratio of length to width of the minimum enclosing rectangle is termed “aspect ratio” while the term “roundness factor” refers to the closeness of the shape to a circle. Meanwhile, Fourier analysis is suitable for measuring the deviation of particles from roundness.

In Fourier analysis, the third harmonic is a measure of triangularity, while the fourth harmonic is a measure of blockiness or squareness. The way to identify whether a shape has properties of triangularity, blockiness or squareness is by calculating the C_n coefficient for the particular shape. Then, the value of the coefficient is matched with the number of harmonics, where the coefficient value shows the high value. Figure 2-8 and Figure 2-9 provide an example on how a

shape is identified using the third harmonic for triangularity. In figure 2-9 the highest amplitude refers to the third harmonic.

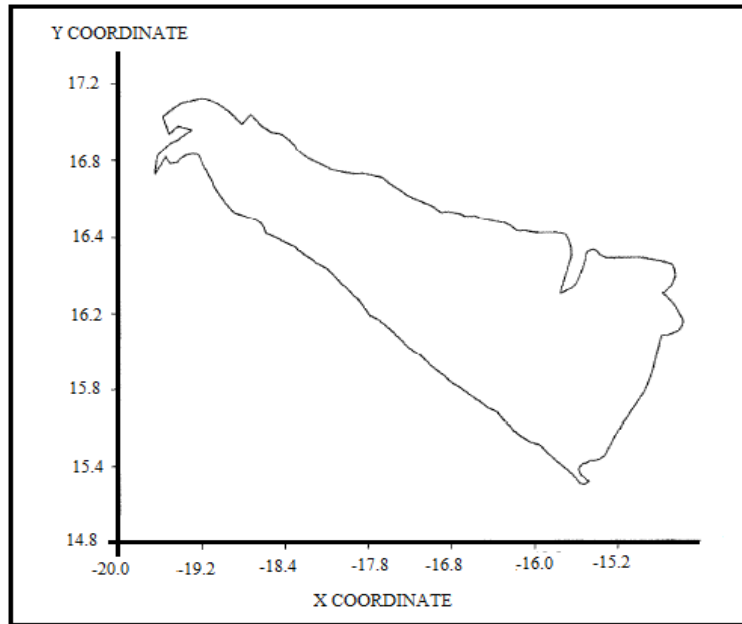


Figure 2-8 Original profile of a particle obtained during severe sliding wear.
[84]

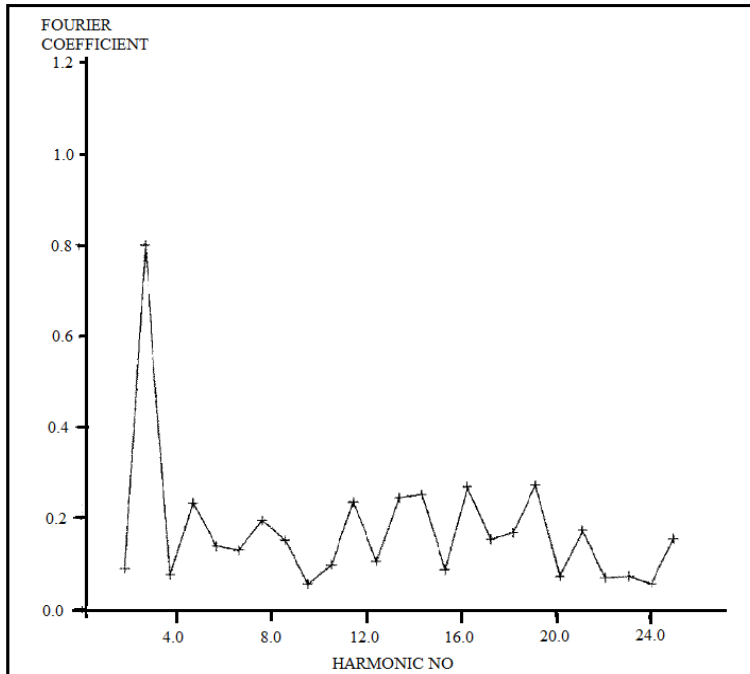


Figure 2-9 Harmonic plot of profile shown on figure 2-8 [84]

The function of curvature analysis is to measure the nature and angularity of the edges of wear debris particle borders. This refers to angle changes that occur along the perimeter profile by moving three adjacent points located on the

border. Then, two lines are drawn through the points and intercept to form an angle. The angle is measured from line 1 to line 2, which is positive when rotating clockwise and is negative if rotating anti-clockwise [30]. A positive angle represents a convex shape, while a negative angle indicates a concave shape. Fig 2-10 shows the technique of edge details.

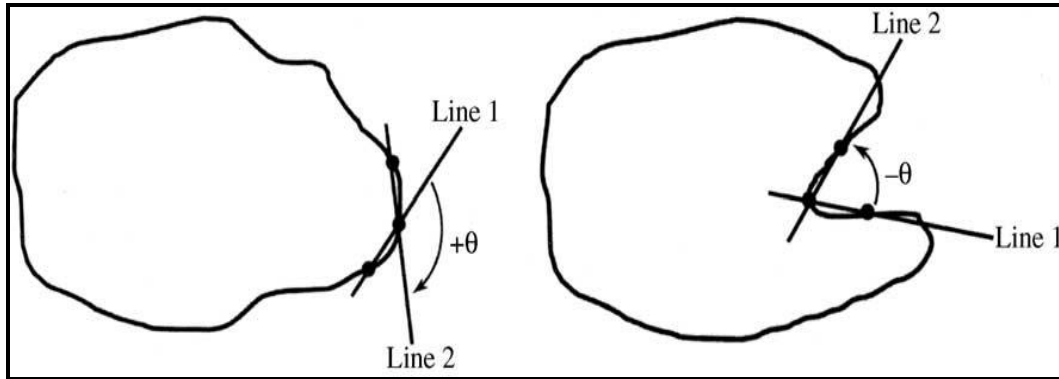


Figure 2-10: Technique of edge detail [30]

In addition, some researchers also use statistical techniques in curvature analysis. Aspect ratio (AR), Roundness Factor, standard deviation, skewness and kurtosis were applied to different type of known particles. The parameters in Table 2-6 show the data for different shapes of particles published in previous research where statistical technique and equations listed in Table 2-5 were applied.

Table 2-6: Shape parameters [34]

Particle type	Shape parameters				
	AR	RF	R _q	R _{sk}	R _{ku}
Rubbing	1.1-1.2	1.5-1.6	22-24	0.0-0.6	4.0-5.0
Sliding	1.5-4.0	2.2-3.6	27-32	0.5-1.5	4.2-5.7
Pitting fatigue	1.5-2.0	2.6-2.9	40-43	(-0.4)-(-0.9)	3.4-4.5
Cutting	3.3-12.5	6.9-17	30-35	0.7-2.5	5.9-6.8

Weibull analysis is used in examining size distribution for determining the wear condition of gears. Mean and variance are the two important indicators in predicting the change and extent of wear of the component. For example, the

change from a mild to severe wear in one ball point test was indicated by the increase of mean particle size. In addition, an increase in the number and size range of particles being generated indicates the increase in wear rate and corresponds to an increase in the variance of the distribution [85].

2.5.1.4 Colour

Myskin [35] used colour to identify material composition using an off-line technique in which samples are placed under a microscope and colour images are captured by a charge coupled device (CCD) camera. While the technique is able to recognize common material compositions such as brown for copper and a reddish colour for iron, it could not differentiate metals such as antimony and aluminium, which have the same colour.

2.5.1.5 Surface texture

Laghari classified surface texture of wear debris into smooth, rough, striation, holes, pitted, cracked, and serrated. Some of the image samples are presented in Fig 2-11 [36].

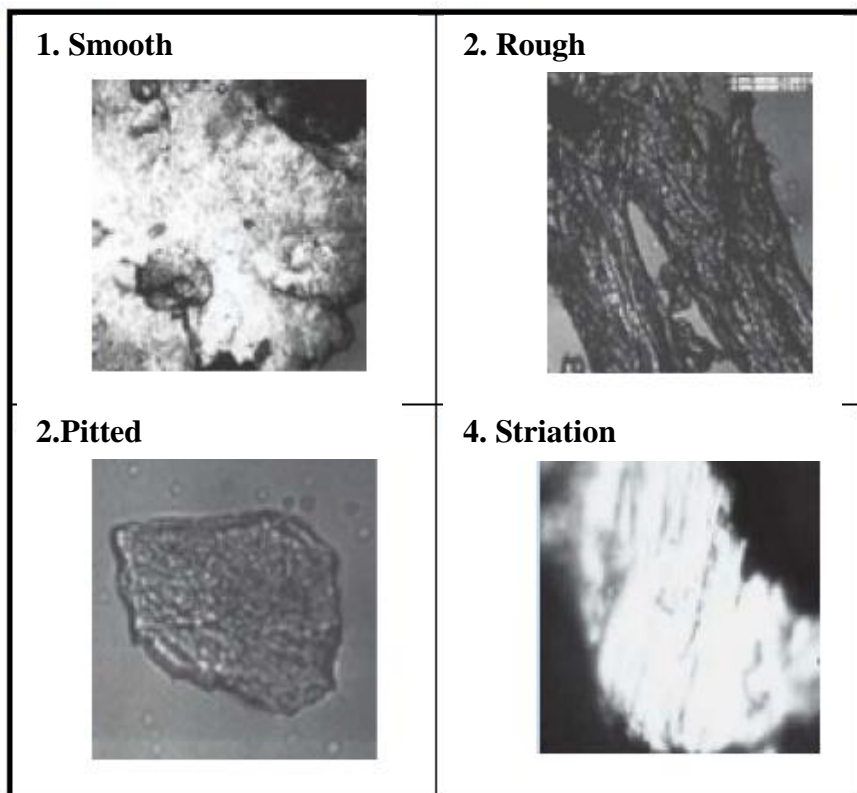


Figure 2-11. Types of surface textures [21]

2.6 Types of wear debris particles.

Recently, many researchers have tended to concentrate on six main types of wear debris particles and provide diagnostics in terms of the presence of the types of the particles as stated below [11; 32; 33; 36]:

- **Rubbing** – Random outlines of shape boundary images. Generated through the broken parts of a shear mix layer and categorized as a normal wear particle; an increase in quantity forecasts impending disaster. The particles are found in most lubricants in the form of platelets.
- **Severe Sliding** – Recognized by a surface containing scratches as parallel grooves, signifying the breakdown of lubricating films and resulting in an unhealthy machine condition. Severe mode reached when the concentration of the particles increases, and scratches and striation marks become more prominent.
- **Cutting wear** – Long curved particles, which are generated when one surface penetrates another, and the presence of large numbers of cutting particles indicates the cutting wear process is ongoing.
- **Spherical** – Like a small ball, these are normally generated in bearing fatigue cracks from rolling bearing fatigue, cavitations, erosion, welding, or grinding processes with high temperatures.
- **Chunk** – Chunky particles will normally have one flat or worked surface, while the other three perpendicular dimensions are uneven and irregular with a jagged boundary profile. These particles are normally generated from rolling fatigue and combined rolling and sliding. The presence of chunk particles indicates a high load and/or excessive rotational gear speed. Figure 2-12 shows images of wear debris particle types.

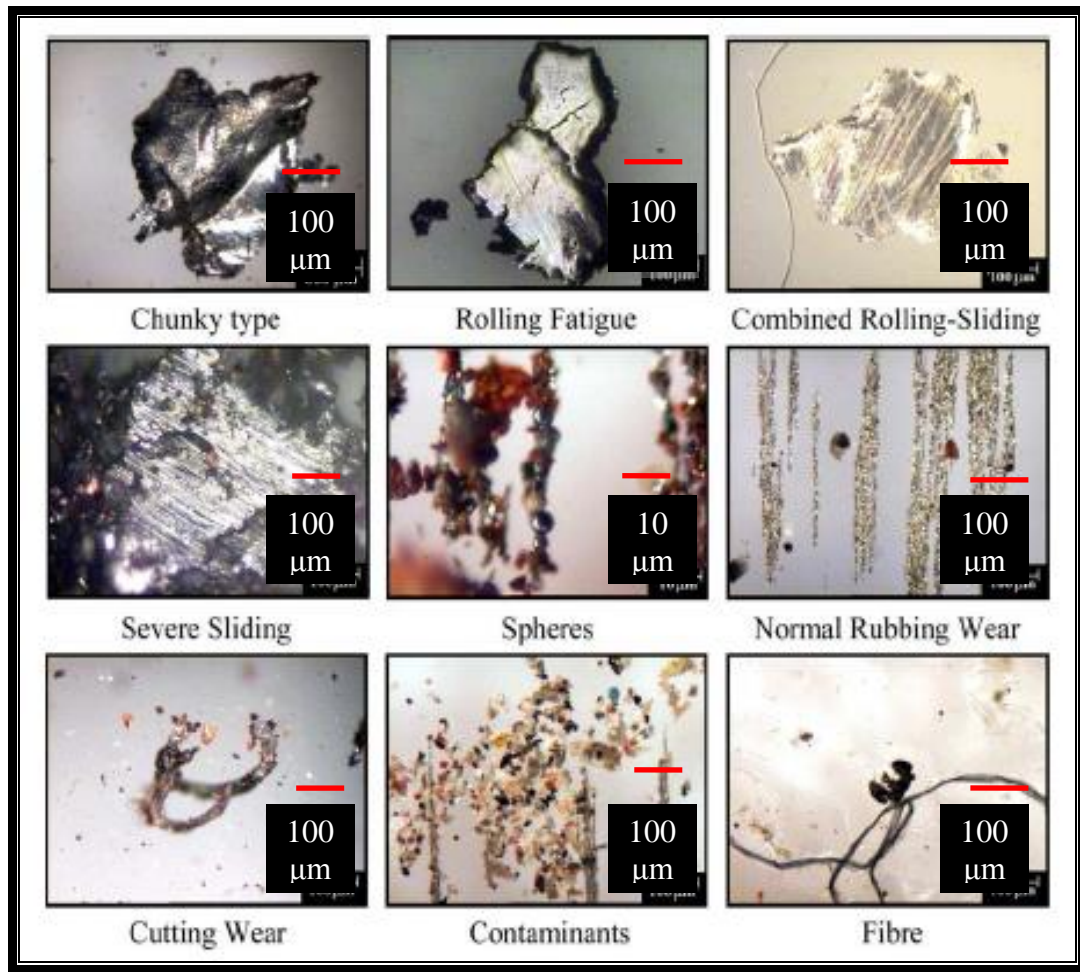


Figure 2-12: Types of wear debris particles [30].

2.7 Techniques of wear debris analysis Technology

There are various techniques implemented in wear debris analysis. The following are the most common techniques used:

- **Dielectric Constant** - A dielectric is an insulator and a dielectric constant is the ratio of electric flux density created in a material to the value in the vacuum provided by the same electric field strength. The sensor [10; 37] detects any change of dielectric constant due to contaminants such as oxidation, water, mixed fluids, acids, and wear debris.
- **Magnetic Flux** - Estimation of the concentration of ferromagnetic particles is done through means of a fixed magnetic field. The field detects the particles and is subsequently modified by the presence of the particles. The change in flux can then be translated into the ferromagnetic particle concentration through an algorithm [10; 37].

- **Magnetic Collection Switch/Grid** - Opposing electrodes by means of an electric grid or plates attract ferromagnetic particles and the existence and general quantity of conductive magnetic particles are detected by current flowing between the electrodes. This method estimates particle size and concentration by means of the gap between the grid/plates and a time-sequence [10; 37].
- **Induction Sensors** - When a particle enters the magnetic field generated by the sensor, the magnetic flux is modified. Induction techniques use this concept to detect the presence of the particles. A fluid sample containing the wear debris particles is introduced into a container or tube with an inductive coil attached around it to create the magnetic field. The sensor is capable of differentiating between ferrous and non-ferrous debris and electronic circuitry has the ability to ignore signals from air bubbles [10; 37].
- **X-ray Fluorescence (XRF) Spectroscopy** - In identifying and quantifying the chemical element of wear debris particles, the sample is irradiated with X-rays, energizing electrons to higher levels. As electrons return to their initial state, they release X-rays at an energy level, which contains the signature of a particular element. The magnitude of the energy level is directly related to the concentration of the element. The element and its concentration can then be identified and measured [10; 37].
- **Laser imaging** - A laser imaging optical flow cell is used to examine equipment fluids such as hydraulic oil, lubricants and fuels. It captures images of the fluid which contains wear debris particles as it passes through a flow cell, and is able to measure the size and classify the type of the particles [10; 38-40].
- **Dielectric Loss Factor** - Water, glycol and oxidation product contamination all increase the dielectric loss factor or Tan delta. Similarly, metallic wear, debris, and soot, which are electrically conductive, also increase Tan delta [10; 37].
- **Electrostatic sensor** -This technique, originally invented to detect debris in the gas path of a jet engine, monitors the electrostatic charge and any changes associated with debris. An advantage of the electrostatic technique is that it can directly measure debris concentration and hence can be used to provide an early warning for component degradation [10; 37; 41-42].

2.8 Wear debris Analysis sensors [40]

There are many sensors on the market that use the techniques described in the previous section. Table 2-7 lists some of the sensors which use different technology and methods. It shows numerous efforts used to ease the analysis of wear debris and its related parameters.

The technology use by the sensors ranges from magnetic collection, magnetic flux and inductance, dielectric loss factor, infra-red, optic, laser imaging, microscope, and ultrasonic methods. The majority of these techniques use particle counting and size measurement to predict equipment deterioration and others look at parameters such as viscosity, oil quality, and cleanliness and wear metal. There are various limitations in the sizes that are able to be measured by these different types of sensors. The sampling methods are broadly online and inline in nature. The newer technology sensors appear to be applying laser sensor and particle detection automatically, further reducing the need for labour.

The table below shows the application of wear debris in various types of industries, which indicates that the wear debris analysis technique is gaining more attention in condition-based maintenance from industry. In the context of this research, there are still very few sensors which evaluate the image of the particle and its volume. Therefore, research on particle imaging, either in 2D or 3D (with the volume of the particle) should be very rewarding.

Table 2-7: On line / in-line / off-line sensors for condition monitoring of lubricants. [40]

BASIC TECHNOLOGIES						
Product	Company	In-line/On-line/Portable	Technology used	Measure	Application	
Smart Zapper® Electric Chip Detector	Eaton Engineered Sensors	In-Line, On-Line	Magnetic collection/grip	Particles ≥ 100 µm	-----	
QDM® (Quantitative Debris Monitor)	Eaton Engineered Sensors	In-Line, On-Line	Magnetic flux	Particles ≥ 50 µm	Gas turbines	
TechAlert™ 30	MACOM Technologies Ltd.	On-Line	Magnetic flux	Particles > 1 µm	Gearboxes, oil collectors	
TechAlert™ 20	MACOM Technologies Ltd.	In-Line, On-Line	Magnetic flux	Particles > 1 µm	Gearboxes, hydraulic systems, bearings	
TechAlert™ 10	MACOM Technologies Ltd.	In-Line, On-Line	Magnetic inductance	Particles > 50 µm	Gearboxes, pumps, turbines, bearings	
TechAlert™ TA Diviner	MACOM Technologies Ltd.	In-Line	-	Water	Hydrocarbon fluids	
MetalSCAN	GasTOPS Ltd	In-Line	Magnetic inductance, magnetic flux	Part. ferro ≥ 100 µm Part. No-ferro ≥ 500 µm. Total contamination	Severe environments, gears, bearings, military applications	
PATROL®	Manor Technology Monitoring Ltd.	In-Line	Magnetic inductance, magnetic flux	Particles ≥ 25 µm	-----	
MIDAS	Manor Technology Monitoring Ltd.	On-line, off-line	Magnetic inductance, magnetic flux	Ferrous Particles	-----	
Grid Switch®	T. F. Hudgins Inc. Spinner II Products	On-Line	Magnetic collection switch/grip	Wear Particles	Engines, gearboxes, transmissions, compressors	
ANALEXrs Oil Condition Sensor	Lubrigard Ltd.	On-Line	Dielectric loss factor	Oil condition	Engines, gearboxes, transmissions, compressors	
ANALEXrs Particle Content Sensor	Lubrigard Ltd.	On-Line	Inductive coil	Particle content	Engines, gearboxes, transmissions, compressors	
ANALEXrs Total Ferrous Debris Sensor	Lubrigard Ltd.	On-Line	Magnetic inductance	Ferrous debris	Engines, gearboxes, transmissions, compressors	

Table 2-7: continued

Product	Company	In-line/On-line/Portable	Technology used	Measure	Application
Lubrigard Oil Condition Sensor	Lubrigard Ltd.	On-Line	Dielectric loss factor	Soot, Oxidation products, Water, Glycol, Metallic wear particles, Changes in TBN	Engine Oils, Hydraulic Oils, Gearbox Oils, Transmission Oils, Compressor Oils
FluidScan™	Foster-Miller	On-Line	FTIR	TAN,TBN; oxidation, water, glycol, soot, nitration, sulfatation, additives AO, AW and contamination with other oils	Railroad locomotives, mining & heavy construction, power generation, marine,
OILPro	PNNL/Belhaven	On-line	X-ray, IR,	TAN, TBN, Cleanliness, oxidation, Viscosity, water, fuel, wear metal	Size:30cm/60cm/90cm. Hydraulic systems, lubrications
Debritect DT100/200/300	Elcomatic	On-line	Magnetic	Submicron and greater / Water and Moisture	Industrial applications
Continental TEMIC	QDiS - Innovative Online Diagnosis of Engine Oils	In-line	Dielectric	Oil temperature, level and quality	Automotive
Fraunhofer Munich	Oil Sensor	In-line	Dielectric	TAN, TBN, oil quality	Automotive, engines, hydraulic systems
Fraunhofer Munich	Broadband Spectrometer (BBS)	On-line	Mid-IR	Water	Industrial processes
Fraunhofer Munich	Dynamic Derivative Spectrometer (DDS)	On-line	UV	Detection of fluids, gas and solids	Industrial processes
MSC	CSI TRIVECTOR Oil Analyser	Off-line	-	Water, wear, particle count and wear debris analysis	Industrial processes
EESIFLO	EASZ-1	On-line	Dielectric	Water	Fuel, lubricating and hydraulic oil
TRANSLUME	OS-21	On-line	Optic	Oil quality	Engine oil

Table 2-7: continued

NEW TECHNOLOGIES					
Product	Company	In-line/On-line/Portable	Technology used	Measure	Application
On-line Model 600T-LP	Spectro Analytical Instruments Inc	In-Line	X-ray fluorescence XRF	N/A	Lubricants
Laser Net Fines	Lockheed Martin Corp. and FRAS Technology	On-Line/Off line	Laser imaging	Counters >5 µm. Shape classifier >20 µm	Hydraulic Oils, gear oil, and all kind of oils
Oil-Line Sensor	Smiths Aerospace Electronic Sensors	In-Line, On-Line	Electrostatic collection	Particles ≥ 20 µm	Aerospace industry
CPD-DAQ Sensor and Software	Qcept Technologies	Off-Line	Blotter analysis	N/A	Industrial application
RULER	FLUITEC Int.	Off-Line	Voltammetry	AO concentration	All kind of Oils with AO additives
Rockwell Automation	Enpac Oil	On-line	Pore blockage	Viscosity, wear particles	Oil cleanliness, gear, bearing and pump wear
Malvern	Microscope image analysis	Off -line	Microscope	Measure size 0.5 to 1000 µm and identify shape	All type of particles
Schubert & Salzer	Particle detector	In-line	Ultrasonic	Particle detection	All types

2.9 Computer aided software, artificial intelligence and algorithms on WDA

In wear debris analysis research, it is necessary to understand the software used in assisting the analysis of wear debris. Software functions typically include data acquisition such as image capturing and data processing. Examples include calculating dimensions, identifying edges, classifying shapes and diagnosing the failure of machine components.

- **CAVE** - Computer Aided Vision Engineering [6; 43-45] – Developed to classify particles using an image analysis approach and involves being connected to a microscope-mounted camera. CAVE uses Fourier transform and curvature analysis of particle outlines as input parameters to a neural network which classifies the particles. The system was considered for implementation by the Royal Air Force (RAF) but was not adopted due to complexity. In addition, is the system was not able to distinguish between overlapping particles and tended to count them as a single entity.
- **CASPA** – Computer Aided Systematic Particles Analysis [6; 43; 45] – an offline debris classifier. Using this system, the operator answers questions regarding the morphology of the particles. The system uses a combination of expert systems and fuzzy logic algorithms. Users claimed that the system was not fully successful as it could not adequately capture the expert's thought. The system was highly tedious due to repeated human intervention.
- **Visual CASPA** – an electronic wear particle atlas [43]. Morphological characteristics were used to match an image against a number of stylized cartoons. The task requires the user to go through a decision-tree process. The limitation of this system is that particles are not always classified into discrete morphological types. Errors in the early stages of the process will lead to misclassification in the decision tree process.
- **SYCLOPS** – This software-based wear debris classification system was developed for the RAF to detect early failure in helicopter gearboxes. It incorporated classification data into a graphical user interface specifically developed to meet the requirements of the operators. It removes inconsistency in interpretation of wear debris among different personnel. However, the data needed to be inserted manually into the system for classification. This system was still

dependent on the off-line method and human input. Figure 2-13 shows the SYCLOPS classifier menu [6; 43; 44].

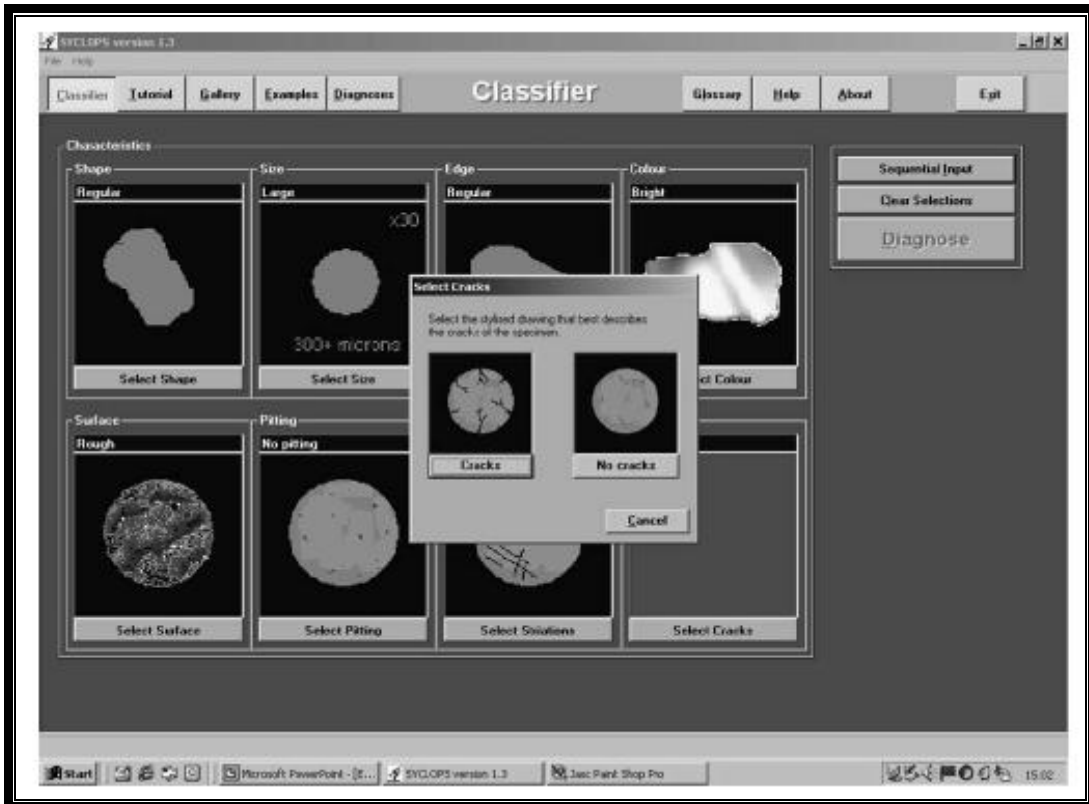


Figure 2-13: SYCLOPS classifier [6; 43].

- **WPTA (Wear Particles Texture Analysis) & CATA (Computer Aided Texture Analysis) [46]:**

The former is a multiple-window, hierarchical interactive graphics interface that controls the software environment. CATA is a computer system that assists in texture analysis.

- **Expert system [47; 48]:** A system designed to emulate the human ability to interpret comprehensive data obtained from particle analysis in order to assess wear modes and wear rates. The data need to be entered manually into the system to obtain diagnostic results. Subsequently, it will provide a recommendation of further action which needs carried out on the component that generated the debris. The objective of the system is to identify the failure modes and wear rates, and to have an analysis of changing trends. The system is fully computerised and evaluates three dimensional (3D) images acquired using Laser Scanning Confocal Microscopy (LSCM). It uses an offline sampling method, which requires samples to

be prepared before the analysis. However, the software itself is an extremely useful tool to determine wear rates and wear mode.

- **Fuzzy grey system** [49]: The primary purpose of this system is to reduce the role of human experience and expertise in analyzing the wear particles. It uses numerical descriptors to characterise features of the following six wear types of particles: rubbing, cutting, spherical, laminar, chunk, and severe sliding. In summary, this system has the capacity to identify images and classify them numerically, as shown in the following Figure 2-14 and Table 2-8.

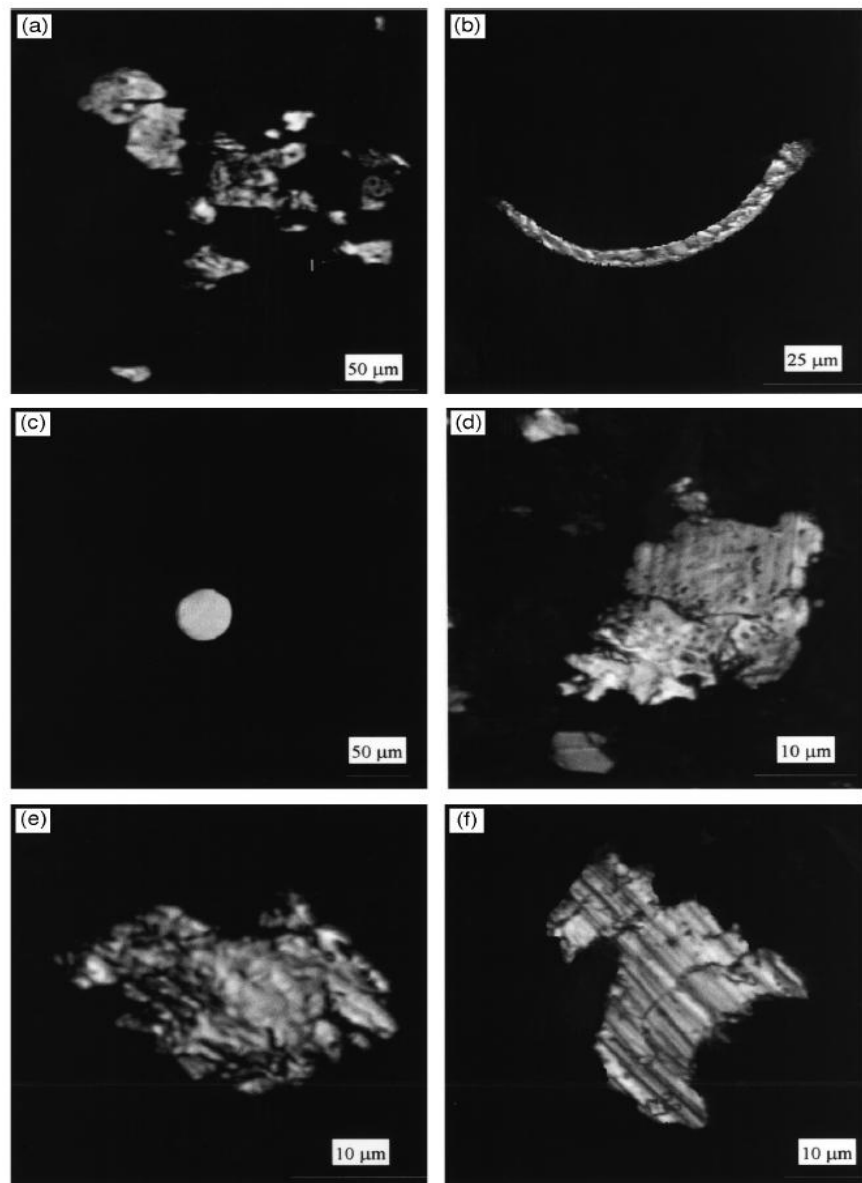


Figure 2-14: Images of wear debris particles [49].

Table 2-8: The relational grades of the test particles shown in fig. 2-12 to six types of wear debris [49].

Figure	Rubbing	Cutting	Spherical	Laminar	Chunk	Severe sliding
a	1.00	0.00	0.00	0.00	0.00	0.00
b	0.00	1.00	0.00	0.00	0.00	0.00
c	0.00	0.00	1.00	0.00	0.00	0.00
d	0.00	0.00	0.00	0.84	0.75	0.77
e	0.00	0.00	0.00	0.75	0.81	0.09
f	0.00	0.00	0.00	0.74	0.70	0.80

- **Neural network** [45; 50; 51] – This is another system which automatically classifies wear debris particles to reduce human intervention. It uses two networks, which are Fuzzy Kohonen Clustering Networks (FKCN) and Multi-Layer Perception neural networks (MLP). Both networks can naturally capture the characteristics of wear particles after several phases of training. These systems are also able to classify particles automatically.
- **Integrated intelligence system** [52] – This system shows how a complete system could be developed for analyzing wear debris particles. The system has at least three main tasks. The first task consists of particle counting, the measurement of particle sizes and size distribution, particle shape, surface roughness and surface texture. The second task is using the neural network of the grey system to classify the particles numerically by describing distinctive characteristics of wear debris. Finally, an expert system acts as a machine-condition monitoring and fault diagnosis tool. It assesses the information and translates it into features of wear debris as well as predicting the condition of the machine. Figure 2-15 summarizes the components of this system.

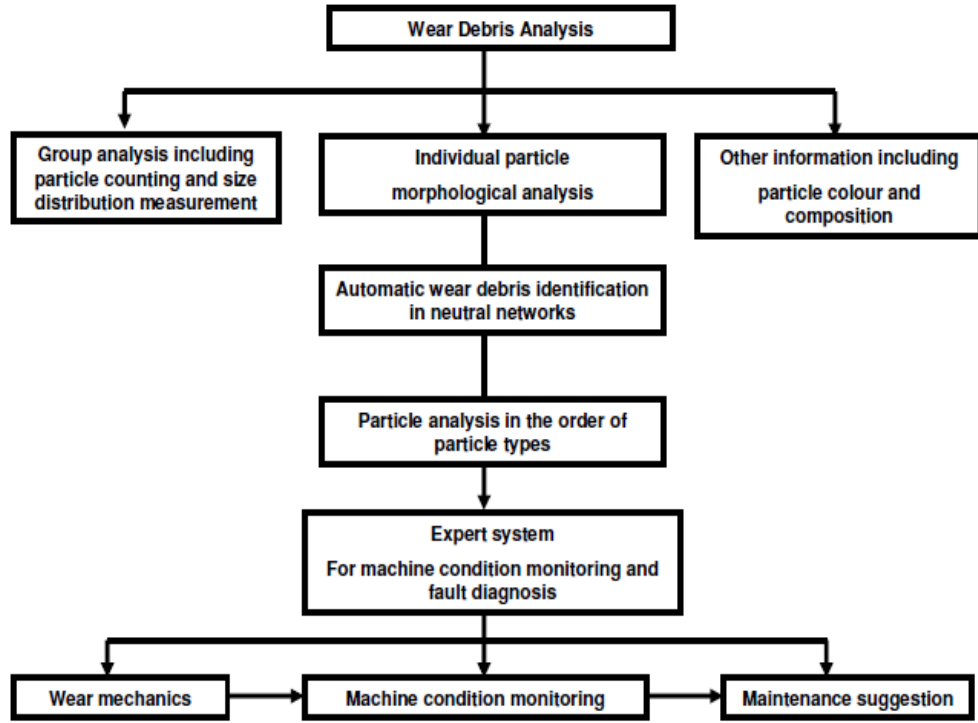


Figure 2-15: The components of the integrated intelligence package for wear debris analysis [52]

Table 2-9 shows a sample of a result from the analysis of particles. Two techniques (neural network and fuzzy grey system) are used to assist in automatically classifying the wear debris numerically.

Table 2-9: A sample of three dimensional analysis results of particles. [52]

Boundary analysis					Surface analysis			3D info	
Area (μm^2)	Length (μm)	Fibre Ratio	Roundness	Fractal dimension	Rs	Rq	γ^2	Height aspect ratio	
5463					2.43			0.13	
	105.38					3.04		0.13	
		2.44	0.63				0.5		
			0.63	1.12					

Finally, all of the above functions are integrated using interfaces which act as a communication channel between the user and the package [52].

- **Knowledge Based Wear Particles Analysis (KBWPAS)** [51; 53] – This system allows an automated and systematic approach to wear particles identification. To ensure consistency in wear judgment predictions, the system links directly to wear processes and wear modes occurring in machinery. Eventually, it becomes able to standardize and reduce dependency on human experts. In KBWPAS, particle knowledge is represented as a class which is used to identify particle types, their attributes, and their relationships. The class could be represented by six wear particle morphologies, with priorities related to each attribute and percentage weighting factors associated with each priority. The strategy of the KBWPAS is summarized in Fig 2-16.

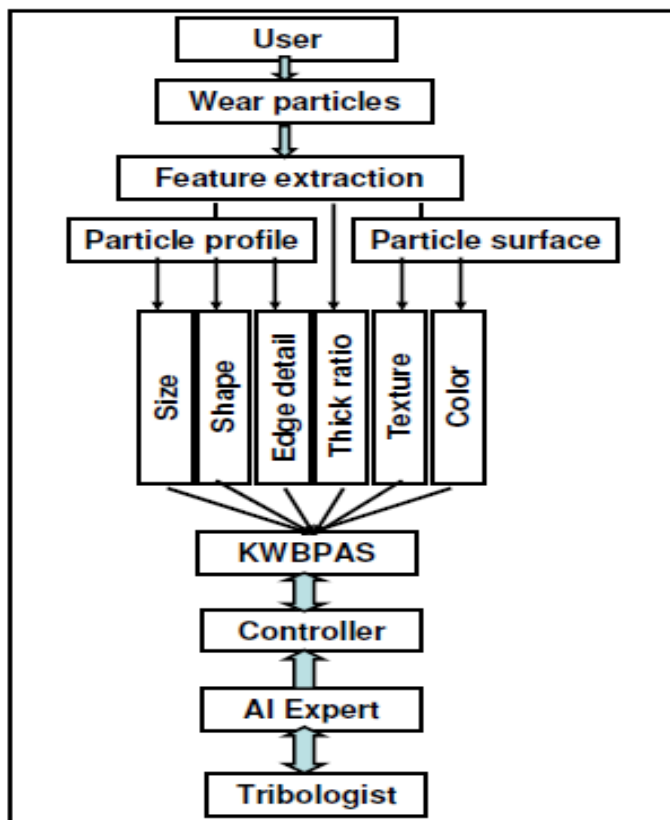


Figure 2-16: Strategy of Knowledge Based Wear Particles Analysis [51; 53].

2.10 General sampling techniques

The most unreliable part of wear debris analysis is the method used to extract wear debris from the system [43]. There are three types of wear debris sampling: offline, online and in-line. These determine how analysis is conducted. Fig 2-17 illustrates their differences [37]. Offline sampling is the most widely used sampling method, in which the sample is collected using a container such as a bottle. The test can be conducted on-site using a portable wear debris analyser, or in a laboratory where the samples are tested using laboratory-grade wear debris analysers and particle counters.

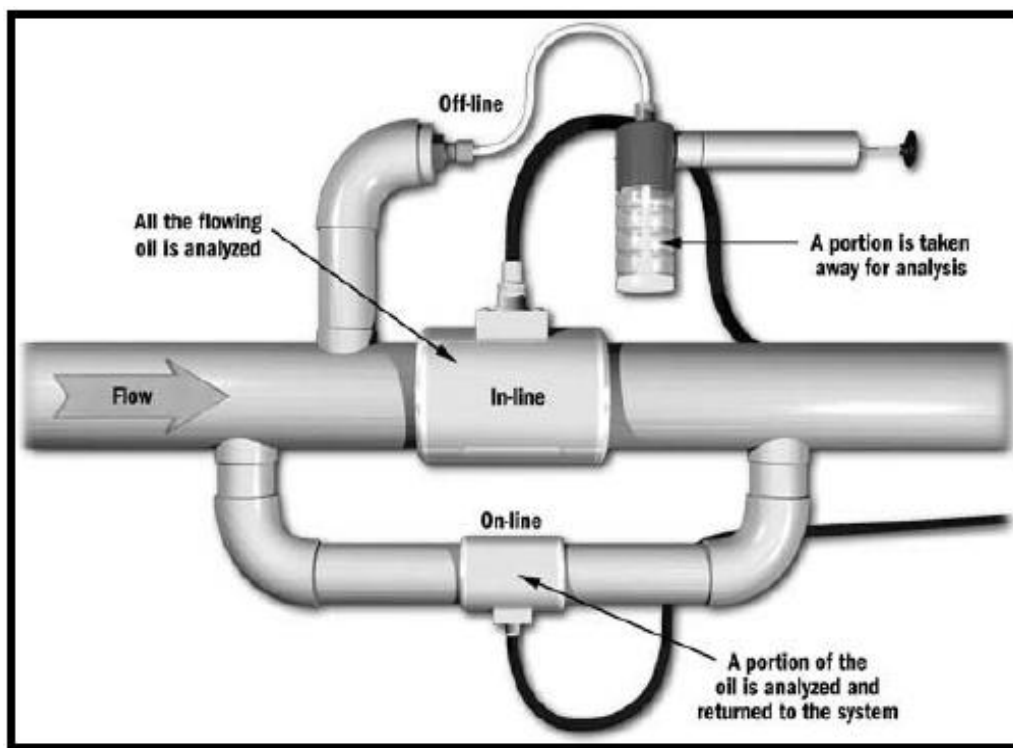


Figure 2-17: Types of wear debris sampling [37]

The disadvantages of off-line sampling are that it is laborious and time consuming, produces a delayed result, and is exposed to the risks of outside contaminations and influence [37]. On the other hand, on-line sampling continuously monitors a portion of wear debris, reducing labour and time consumption for quick results reducing risks of contamination. However, this technique may misrepresent conditions if the samples monitored are relatively small compared to system flow. A small sample size might give results which do not demonstrate machinery problems, even though the sample may contain some wear

debris. This makes inline sampling the best approach compared with the previous two techniques. In-line sampling monitors the total flow of the wear debris and gives real-time data which enables the user to implement trending of the results continuously [37]. However, some analysis methods are not able to cater to a large number of samples and high-pressure lines during in-line sampling. Therefore, on-line sampling methods are usually preferred when the drawing of the sample from the oil sump can be adjusted to the necessary parameters, such as pressure and flow rate, to suit the ability of the analyzer.

2.11 Sampling equipment

In this subsection, the common types of sampling equipment are briefly described.

- **Magnetic plug** – Constructed into two parts, in which one part is fixed to the oil sump and the other is a removable magnetic plug [18]. The collected debris is removed from the magnet using sticky tape or by washing in fresh oil. Khan devised a cap on a magnetic plug, which aims to collect the wear debris particles. This will be further explained in the preliminary results section [54; 55]. When the first plug is removed, a spare plug is inserted into the system and removed periodically for trending purposes. Figure 2-18 illustrates the magnetic plug.

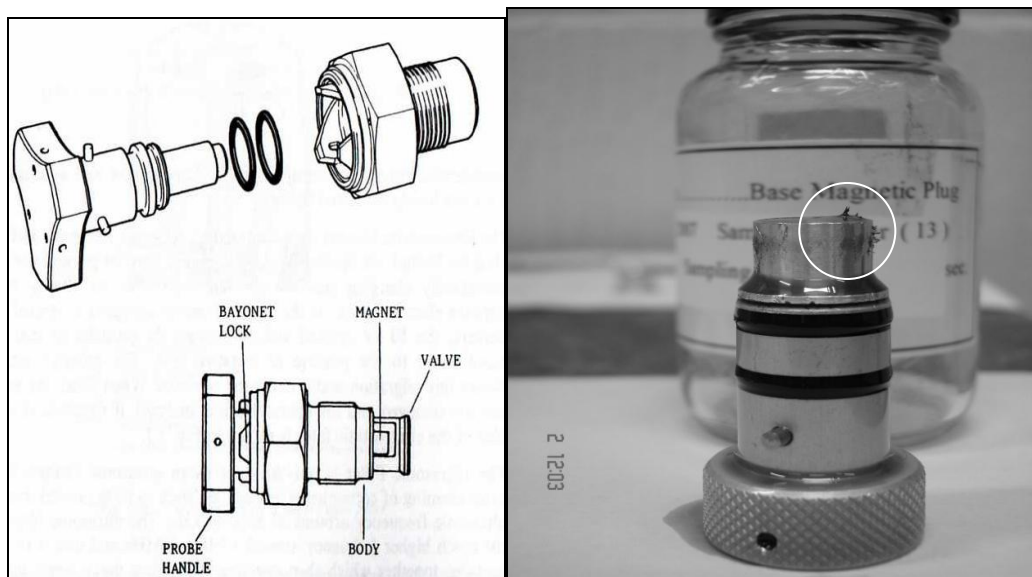


Figure 2-18: Example of Magnetic chip collector [10] and magnetic plug used in the experiment [54]. Wear debris particles stick on the magnetic plug in the white circle.

- **Bottle sampling** –Oil is taken from the system and placed in a bottle. There are many ways of undertaking bottle sampling. The most common method involves draining into a bottle, or using a pump as shown in figures 2-17.



Figure 2-19: Bottle sampling techniques. [33; 56]

- **Filter** – Wear debris particles can also be collected using filtration. Oil containing a debris sample is allowed to pass through a filter where any debris is collected, and the filter is then removed from the system for analysis.
- **Sampling valve** – This equipment allows the user to draw an oil sample from the system and comes with leak protection and a cap to avoid any contamination. The cap is also adaptable to pressure, atmospheric and vacuum locations [56].

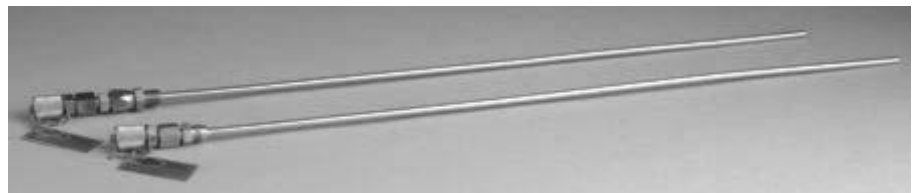


Figure 2-20: Sampling valve [56]

- **Online soft tube** - This tube draws a sample from the oil sump and delivers it to equipment such as a flow cell for further examination of the sample. A small pump such as a peristaltic pump normally assists the drawing of the sample, and can draw the wear debris from any part of the oil sump, which can give the best representation of the oil. However, the tube needs to be placed properly in the oil sump. The most representative area is the region closest to the gear mesh. In

In addition, online sampling is able to give a real-time sample for analysis with reduced risk of contamination.

2.12 Image capturing and processing in wear debris analysis

Due to the sizes of the wear debris (1 μm to 1 mm), microscopy has an extremely prominent role in the image capturing of the debris. The following are the types of microscopy that are common in wear debris analysis:

- **Optical microscopy** [57] is the simplest and most common microscopy used in wear debris analysis because it uses normal light for illumination, instead of a laser. However, the quality of the image captured is not good in comparison to other laser optics and is limited to certain sizes ($>1 \mu\text{m}$). However, optical microscopy coupled with a Colour Charge Couple Device (CCD) Camera is able to give sufficient quality to colour images of wear debris. Its limitation is that the magnification, in that it can only achieve up to 400x, while laser types can magnify an object to more than 1000x. 400x means the image can be 400 times its actual size while 1000x means the image can be magnified to 1000 times its actual size. Microscopes' magnification refers to how much the microscopes can enlarge the size of an image, but does not necessarily mean they give a good resolution. An image may be magnified but at the same time blurred.

On the other hand, resolution means the ability of the microscopes to produce a sharp and clear image. Resolution shows a smallest distance between two points that can still be distinguished as two separate entities. The distance can be represented by the equations below [58;59]:

$$d_{\min} \equiv 0.61\lambda/\text{NA} \quad \dots \dots \dots \text{eq. 2}$$

$$NA = n \sin \alpha$$

Where

λ – Illumination wavelength (light)

NA – numerical aperture

α -One half of the objective angular aperture

n-imaging medium refractive index

Resolution will improve (smaller distance d_{\min}) if the wavelength of the light decreases while n and α increase.

Figure 2-21 shows the clear differences between the magnification without resolution and the magnification with resolution. The image produced with magnification and resolution taken into account is clearer, sharper, and provides the details of the image which this research requires.

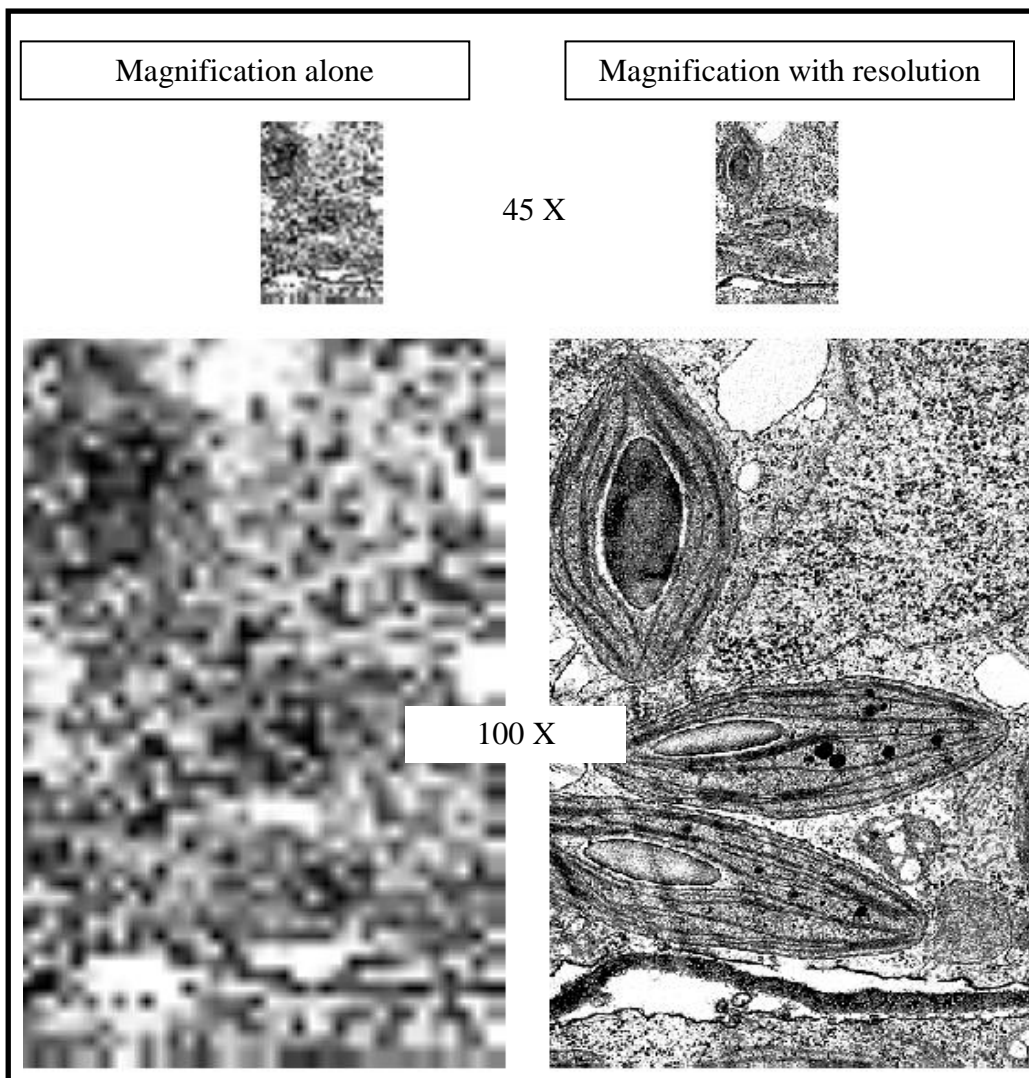


Figure 2-21: Differences between magnification and resolution [58]

The advantage of optical microscopy is that sample preparation is not necessary unless sample slides are required, and also that it has the potential to be converted to on-line image capturing. The disadvantage of optical microscopy is that the minimum wavelength of light it can handle is about 500 nm while the SEM can use electrons with wavelengths as low as 0.2 nm [59]. Therefore, SEM can have extremely high resolution and as well as higher magnification of the images.

- **Scanning Electron Microscopy (SEM)** –The following is the SEM process to produce images of particles. Firstly, the specimen is scanned by a focused electron beam, which liberates secondary electrons from the sample's surface, which are counted by a detector in the microscope. Simultaneously, the detector records data on their origin and their emission intensity, which can then be organised into a high-contrast and high-resolution images [60-63]. SEM gives the best quality image because it gives high magnification, high resolution and depth of field, which is better than optical microscopy or transmission electron microscopy. The disadvantage of SEM is the intensive method required to prepare the sample for scanning. The sample must be dried and cleaned under vacuum conditions. Certain samples need to be treated with a gold coating, but metallic samples can be mounted in the sample chamber immediately. The sampling requirements make it particularly difficult to use SEM for online or in-line wear debris analysis [50].
- Figure 2-22 illustrates the SEM equipment and the images taken by SEM:

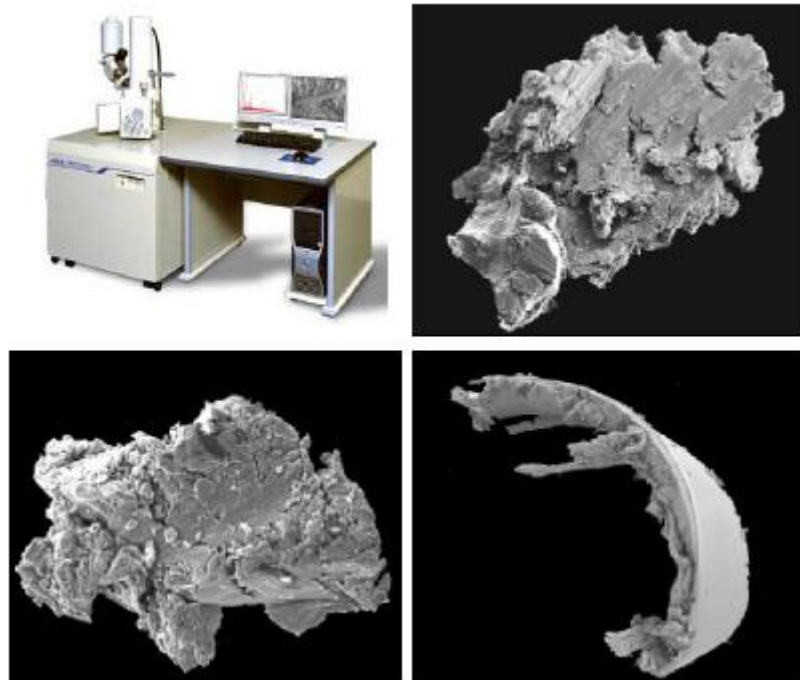


Figure 2-22: Scanning electron microscopy and images [60-63]

- **Transfer Electron Microscopy (TEM) [64]** – In the TEM approach, an electron beam illuminates a thin layer of the wear debris sample, which is less than $0.5 \mu\text{m}$ thick. In this technique, electrons pass through the sample to a system of electromagnetic lenses where the images are captured. These lenses focus and

enlarge the image on a digital camera, fluorescent screen, or photographic film. It has the capability to magnify beyond 10^6 X. Magnification of 10^6 x has the resolution of 1 nm which means that it can still distinguish two points 1 nm apart. The disadvantages of TEM are the extensive sample preparation required to provide an extremely thin sample to be electron transparent. Sample preparation takes a long time, which results in a low throughput of samples. The other downside is that the sample's structure such as shape and size may also be disturbed during the preparation process. Finally, TEM has a relatively small field of view, which runs the risk that the region may not be representative. Figure 2-23 shows TEM equipment. An exercise was done to experience the way sample preparation was done and to produce the result of the images. The oil sample was poured onto a round filter paper and left overnight to dry the oil. Then image capturing was performed on the particles deposited on the paper. The work was extensive, but the image is still not sharp. Examining the way the sample preparation was done, it would be difficult to adapt this approach to an online technique.



Figure 2-23: Transfer Electron Microscopy (TEM) [64]

In order to better understand the capability and the applicability of TEM on wear debris analysis, several tests were conducted on gear oil samples containing wear particles. Figure 2-24 shows an image of particles captured using TEM. The conclusion was made that even though TEM can provide clear boundaries for particles if analyzed closely, the work on sample preparation and capturing the images is extensive and not adaptable to an online approach.

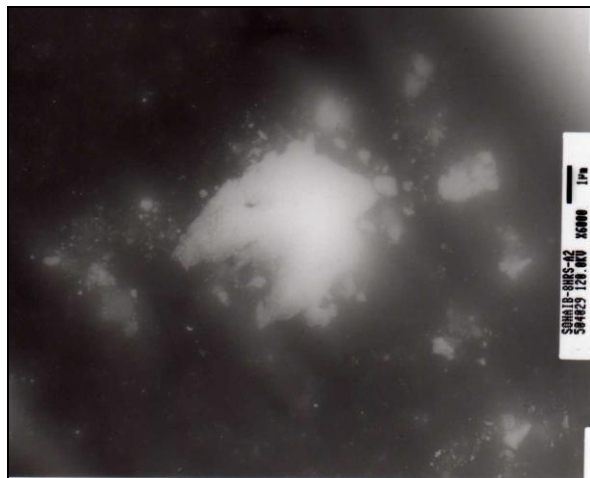


Figure 2-24: TEM image of wear debris on film
(Image taken at TEM lab at The Univ. of Manchester)

- **Laser Scanning Confocal Microscopy (LSCM)** - A relatively new three-dimensional digital images technique using a high-resolution laser beam directed to a tiny patch of a specimen. Light from the exact plane of focus is allowed to return through a small aperture to reach a photomultiplier, which converts the light into a digital image to be presented on a computer display. The advantages of LSCM are a minimum requirement of sample preparation and quick acquisition of a collection of images in comparison to SEM. Another advantage is the fact that it is an open system, easily modified to suit different applications. Figure 2-25 was captured using LSCM [50; 65].

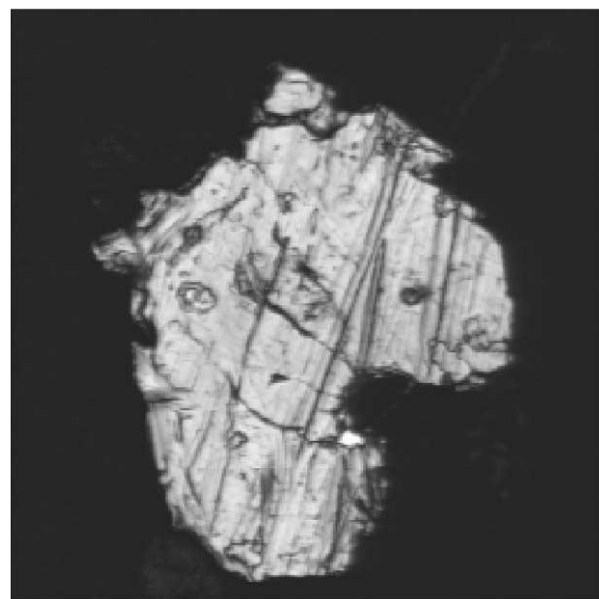


Figure 2-25: Wear debris images taken using LSCM [50]

Table 2-10 the data for the particles in figure 2-25 [50]

Boundary analysis				Surface analysis			3D information	
Area (μm^2)	Length (μm)	Fibre ration	Roundness	Fractal dimension	$R_a(\mu\text{m})$	$R_q(\mu\text{m})$	γ^2	Height aspect ratio
5463				2.43				0.13
	105.38					3.04		0.13
		2.44					0.5	
			0.63					
				1.12				

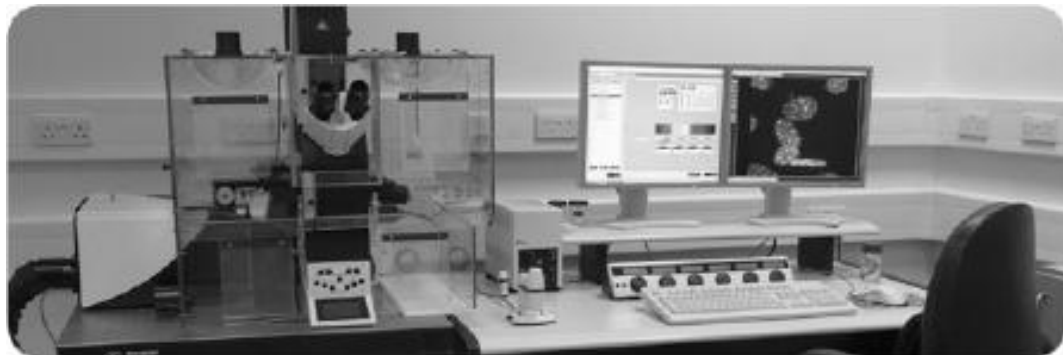


Figure 2-26: Laser scanning Confocal microscopy [65]

2.13 Three-Dimensional (3D) wear debris images.

A 3D image will give more information than a two-dimensional picture. However, acquiring 3D images of particles while they are flowing in the oil system is a complex and challenging task. The most recent study on 3D by Peng and Stachowiak [50; 62] was conducted on stationary particles using Laser Scanning Confocal Microscopy (LSCM) and Scanning Electron Microscopy (SEM).

- **3D using LSCM.**

LSCM does not require very much sampling preparation and can clearly and easily identify particle boundaries. LSCM has a lower resolution compared to SEM. However, the lateral resolution of LSCM at 0.2 μm is sufficient to provide a superior image quality. A disadvantage of LSCM is its limitation to particles greater than 5 μm [50; 66; 67]. However, Peng argues that a larger particle ($>5\mu\text{m}$) is usually required rather than smaller particles. Figure 2-23 shows how images taken using LSCM are analyzed.

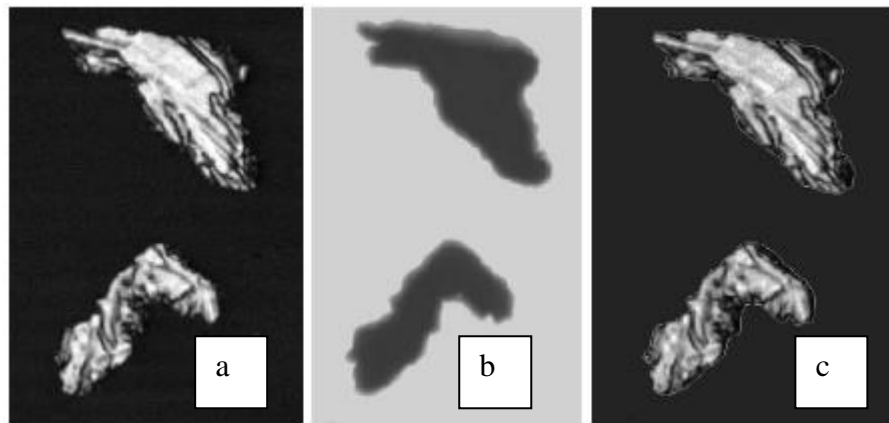


Figure 2-27: (a) Original image particles taken by LSCM (b) Edge detection using transmission channel LSCM (c) Applying the boundary from (b) to original image [50].

Figure 2-27 (a) shows the original image taken by LSCM without a clear boundary. The edge detection process using transmission channel yields the silhouette image with a clear boundary in Figure 2-27 (b). Finally, the boundary is applied to the original image, which produces figure 2-27(c) showing particles with very clear boundaries.

Even though LSCM can provide a remarkably clear particle image, all the described image processes require stationary particles. Despite the claim that there are prospects for LSCM to provide online or in-line imaging and processing, there is as yet no evidence that this can be accomplished. In addition, the large capital cost to acquire a single LSCM makes it an uneconomical option for an online or inline sensor.

- **3D images using SEM.**

It is evident that SEM is capable of delivering excellent 3D images of wear debris particles. The image processing consists of noise reduction, edge detection, threshold, stereoscopic matching, calculation of surface elevation, and interpolation [68]. Figure 2-28 is a self-explanatory demonstration of the high quality of the images captured using SEM [62]. In fact, the ability for an image to be analyzed in so many ways, such as range images, makes extracting more information easier. However, the sample preparation and requirements, such as a vacuum environment and gold coating, makes it difficult to convert to online or in-line sensors [69].

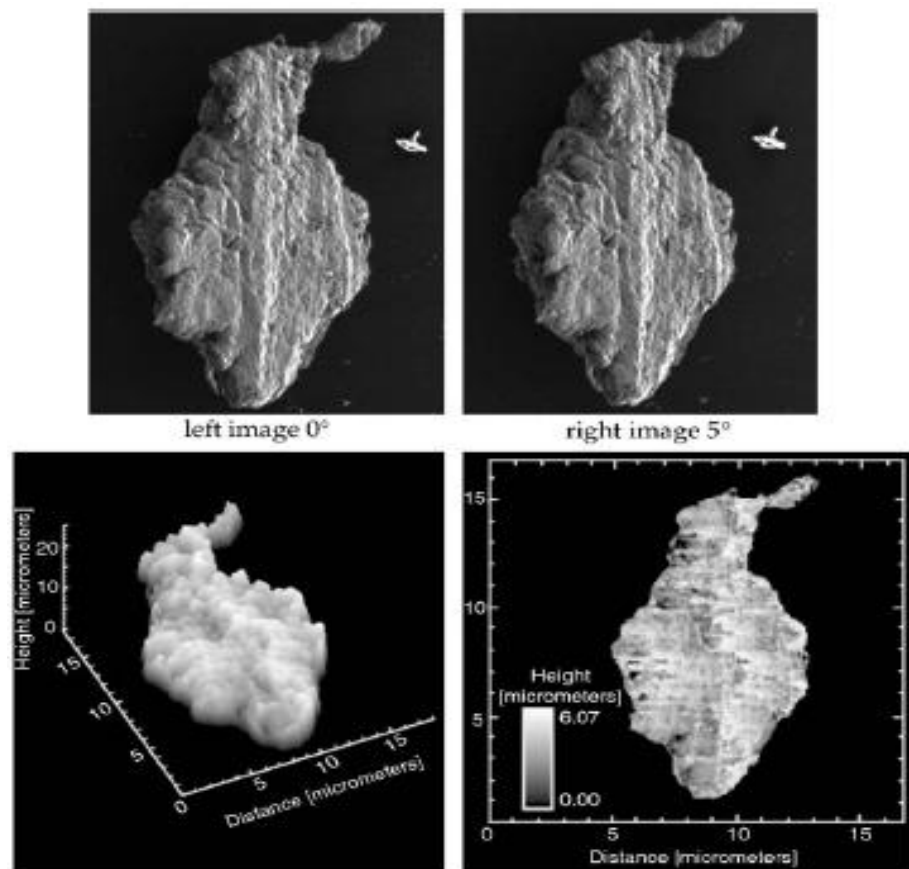


Figure 2-28: Encoding SEM images surface elevation data into range images [61-62]

2.14 Constructing 3D images from 2D images.

Due to the difficulty of using LSCM and SEM as online and in-line wear debris sensors, there is a need to develop other ways of constructing 3D wear debris particle images. One of the methods is reconstructing 3D images using 2D image photographs. The following is a sample of a study conducted regarding reconstructing 3D images in other disciplines.

- **3D reconstruction from 2D bioluminescence images** - This work was done to reconstruct a tumour in 3D. A small animal with a tumour in its abdomen was placed in a tube and then rotated while images were captured at different angles of rotation. Then, Hull intersection lines were applied to create the 3D images. Hull intersection line is methods where lines are drawn from the images according to its individual angle, which makes the lines, intersect at a common point as in figure 2-29. Then the 3D reconstruction will keep only the parts of the lines which intersect, producing a structure formed from lines as per Figures 2-30 and 2-31. The 3D image dimensions were subsequently measured and compared to the actual size. There were only minor differences between the actual and the reconstructed images, which indicates that the procedure was successful in reconstructing 3D images of the tumour [70].

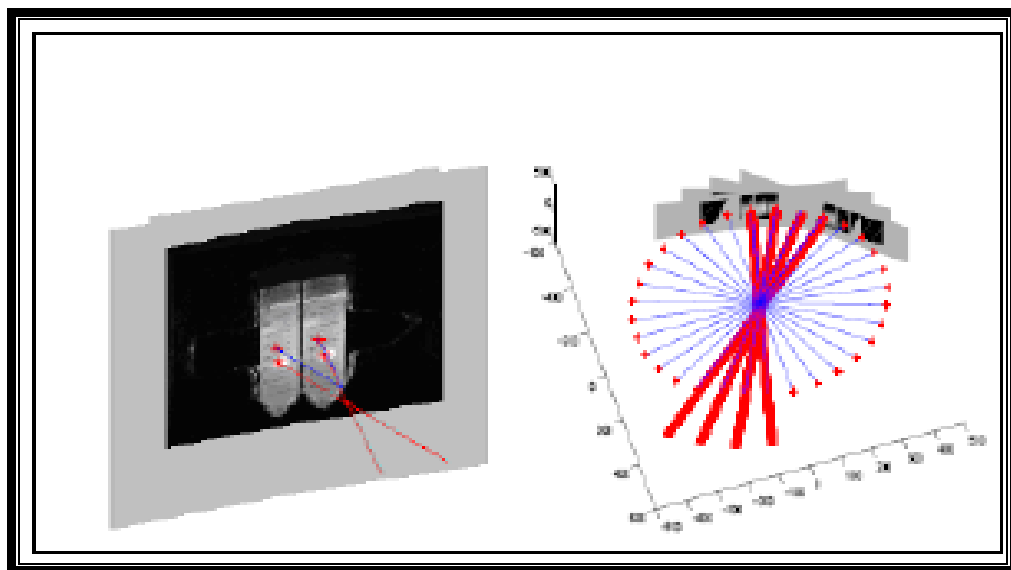


Figure 2-29: Line intersection method and Hull cylindrical intersection [70].

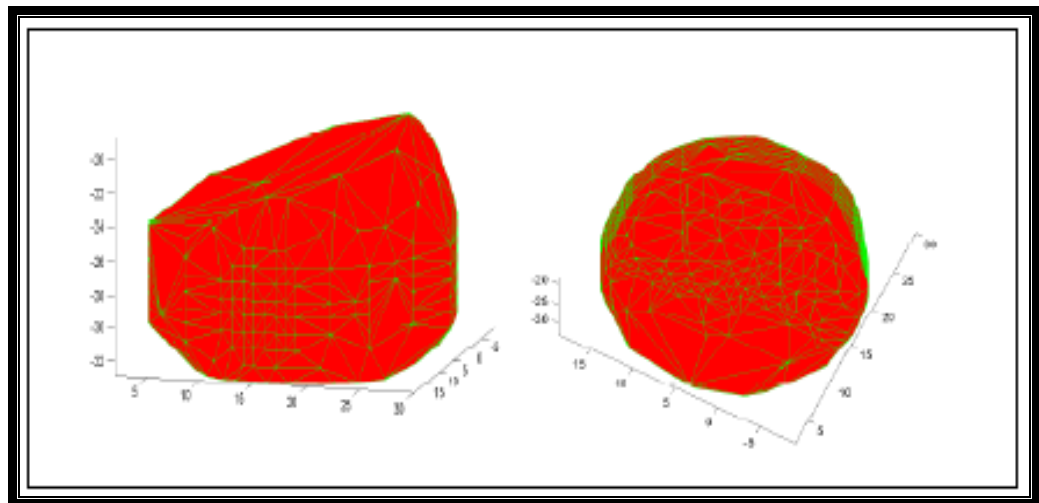


Figure 2-30: 3D reconstruction [70].

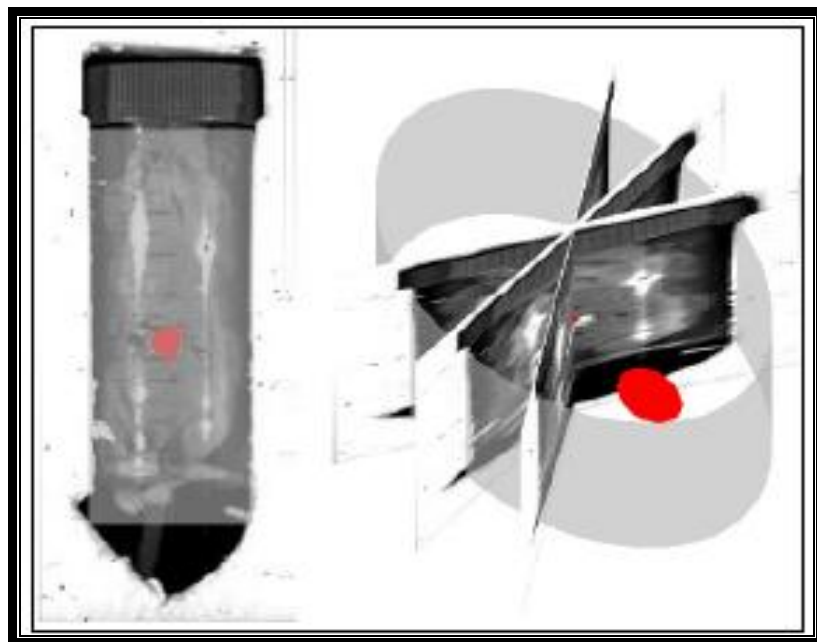


Figure 2-31: Reconstructing the 3D tumour (red) images in a grey tube from two views [70]

2.15 Critical analysis of literature review

- Many methods are still based on two dimensions, or on analysis of one side of wear debris particles. Hence, diagnosis is only based on one side or one view of the particle. Techniques such as magnetic plug, magnetic collection switch/Grid, induction sensor, Laser imaging and electric sensors are based on two dimensions of the particle. As there could be more than one aspect to a particle, if only one side is examined this might not give an accurate interpretation of the particle. For example, if the particle is platelet type, the volume of the particle will be very different in comparison to one which has bulky and chunky particles. Hence, looking at one view of the particle will assume all of the particles have the same thickness which will not give an accurate trend to the deterioration of the gear.
- The current three-dimensional techniques of wear debris analysis are still limited to very few researchers, which makes more study in this area promising. Peng on LSCM and Stachowiak on SEM are the only two researchers who have undertaken a significant amount of work on three-dimensional wear debris analyses. However, the analysis of three dimensions is only on one side of the particle, as shown in Figures 2-27 2-28. In other words, the analysis disregards features on the other side of the particle. The existing three-dimensional techniques of wear debris analysis such as LSCM and SEM are not possible for on-line or in line conversions. There is no evidence yet that both techniques could be converted to on-line due to time-consuming sample preparation. In addition, the equipment is expensive which limits the opportunity to be widely used in industry.
- Three-dimensional approaches give more information on particles than a two-dimensional technique, and can provide a more comprehensive or “all-around” image of the particle. Three-dimensional images can be constructed using multi-view images of a single particle. This has been implemented in other fields of research such as the biomedical field.
- There is an opportunity for innovation in an online three-dimensional technique in wear debris analysis. There is no known research of WDA attempted on online sampling three-dimensional analysis in the past and no current research has been reported to regarding this approach.

- Analysing two sides of a particle had never been explored in any existing WDA techniques. Most of the time, only the largest area of a particle is analyzed to extract information regarding the health of machinery. Therefore, exploring multi-view images of a single particle is novel research.

2.16 Conclusions

Chapter 2 describes wear particle generation, classification and wear debris analysis technology in 2D and 3D. Three-dimensional techniques and their potential for conversion into in-line or online sensors are also discussed. These methods promise an area of novelty. A review of a case of 3D reconstruction from a multiple-view imaging technique outside the area of WDA demonstrates the possibility of constructing 3D images without using sophisticated techniques such as Scanning Electron Microscopy and Laser Scanning Confocal Microscopy. Critical analysis of the literature gives a direction of research, in which a multi-view and 3D image approach is considered for the focus of the research. In fact, there were no WDA techniques which attempted to look at a particle from more than a single view, its volume, and thickness parameters. Analysing only one side will give only front view of the particles without attempting the side view of the particles. Some particles have a laminar shape, but when inspecting their side views, they might be seen in the form of curl or cutting shape. Therefore, without considering both views, analysis might not be accurate. Similarly, without looking at the thickness of particles, the analysis assumes that a particle has a constant thickness throughout the length of the particle; however, it could have a bulky type in which thickness varies. A bulky type of particle would there have more volume in comparison to thin platelet particles. Hence, this should be one of the novel areas explored further in WDA research.

Chapter 3.0 Research methodology

3.1 Introduction

This chapter will detail the research methodology, the justification of the choice, the direction of the research, the data collection process, the analysis of data, and conclusions from the process.

3.2 Research methodology

The literature review provided the background to the current techniques in Wear Debris Analysis (WDA) in sampling, data processing and diagnostics. Furthermore, it identified and proposed an online multi-view images and three-dimensional (3D) wear debris analysis technique as a field of research that has novelty. The multi-view and 3D technique can provide more information on particles than the two-dimensional (2D) approach which has limited the analysis of wear debris particles to only one side of the particle. As many of the previous attempts were carried out on static wear debris samples, a series of laboratory experiments were devised to simulate the wear process of helical spur gears and to monitor the wear debris sample online. They allowed identification of relationships between a small number of variables under study, such as loading, wear rate and onset of failure. The study applied quantitative and qualitative analytical techniques with the prospect of making a general statement applicable to real-life situations. The laboratory experiments were setup in such a way that multi-view images of particles could be captured. This leads to the need for the particles to either be rotated while flowing in the flow cell or for multiple cameras to capture images at different angles. In view of the small flow cells and the size of the particles that are being analyzed, the first option of rotating the particles while flowing in the oil sample is more realistic. In simulating the wear processes, helical spur gears were selected for the research study rather than other machinery such as bearings. Gears allow easier identification of damage because the stress points on gears are easily viewed while stress points on bearings are normally hidden inside the casing. Fig 3-1 summarizes the research methodology.

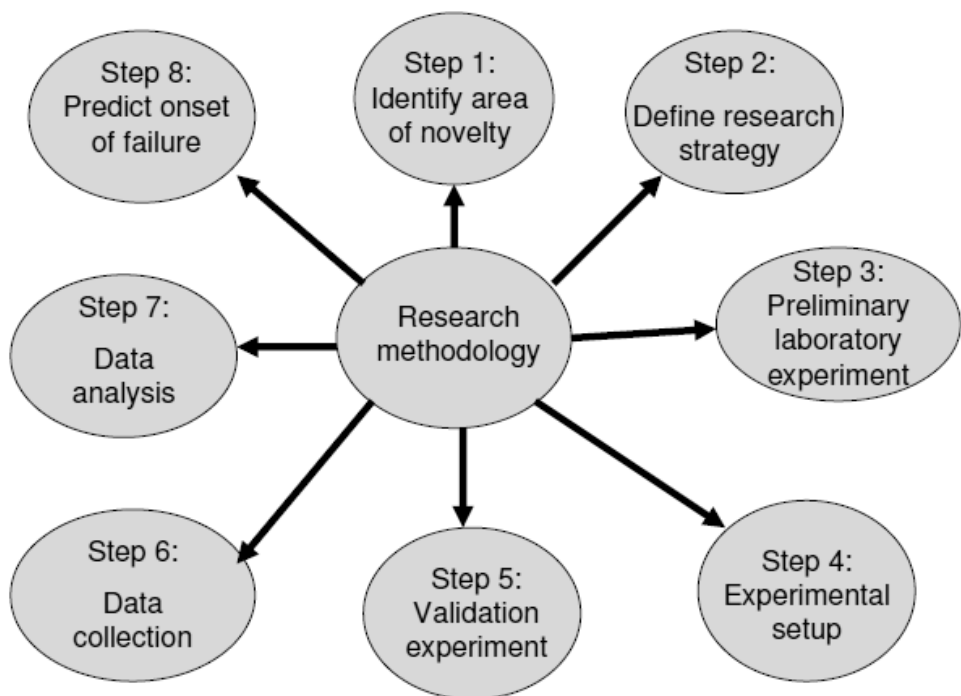


Figure 3-1: Research methodology approach

- **Preliminary laboratory experiment.** For the purpose of familiarization, preliminary scuffing and pitting experiments were conducted on a gear test rig to measure the wear rate of gears under abnormal loading, and to identify the onset of failure of the gears. Samples for the wear debris were collected for particle counts and image analysis, and images of the damaged gears were taken at hourly intervals to substantiate the test. The experiment used bottle sampling and a magnetic plug to collect the wear debris samples. The particle counts were trended to compare with the theoretical concept of the wear debris generation, in deciding the onset of failure of the gears. 2D images of the particles generated were captured and analyzed. Images of the deteriorating gear mesh were also taken at hourly intervals to provide visual evidence in assisting with predicting the onset of failure of the gears. The offline sampling method used in the preliminary experiment confirmed that the method is time intensive due to repetition of the same tasks over many hours of the experiment. In addition, the experiment confirmed that the two dimensional images collected only gave information for one side of the particles. During analysis, most of the time only a face view of a 2D image of the particle was analyzed at one time

and the edge view, which can give a thickness for the particle, was always neglected. This can be explained because the face view gives the largest area of the particle. Therefore, since the edge view image is not analyzed, the 2D images cannot give a direct thickness measurement of the particle and no decision can be made whether the particle is a thin layer platelet, or a large chunk. To illustrate, Fig 3-2 shows how significant is the difference in the volume of two particles, relating to the different amounts of metal removed from the gear mesh surface. A 2D approach is not be able to differentiate this because images of the particles are taken from one direction.

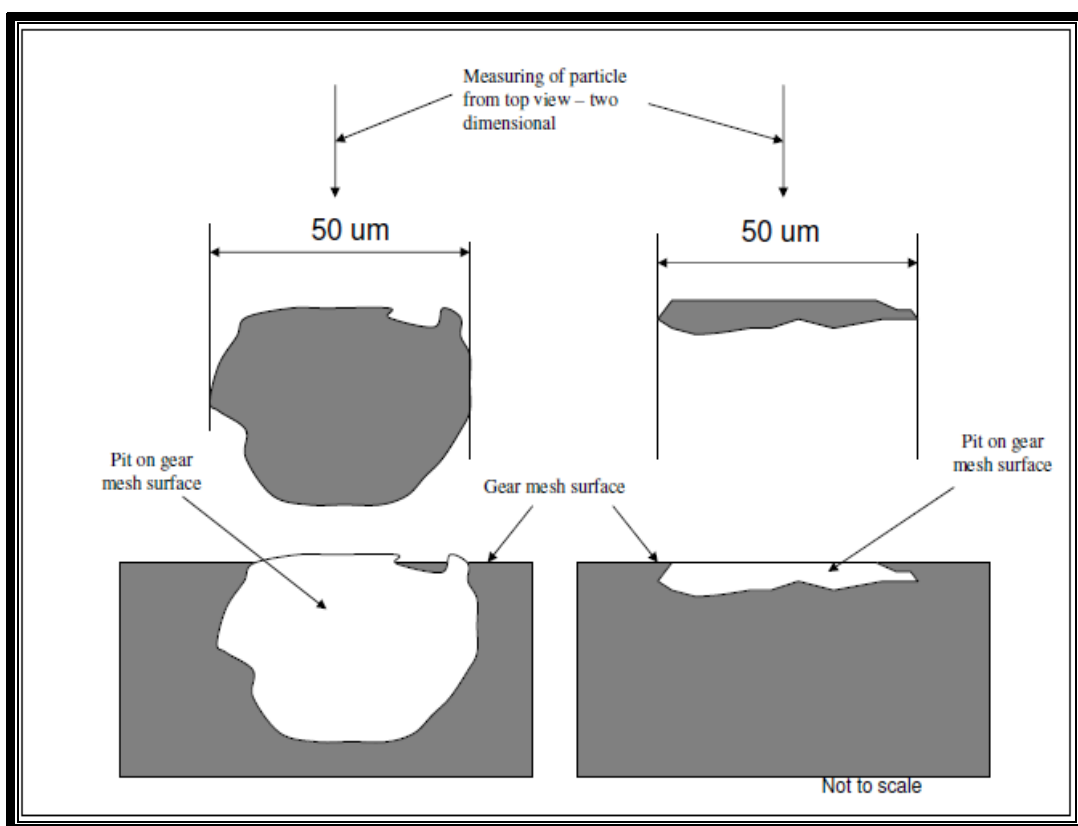


Figure 3-2: Difference of mass of metal removed from two different gear mesh surfaces though particles have same length

- **The Experimental setup.** In order to address the sampling and the two-dimensional images issues, an experimental setup that allows for online sampling and multi-view image capturing of the same particle was designed. A sample of oil from the sump was drawn using a soft tube and a peristaltic pump to a flow cell. The flow cell was developed to provide a window, which enables a view of a thin

layer of the oil sample which contained wear debris. In capturing multi-view images, a peristaltic pump with an automatic time-based controller was used to draw the sample to the flow cell and automatically change the direction of the fluid for every 2.0 minutes. The specified time interval was chosen to ensure that no particle images were captured twice. The change in the direction of the flow causes the particle to rotate due to hydrodynamic force acting on the particle and multi-view images could be captured using a single camera. A validation experiment was designed and conducted during the third year of the study with pitting experiments. The objective was to retest the developed imaging system, ensuring that it fulfilled the requirement to detect the onset of the failure of the gears being tested.

Data collection. The experiments collected data in the form of video images of the particles and the particle count. The multi-view images were taken using optical microscopy while the particle count was carried out using the “off the shelf” Portable Oil Diagnostic System (PODs). Fig 3-3 shows the route of the oil sample which passed through the particle counter and a flow cell for image capturing process.

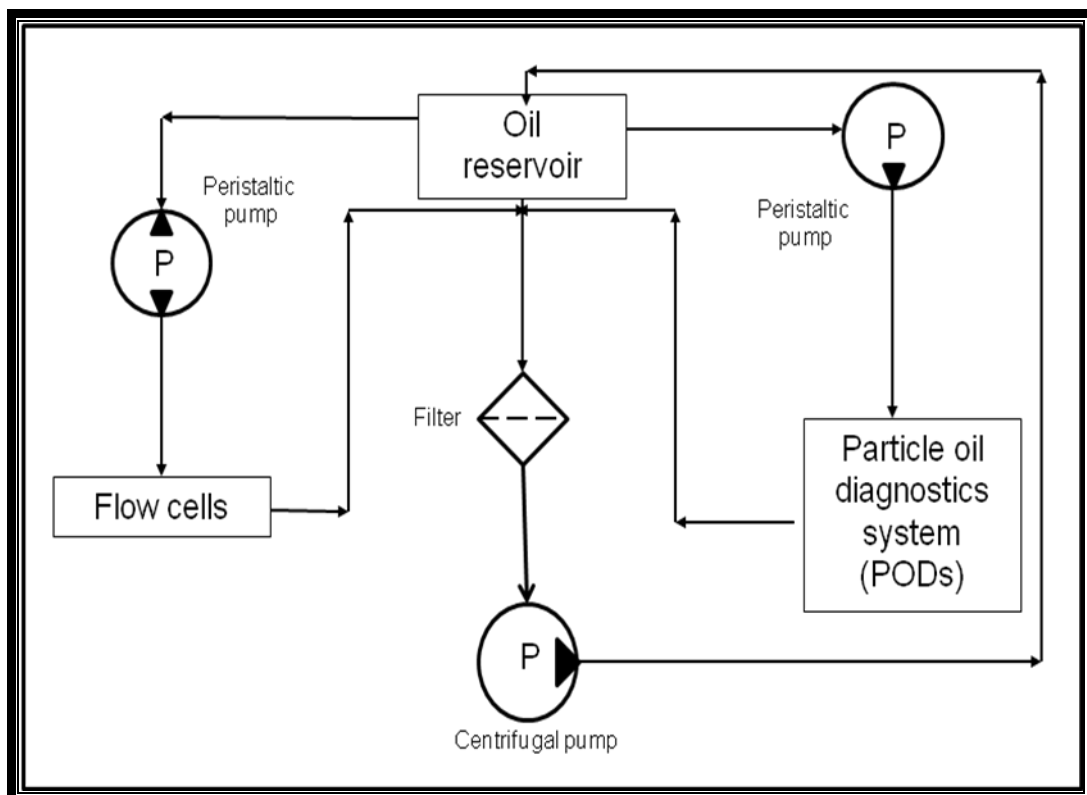


Figure 3-3 Wear debris sample flow route during experiment.

- **Data analysis.** The particle counts quantitative data were analyzed by plotting trends on a graph to determine the onset of gear failure. The video images of the flowing particles were converted to multiple still images, providing coordinates for reconstructing pseudo-3D images, measurement of thickness, and volume calculations. The volume of the particles was calculated, and a graph of volume over size was produced to show the average volume related to particle sizes at 15, 25, 50 and 100 μm . These sizes of particles were used because smaller particles such as 1,5 and 10 μm might be counted twice, because the filter size used in the circulation is only 10 μm . The size of the filter used is due to the availability of the filter for the rig being used. The average volumes' data will be multiplied with the density of the material to produce a mass weight of particles, which will be multiplied with the quantity produced to yield a graph of weight produced over time. A wear rate graph in micrograms per minute over the experimental hours was also produced to pinpoint the onset of the failure of the gears tested. The qualitative data in this experiment focused on the edge details, aspect ratio and roundness factor. They were used to give information on the types of wear debris produced during the experiment. In reconstructing 3D images, the video images taken online were used to produce multiple views of still images. The multi-view images of the wear debris images were used to establish coordinates for 3D image reconstructions, the details of which will be explained in Chapter 5. All of these exercises converting the video images to still images until the reconstruction of 3D images were done manually.

3.3 Conclusions

This chapter describes the research methodology of the study and explains the systematic tasks required to accomplish the research. It links the findings in the literature review exercise, planning of the research to the practical aspect of experimenting to achieve the objectives. This research proposes a laboratory experiment to test the concept of multi-view and pseudo-3D images to gather information on particle thickness and volume in order to predict the onset of failure of the gears. The experimental setup was planned to facilitate the possibility of mechanically rotating the particles to produce multi-view images. In the course of the work, changes and amendments were implemented to achieve these objectives.

Chapter 4.0 Preliminary experiment results and experimental setups

4.1 Introduction

This chapter expands on the objectives of the experiments, the experiment methodology, the experimental setup, image capturing tools, procedures employed during the experiments, testing conducted on samples and methods used to reconstruct the three-dimensional (3D) images of the wear debris. It also includes the results of the preliminary experiments.

4.2 Objectives of preliminary experiments

The objectives of the preliminary experiments are:

- To become familiar with the setting up of the existing gear rig, how to evaluate its performance and identify any problem that might arise while running the experiment.
- To identify the improvements that can be implemented in order to develop an online sampling wear debris analysis that reduces the human intervention.
- To understand the requirements of hardware and software that fulfils the needs of online wear debris analysis.
- To compare the actual results of particle generation trends with the theoretical trends of machine failure.
- To develop a method for 3D reconstruction of wear debris particles.

4.3 Experiments' Methodology

In order to achieve the stated objectives, two experiments were conducted. First, a gear test rig was selected to simulate and accelerate the wear process on helical gears by introducing a misalignment between pairs of gears. Second came the actual collection by magnetic and bottle sampling of wear debris and further analysis on wear debris features, such as size, size distribution, shape, and edge detail. Third was the measurement of wear debris particles, both quantitatively and qualitatively, through particle counting and image capture. This involved the use of an image processing program using MATLAB, which will be explained in Section

4.6.4). Fourth came the analysis of data through trending and wear debris feature analysis such as shape, size, and edge detail.

4.4 Selection of the machine and experimental setup [71]

The gear test rig permits the testing of industrial spur and helical gears. It consisted of two parallel shafts (main and driven shafts) connected with a pair of drive gears at one end and a pair of testing gears at the other. Once the gears were installed, they locked the two shafts in mesh at each end of the rig. A D.C. motor with variable speed of 0 to 3600 revolutions per minute (rpm) drives the main shaft. The driven shaft was made up of two stub shafts, which are connected to each other by a torsion misalignment device, which itself consists of two concentric flanges. One stub shaft end extended through both flanges to ensure both shafts are aligned, and because one flange is fixed to each stub shaft end, the gears are loaded when the flanges are twisted relative to one another. This step introduced angular misalignment (torsion) in which the gears are loaded to transmit force. Subsequently, a load was also applied to the testing gear, which is fixed at the end of the driven shaft. The test rig was capable of testing different sizes of gears because the driven shafts can be adjusted to suit the various gear sizes. Figures 4-1 and 4-2 display an image of the experimental gear rig and a schematic diagram respectively.

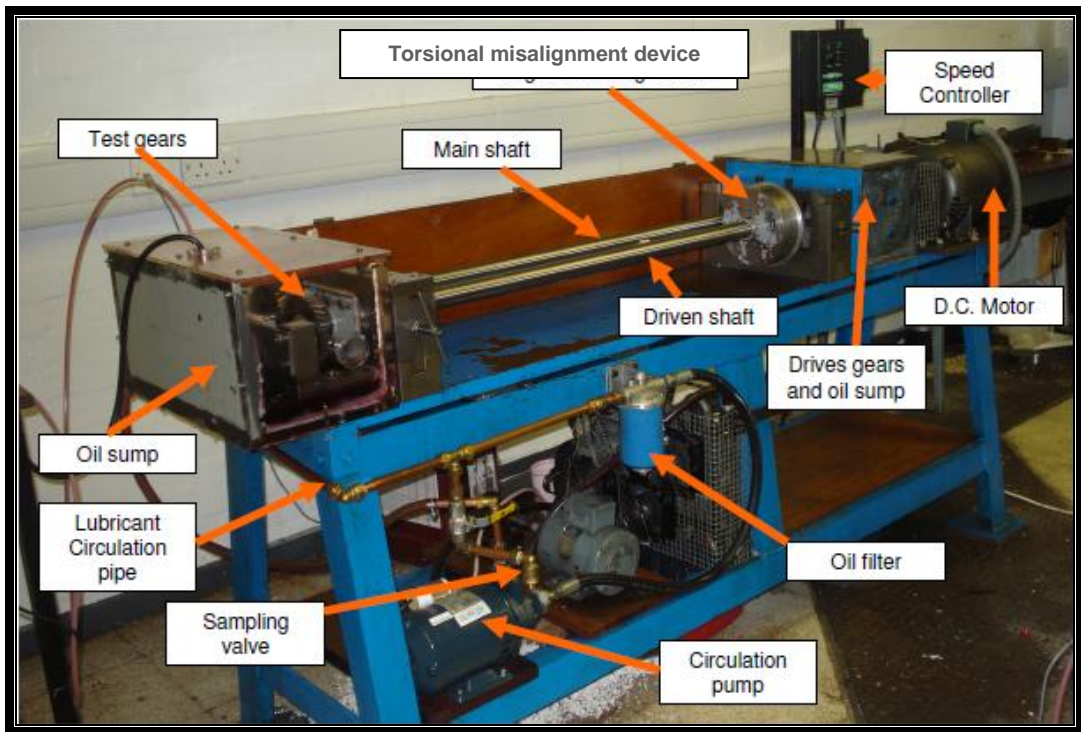


Figure 4-1: Test gear rig setup

The lubricants were circulated from the oil sump, passed through an oil filter of $10 \mu\text{m}$, and returned to the oil sump.

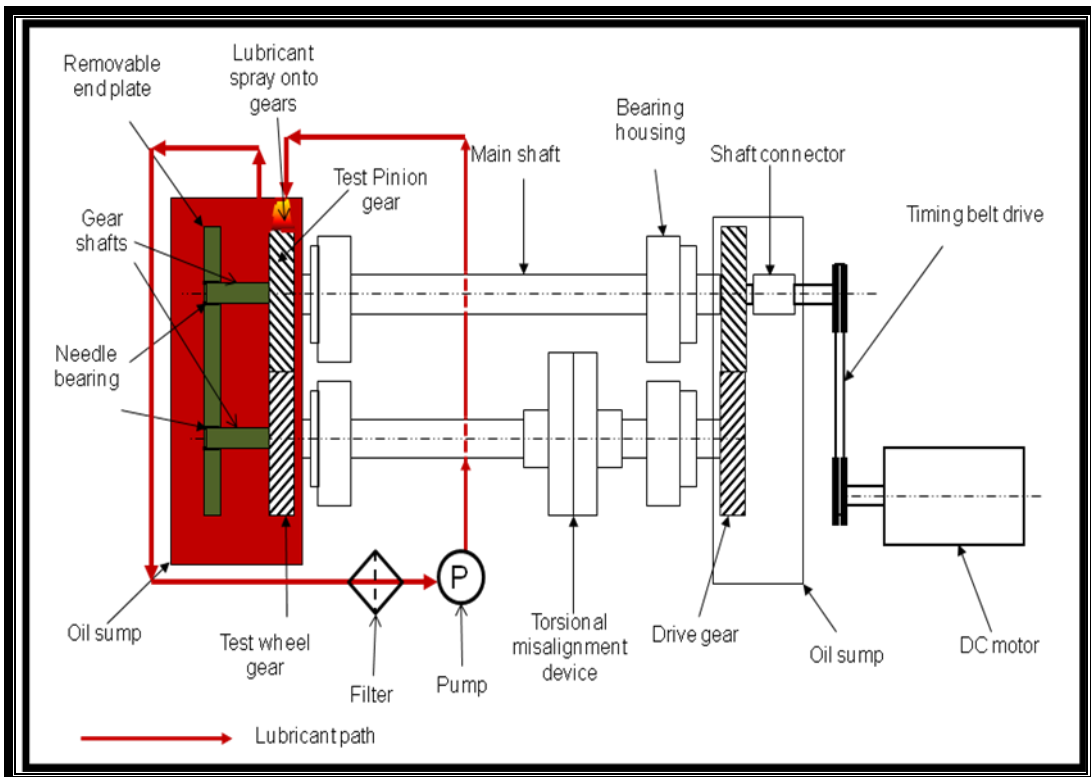


Figure 4-2: Schematic test gear rig with path of lubricant [71]

4.4.1 The lubricant system

The amount of the lubricant in the circulation system was maintained at 4.0 litres, which is sufficient to bath the gear tooth and sufficient supply of oil by spraying onto the pinion gear. The pinion gear was fully lubricated with the spray and able to transfer the lubricant to the mating gear sufficiently when they are meshed. The lubricant originated from the oil sump where the gear teeth were bathed and drawn to the filter through an exit outlet at side bottom of the reservoir using a positive displacement pump. After going through a 10 µm filter, the oil was circulated back to the oil sump and sprayed onto the pinion gear directly. The particulate collected by the filter was not normally be inspected unless there is a need to change the filter due to low flow rate.

While reducing the temperature of lubricant is important, the measurement of the temperature of the oil bath closest to the test gear indicated that the oil temperature fluctuated between 25 to 45 degrees C. At this temperature, it was assumed that the heat did not have any significant effect on the distortion of the gears. In addition, the gears only ran for a maximum of 3 hours due to the physical inspection requirement for the wear stage of the tooth surfaces. Therefore, the need to cool down the lubricant was not significant in the experiment.

The needle bearing function in the schematic diagram, while easing the shaft to rotate, was also required to hold the shaft to a straight path. Without having the needle bearing and its housing, the torsion spring load applied on the shaft and gear might have caused the shaft to bend.

In all of the experiments conducted, Dexron III lubricant, an automatic transmission gear oil, was used. Dexron III is the second-newest oil after Dexron IV, which is more expensive. Dexron III provides anti-wear, anti-corrosion and excellent anti-foam resistance [72; 73]. Anti-foam resistance is important in the experiment because the excessive bubbles from foam reduce the sharpness of the particle images under microscope. It seems that the anti-wear characteristics do not accelerate wear, but since the focus of the experiment is on wear due to misalignment, this characteristic is discounted.

The 4000 N load for scuffing was chosen by using the maximum available ballast in order to accelerate the wear condition. Meanwhile, for the pitting test, it was assumed that accelerating pitting damage on the gear requires a higher load, therefore, an additional 2000 N was applied. However, due to insufficient ballast,

the setting of the load was done by measuring the displacement of the torque plate when the available ballast was placed. So, the additional 2000 N was applied by increasing the displacement of the torque plate proportionately.

4.4.2 Gear installation.

The pair of test gears needed to be installed correctly because any misalignment would introduce another source of failure to the gear sets. The two pairs of gears must be correctly engaged and in a straight line if viewed from the side. The gears were slid into their position on the shaft and the retaining circlip was installed into its designated groove. A loose circlip would cause the gears to dislodge when the machine is running. Fig 4-3 illustrates the installation of the gears prior to testing.

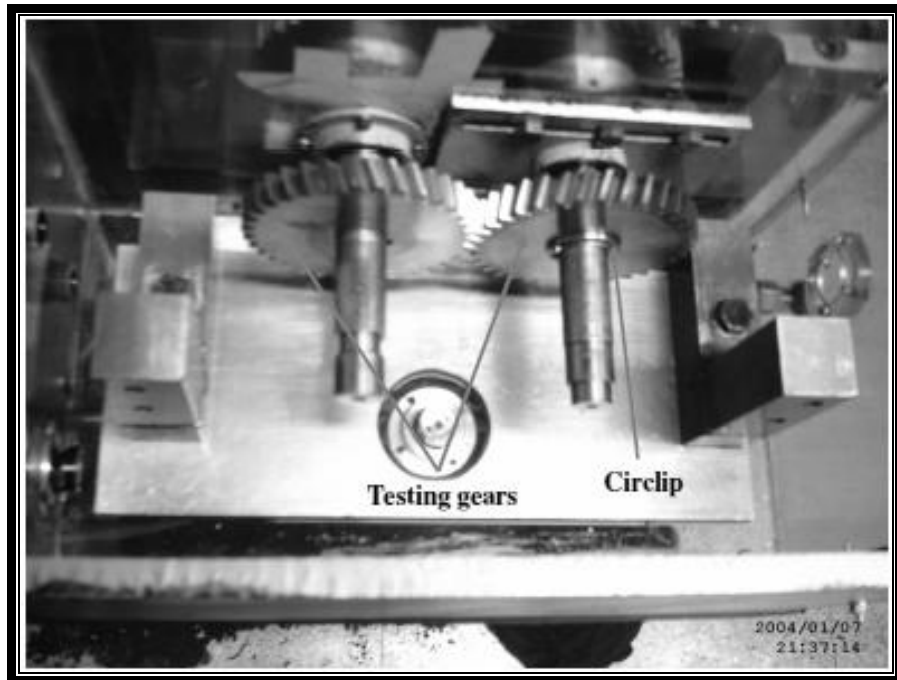


Figure 4-3: Installation of the testing gears.

4.4.3 Gear selection

The below parameters were selected for the gears under study.

Table 4-1: Gear selection

Type of gear	Helical
Helix angle	17.75
Pressure angle	20
Centre to centre distance	113 mm
Module of gear	3
Number of teeth on gear	35
Face width	15 mm (pitting) / 35 mm (scuffing)
Tip diameter	116.25 mm
Pitch diameter (Also selecting as a reference diameter)	110.25 mm
Applied tangential loading (for pitting)	4000 N (scuffing) / 6000 N (pitting)
Lubricant	DEXRON III Petro Canada
Gear Material	En32, Casehardened

4.4.4 Loading setup.

Once the test gears were installed, the load needed to be applied before the testing started. First, the drive's gears needed to be locked by placing a metal bar in between them in order to prevent them from rotating when mass weights were applied to a handle that is attached to the angular twisting device. The purpose of this locking was to hold the gears so that a right displacement of the twisting device occurs as the load increases gradually. Failure to ensure that the gears were locked properly would introduce error when the loads were applied because they were loose, so the displacement does not represent the actual increase of the load. Figure 4-4 shows how the weight was applied to the angular twisting flanges to set the loading that caused displacement of the flanges. Once the load was applied, the flanges were tightened to hold the torsion load on the driven shaft. This load was subsequently applied to the gears being tested at the end of the driven shaft, in other words applying a misalignment to the gears.

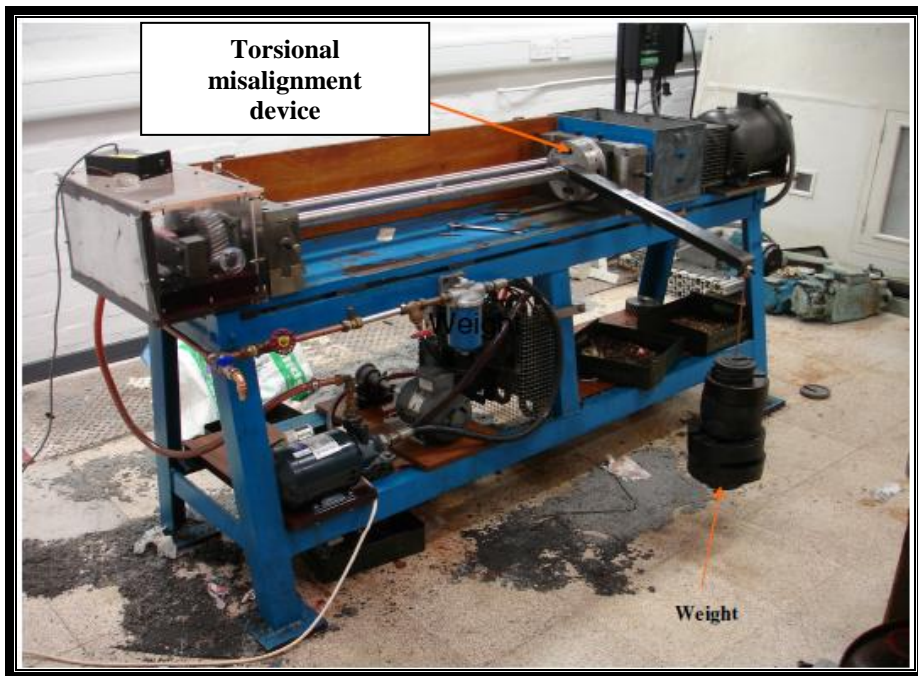


Figure 4-4: Applying loading to the gear

4.4.5 Calculation of theoretical life

For calculating the loading to be applied to the gears, reference was made to British Standard BS 6336-2:2006 “Calculation of load capacity of spur and helical gears” [74]. For the scuffing experiment, 4000 N was applied, while for the pitting experiment, 6000 N was applied. This difference was meant to generate a wear pattern of scuffing and pitting, whereas for pitting wear, the amount of metal removed is much more severe in comparison to the scuffing wear. The decision for the selection of the load in this preliminary experiment was simply based on the maximum available mass balance during the experiment. Additional load was based on the incremental displacement of misalignment torque disk. The calculations were able to give an estimation of when wear or the onset of failure would begin. The complete calculations for the theoretical life of gears subjected to pitting for load of 4350 N are presented in Appendix I. For a pitting test with load of 4350 N, gear life was estimated at 12.8 hours while for a load of 6000 N, the gear life is estimated at 10.7 hours.

4.5 Sampling and inspection procedures

4.5.1 Visual inspection and image capturing.

Visual inspection and image capturing of the tested gears using a digital camera was conducted at hourly intervals. This enabled us to determine the onset of gear failure, which could be determined by signs of material removal from the gear teeth. The camera used was a Sony compact camera with a 7.0 Megapixel resolution. The advantage of capturing the gear image, even without a jig, was that the width of the gear could be used as reference for measuring pit sizes on the surface of the tooth.

4.5.2 Bottle sampling.

Oil samples were drawn through a draining valve provided at the circulation pipe at hourly intervals, using clean and unused bottles. The bottle sampling was done at the circulation line in order to get the most representative sample of the wear debris generation over time. The amount taken during each interval was 75 ml, which is about 1.9 % of total amount of gear oil in the circulation. In order to ensure the level of lubricant in the oil reservoir was maintained at the same level, the same amount of fresh lubricant was introduced after each sample was obtained from the circulation line. The sample was properly covered to ensure that any possible contamination was minimized. Because the particles were as small as 1 micrometer, contamination would substantially alter the particle counting result. During the test, the oil became warmer. As mentioned earlier, the temperature fluctuated between 25 to 45 degrees Celsius. The addition of the fresh oil would not significantly alter the temperature as it was done while the machine has already stopped. In fact, the temperature of the oil in the circulation also reduced as the operation was stopped to allow image captures and the oil sampling.

4.5.3 Magnetic plug sampling.

Two magnetic plugs were inserted into the body of the oil reservoir. Figure 4-5 shows the locations of these plugs, one of which was located at the wall of the oil sump and the other at the base of the oil sump. The magnetic plugs were removed at hourly intervals to collect the wear debris that had deposited on them; however, it did not leave a hole to allow oil to leak. The oil would not leak as the socket for the magnetic plug had a built-in self closing valve; without the magnetic

plug the self closing valve will cover the hole at the socket. When the magnetic plug was inserted to the socket, the self closing valve was pushed upwards to allow the magnetic parts to be exposed to the running oil in the sump as shown in Fig 4-6.

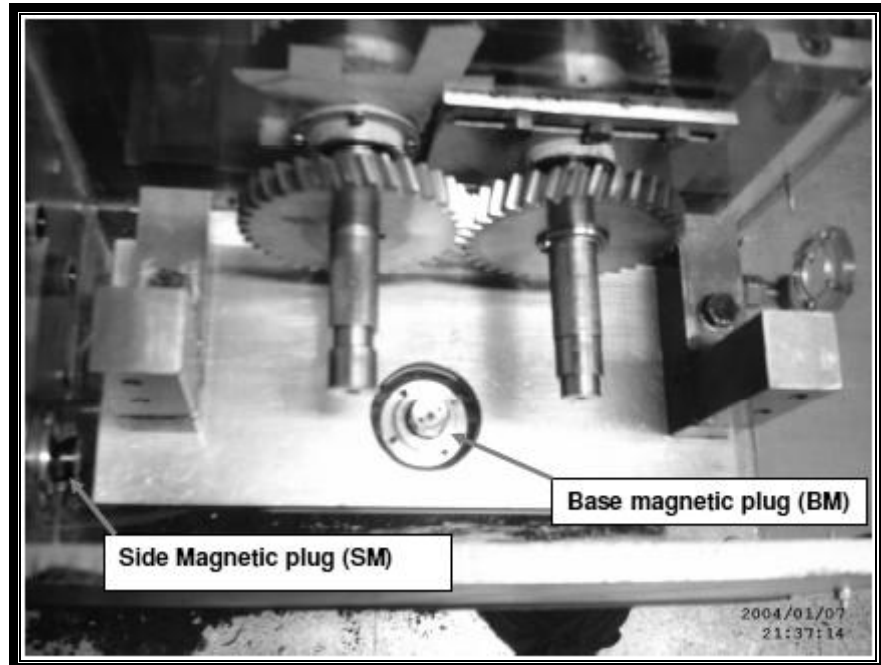


Figure 4-5: Location of magnetic plugs inside the oil sump

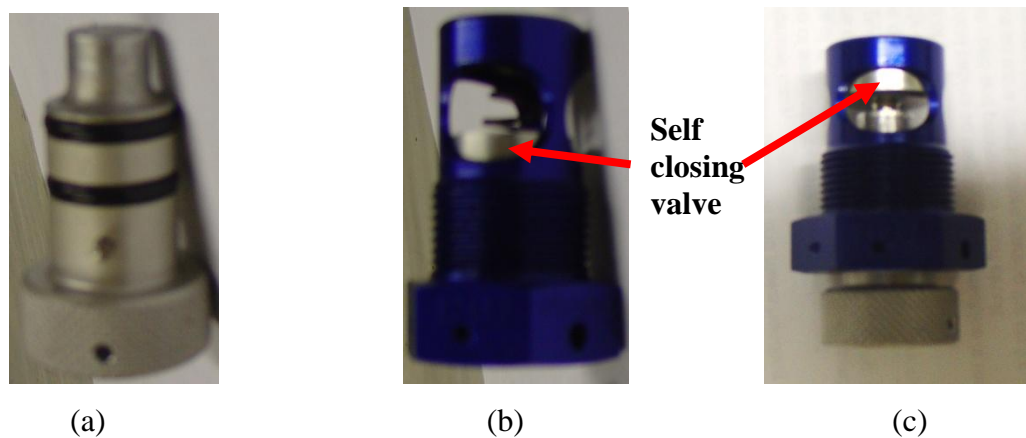


Figure 4-6: (a) Magnetic plug (b) socket of magnetic plug –self closing valve close the socket way (c) magnetic plug inserted in the socket where the self closing valve is pushed upward revealing the head of the magnetic plug.

Magnetic plugs will only attract ferrous materials including the gear materials. They will not attract other material such as brass which might come from the impeller of the centrifugal pump. However, the possibility of the wear of this impeller was low as the circulating oil passed through a filter before reaching the

pump. The oil will be less harmful as the bigger particles should have been filtered out. The circulation system was secured and it was assumed that there were no intrusions of non-ferrous material externally or within the system. The magnetic plug attracted metal wear debris suspended in the lubricant, but its amount largely depended on the location of the plug. In the two experiments, the magnetic plug in the base of the oil sump consistently gave a higher particle reading compared to the side magnetic plug. Apparently, while some of the metal was suspended in the oil, the weight of the metal wear debris caused it to settle to the base of the oil sump after it was dislodged from the gear teeth.

After a magnetic plug is removed from the oil sump, the aluminium cap located on top of the plug was removed using tweezers and placed in a bottle containing 75 ml of fresh gear oil. The bottle was subsequently shaken to dilute the attracted wear debris into the oil. Then, the used cap was taken out of the bottle to be cleaned of any contamination (or any leftover debris) using a solvent before being reused. Figure 4-7 illustrates how the wear debris stuck to the aluminium cap and was transferred into a bottle of fresh lubricant.

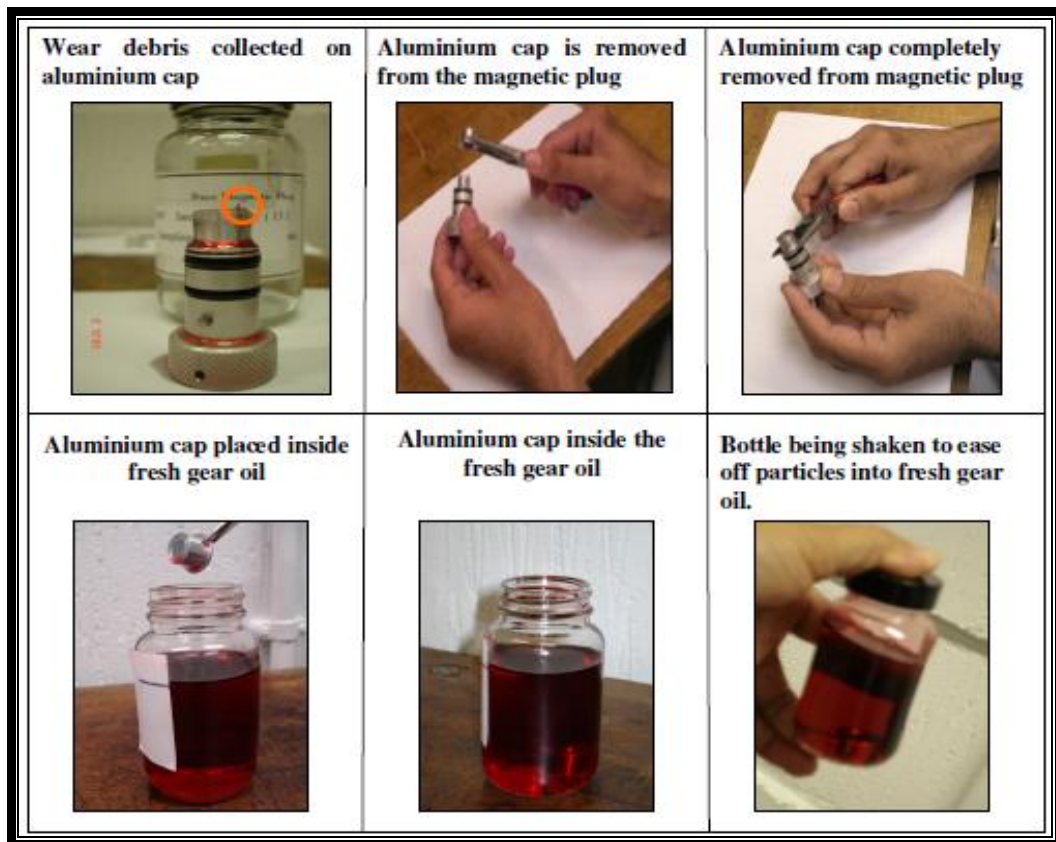


Figure 4-7: transferring the wear debris into fresh gear oil for further analysis.

During the transfer of the debris into the bottle and diluted sample, the machine was shut down to allow the sample to be collected properly. The aluminium cap was modified by Khan in his experiment on 2D wear debris analysis [54]. The size range of the particles collected using magnetic plug did not differ from the sample that was collected using draining valve. However, there was no test conducted on the capture efficiency of the aluminium cap in comparison to the test without the aluminium cap. In fact, as the main idea was to implement online sampling of the wear debris, a need to further examine the efficiency of the magnetic plug did not arise.

4.6 Testing

4.6.1 Portable Oil Diagnostic System (PODS)

All of the samples collected were tested using a Portable Oil Diagnostic System (PODs) for particle counting, which aimed to generate a trend of the wear debris generated during the experiment.



Figure 4-8: PODS (Portable Oil Diagnostic System)

PODS is capable of measuring particle concentration, oil temperature and oil viscosity. It is capable of counting and classifying the particles into 1, 2, 5, 10, 15, 25, 50 and 100 μm groups. The maximum particle size that can be counted is 100 μm and the sample can be tested in both bottle mode and online mode. The

bottle mode requires an external gas supply, such as a carbon dioxide bottle or compressed air. During the test, the flow rate of the sample was measured and automatically regulated and each sample had one run for flushing, which can be set to between 5 ml to 50 ml to clean the sensors, and three measurement runs, which can be set to 5 ml, 10 ml or 20 ml [77]. In the test, 15 ml flush volume and 10 ml runs were chosen and the results of the test were the average of the three measurement runs. The PODS uses a light extinction technique in which a 10 ml sample of oil is passed between a laser light source and a detector, which produces shadows cast by the particles on the detector. These shadows of particles are measured and the data processed through mathematical modelling to determine number of particles per millilitre of oil in for the six sizes mentioned earlier [78].

4.6.2 Off line particle counting procedures.

Sufficient air pressure of 6-7 bars was necessary to complete the test, because any pressure drop of lower than that would terminate the test. The sample needed to be well shaken to ensure all of the particles were suspended and not settled at the bottom of the bottle prior to testing. Then, the bottle sample was placed in a container attached to the PODS. The test normally took about thirty seconds to a minute. The PODs eventually printed the result of the test on a thermal paper roll, which contains the particle counts of all three runs of the test and the final average test. Figure 4-9 shows the step by step procedure during the particle count processes.

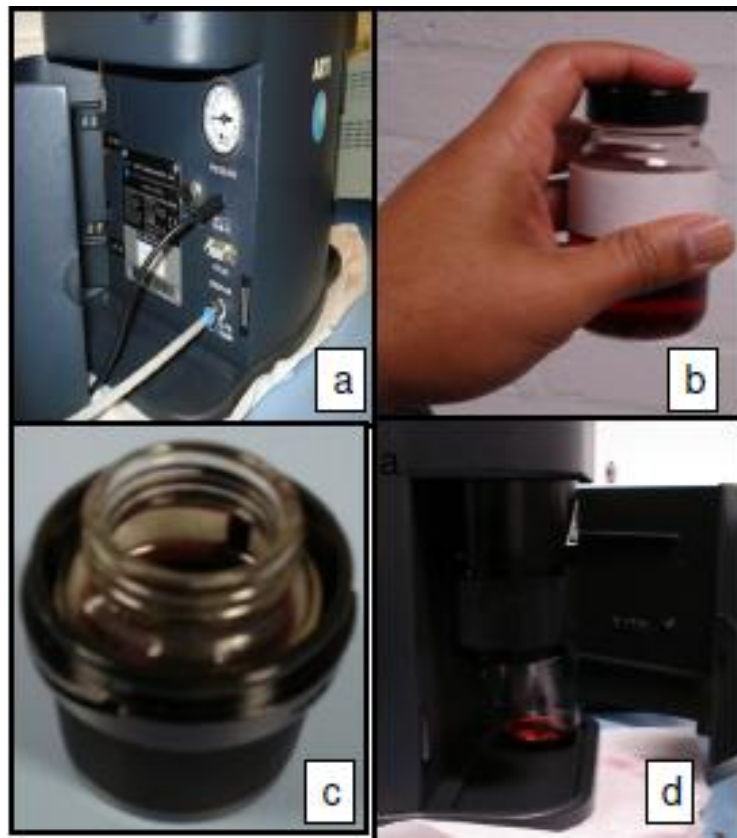


Figure 4-9: Particle counting procedures (a) Check sufficient pressure (around 6-7 bar) (b) shake the sample (c) place the sample in container (d) load the container into the PODS

4.6.3 Image capturing equipment

The equipment used to capture the image of the wear debris consisted of a flow cell, optical microscope, "flexible light" source, colour CCD Camera, Computer and peristaltic pump. Figures 4-10 and 4-11 illustrate the imaging equipment and the schematic diagram of the arrangement.

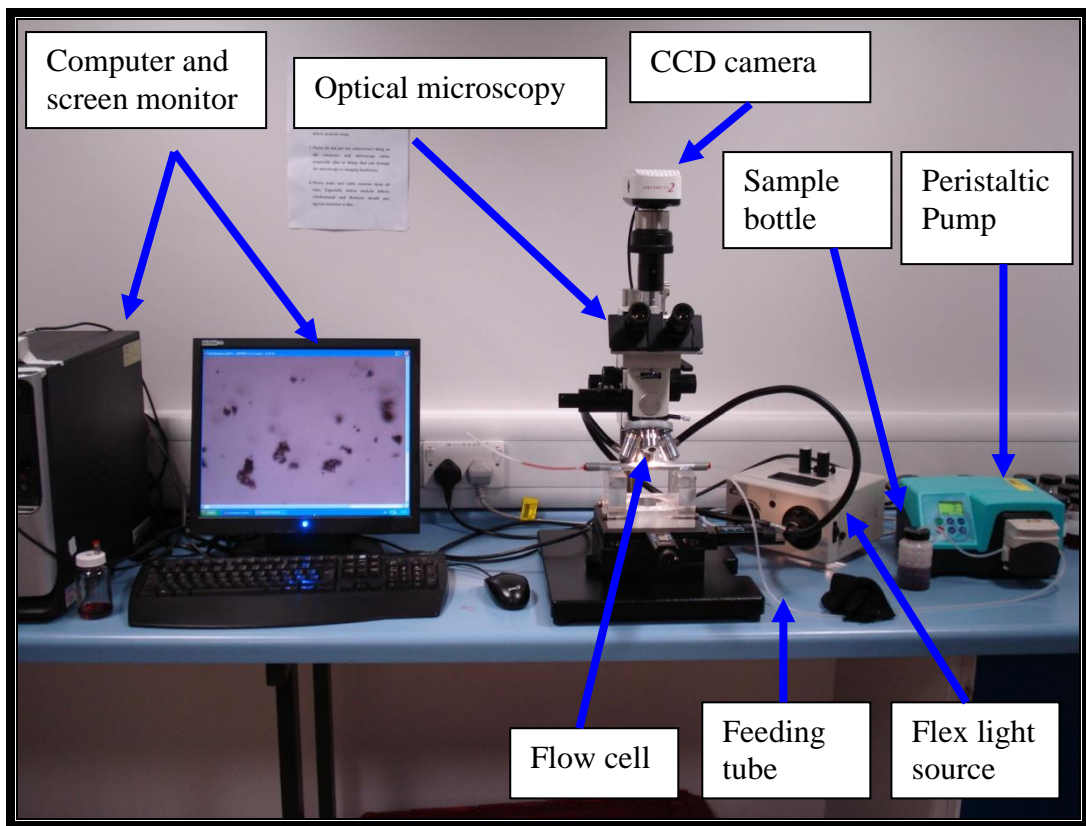


Figure 4-10: Offline setup of image capturing equipment

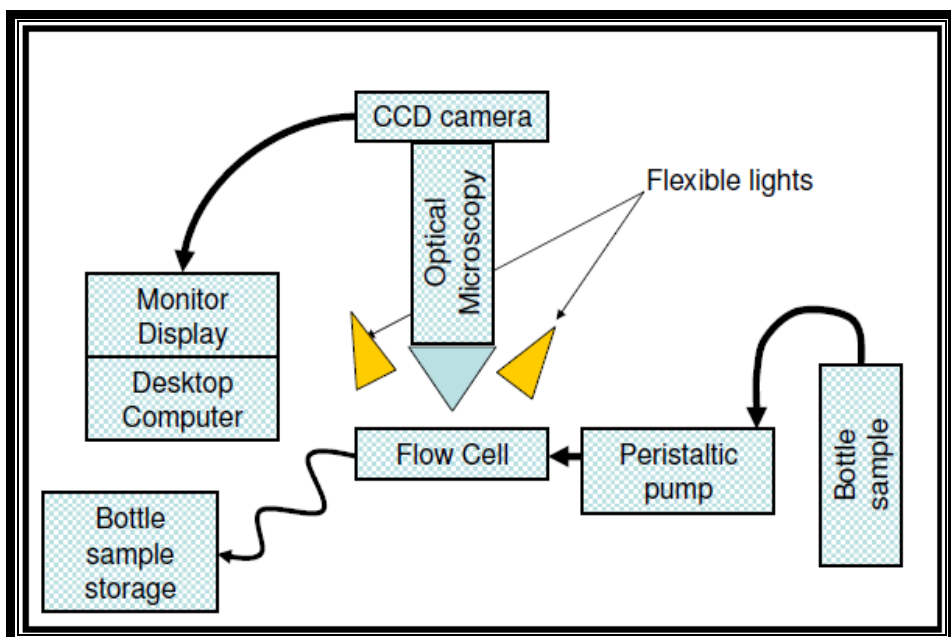


Figure 4-11: Schematic diagram of the image capturing facilities

4.6.3.1 Preliminary design of the flow cell

The flow cell is a mechanism or device which provides a window for ease of image capturing the wear debris under the microscope. Fabricating and designing of a new flow cell was an essential task in the research to obtain a clear picture of the particles online. In designing the flow cell, a few details needed to be considered, such as the internal height of the flow cell, the effective area under the microscope, and the targeted size of the wear debris to be examined. The internal height of the flow cell needed to be minimized to avoid any particle overlap, which would show two small particles as one entity. The width of the flow cell should be the same as the effective area under the microscope (around 2 mm) in order to view as many particles as possible passing through. Particles might have escaped the view of the microscope if the flow cell was too wide. A flat borosilicate off-the-shelf tube, which has an internal dimension of 0.2 mm (height) x 4 mm (width), was chosen to be the flow cell as there was no other type of flat tube that was suitable to meet the required dimension. The flat tube was placed inside a modified plastic tube and sealed with a mixture of window sealant and strong adhesive. Then, the seal was left to dry by allowing hot air to blow on it so as to cure the sealant. The tube was then inserted into a flat steel tube for protection of the fragile borosilicate tube, and finally push-in connectors were attached at both ends of the plastic tube for easy connection to the other tube. The flow cell sat on top of a Perspex holder to stabilize its position under the microscope, as shown in Figures 4-12 and 4-13.

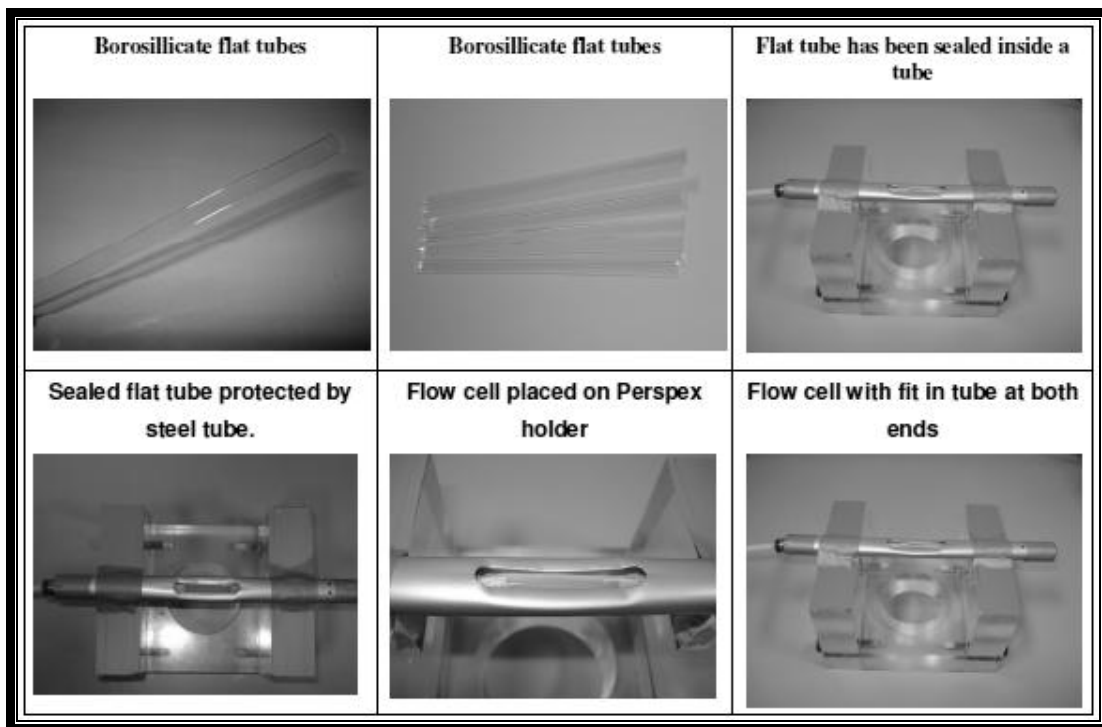


Figure 4-12: Borosilicate flat tube and development of flow cell

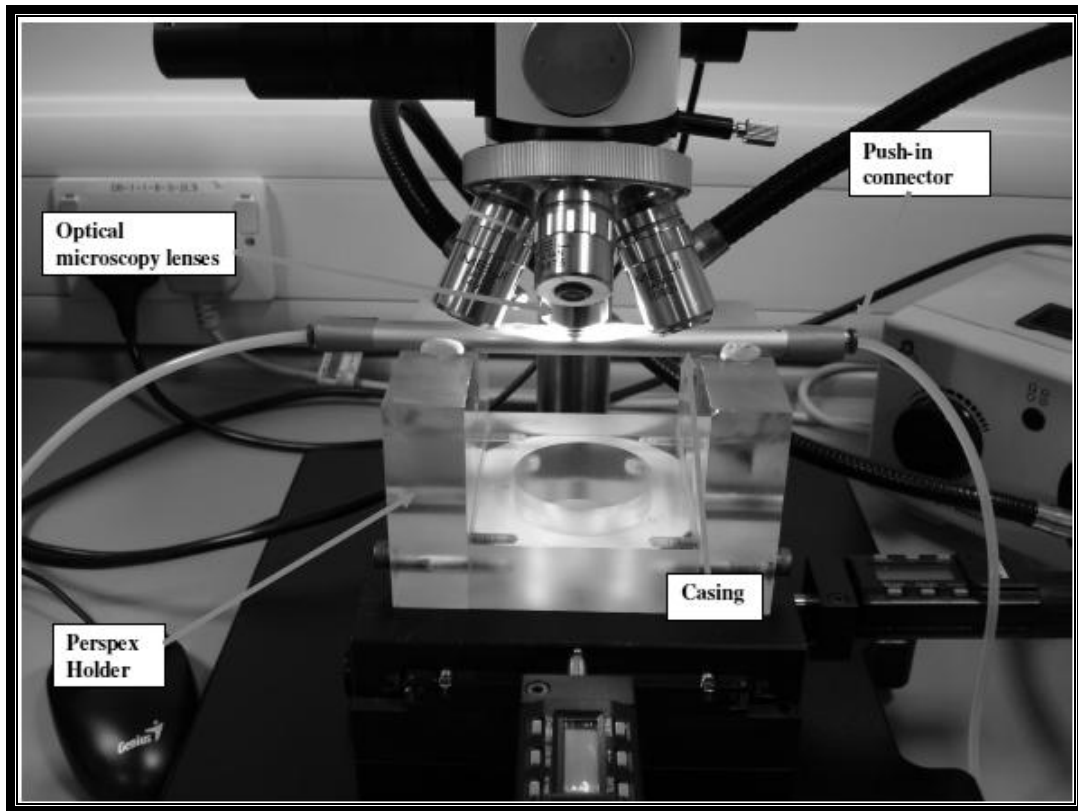


Figure 4-13: Construction of flow cell (flat tube inside the casing)

While the borosilicate tube can give a clear image, it is not robust enough to withstand pressure, is difficult to seal, and is fragile. Therefore, another flow cell

was designed and fabricated which gave a more robust fluid sample passage and a stable view window underneath the microscope with almost no leakage, as shown in Figure 4-13.

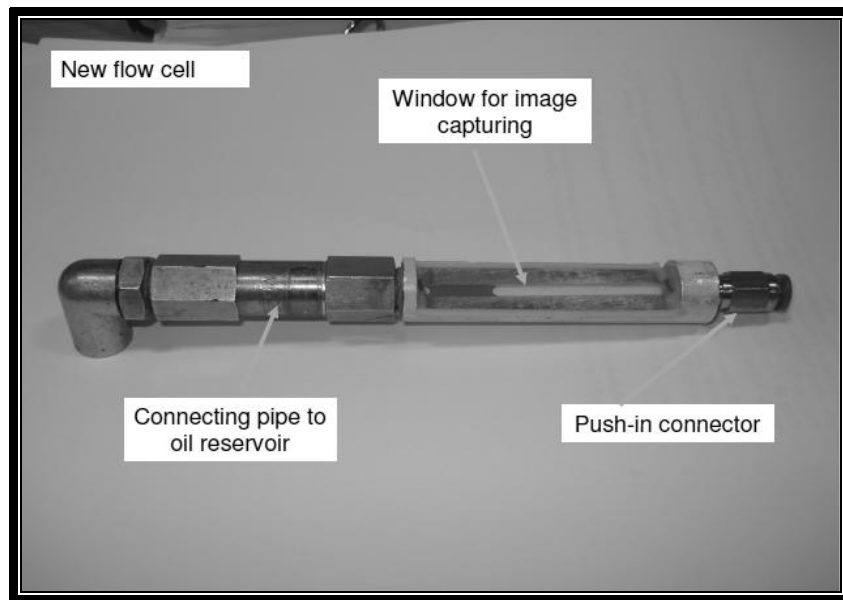


Figure 4-14: New flow cell

This new flow cell in figure 4-14 also could not sustain pressure when the test was prolonged. The window ruptured and oil leaked out during the experiment. Finally, it was decided Khan's flow cell would be used for subsequent experiments as it can sustain pressure of the flowing oil, which will be further explained in Chapter 5. While all of the effort to produce a small flow cell did not achieve the objectives, the knowledge learned was to avoid using thin glass type for flow cell fabrication, as it will not sustain the pressure.

4.6.3.2 Microscope

Optical microscope, Meiji Techno's, MC Series Precision measuring microscope, was used in the image capturing process. The microscope can have magnification of 5x, 10x, 20x, 40x and for the image capturing process 20x was found to give the best images of the particles. The focus depth for the magnification was 20, 9.4, 5.28 and 0.81 mm respectively [54].

4.6.3.3 Peristaltic pump

A Watson Marlow Bredel 323s peristaltic pump was used for pumping the sample through the flow cell. The pump has a variable speed from a minimum of 3 rpm to a maximum of 400 rpm and the flow rate of the fluid depends on the size of

the feeding tube and the speed of the pumping. The variable speed enables the flow of the oil sample into the flow cell to be controlled and regulated for image capturing purposes. The pump flow direction and flow rate can be changed manually by pressing designated buttons on the pump. The peristaltic pump was selected because it does not require any valves, seals or glands to clog or corrode, and it restricts fluid contact only to the bore of the tube, which removes the dangers of the pump contaminating the fluid or the fluid contaminating the pump [75;76]. These attributes made the peristaltic pump the best option, as contamination can greatly affect the wear debris analysis. In addition, the lube circulation pump is a centrifugal pump where the risk of wear debris generated from the impeller of housing of the pump is low in comparison with gear pump. In fact, the circulated lube will be filtered before passing through the circulation pump, which reduces the probability of particles inside the lube damaging the components inside it.

4.6.3.4 Colour CCD camera

The Infinity colour CCD camera used in this experiment had a resolution of 1.4 Mega Pixels (Mp) and was able to capture a maximum of 15 frames per seconds (fps) [54]. The camera allowed a direct display to a monitor screen and had the capability of capturing the image even though the particles were in slight motion. The camera came with an industry standard C-Mount lens mount compatible with standard lenses or microscope mounts and software for image analysis and dimensional measurement. Dimensions of particles that could be measured using the software are parameters, size, distances, and areas.

Table 4-2: List of equipment for image capturing

Component	Details
A flow cell	Fabricated flow cell for imaging purposes.
Peristaltic pumps	Watson MARLOW MODEL 323s.
Microscope	Meiji Techno's MC Series Precision measuring microscope, similar to model MC-50T
Light source	Meiji FT190 Series fibre Optic Illumination Systems, Model FT191 Dual Arm System
CCD Camera	Infinity 2C, microscope C mount camera, 1.4 Mega pixel resolution
Soft tube	Silicon tube - Internal diameter 3.2 mm.
Computer	Dell Optiplex GX620, Intel Pentium 4 with Windows XP
Display	Dell 17" LCD displays

Table 4-2 lists down the equipment used in image capturing of offline bottle sampling in preliminary experiments for scuffing and pitting tests.

4.6.4 Software

MATLAB was used for image acquisition and processing to measure size and area and for boundary tracing, establishing the coordinates of images and for 3D image reconstruction. MATLAB or “matrix laboratory” is a language for technical computing which combines computation, visualization and programming and solutions are expressed in familiar mathematical notation [79]. It was chosen because it is easy to handle and very useful in image processing. In addition, continuous improvements in MATLAB’s image processing make it an attractive and user-friendly tool.

4.6.5 Calculation of shape descriptor in preliminary MATLAB program

In the program in Appendix III, Area is a scalar function, which represents the actual number of pixels in the region. The perimeter of the image is calculated by summing up the length boundary of the image. The equation used is presented below (and as an illustration in figure 4-15) to show how the perimeter equation was derived.

$$\text{Perimeter} = \sum(\sqrt{\sum L^2}) \text{ while } L^2 = (X_2 - X_1)^2 + (Y_2 - Y_1)^2 \dots \dots \text{eq.3}$$

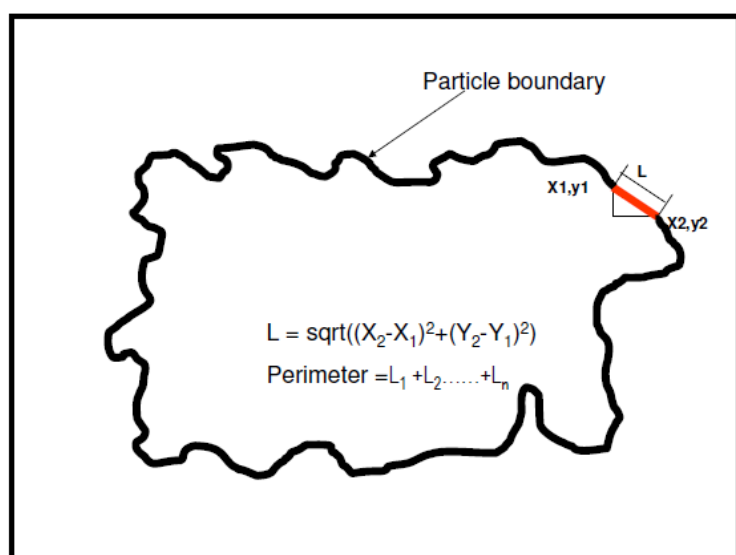


Figure 4-15: Illustration of perimeter calculation [16]

However, in the final program in Appendix V a simpler standard Matlab function was used as below

$$\text{Parameter} = \text{bwperim}(\text{BW1}) \dots \text{eq. 4}$$

The function of bwperim is finding the parameter of the perimeter of objects and binary images. Selection of the first method is only to encourage understanding of the basic calculation of the perimeters during the preliminary experiment.

In calculating the roundness factor of the particle, the perimeter value is required and equation 3 gives the roundness factor of a particle [16].

$$\text{Roundness factor} = \frac{(\text{perimeter})^2}{4\pi.\text{area}} \dots \text{eq. 5}$$

4.7 Preliminary Results

4.7.1 Analysis of data

In analysing data, several statistical techniques were implemented for easier analysis. One of the techniques used was normalization, in which the particles counts for each sizes of the particles were rescaling so that all of the particles count which are very much different in the counts can be presented on the same graph. The normalization method was implemented using the below equations.

$$X_{\text{new}} = (X - X_{\text{min}}) / (X_{\text{max}} - X_{\text{min}}) \dots \text{eq. 6 [80]}$$

Where X_{new} : the new data after normalization method.

X : the actual particle count data at the particular hour

X_{min} : Minimum particle counts in the group sizes

X_{max} : Maximum particle counts in the group sizes

By using the normalization method, the differences in trends of the three sizes of the particles can be determined.

Another technique which could have been used was the standardization method, with the same intention of rescaling the data. The standardization method involves the use of standard deviation in showing the differences in trends of particle counts.

$$X_{\text{new}} = \frac{X - \mu}{\sigma} \dots \text{eq. 7 [80]}$$

Where X_{new} : the new data after standardization method.

X : the actual particle count data at the particular hour

μ : Average calculated from the group particle counts

σ : Standard deviation calculated from group particle counts

However, it was not implemented in this project as the normalization method achieved the same result that could be obtained by standardization method.

In addition, R squared method is also used to get the correlation between the variables. R square is a statistical measure used to find how well a regression line approximates real data points, where an R squared of 1.0 shows a perfect fit. [80]

4.7.2 Assumptions in analysis

1. As gear health condition deteriorated, the small particles count is reduced while large size particles increase.
2. The rubbing and rolling process of the gear meshing causes the gear surface to crack and metals to be removed. After the metal is removed, the polishing process occurs at the damage point. However, if the overloading of stresses continues, another big chunk of metal will be removed. High wear will continue to be shown as the metal is removed and the frequency of the high peak will increase.

4.7.3 Particle counting and trend

The results of the wear debris generated for the valve, base magnetic and side magnetic sampling are presented in trending graphs. The objectives of the trending graphs are to identify the running-in zone, useful working life zone and failure zone of the life of the gears. Particle counting was done offline and each bottle of samples oil gears was tested. Tables in Appendix II show the results of the particles counts. As it was an offline particle counts exercise, it was not done continuously, as shown in the appendix tables II-1, II-2 and II-3. The times in the table show the start time for the samples being placed on the PODs. Once the sample completed the test, a new bottle containing the next sample was placed for the subsequent test. These exercises were not completed in one day as shown in the

different dates for the test. However, it was in correct sequence for the data to show some trends at hourly intervals. As the date and time were not really significant, the recording of time in pitting test particle count were omitted, as shown in Appendix tables II-4, II-5, II-6.

The data collected are in terms of number of particles. Therefore, in order to determine the wear rate, the counts need to be divided into the time taken to count the particles.

$$\text{Wear rate} = \text{Number of particles} / \text{Test Time} \quad \dots \dots \dots \text{eq. 8}$$

For example :-

If particle counts (table App II-1) for 25 μm is 2.13×10^4 , at machine hour 9, and the time taken for the test is 15 seconds, the wear rate

$$\begin{aligned}\text{Wear rate} &= (2.13 \times 10^4) / (15 \text{ seconds}) = 1.42 \times 10^3 \text{ (particles/seconds)} \\ &\quad = 8.52 \times 10^4 \text{ particles/minute}\end{aligned}$$

In order to get the wear rate in term of mass per unit time, the counts need to be multiplied with the amount of mass of a single particle. This will be detailed in the validation experiment.

4.7.3.1 Result of scuffing test.

This section will show the trending graphs for the overall results, which contains the particles' count for each size group graph. These graphs are in the three following sets: large diameters (LD) with a diameter of 50 μm and 100 μm , medium size (MD) particles with a diameter of 15 μm and 25 μm and small particles (SD) with a diameter of 1 μm , 2 μm , 5 μm and 10 μm . The selections of the graphs are for a comparison of small diameter, medium diameter and larger diameter particles generated over time. In presenting the data, rescaling method of normalization was used to place all of wear rate data on the same graphs.

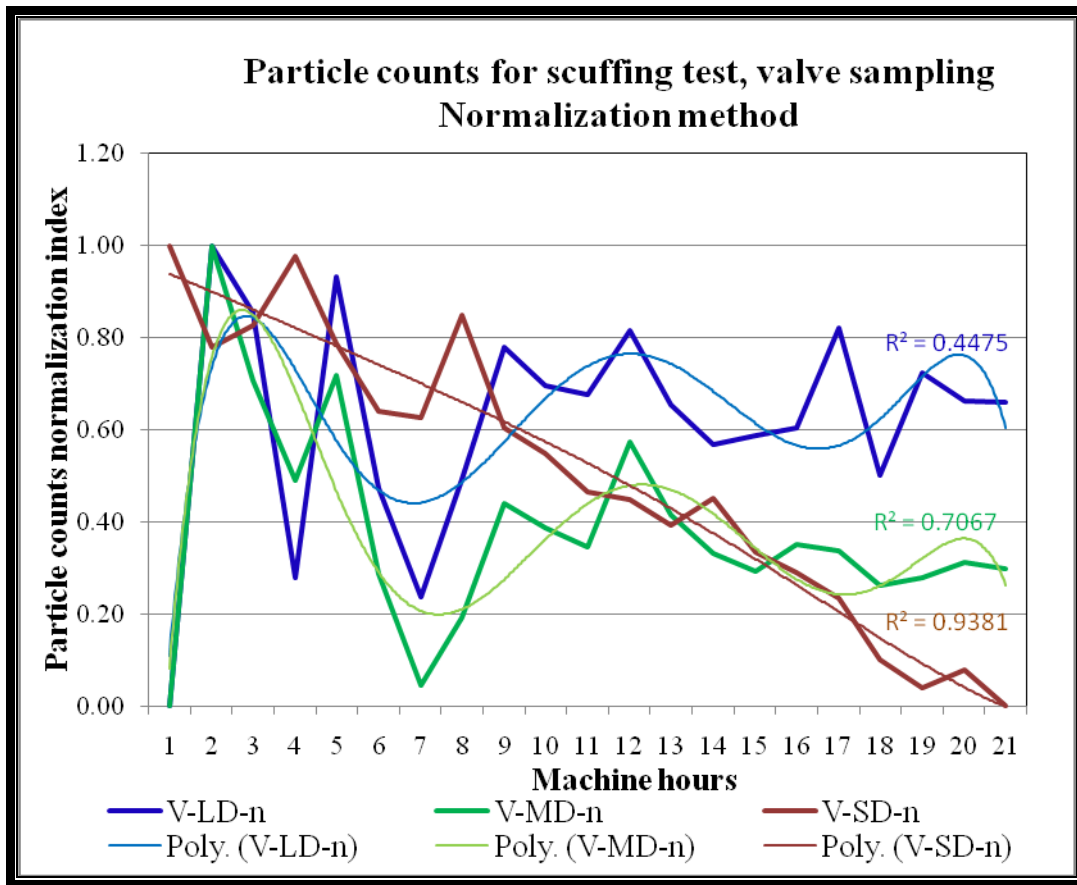


Figure 4-16: Particle counts for scuffing test, valve sampling normalization method

In Figure 4-16, LD, MD and SD recorded a high normalization index, which represents a high amount of particles removed from the gears at the beginning of the experiment. This phenomenon is quite normal, as at the beginning of machine hour, the rubbing and rolling process during gear meshing polishes and removes the asperity on the gear surfaces due to imperfect surface finish. Once the asperity was removed the particle counts recorded by the PODs seemed to be stabilized and lowered. Hour 5 shows the start of the reduction of the wear particle generations for all of three group of size distribution. After that hour, the SD seems to continue to lower until the end of the experiment. This agreed with the theory as the deterioration of the gears worsening the small particles reduces while the larger particles count increases. The MD particles also reduced to a certain extend but then stabilized, which shows that while the deterioration seemed to produce fewer small particles it still produced a certain amount of MD particles until the end of the experiment. The LD particles continued to record a high index which shows that

the particles counts was still high until the end of the experiment this agrees with the theory that the severity of the damage produces a lot more LD particles.

The R^2 values for SD and MD are quite high which shows that the trend line closely match the actual data while the R^2 value for LD is quite low which indicate the trend line quite far from the actual data. However, it still shows that at least almost half of the actual data follow the trend line.

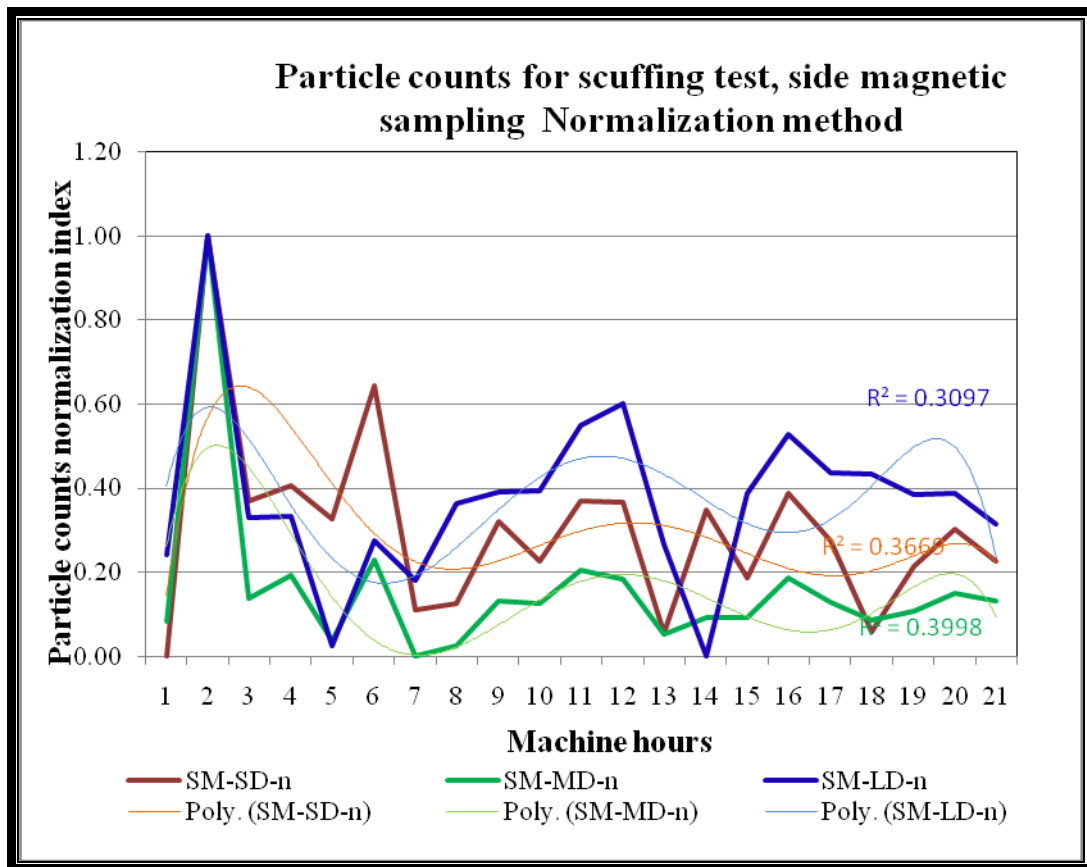


Figure 4-17: Particle counts for scuffing test, side magnetic sampling normalization method

From Figure 4-17, the LD, MD and SD particles started an increasing trend, which shows that the number of particles produced was high, confirming that the polishing and rubbing work on the surfaces of the tooth removed asperity from the gear surfaces. This is a normal phenomenon for gears because the fabrication of the gears cannot give perfectly smooth gear teeth. Therefore, at the beginning, the number of particles being removed was high, which indicates the running in zone. As the surfaces of the gear teeth were polished, the removal of the particles reduced, which is represented by the reduced range of the index for the MD and SD. After hour seven, the range index of the SD was between 0.1 and 0.35 while the range index for the MD was between 0.0 and 0.20. This shows that the wear rate

stabilized after hour 7. On the other hand, the range of index from the LD particles remained as high as from 0.0 to 0.6. This shows the removal of metal debris as erratic and indicated a high wear rate. This confirms that as stresses on the gear teeth continued to exceed their maximum stress, deterioration continued to occur, but with the removal of bigger size particles on the rise.

The R^2 values for LD, SD and MD were quite low, demonstrating that the trend line is quite far from the actual data. However, the R^2 values still show that at least 30 to 40 percent of the actual data follow trend lines.

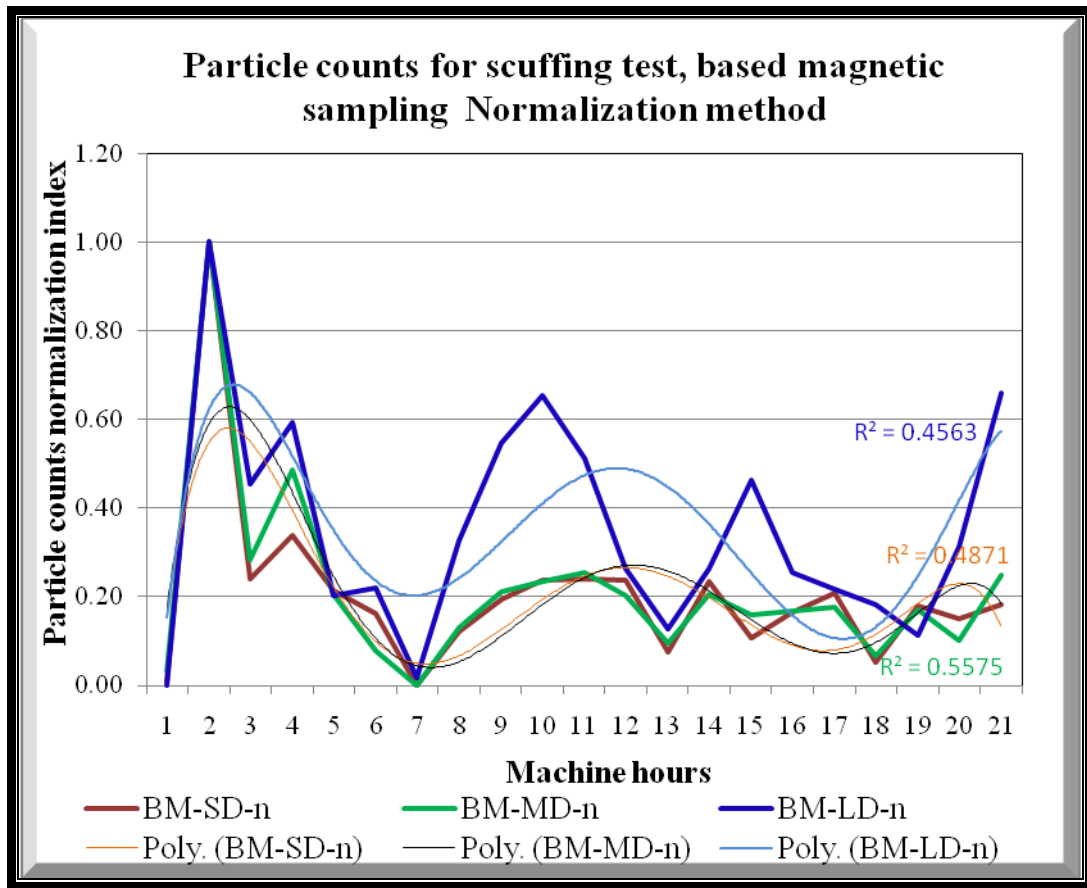


Figure 4-18: Particle counts for scuffing test, based magnetic sampling normalization method

A similar trend is evident in the based magnetic sampling in Figure 4-18; all group of particles show a high trend at the beginning, which confirms the running in zone. The range of the index from hour 1 to hour 5 was between 0.0 to 1.0. After hour 5 the range for the MD and SD seemed to lower and fluctuate between 0.0 to 0.25. This indicates that the removal of MD and SD particles due to gear engagement was stabilized until the end of the experiment. On the other hand, the range for LD index appeared to be erratic, varying from 0.0 to 0.62 until the end of

the experiment. This indicates that the removal of the LD particles was still high towards the end of the experiment, representing a deterioration of the gear surfaces.

The R^2 values for LD, SD and MD are quite low, which shows that the trend line the trend line is quite far from the actual data. However, the R^2 values still show that at least 45 to 55 percent of the actual data follow the trend lines.

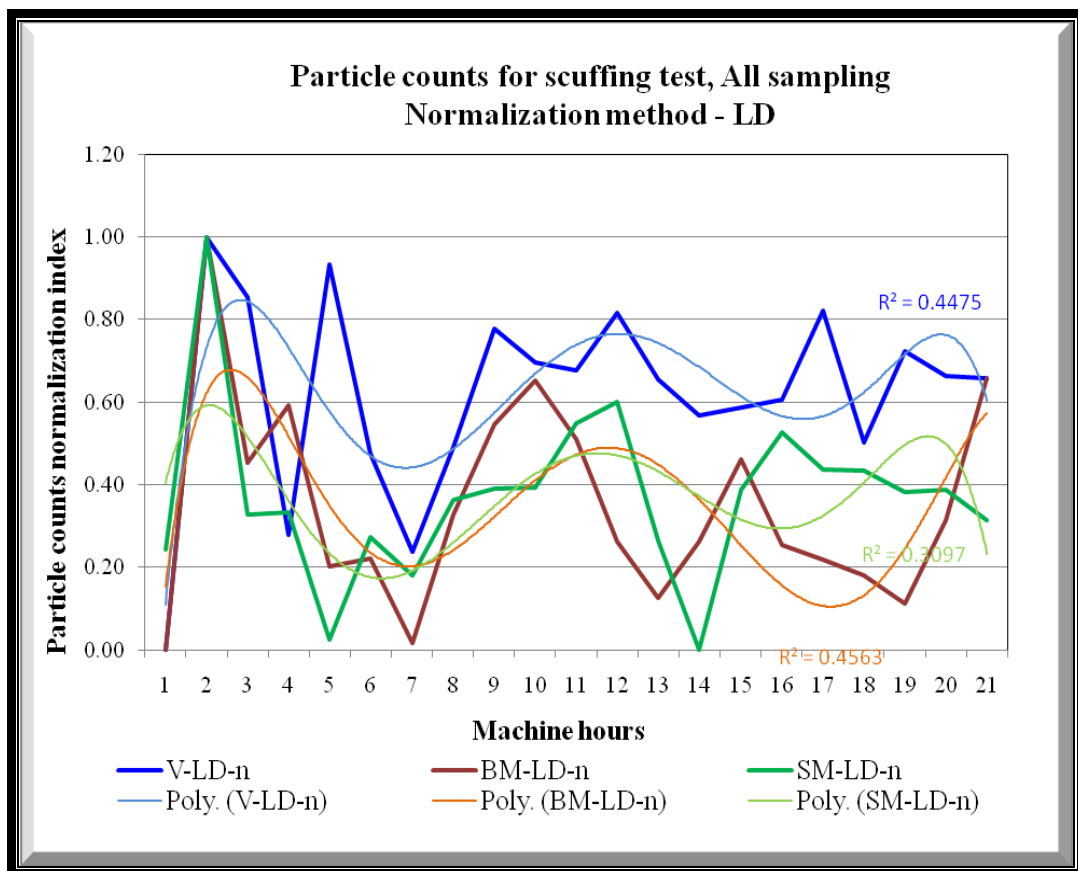


Figure 4-19: Particle counts for scuffing test, all sampling normalization method - LD

After looking at all particles for three different types of samplings separately, Figure 4-19 compares the same size particles on the same graph. The purpose was to find any relationship or similarity of the trends among the three sampling methods. Theoretically, the trend will be about the same if the deterioration of the gears is the only influencing factors. All three sizes recorded a high index at the beginning of the experiment, which represented the running in period. The running in period ended at hour 6 to hour 7 for at least the valve and side magnetic sampling, and the trend of the index after that varies. Valve sampling seemed to

record a stable high index, which shows the particle generation continued to occur at a high level towards the end of the experiment. On the other hand, SM and BM recorded an erratic trend of index fluctuates from 0.0 to 0.6. This shows that the particle generation was intermittently high for these types of samplings. The valve sampling showed a pattern in which it started with high particles generation, lowered in the middle, and then showed a stable high particle generation towards the end.

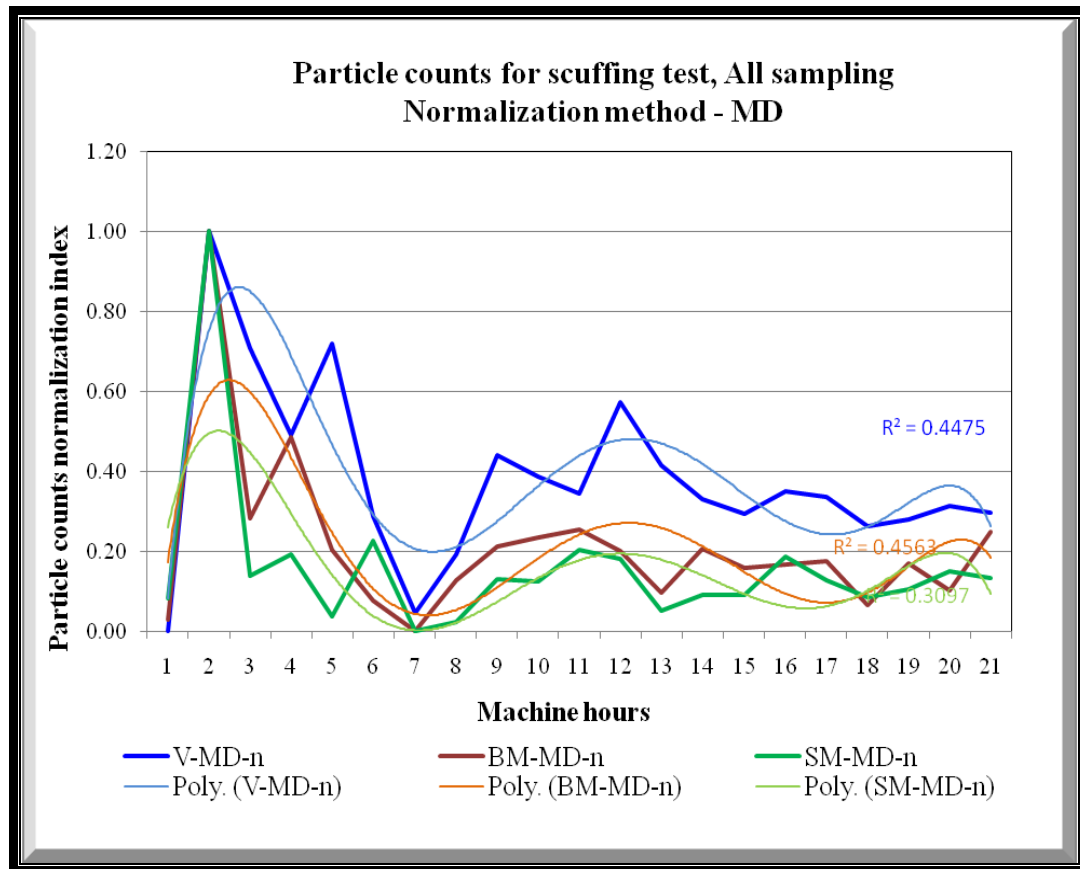


Figure 4-20: Particle counts for scuffing test, all sampling for MD

In comparing the MD particles generation overtime, it is interesting to find that there were similarities at the beginning of the experiments in which all samples recorded a high index, showing particle counts on the high side. This could be explained by the running in zone phenomenon where polishing and rubbing process of the asperities of the gear surface was underway. Then, particles generation was reducing and even though the samples were tested separately, they recorded a low particles generation at hour 7. It may be suggested that the surface of the gears at this time was highly polished and the chances of metal breakaway from the surface

was very low. At the same time, when the abnormal loading continued to exert stress on the surface, the surface started to break away again.

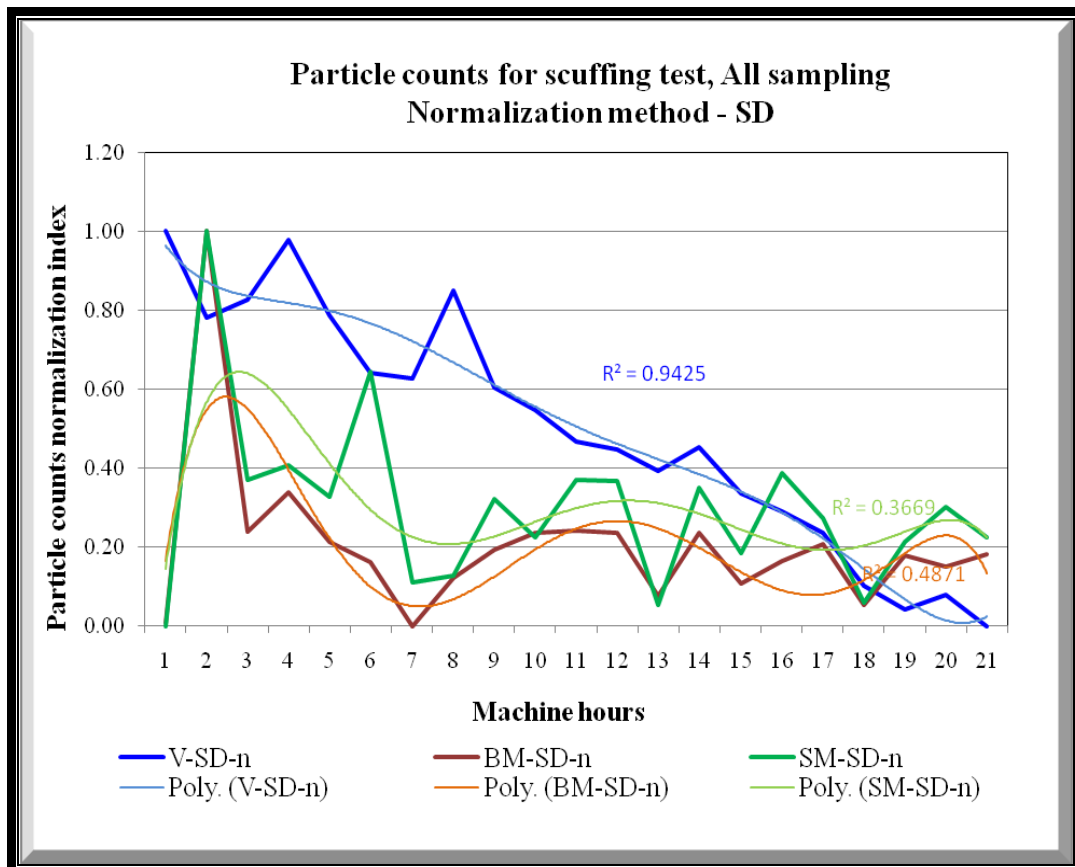


Figure 4-21: Particle counts for scuffing test, all samplings, normalization method - SD

Figure 4-21 compares the three types of samplings for SD; there are similarities between the base magnetic and side magnetic sampling but the trends differed with the valve sampling method. All of the samplings recorded high indexes at the beginning of the experiment, which is explained by the running in zone phenomenon. Then the SM and BM trends continued to stabilize at index ranging from 0.0 to 0.40 but the valve sampling continued to decrease until the end of the experiment. While the trends continued to agree with the assumption that smaller particles reduce towards the end of gears life, the valve sampling showed a more gradual downtrend from the beginning to the end of the experiments. This can be explained by the fact that the valve sampling was done at a common circulation route of the lubricants. Therefore the change in the particles counts

could be easily detected, while the magnetic sampling at both positions would only catch the particles closer to its position.

The experiments tried to establish the relationship between the different types of sampling and different sizes of the particle generations. For all of the three sampling methods, it is quite clear that the running in zone can be established by looking at the high index at the beginning of the experiment followed by a large reduction in a very short period until the reduction stops. For all of the sampling methods, the LD particles tended to increase towards the end of the experiment while the MD and SD tended to reduce towards the end of the experiment. These scenarios agreed with the assumption of analysis in Section 4.7.2.

For Figures 4-16, 4-17, 4-18 and 4-19, the running in zone is where the asperity on the surface of the tooth gear was being polished, resulting in the number of particles produced reaching at peak. Once the asperity due to imperfection in gear manufacturing was removed, debris generation was reduced. These trends can be seen in all of the figures (4-16 to 4-19) above even though the period might be different by 1 or 2 hours. The polynomial trend lines support this claim in all four graphs when they show peaks at hour 2 to hour 3 and the trend lines dip down at hour 6 to hour 7 for the said figures. The lowest index is from hour 6 to hour 7, which indicates the end of running in zone. Figure 4-19 shows that all types of sampling show the same trend. This trend supports the claim that the running in zone is very well distinguishable. The erratic up and down trend after the running in zone in these figures can be explained by the fact that the removal of the particles was not at the same rate all the time. The particle counts were high when there was a relatively big chunk of debris being removed from the gear teeth surface. Then, there is a period during which the damaged surface underwent the polishing process again, and debris being removed was low. Once the polishing process completed and the abnormal load continued to be applied on the gear teeth surface, another removal of a relatively big chunk of wear debris occurred, which was reflected in the high trends of particle counts in all of the figures (4-16 to 4-19).

None of the trends meet the bathtub criteria, because the bathtub curve is an ideal criterion where a population of equipment failure data is grouped together and analyzed. For a single component as in the experiments conducted, that trend

is hardly ever achieved. For a pair of gear mesh, the hourly single data show the wear rate was high when big chunks of particles were removed from the surface; once this process completed, a polishing process on the gear teeth surface took place. During this polishing process, fewer particles were removed from the surface, which shows a low wear rate in the graphs. These processes produced an up-and-down trend towards the end of the experiment. Therefore, it is difficult to achieve a bathtub curve trend on the wear rate of a single mesh gear.

4.7.3.2 Result of pitting test

This subsection presents the results of the pitting experiment to establish the rate of the particle generation over time.

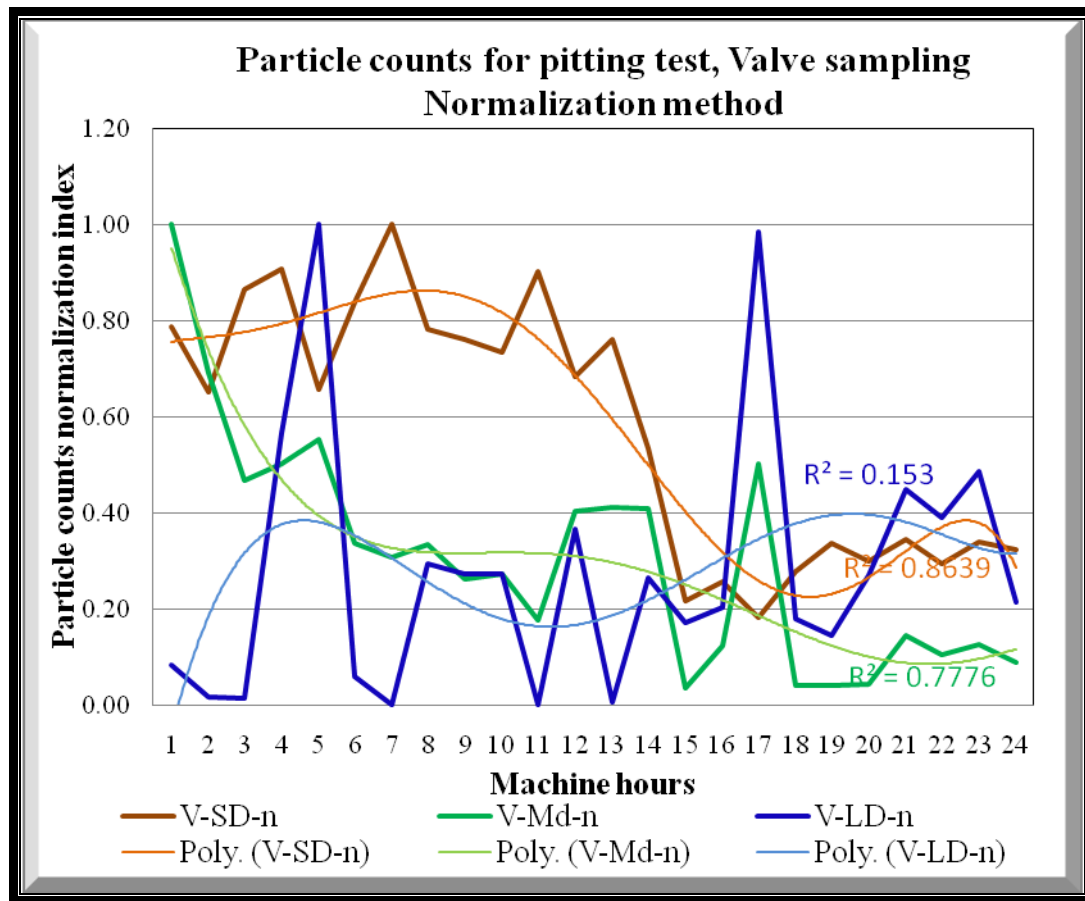


Figure 4-22: Particle counts for pitting test, valve sampling all sizes normalization method

Figure 4-22 shows a trend of multiple size distribution in the valve sampling method. SD trends do show resemblance to SD trends in the scuffing test, starting with a high index at the beginning of the experiment, then following

a decreasing trend towards the end of the experiment. This reaffirms the theory that a smaller particle count will be reduced as the gears health deteriorates. On the other hand, the MD particles showed a gradual decrease in number towards the end of the experiment, but similarly to LD showed an increase in index at hour 16. Both MD and LD showed a higher index at the beginning of the experiment. These phenomena again support the assumption that the bigger particles tend to uptrend when the failure of the gears is imminent. During this process the micropitting damage became destructive, and the small pits become big craters on the surface of the gears.

The MD and SD actual data are quite close to their trend lines which are proven by the R^2 values of 0.77 and 0.86 respectively. However, the R^2 value for the LD particles is quite low, which shows that majority of the LD particle counts data do not follow the trend line presented.

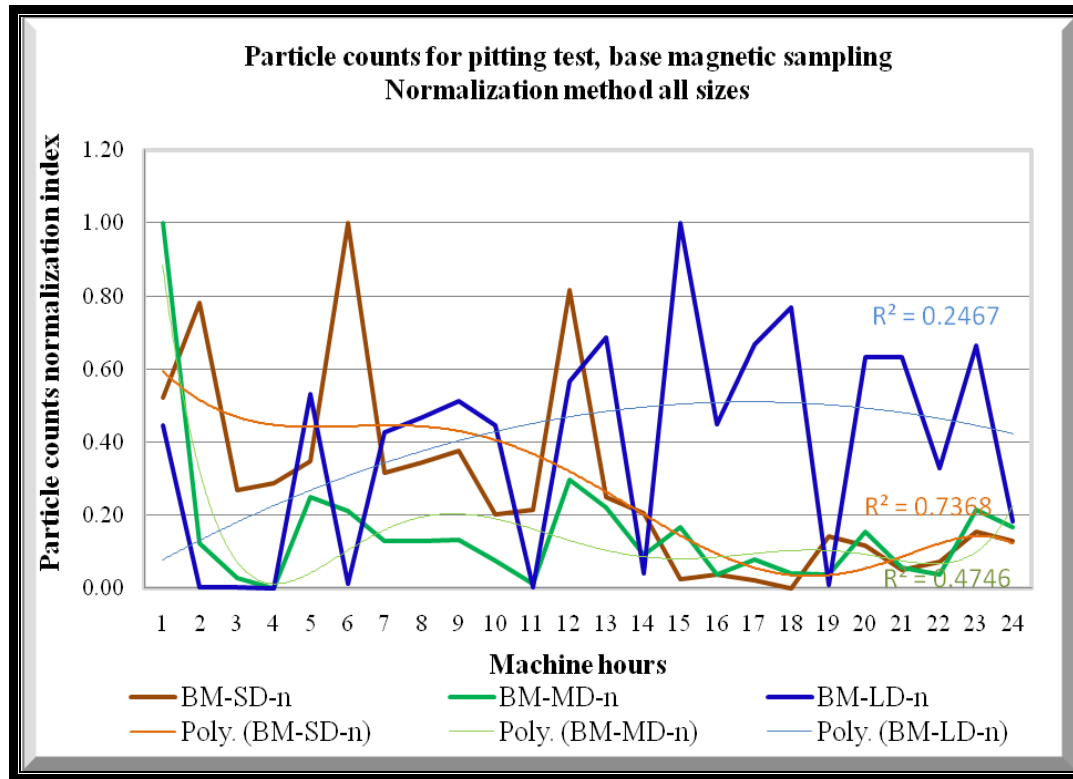


Figure 4-23: Particle counts for pitting test, base magnetic sampling all sizes – normalization method

In Figure 4-23, it is quite clear that the MD and SD the particle counts continued to be low after hour 13 where their normalization index ranged from 0.0 to 0.2. On the other hand, the range index for the LD after 13 hours continued

on the high side with an intermittent low particle count. This agrees with the assumption as the gears continued to deteriorate, the bigger size particles would increase while the smaller size particles would decrease.

The R^2 value for the LD particle trendline is lower than the SD and MD particles R^2 values, which suggest that the trendlines for SD and MD is better than that of LD particle.

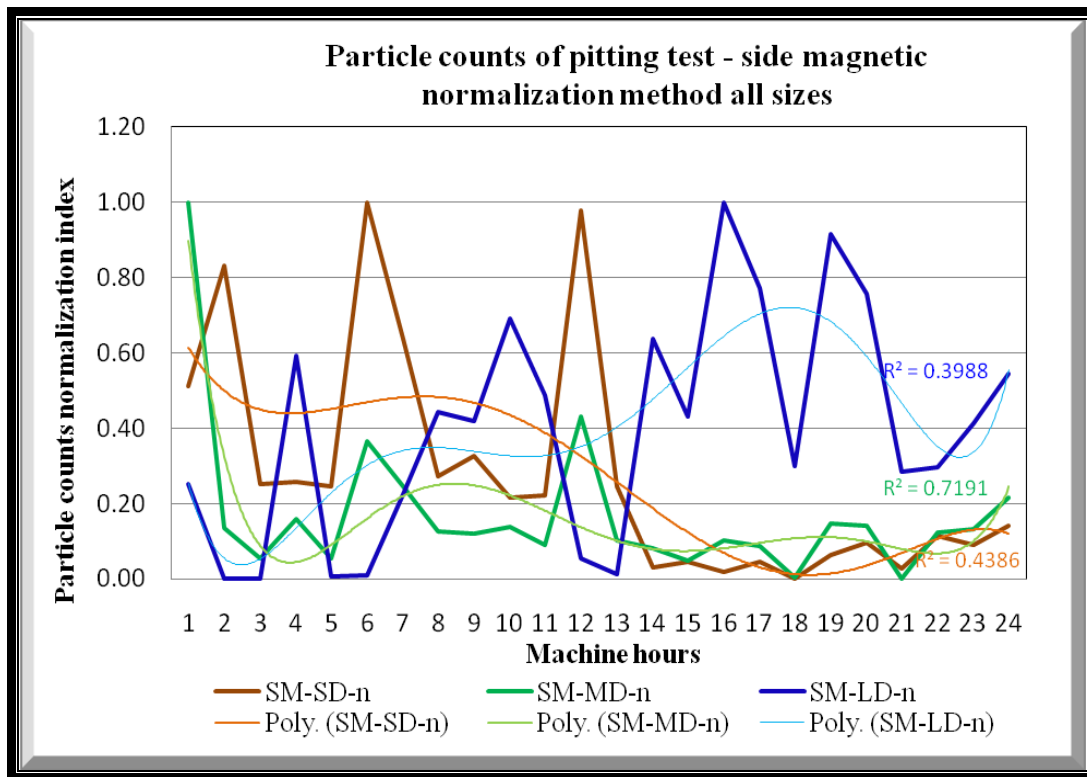


Figure 4-24: Particle counts for pitting test, side magnetic sampling all sizes – normalization method.

In Figure 4-24, the trends resemble the trends in figure 4-23 even though the sampling method as different. For MD and SD, the particles count recorded high index initially but continued to record low counts after hour 13 which is exactly the same trend as in Figure 4-24. The low counts after hour 13 shows a reduction in smaller size particles generation. On the other hand, after hour 13 the LD presented high indexes until the end of the experiment, which reflected a deterioration of the gears.

The R^2 value for the LD particle trendline is 0.39 which shows that about 40 percent of the actual data follow the trendline. The SD and MD particles R^2

values, are 0.44 and 0.72 respectively which suggest that more actual data for these sizes follow the trendline.

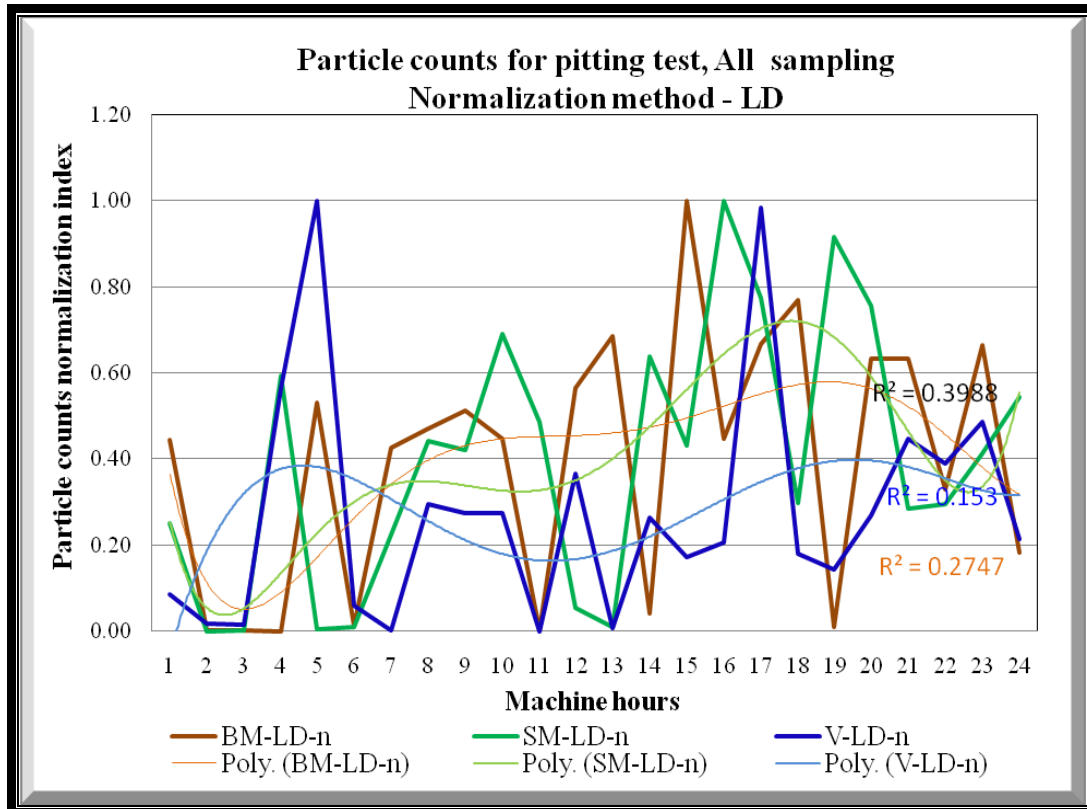


Figure 4-25: Particle counts for pitting test, all sampling LD particles normalization method.

Figure 4-25 compares the trend for the LD particles for different sampling methods. Even though the trends are not exactly the same to each other, a conclusion can still be made that while they recorded a high index up to hour 5 which represents the running in zone; they also recorded a high index after hour 13. These similarities show that the damage of the gear surface after the hour 13 caused the increase of bigger sizes particles count and as the number of peaks just supported the increase removal of metal from the gear surfaces.

All the trends shown in Figure 4-26 are quite similar because the trends were of decreasing particle counts towards the end of the experiment. It shows that the running in zone ceases at about hour 4 to hour 5, then the generation of the MD seems to be stabilized at lower rate. This demonstrates that the tendency of generating the MD particles towards the end of the experiment reduced significantly and the deterioration of the gears tended to produce higher LD particles. The R² values for all of the trendlines are quite high, exceeding 0.7, which shows that more than 70 percent of the data follow the trendlines.

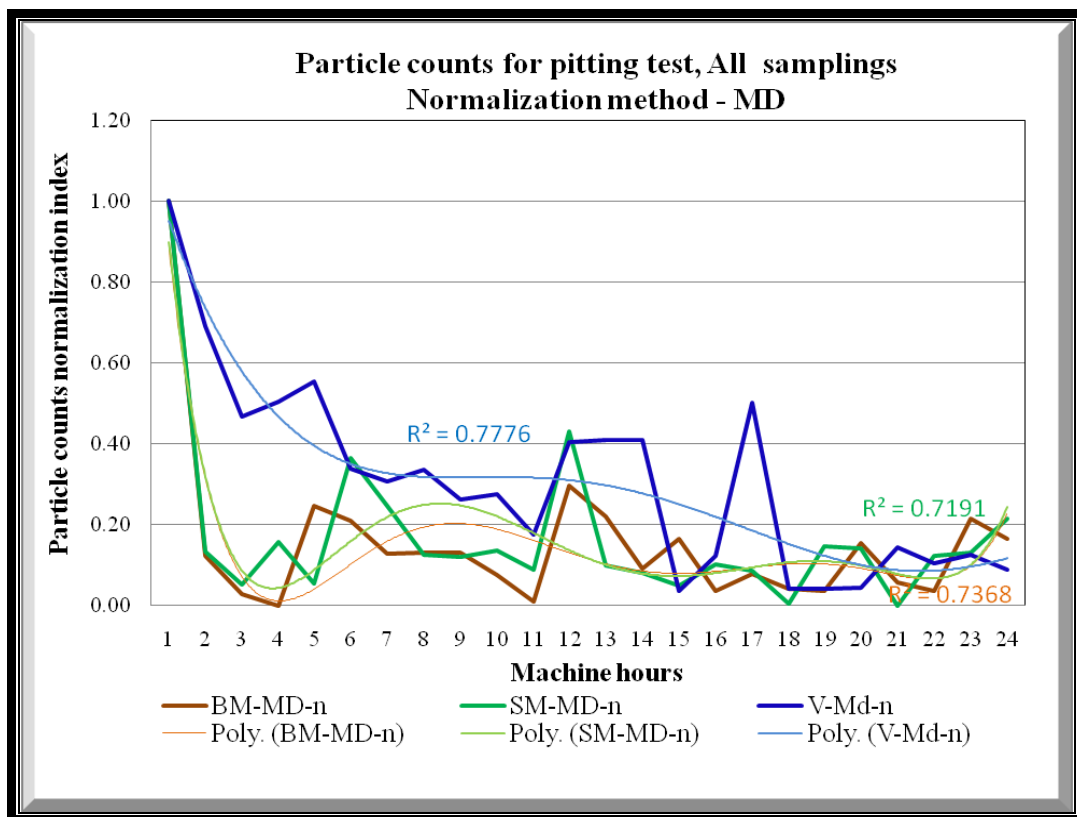


Figure 4-26: Particle counts for pitting test, all samplings MD particles normalization method

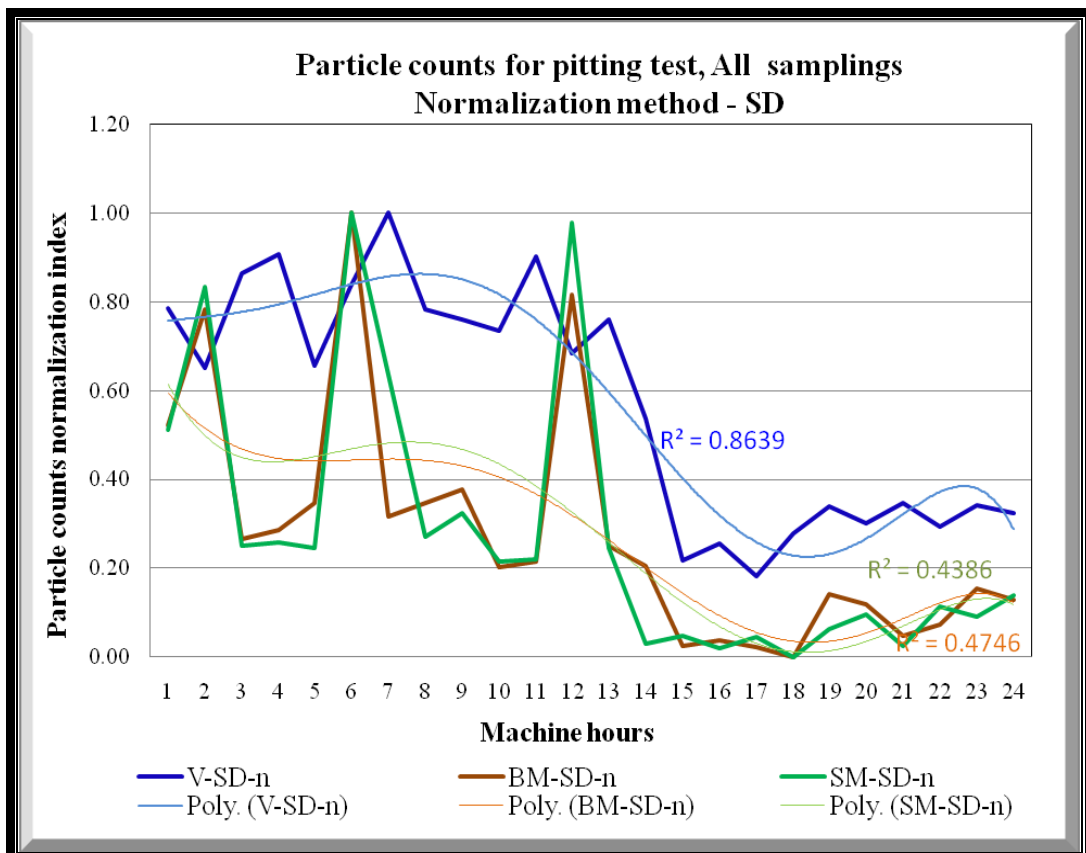


Figure 4-27: Particle counts for pitting test, all samplings SD particles normalization method.

Figure 4-27 trends resemble Figure 4-26 in a way as they recorded a higher index at the beginning followed by reducing trends after hour 12. This could be explained that as the deterioration of the gears was reaching onset of failures, the SD particles tended to reduce and stabilize at a low rate, which represents a low generations of particles. This agrees with earlier assumptions on the theory of particle generation.

Result from this pitting experiment, if analyzed in detail, shows a resemblance to the scuffing test. First, the running in zone can be established quite clearly, as high indexes were recorded in all of the graphs and the reductions in the index occurred abruptly and stopped reducing after certain hours. Secondly, the trend of the LD particles was to increase for all sampling and sizes while the MD and SD particles tended to reduce and stabilize at a low rate towards the end of the experiment. The two phenomena occurred at about the same time; for instance, the SD particles tended to stabilize at low indexes at hour 14 (Figure 4-27) while the LD particles begin to increase their indexes at the same hour in Figure 4-25.

There seems to be differences in determining the onset of failures among the different methods of sampling and different sizes. As valve sampling is a more representative method due to its efficiency in collecting the sample particles, and large diameter particles are able to show the severity of the damage, these two criteria were considered in determining the onset of failure. Valve sampling was more representative compared to magnetic plugs because it was installed on the main route of the oil circulation system and most of the particles in the oil followed that route. The probability of the particles being collected using this method was higher than the magnetic plug.

Furthermore, a 10 μm filter used in the experiments was not able to filter out any smaller particles such as 1, 2 and 5 μm which ran the risk of the particles being circulated back into the system and getting counted twice. The reason for using 10 μm filters was because they were the best available filter for the rig. As a consequence, the smaller particles are not ideal for the determination of the onset of failures in these experiments.

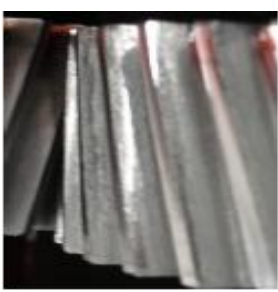
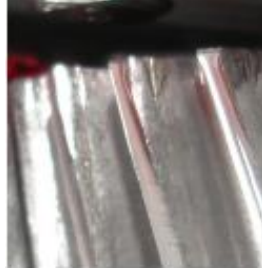
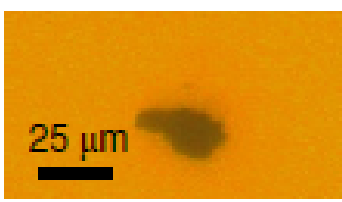
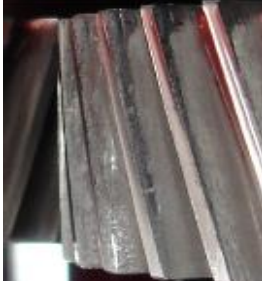
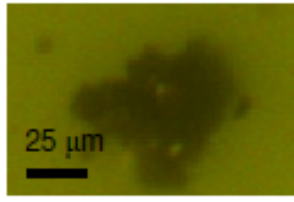
Moreover, similar observations were found in the pitting test and scuffing test that the quantities of the particles recorded were also different for the three different methods of sampling. On that note, the valve sampling collected more wear debris compared to the base magnetic and side magnetic sampling due to the weight of the particles. Some particles tended to settle down at the base of the oil sump, which enabled the base magnetic to collect more wear debris than the side magnetic sampling.

4.7.4 Image capturing and analysis

Once the samples went through the particle counting exercise, they were examined under the microscope for image capturing. However, the image capturing was not done immediately. All of the images were taken off-line from an oil sample collected during the hours the machine ran. Table 4-4 shows examples of some of the shapes of the particles captured during the tests. The background images of the particle are different because the image capturing process were not done continuously on every bottle of oil sample and the amount of light applied was also varied. However, these samples came from the same oil sump but at different machine hours. Initial analysis of the images shows that the available sizes of particles collected from the bottle sampling increased as the

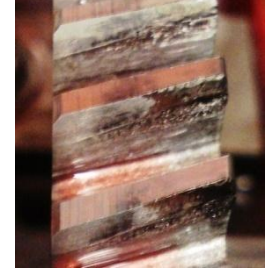
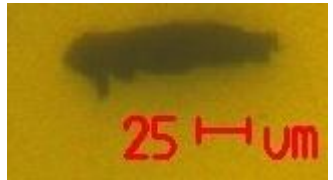
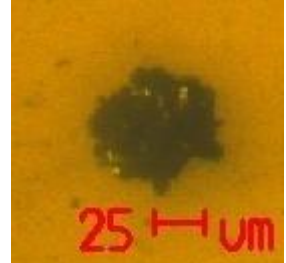
gears deteriorated. In addition, the particle edges also seem to become more irregular rather than smooth.

Table 4-3: Images of gear damage and associated wear particles from scuffing test

Hour	Gear Image	Particle image
3		
6		
9		
12		

15		
18		
21		

Table 4-4: Images of gear damage and associated wear debris particles for the pitting tests.

Hours	Gear damage image	Particle image
12		
15		
18		
21		
24		

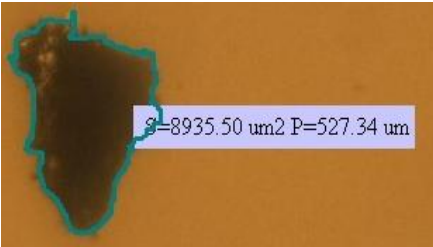
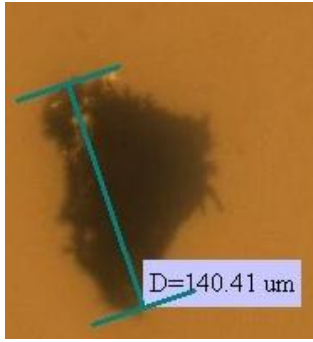
Initial analysis of the images in table 4-4 shows that as the machine clocked longer hours, the available maximum size of the particles also increased

and the edges of the particles became irregular and rough, especially for images taken for machine hours 18, 21 and 24.

4.7.5 Quantitative measurement of wear debris particles

The sizes, perimeter and roundness of the particles can be measured using a MATLAB program and the camera analyzer software. In the left hand images in Table 4-5, the measurement of area, perimeter and roundness were done automatically using the MATLAB program. However, the perimeter and the area on the right hand images were taken manually by drawing the perimeters at the edges of the particle.

Table 4-5: Measurement of the particle's area, perimeter, roundness and size

 AREA PERIMETER ROUNDNESS 9346.00 512.00 0.45	 <i>S=8935.50 um² P=527.34 um</i>
Determination of area, perimeter and roundness using MATLAB program	Determination of the area and perimeter using camera software analyzer
 <i>D=140.41 um</i>	
Determination of longest length of particle using camera software analyzer	

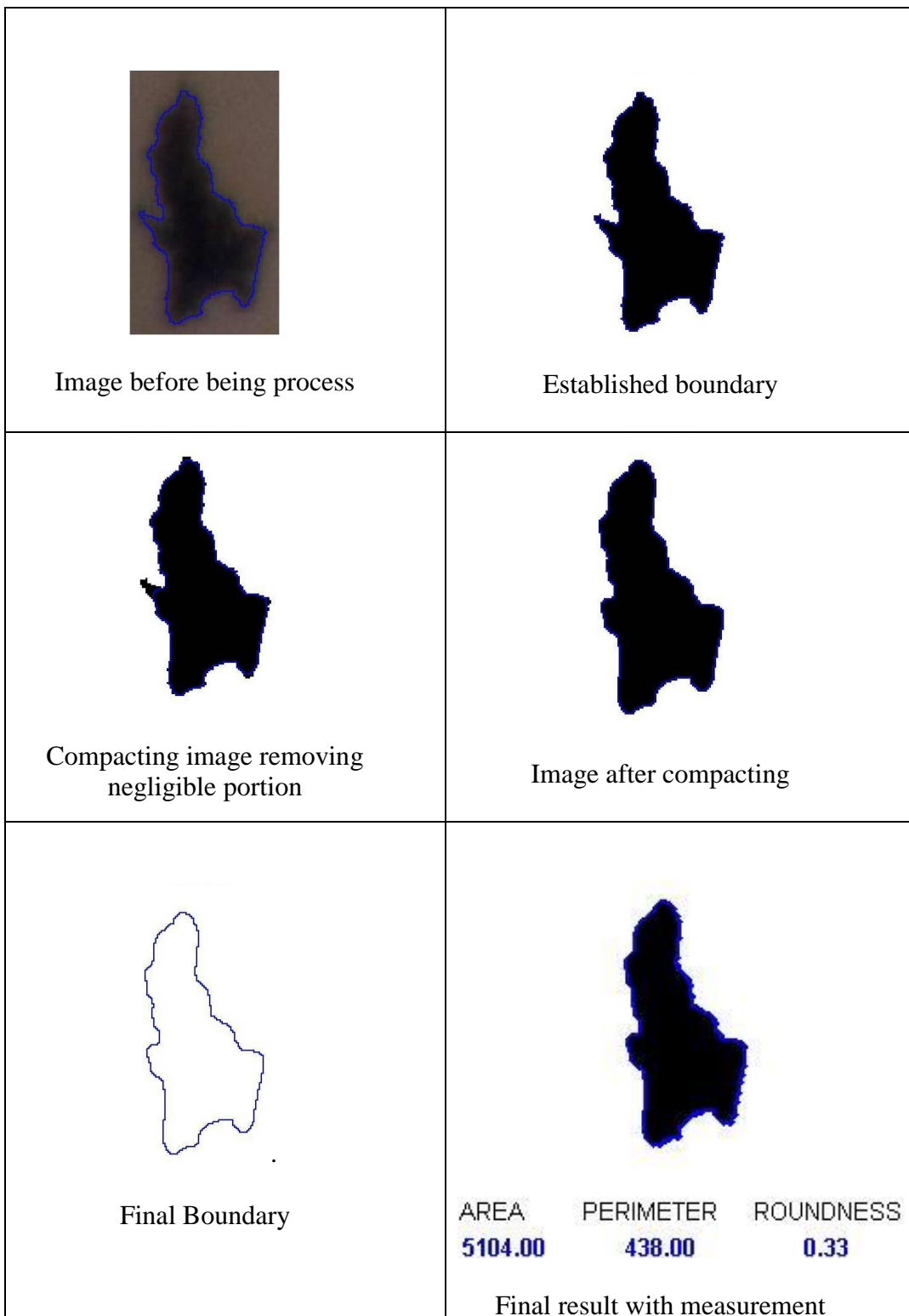
There are some differences between the camera software results and the MATLAB software results. The differences came from the manual drawing of the boundary of particles by placing the cursor and dragging it around the image; this manual tracing can lead to errors.

The percentage of errors for the area of particle in Table 4-5 was about 4.5 % in comparison to computer analysis while for the perimeter; the error rate was about 3 %. This shows that use of computer analysis for such image processing is required in order to obtain accurate dimensions. Inaccuracies will affect the volume calculation of the particles and subsequently will affect the wear rate determination of the gear under study. The result of the area measurement using the MATLAB program is more accurate since it counts the number of pixels inside the border area. This is where the resolution is important; the higher the resolution, the more pixels inside the area.

4.7.6 Preliminary 3D images reconstruction

Table 4-6 illustrates how the coordinates of the particle boundary were established by using the MATLAB program. These coordinates were used to reconstruct the pseudo-3D images. In determining the boundaries of the particles, a small area (less than 30 pixels) was taken out from the actual images. The method aimed to remove and to smooth the particles edges for easier overlay in the later path of 3D images construction. The other reason was to remove any small particles that might appear around the main particles that may be connected to the main particles if it is not removed during boundary determination. Thirty pixels is equivalent to a 30 microns area inside the border of the particles and does not refer to the ferret length of the particles, being used as the size of the particles.

Table 4-6 Images of same particles undergoing filtering



After the boundaries of the same particles from different viewpoints were established, the images were overlaid using a common axis. Figures 4-28 to 4-31

show how this was achieved. The height of the images of both views of the particle (that are later considered as the z-axis) should be the same.

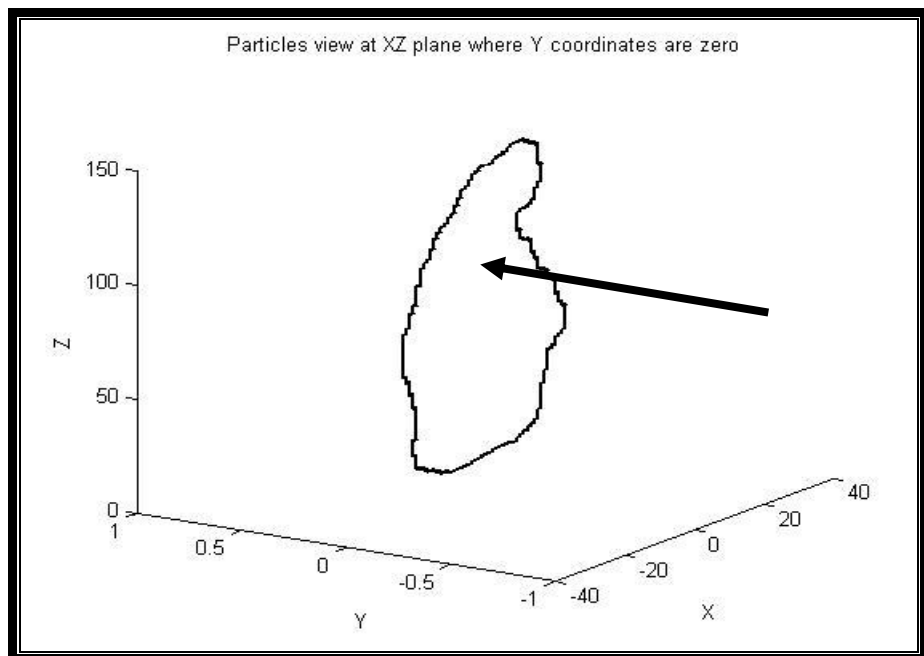


Figure 4-28: particle image view at XZ plane

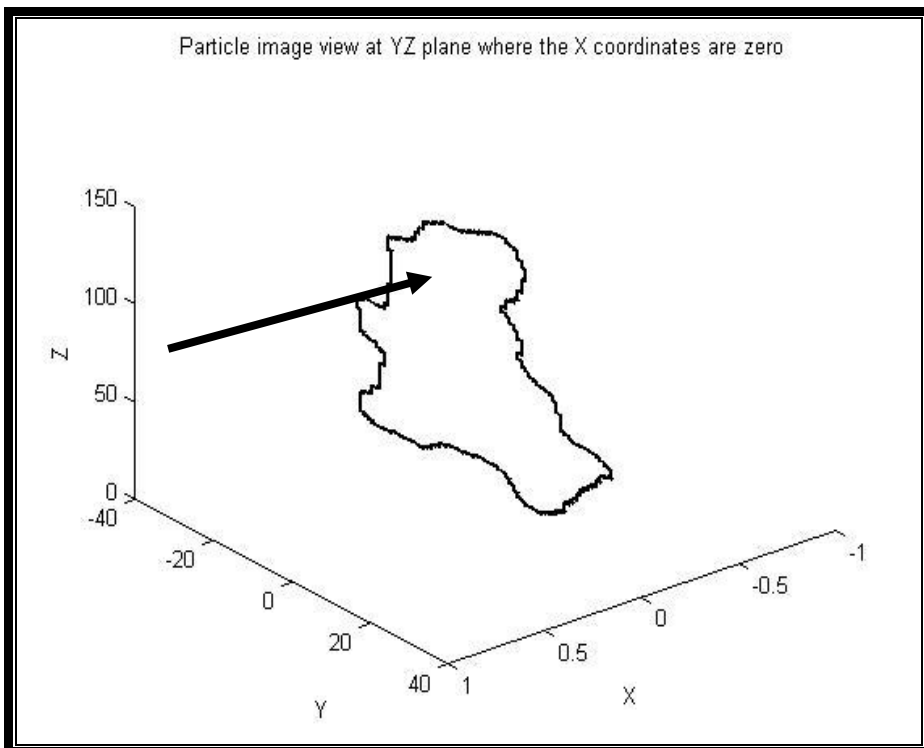


Figure 4-29: Particle image view on YZ plane

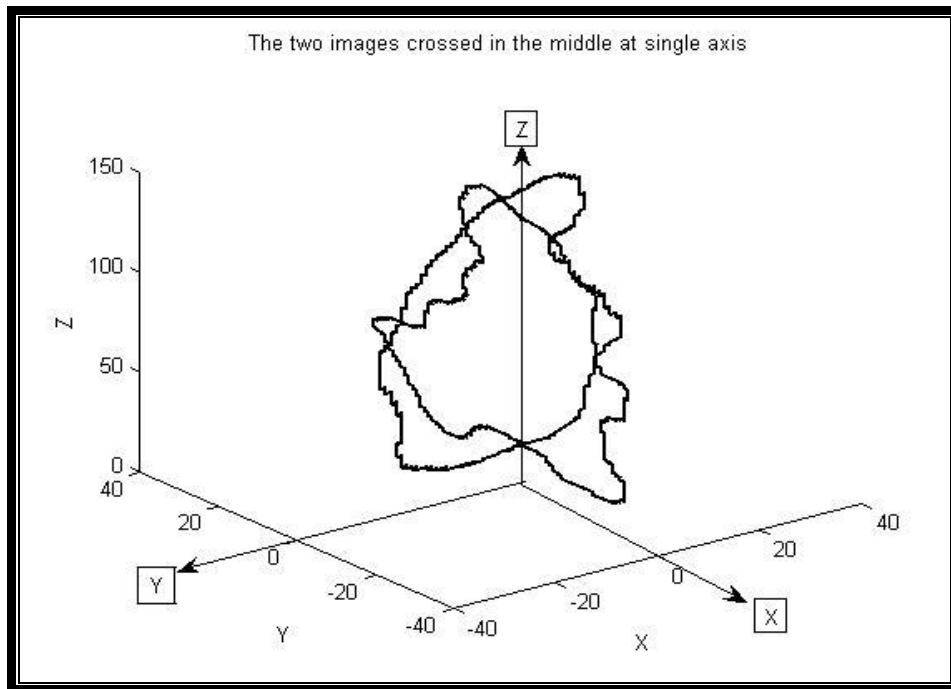


Figure 4-30: Two images crossed along a single axis

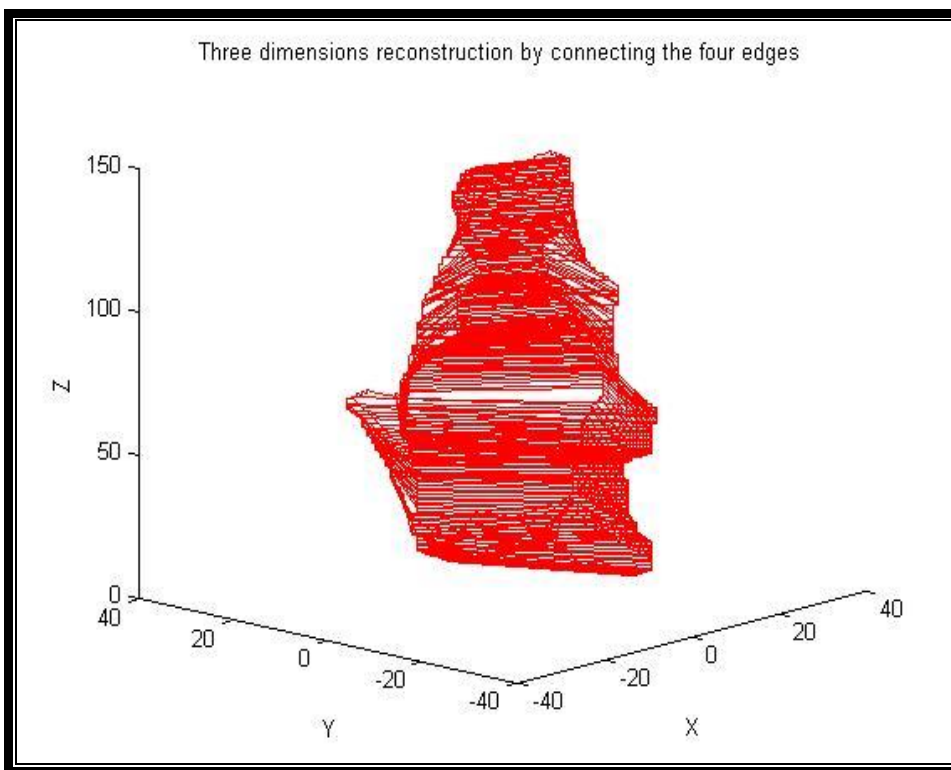


Figure 4-31: Lines connecting the four edges to reconstruct pseudo-3D images

The outcome of this exercise is not a perfect 3D reconstruction but has paved the way for further studies to be conducted on the 3D imaging reconstruction of wear debris particles in the later part of this thesis.

4.7.7 Volume estimation

Particle volume was another quantitative analysis that was pursued in this research, and in this preliminary experiment, simple volume estimation was used, as shown in Table 4-7. Estimation used a front view of the particle, which referred to the largest area view, while the side view referred to the smallest area view of the particle.

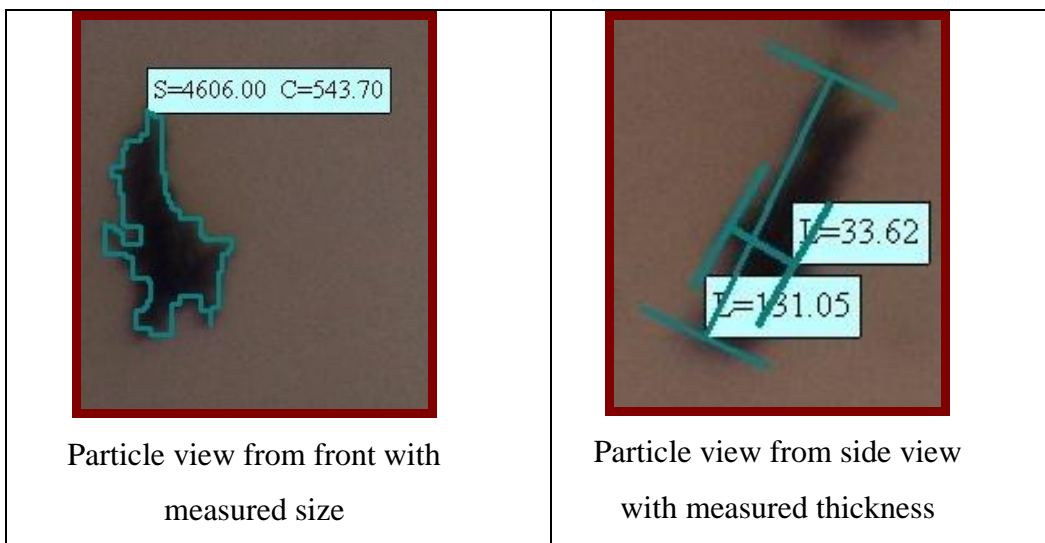


Figure 4-32: Estimated volume calculation

$$\begin{aligned}\text{Simple Estimated Volume} &= \text{Area} \times \text{thickness} = 4.6 \times 10^3 \mu\text{m}^2 \times 33.6 \mu\text{m} \\ &= 1.54 \times 10^5 \mu\text{m}^3\end{aligned}$$

4.7.8 Issues on camera and supply tube for online particles count and image capturing.

Since the objectives of the research include online particle counts, and volume and thickness estimation, the sample was also tested for an online particles count where the sample was directly feed to the PODs from the oil sump. Online particle counts using PODs did not use pneumatic pressure as in the offline sampling. The pressure build-up through the pumping of the fluid to the PODs was used to push the sample into the machine for the counts. The pressure needed to reach 3.0 bars before the counts started. However, the tube that was used for the counts was a silicone tube which could not sustain the 3.0 bar

pressure, causing it to burst. In order to address this issue, a special tube made of neoprene material was used which managed to sustain the pressure. During the experiment, the images of the particles viewed on the display were blurry and not sharp if the sample flow rate was high. This is due to the fact that the camera capturing capability was 15 frames per second. If the particles moved with the speed exceeding the capturing capability of the camera, it gave a blurry image without a clear boundary. In order to get sharp images, the flow rate was maintained at 0.81 ml/min or 0.81 cm³/min with peristaltic pump speed of 3.0 rpm [75-76].

Figure 4-32 shows the cross sectional area of internal section of the flow cell, with a height clearance of 0.3 mm and width of 77.5 mm.

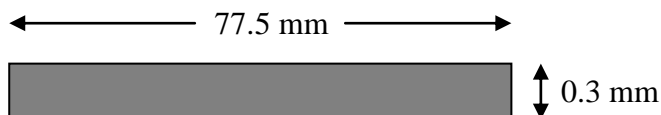


Figure 4-33 : Cross-sectional area of internal volume flow cell

If the flow rate of the fluid sample was 0.81 cm³/min, the equivalent velocity of the fluid inside the flow cell can be estimated as follows

$$\begin{aligned} \text{Velocity} &= \text{flow rate/ area} = 0.81 \text{ cm}^3/\text{min} / (7.75 \text{ cm} \times 0.03 \text{ cm}) \\ &= 3.48 \text{ cm/min or } 34.8 \text{ mm/min or } 0.58 \text{ mm/s} \end{aligned}$$

However, the particles inside the flowing fluid may not have the same velocity, which was dependent on their mass. The larger particles tended to have a lower velocity in comparison to the small particles. Figure 4-33 shows the size of the window of area capture under microscope. The size of the window was 1.39 mm length and 1.04 mm width. In order to determine the velocity of a particle, the time of a particle to move from one end to the other was measured. Observation showed that the larger particle could move as slow as 0.008 mm/s and smaller ones had velocity as high as 0.070 mm/s. These numbers were arrived at by dividing the distance the particles covered with the time taken. The time as taken from the actual running video and the distance was measured using the infinity camera software.

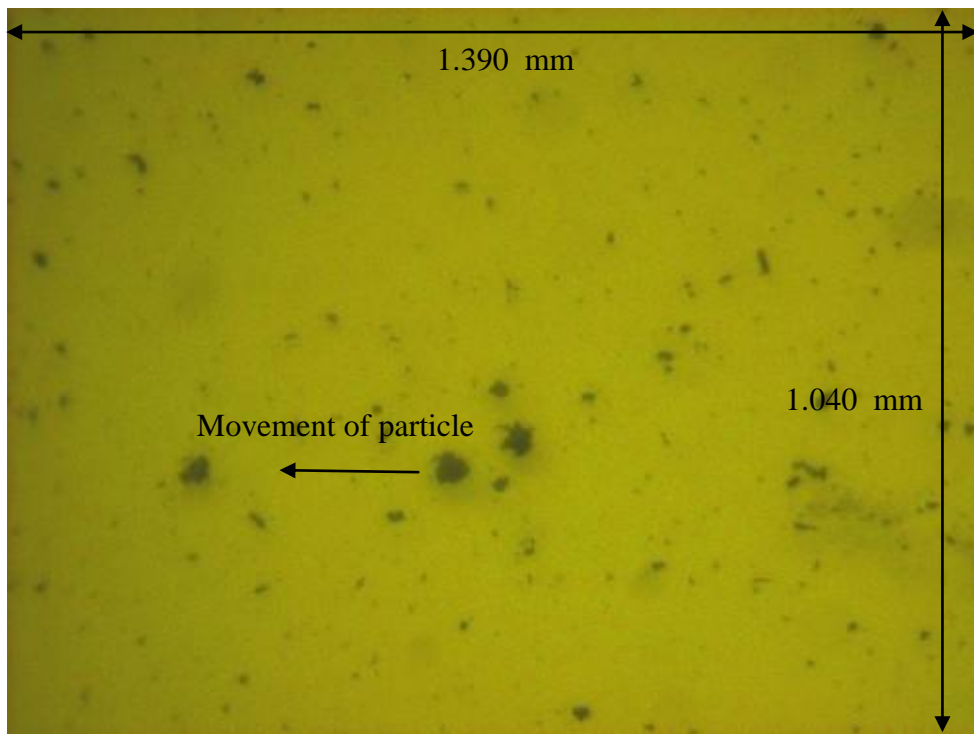


Figure 4-34: Actual size of image under microscope

4.8 Lessons and observations from the preliminary experiment

- Off-line sampling is laborious, tedious and exposes the sample to the risk of contamination through the transfer of samples from the magnetic plug to the sampling bottle.
- The off-line bottle sample needs to be shaken to avoid the wear debris metal from settling down to the base of the bottle for a better representative of the sample during the particle counts. This is due to the fact that the particle counts were not done immediately and were only conducted when the experiment completed. Obviously the particles have settled down at the bottom of the bottle.
- The valve sampling apparently collected the most wear debris to be tested, which indicates that this method of sampling can be the best way to collect particles from an oil system. Nevertheless, it must be noted that the valve sampling collected all of the debris from the oil sump, which contains the oil that circulates through the oil line, regardless of whether this debris are metal or contaminants. However, since the source of the debris for this particular experiment can be assumed to have originated from the steel gears under study, and the oil is reasonably contaminant-free due to an enclosed oil sump, the presence of another metal can be discounted.

- Base magnetic sampling attracted more wear debris in comparison to side magnetic sampling, which suggests that this location can be the best place to locate any online sampling tube to directly bring the sample to the flow cell or PODs.
- Most of the wear debris particles counts did not generally follow the shape of a “bathtub” curve.
- The rate of 1 μm , 2 μm , 5 μm and 10 μm particle generation largely decreased as the life of the gears moved towards the failure zone for all of the tests and sampling methods. However, due to the filter size of 10 μm , the smaller size particles may have passed through the filter and circulated back into the system, which risk of being counted twice. Therefore, the small diameter wear particles are unreliable choice in indicating and identifying the onset of failures.
- In order to support the identification of the phases of the life of the gears, additional inspection regimes such as gear damage images were implemented in these experiments.
- Particle counts by PODs are based on light extinction where only one view of the particles is taken. It disregarded the thickness and the volumes, which are important features of wear debris. While PODs can be relied on to count the particles and present the size distribution, it is essential to take the measurement of the volume and thickness of the particles to show the severity of the wear of the gears.
- Particles in the flowing oil sample can be rotated by intermittently changing the direction of the flow. In order to implement this, some modification of the existing peristaltic pump was required to allow the pump to be controlled automatically using a time based system.
- Direct supplies of oil from the oil sump are possible for the imaging of the particles and for particle counts using PODs. However, a more durable tube is required to sustain the pressure (3.0 bar) required to run the test.
- The CCD camera can only capture images up to 15 frames per seconds, which limits the set speed of the peristaltic pump to only 3 rpm, which is equivalent to 0.81 ml/min throughout the experiments.

4.9 Conclusions

This chapter gives details of the preliminary experimental arrangement and the particle count results of the preliminary tests. It also explains the procedure for image capturing and debris features measurement such as volume, thickness and area. The result further suggests lessons to be learned from the experiments that will provide ways for modification work to be done on the apparatus. The two experiments suggest that the best sampling location is at the base of the oil sump and the pitting test is the better choice in determining the onset of failure as the damage of the gears is more visible. Furthermore, the findings conclude that while ideally the wear rate should follow the “bath tub” curve trend, none of the results could be easily adapted to this shape to identify the onset of failure of the gears. Generally, online sampling is the best option for future experiment and in order to capture multi-view images of a single particle, a modification is required to provide the facility to mechanically rotate the particles.

Chapter 5 Final and validation experiment results

5.1 Introduction

This chapter will highlight the modifications and changes to the apparatus for the final and validation experiments, the algorithms for the wear debris analysis, the result of all the experiments, and the onset of failure determination for the gears under study.

5.2 Hardware modification and experimental setup

The preliminary experiments showed that there was a need to reduce human intervention in the wear debris analysis, and several actions were taken to address the issue. Firstly, the peristaltic pump that brings the sample to the flow cell for analysis was upgraded from model Watson Marlow 323s to 323DU, which allowed the pump to be controlled automatically by the RS232 serial computer link. The modification of the pump involved the installation of an RS232 card to enable the pump to receive instructions externally where in this case the instruction comes from the computer, which has a HyperTerminal program. The purpose of controlling the pump automatically was to enable the pump to change its direction of flow within certain set time intervals and then change back to the original flow direction. The computer sends a specific command code to the pump. Table 5-1 shows the RS232 command codes for running the pump.

Table 5-1: RS232 Command codes- peristaltic pump Watson Marlow [64]

Com man d code	Function command	Command code	Function command
1SP 003	Set pump speed to 3 rpm	1RR	Set clockwise direction
1RC	Reverse direction	1SD	Reduce speed by 1rpm
1SI	Increase speed by 1rpm	1RL	Set counter-clockwise direction
1GO	Start pump	1RS	Show all pump information
1ST	Stop pump 1ZY	1ZY	Show running status of the pump.

In order to send the instructions through the HyperTerminal, a simple program provided by the manufacturer was used in order to establish a connection

between the computer and the pump. Once the Hyper Terminal program was connected, a simple list of instruction as shown in the appendix V was placed in the HyperTerminal dialog box and sent line by line to the pump. A display enabled continuous monitoring of the tasks that are currently being received and acted by the pump.

The purpose of changing the flow direction was to disturb the flow of oil containing debris, and the sudden change creates a shearing effect whereby while the debris in the oil was flowing in the outlet direction, it was forced back in the inlet direction causes the particles to rotate. In addition, the irregular and twisted shape of the particles, assisted in the probability of the particle to rotate when the flow direction changes suddenly.

Software specifically for the use of PODs was installed into the computer to download and to present the data on particle counts. The downloading of the data was also done through a RS232 connection, which enabled monitoring, in near real time, the particle count data. Figure 5-1 illustrates the PODs windows software that displays the particle count graphs and data

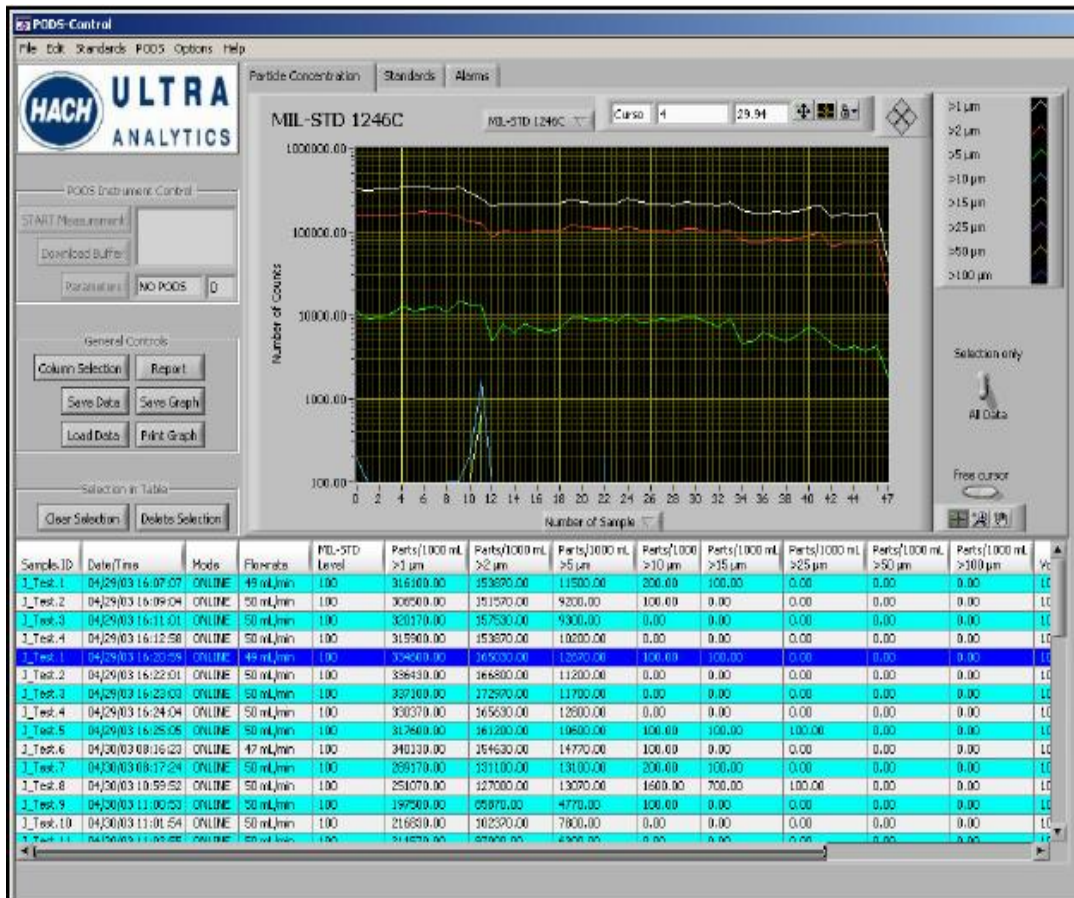


Figure 5-1: PODs window display software.

The flow cell that was used in the final experiments was initially used by Khan in his experiment and the schematic of the diagram is presented in figure 5-2 and figure 5-3 [73]. The previous flow cell used in preliminary experiments could not sustain the prolonged supply of the oil samples as its glass window tended to rupture and leak. This is because the glass used in the previous flow cell's window was fragile, but the Perspex material used in this experiment was more durable and could sustain the pressure of the fluid sample. In addition, the previous flow cell could manage a much smaller volume of samples which may exclude the sample from being representative.

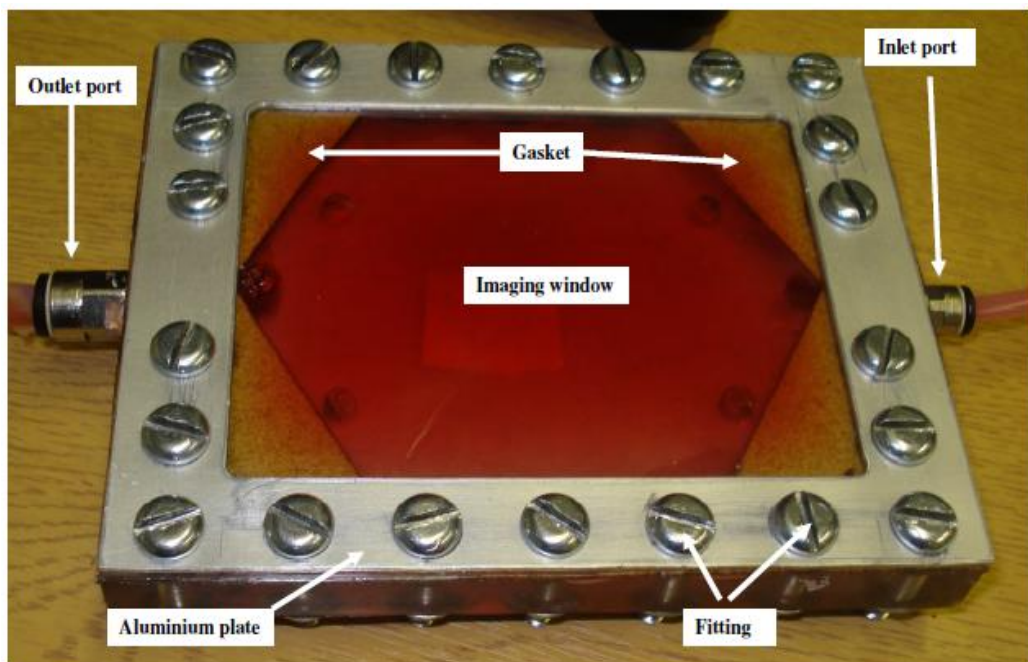


Figure 5-2: Flow cell [73]

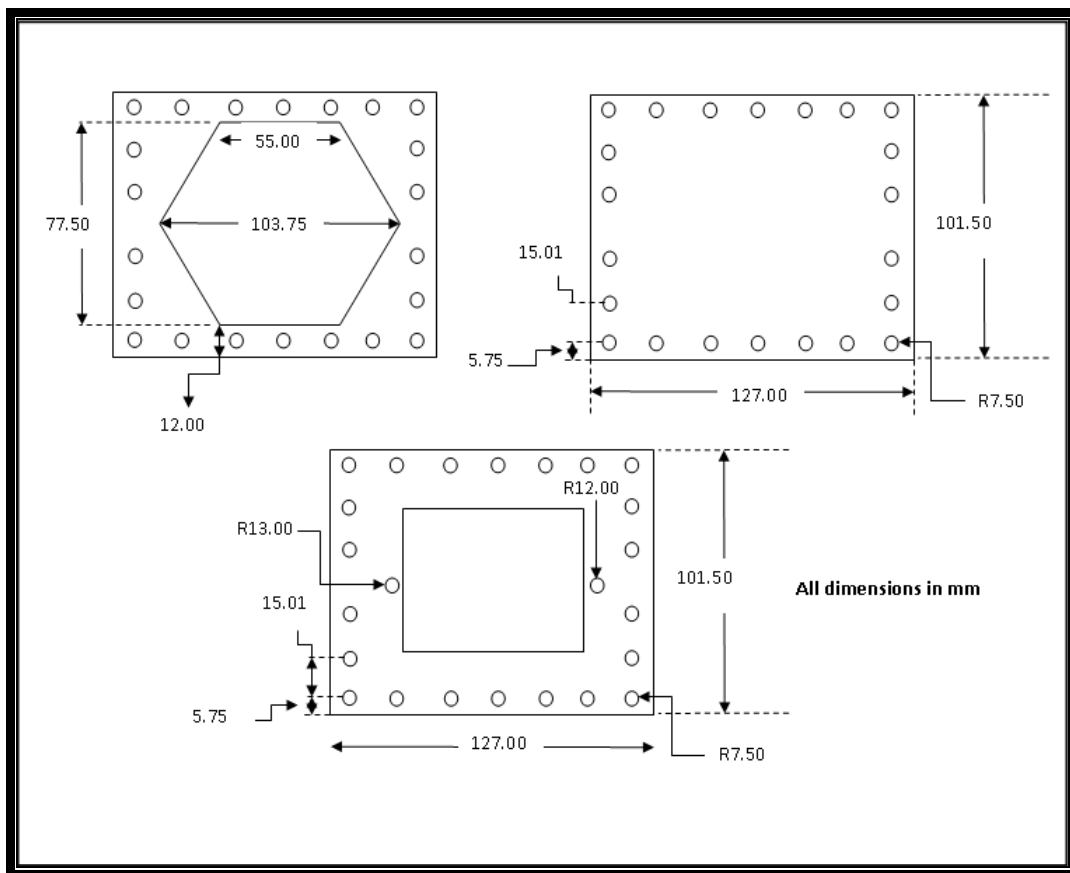


Figure 5-3: Schematic diagram of flow cell [73].

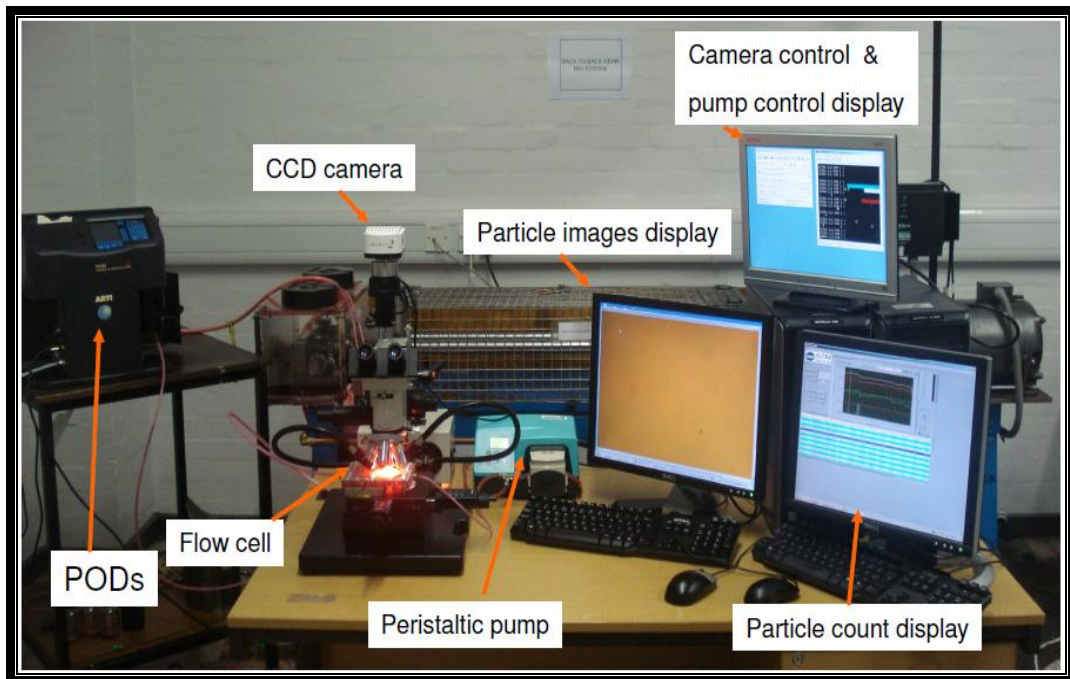


Figure 5-4: Final setup of experiments

The final setup for the experiment is shown in Figures 5-4 and 5-5, which addresses the issue of online sampling and multi-view image capturing of particles. The pink line in Figure 5-5 shows that the flow route of the oil sample containing wear debris was sent to the flow cell using a 3.2 mm silicone soft tube and to PODs using a neoprene tube. The delivery of the oil sample to PODs required a high pressure and durable neoprene tubing to be used, due to the pressure requirement of 3.0 bars before the particle counting process can be initiated. Once the oil sample went through the image analysis and particle count process, it passed through a filter before returning to the oil sump. This removed debris greater than 10 μm from circulation and reduced the probability of the same particle being counted twice or their images examined repeatedly. In addition, there was another pink line from the oil sump to the filter, which represented the normal circulation of gear oil in the system for filtration.

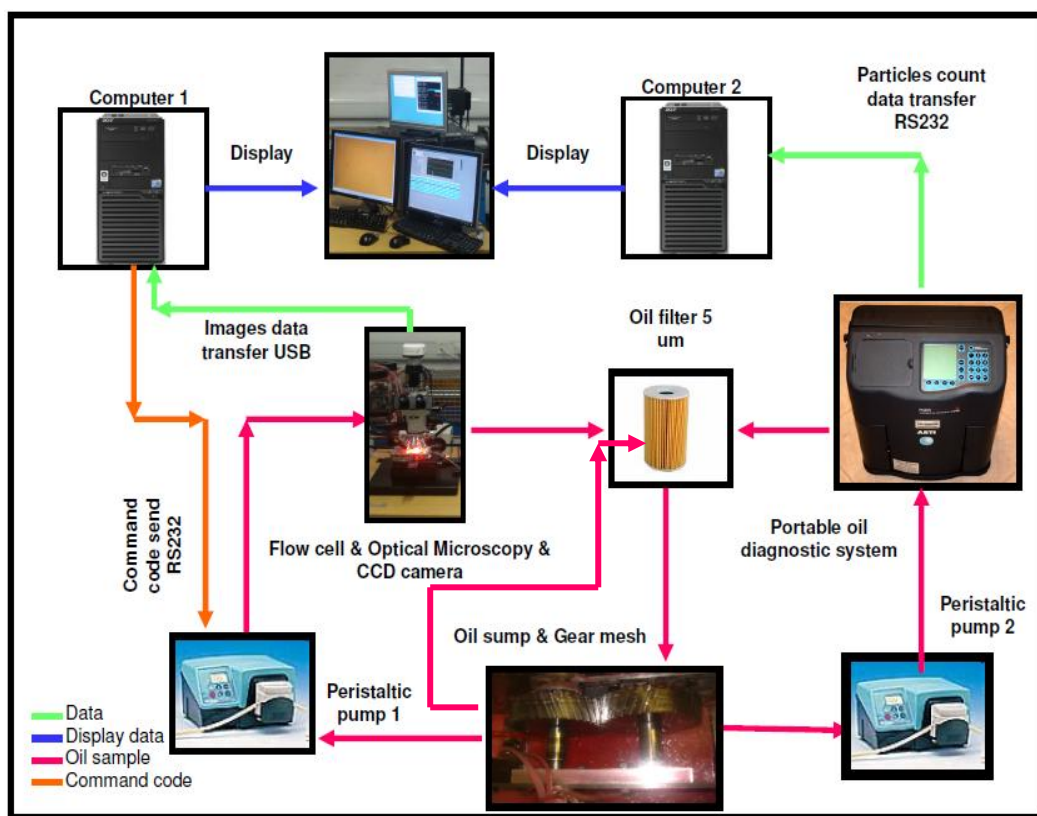


Figure 5-5: Schematic diagram of final setup showing the flow of sample and data.

The green lines in Figure 5-5 represent the transfer of data from PODs to computer 2 and from the CCD camera to computer 1. Due to only a single serial port being available in each computer, two computers were used; one was used to send command codes to the first peristaltic pump in order to regulate the flow of the oil sample to the flow cell and the second was used to receive particle count data from the PODs. The orange line represents the sending of command codes through the RS232 connection to peristaltic pump 1. The codes were sent periodically to control and change the direction and speed of the flow sample, which was intended to provide a means for the particles in the oil sample to be rotated. The blue lines were just the connection from computers to the display monitors for the purpose of monitoring. Three LCD monitors were used to display images of the particles generated by the wear process, particle count data and the command instruction to the peristaltic pump 1.

As the first four steps were explained in the hardware section of the flow cell, peristaltic pump and CCD camera, the software system will start with the conversion of video images to multi-frame of still images.

5.3 Image processing

5.3.1 Dynamic of wear debris analysis particle motion

In studying the dynamic of the particles, the concept of degrees of freedom of suspended particles in gear oil was used. Degrees of freedom refers to the number of independent spatial coordinates that must be specified to define the position of a body. For a point mass body, only three coordinates are required to determine position. On the other hand, if the body is extended, such as a particle, three position coordinates and three angular coordinates are required to completely specify its position and orientation in space. In this study, the possible motions of the particles were defined in Figure 5-6.

In this study, it is clearly recognized that a particle has six degrees of freedom as indicated in Figure 5-6, which are: rolling, in which the particles tumble and roll left and right, pitching, in which particles tilt forward and backward, yawing, in which the particle turns left and right, swaying, in which where the particles move left and right, surging, in which the particles move

forward and backward, and heaving, in which the particles move up and down in the flow cell.

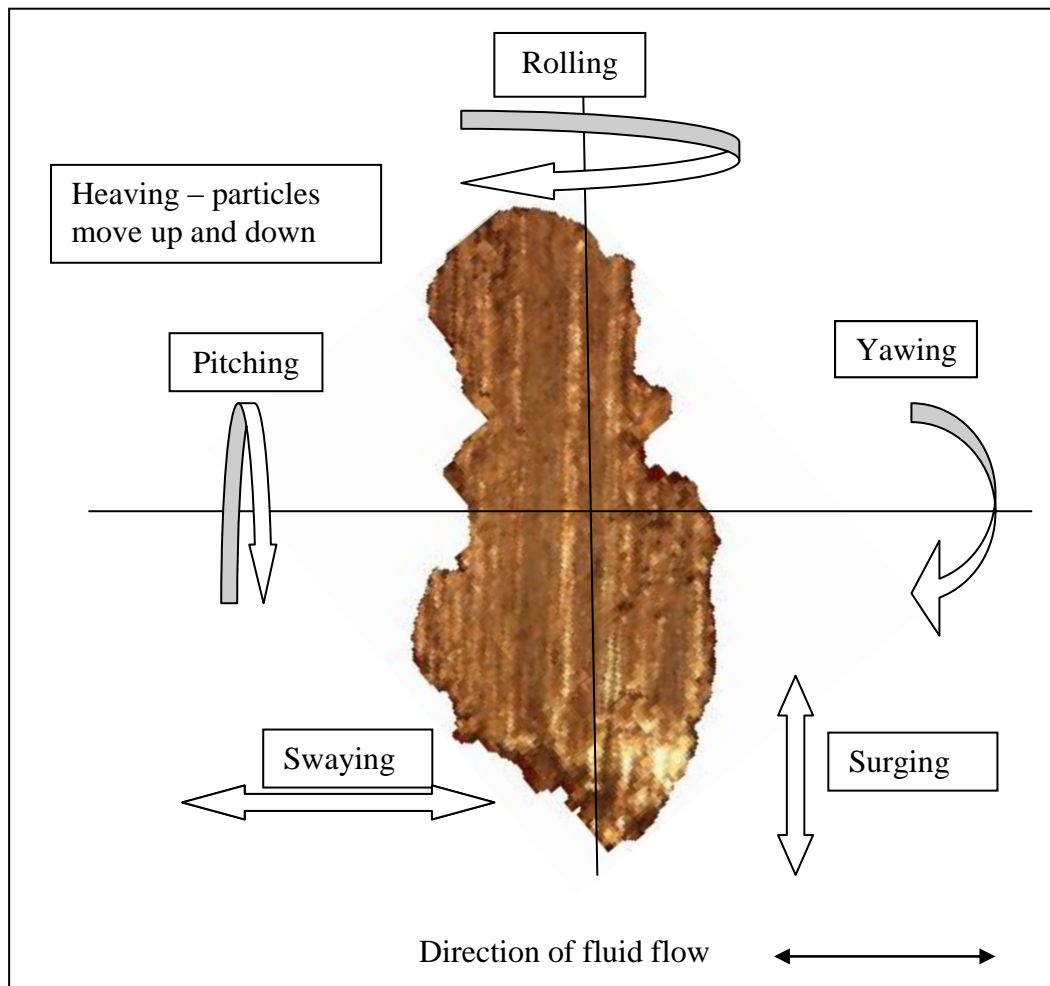


Figure 5-6 Degree of freedom of wear debris particle motions.

The desired movement in this study was the rolling motion, in order for the thickness of the particle to be seen. The pitching motion is very limited because the flow of the fluid is from left to the right of the flow cell as indicated in Figure 5-6. Yawing is other motion of particles which could be seen. This type of motion happens to big size particles which cannot tumble and instead slide to the floor of the flow cell.

Appendix VIII shows some results of particle motions in the flow. The particles were traced individually and their behaviour was matched with degree of freedom motion. From 120 sample particles that were traced individually, 82% or 99 particles showed rolling motions while 15% or 18 particles showed swaying

motions and 3% or 4 particles showed yawing motions. Figure 5-7 shows that the majority of particles motions were rolling, which as the desired movement in order to get a view of the thickness of the particles.

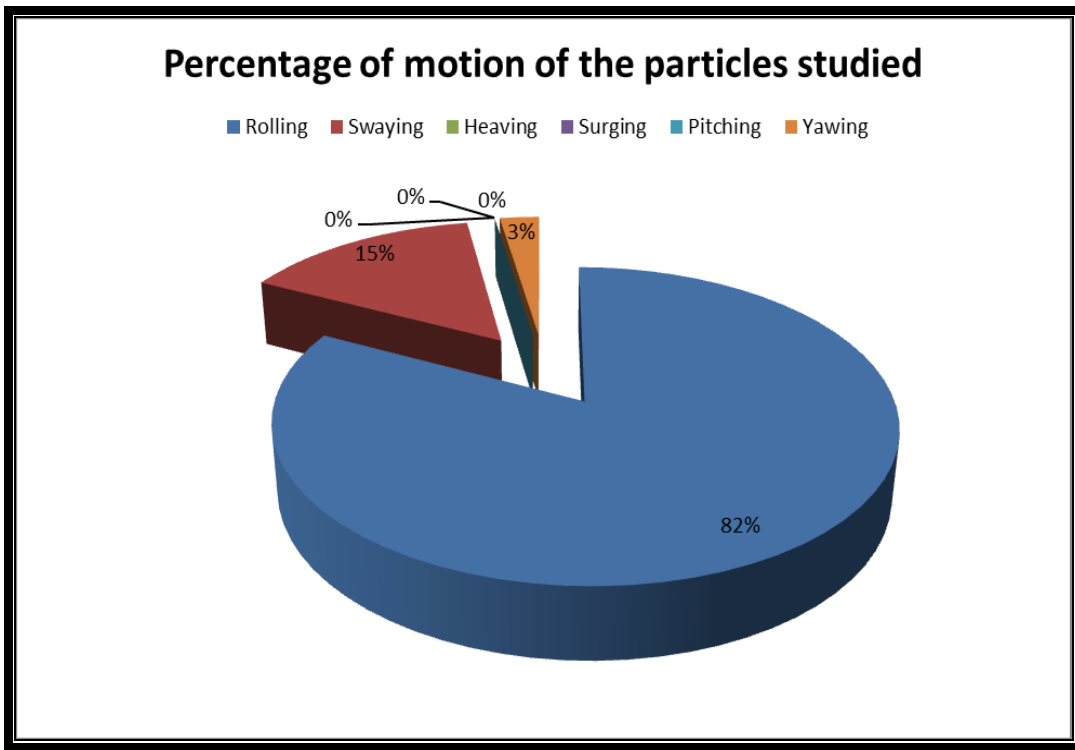


Figure 5-7 Result of the percentage of motion according to six degree of freedoms

In addition to the motion of the particles, the study also measured the speeds of rotation of the particles specifically for the rolling motions particles. The individual particles were traced individually to measure how long it took to complete one single rotation of 360 degrees. The time it took can be retrieved from the camera software, which shows the length of the images displayed. In this case, the time taken to display the image is the actual time taken by the particles to rotate or move from one point to another point. Appendix VIII shows the time taken for each individual particle that resembles the rolling motions in seconds per rotation which can be further converted to RPM. Figure 5-8 shows the rotation speed (RPM) of particles versus the size of the particles. Even though the data is still insufficient to conclude the relationship between the speed of the particle rotation and the size, the bigger size particle particles tend to rotate slower which is below than 4 RPM.

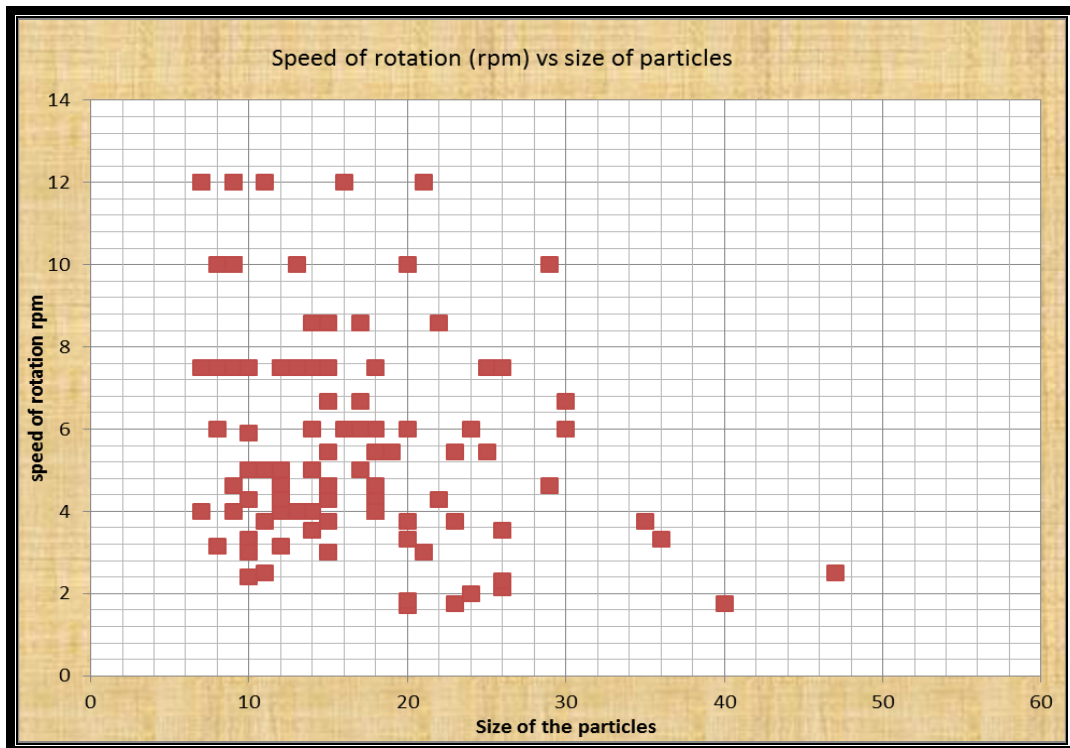


Figure 5-8 Result speed of rotation versus size of particles

Figure 5-9 shows the distribution of the particles studied. It shows that majority of the particles were platelet shaped. The study also showed that the platelet type particles more easily rolled in comparison with others.

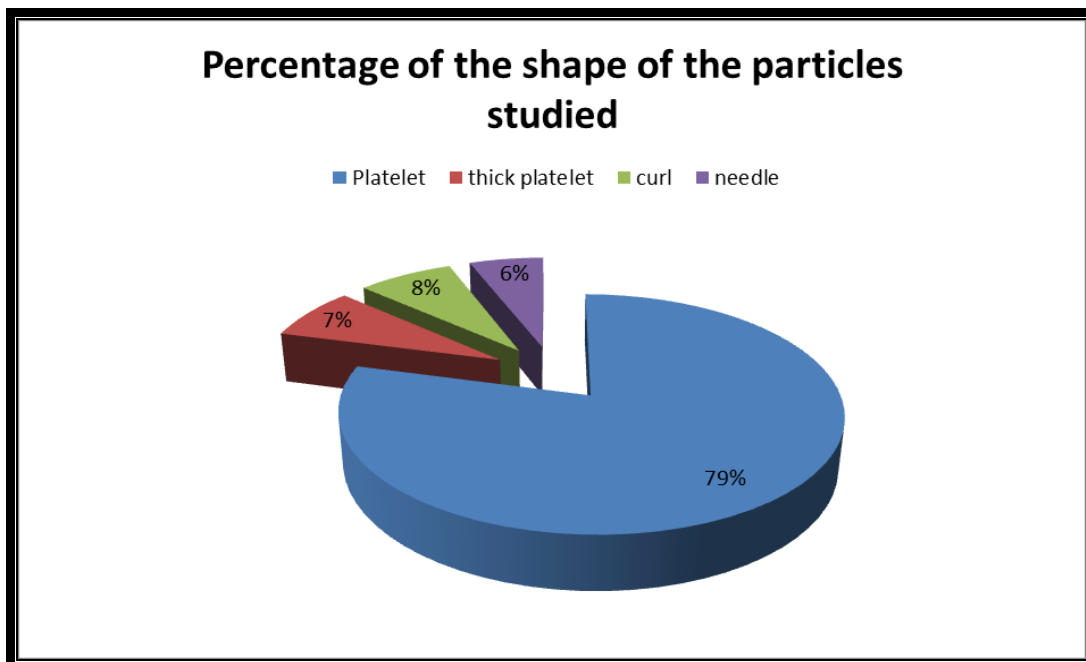


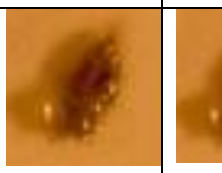
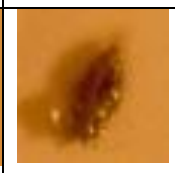
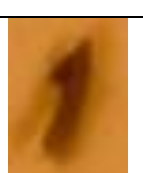
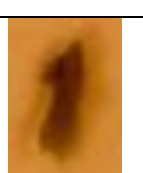
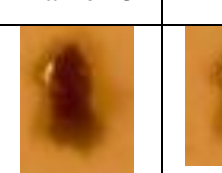
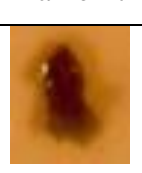
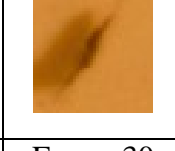
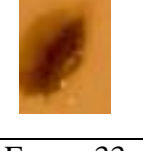
Figure 5-9 Distribution of the shape of particles

These finding provide empirical evidence that the rotations of the particles was required in order to produce a multi-view image of a single particle. In addition, the size and shape of particles have significant bearing on the speeds of rotation. This type of analysis of the dynamics of the particles has never been done before regarding the possibility of rotating the particles.

5.3.2 Conversion of video images to multi-frame of still images

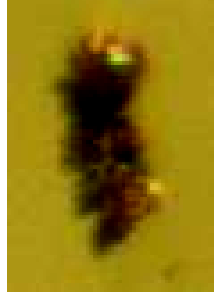
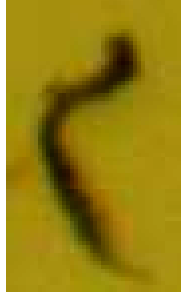
Frame grabber software, which is an off-the-shelf program, was used to convert the video images to still images. The software is capable of transforming the video images to a large number of frames where the best frames can be chosen to construct pseudo-3D images. In this exercise, only images which have relatively same height were chosen. At least two images with a different view angle of approximately 90 degrees of a particle were chosen for further processes of tracing the particle boundaries. The main criteria of the selections are the one with the biggest area image will be the front view and the one with the smallest area image will be the side view. The following table 5-2 shows how the approximation of 90 degrees apart was done. For example, the frame no 1 and frame no 9 were considered 90 degrees apart. Similarly frame no 9 and frame no 15, frame 15 and frame 23, frame 23 and frame 33, and frame 33 and frame 46 were also considered as 90 degrees apart. In other words, the biggest area image and the smallest area image were assumed to be 90 degrees apart. The other information that could be deduced from the table as the direction of rotation; for example from frame 1 to frame 16, the particle rotated from left to right for 180 degrees while from frame 17 to frame 46 the particle rotated from right to left. These images confirm the rolling motion of the particles as claimed in Figure 5-7. There were some particles which did not rotate on the same axis; these particles were not considered in the volume estimation but the occurrence rate was very low.

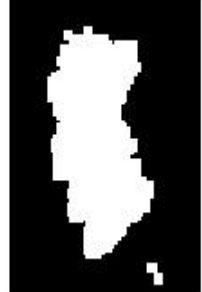
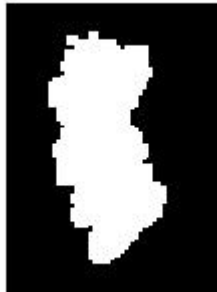
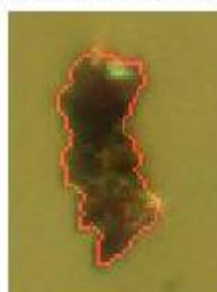
Table 5-2: Frames of still images of a rotating particle

Frame 1	Frame 2	Frame 3	Frame 4	Frame 5	Frame 6	Frame 7
						
Frame 8	Frame 9	Frame 10	Frame 11	Frame 12	Frame 13	Frame 14
						
Frame 15	Frame 16	Frame 17	Frame 18	Frame 19	Frame 20	Frame 21
						
Frame 22	Frame 23	Frame 24	Frame 25	Frame 26	Frame 27	Frame 28
						
Frame 29	Frame 30	Frame 31	Frame 32	Frame 33	Frame 34	Frame 35
						
Frame 36	Frame 37	Frame 38	Frame 39	Frame 40	Frame 41	Frame 42
						
Frame 43	Frame 44	Frame 45	Frame 46			
						

5.3.3 Tracing the boundary of particles

In tracing the boundary of the particles, the study used common functions in MATLAB software and some examples in the MATLAB demonstration section were referred to in producing the soft code. This is due to the fact that boundary tracing of particles is quite a common MATLAB task that has been used by many researchers and it is capable of giving a good boundary outline. Figure 5-6 illustrates how the boundary tracing of particles of wear debris was produced systematically.

Original image		
Convert to Gray image By using <code>rgb2gray</code> function in MATLAB.	Gray image	Gray image
Using Edge detection function ' <code>edge</code> ' and <code>imdilate</code> function to detect edge of the image.	dilated gradient mask	dilated gradient mask

Filled the hole in the area using <i>imfill</i> function in the MATLAB.	binary image with filled holes 	binary image with filled holes 
Remove any small insignificant area using <i>bwareaopen</i> and clear the border using <i>imclearborder</i> function to smoothen the edges.	cleared border image 	cleared border image 
Erode the image using the <i>imerode</i> function.	segmented image 	segmented image 
Use <i>bwperim</i> function to get the perimeter of the white area and then bring back the original RGB image to compare the outline with the original image.	outlined original image 	outlined original image 

Then use the outline only for the boundary tracing result, which will be used in the 3D construction.

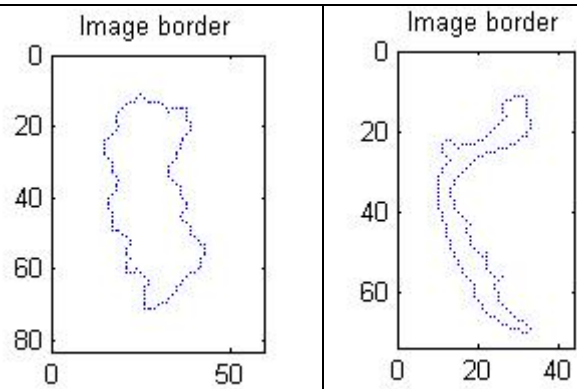


Figure 5-10: Step by step image trace boundary

Once the boundary was traced for both images, there was a requirement to know how they are connected. One of the characteristics of both images was that they had the same height; therefore both images were assumed to share the same Z coordinates. In determining the x and y coordinates, the following algorithms were used.

5.3.4 3D Algorithm

Figure 5-7 shows a sample of particle images showing the front view and side view on a scale graph, indicating that the particle has the same height in both images even though it was viewed at different angles, as shown by the dashed lines across the images.

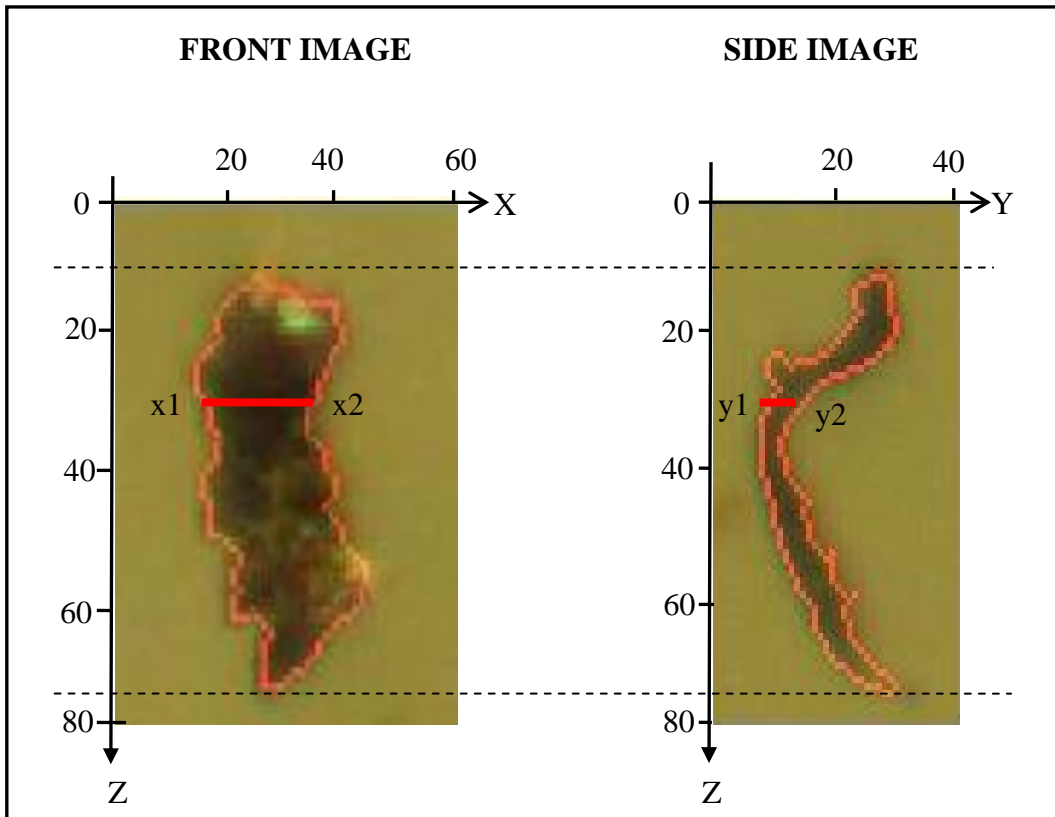


Figure 5-11: Front view and side view of a particle

Both images were taken from the same particle but at an angle of about 90 degrees difference, where the assumption is made that the images share a common axis. In determining the x, y, z coordinates of the pseudo 3D images, front view images at any height of the image represented the z coordinates, y1 and y2 were assumed to be zero, and x1 as the minimum value of x coordinates at $z=a$ while x2 was the maximum value of x coordinates at $z=a$. Similarly, for the side view, x1 and x2 were assumed to be zero while y1 was the minimum value of the y coordinates and y2 was the maximum value of the y coordinates, while the z coordinates were assumed to be the same for both images.

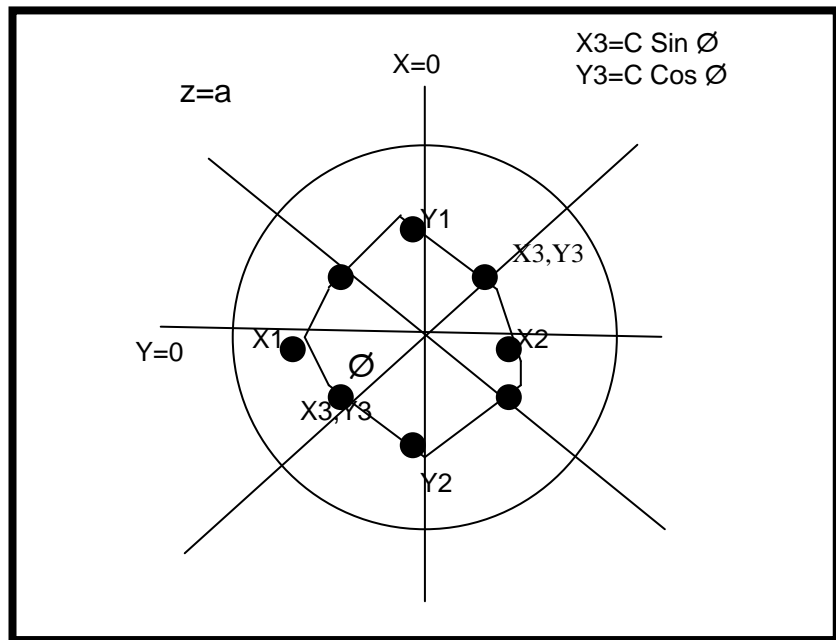


Figure 5-12: Epipolar view of the particle

Once the coordinates were established, the work to superimpose the images was implemented. First, a centre of rotation for the particle was established, which represented an axis around which it was determined that the particle rotated in the image. It also represents an axis about which the boundary vectors are overlaid or superimposed on each other to generate the 3D representation of the particle. The centre of rotation was chosen by comparison of the relative height, or Z coordinates, of the particle boundary vectors to determine the point at which the boundary vectors should intersect within the boundary vector of the particle to avoid distortion of the generated 3D representation. The x coordinates, at which an intersection of boundary vectors occurs, was established by determining a minimum difference in height, or Z-axis, between the boundary vectors XZ and YZ axes respectively. Figure 5-9 shows a comparison of Z coordinates for the two boundary vectors for the respective XZ and YZ axes and the determined centre of rotation. Figure 5-9 shows the two boundary vectors plotted in an XYZ coordinates system intersecting at the centre of rotation. As shown, it was determined that a minimum difference in the Z coordinate between the two boundary vectors occurred at X=28. Next, the boundary vector in the YZ plane was plotted in a three dimensional plot at X=28 and Y and Z coordinates from the boundary vector.

In the case of images being taken at different angles, the X coordinates of the boundary were determined by multiplying the distance from the center to the boundary with $\sin \theta$, where θ is the angle between the 0 degrees plane to the new plane. Similarly, the Y coordinates of the boundary was determined by multiplying the distance of the coordinates to $\cos \phi$. However, since there are only two being used to further construct the pseudo 3D images, these functions will not be used.

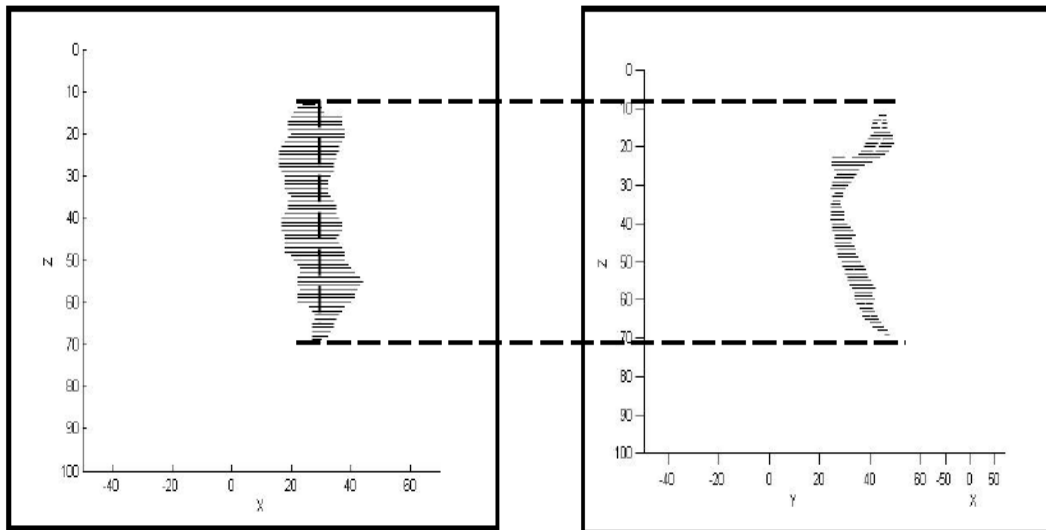


Figure 5-13: Superimposition of two images

A further plot of the YZ boundary vector was then made, with X coordinates established from the corresponding XZ boundary vector for each value of Z. For example, at $Z=a$, a point was plotted at $Z=a$, $Y=$ (coordinate of point in YZ boundary vector) and $X=$ (coordinate of point in XZ boundary vector). This produced two boundary vectors which intersect each other as shown in Figure 5-10. A 3D representation of the particle may then be formed by interconnecting points around the periphery of the two boundary vectors. In other words, points having the same value of z around the boundary vectors were interconnected with lines to form a 3D representation of the particle, as shown in Figures 5-11 from different viewing angles. Arguably, this 3D representation is not perfect, as the depth of the particles will be the same throughout the length of the particles. In order to address this issue, the rectangular equivalent area was used to estimate the volume of the particles. This method was even more accurate than just relying on only one face view to estimate the volume of the particles. Particles with holes in the middle were very rare and should not be a concern when estimating the area of the particles.

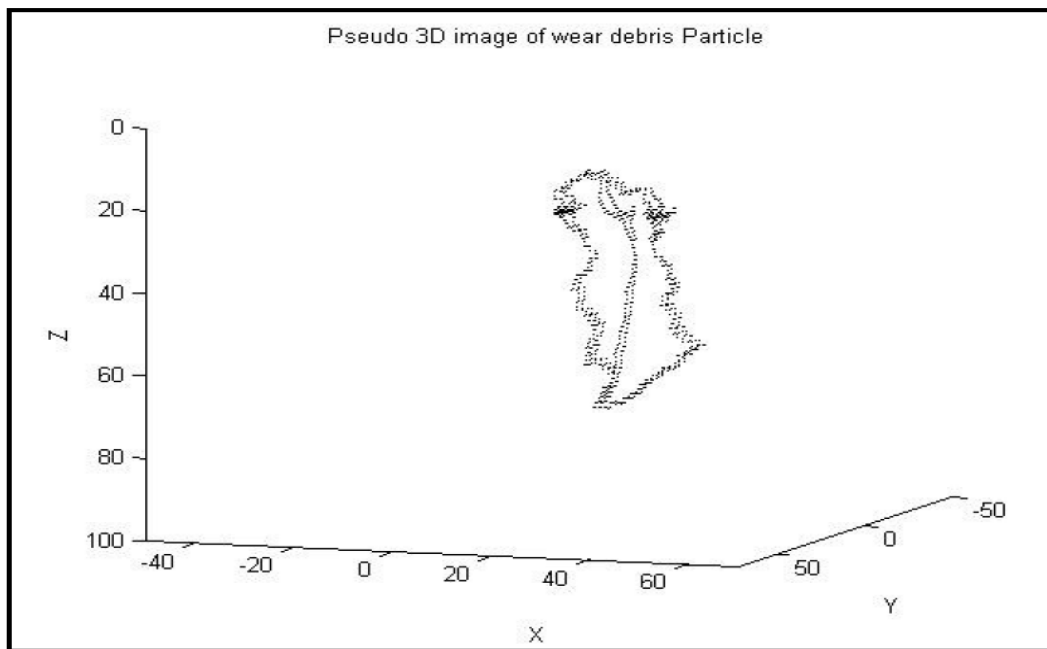


Figure 5-14: Pseudo 3D - two boundary coordinates intersect each other

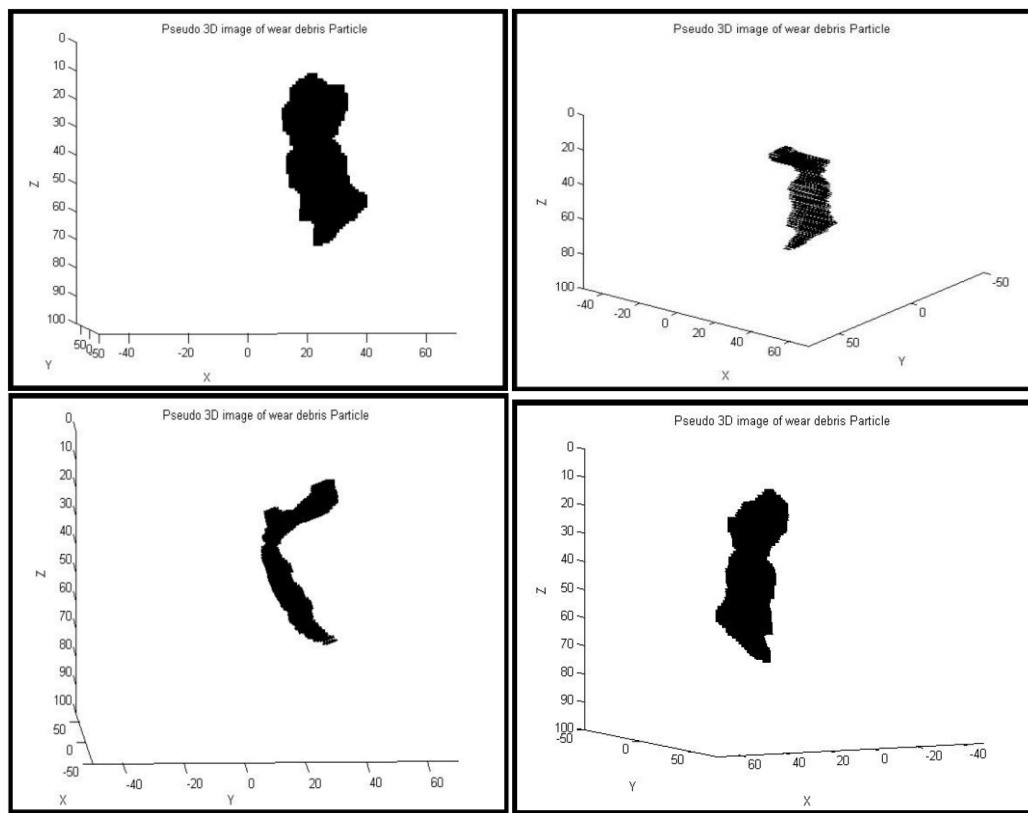
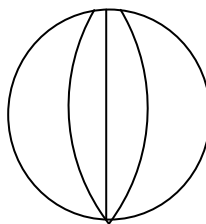


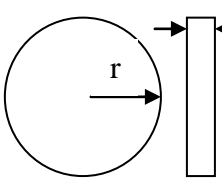
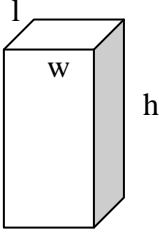
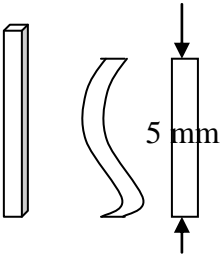
Figure 5-15: pseudo 3d images of particle views at different angles

5.3.5 – Analysis of volume particle of standard shape

In order to estimate the volume of particles using only two aspects of the objects, analysis was undertaken on different shape of known objects.

Table 5-3 Estimated calculation of volume, area and errors of various shapes.

	Shape	Estimated calculation of volume and area.	error (%)
1	Sphere 	Actual volume $R = 2 \text{ mm}$ $V = \frac{4}{3} \pi r^3 = \frac{4}{3} (3.14)(2)^3 = 33.5 \text{ mm}^3$ $A = \pi r^2 = 3.14(2)^2 = 12.56 \text{ mm}^2$ (Area seen on one aspect)	18.9
2	Cylinder 	$r = 2 \text{ mm}, h = 6 \text{ mm}$ $V = \pi r^2 h = 3.14 \times 4 \times 6 = 75.36$ $A (\text{one aspect}) = 4 \times 6 = 24 \text{ mm}^2$	27.4
		$A = 24 \text{ mm}^2$ Thickness = 4 mm	
		New Volume $= A * \text{thickness}$ $= 24 \times 4$ $= 96 \text{ mm}^3$	

	Shape	Estimated calculation of volume and area	error (%)
3	Disk	 <p>$r=2 \text{ mm}$, thickness = 1 mm Volume = Area x thickness = $\pi r^2 \text{ thickness}$ = $3.14 \times 4 \times 1 = 12.56 \text{ mm}^3$</p> <hr/> <p>Area equivalent & thickness $A= 12.56 \text{ mm}^2$ Thickness = 1 mm</p> <hr/> <p>New Volume = 12.56 mm^3</p>	0
4	Rectangular	 <p>$w= 2 \text{ mm}$, $l=2 \text{ mm}$, $h = 6 \text{ mm}$ Initial volume = $w \times l \times h = 24 \text{ mm}^3$ Area on one aspect = $w \times h$ = $2 \times 6 = 12 \text{ mm}^2$</p> <hr/> <p>Equivalent area = 12 mm^2 Thickness = 2 mm</p> <hr/> <p>Thickness = $12 \text{ mm}^2 \times 2 \text{ mm} = 24 \text{ mm}^2$</p>	0
5	Wavy rectangular	 <p>$w= 2 \text{ mm}$, $l=2 \text{ mm}$, $h = 6 \text{ mm}$ Initial volume = $w \times l \times h = 24 \text{ mm}^3$ Area on one aspect = $w \times h$ = $2 \times 6 = 12 \text{ mm}^2$ Thickness = 3 mm</p> <hr/> <p>Area equivalent = 12 mm^2 Thickness = 2 mm</p> <hr/> <p>Volume = $12 * 2.0 = 24 \text{ mm}^3$</p>	0

In Table 5-3, the proposed rectangular equivalent area might have caused major errors in the volume calculations compared to the actual volume of the object, specifically for cylinders and spheres. However, in gear wear, spherical and cylindrical shaped wear debris particles are hardly ever generated. The majority of the wear particles produced are platelets such as wavy rectangles or disks.

5.3.6 Quantitative analysis- volume particle estimation

The volume particle estimation in this exercise used the rectangular area equivalent as shown in Figure 5-12.

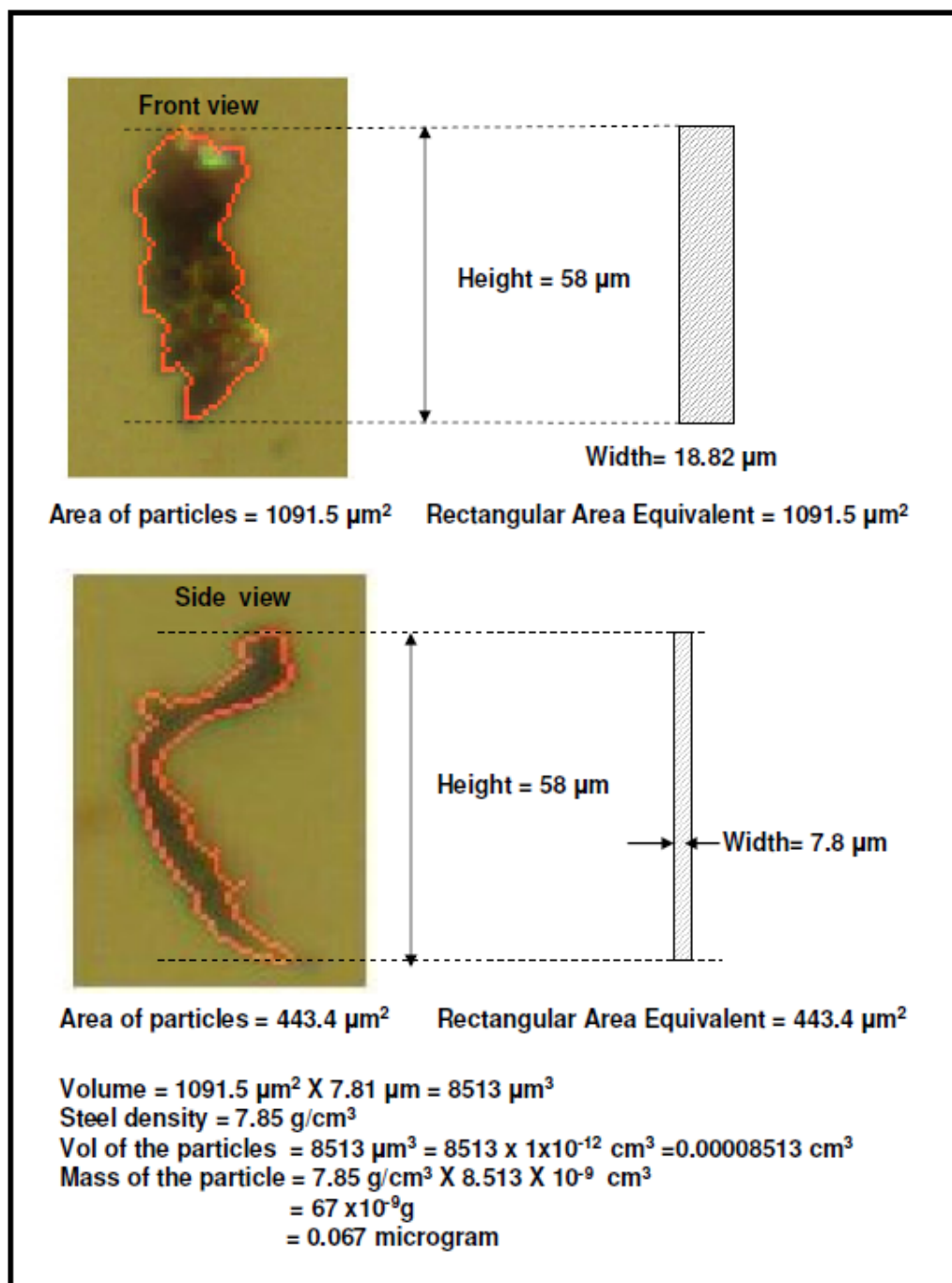


Figure 5-16: The rectangle area equivalent volume estimation

The images of particles in Figure 5-16 are a bit grainy due to the fact that the images were taken when the particle was rotating. However, they can still give a clear boundary line around the particle. In Figure 5-16 the largest area was considered the front view and the smallest area was considered the side view. This is common for the platelet types of metal debris particles. Since the selection of the image of the particles was done manually by looking at the rotating particles, this selection is most representative of the two views. As an example, if a volume of a disk was estimated by this method, the front view would be the circular area while the side view would look like a rectangle. The volume would be the area of the disk multiplied by the thickness of the rectangle.

5.4 Experiment results

Three experiments were conducted to evaluate and to validate the software and hardware. In these experiments the small particle diameter particles (SD), 1, 2, 5 and 10 μm were not analyzed, as their counts are not reliable due to insufficient filtration, as explained in Chapter 4. This left LD (50 μm and 100 μm) particles and medium diameter particles MD (15 μm and 25 μm) to be further examined.

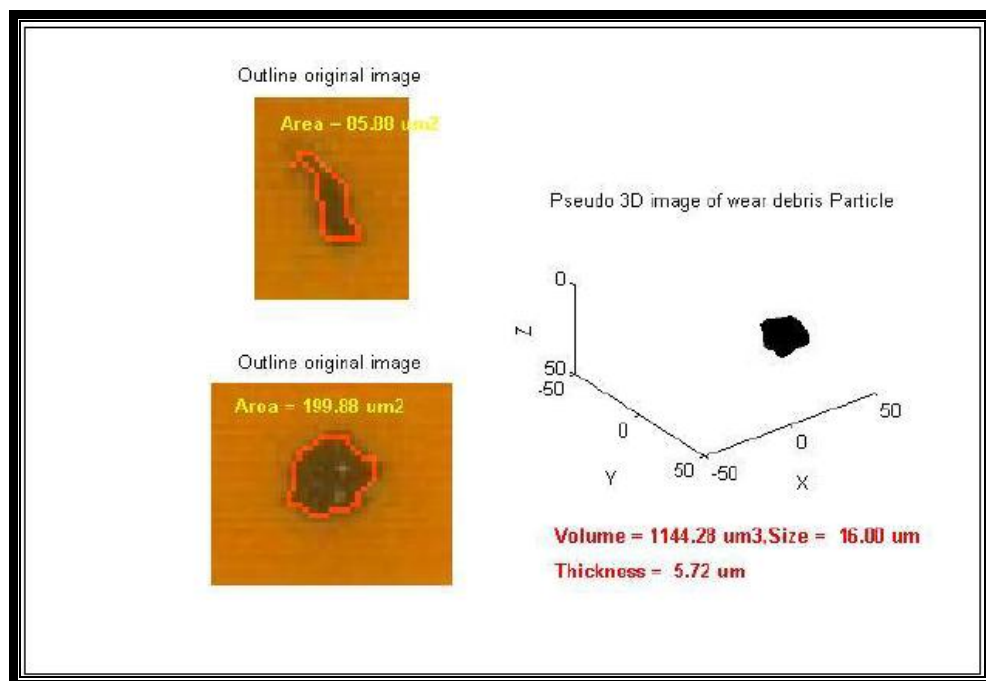


Figure 5-17: Volume calculation of a single particle

Figure 5-17 and fig 5-18 show the result for two particles' volume, which was then used to produce fig 5-19 which represents the thickness versus size of the particles.

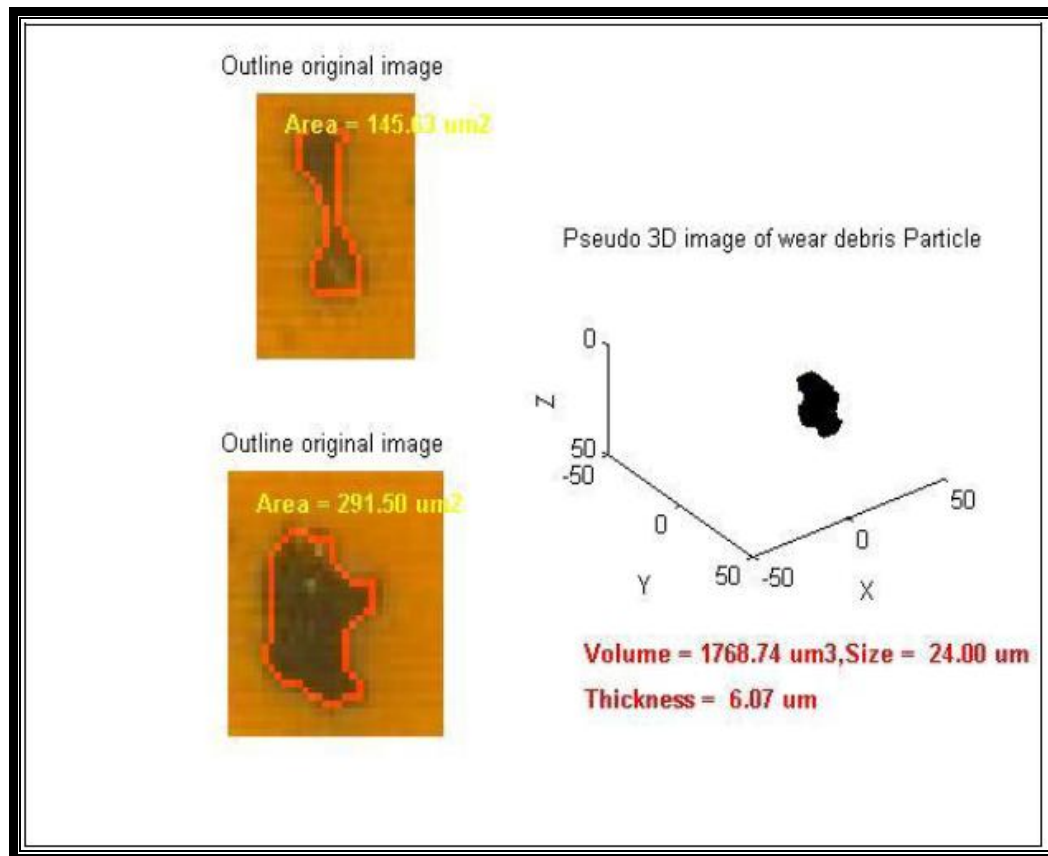


Figure 5-18: Volume calculation of a single particle

Figure 5-19 shows the relation between the thicknesses of particles with the sizes of particles. Since the parameters applied on all three tests were similar, the graph combines the data from test 1, test 2 and test 3. From the graph, the majority of the particles' thicknesses was below 20 μm . In fact, some particles in SD and LD have the same thicknesses as the LD particles. During the experiment, the majority of particles generated were categorized as platelet shape with thin particles and a few of chunky particles, which are thicker. This supports the case that the thicknesses of the particles stayed below 20 μm . Due to this fact, it was assumed that the volumes of particles increased linearly with the size of the particles, because thickness for the majority of particles remained low and the

only parameter that changed with the increase in size was the areas of the particles, which were multiplied with thickness to yield their volumes.

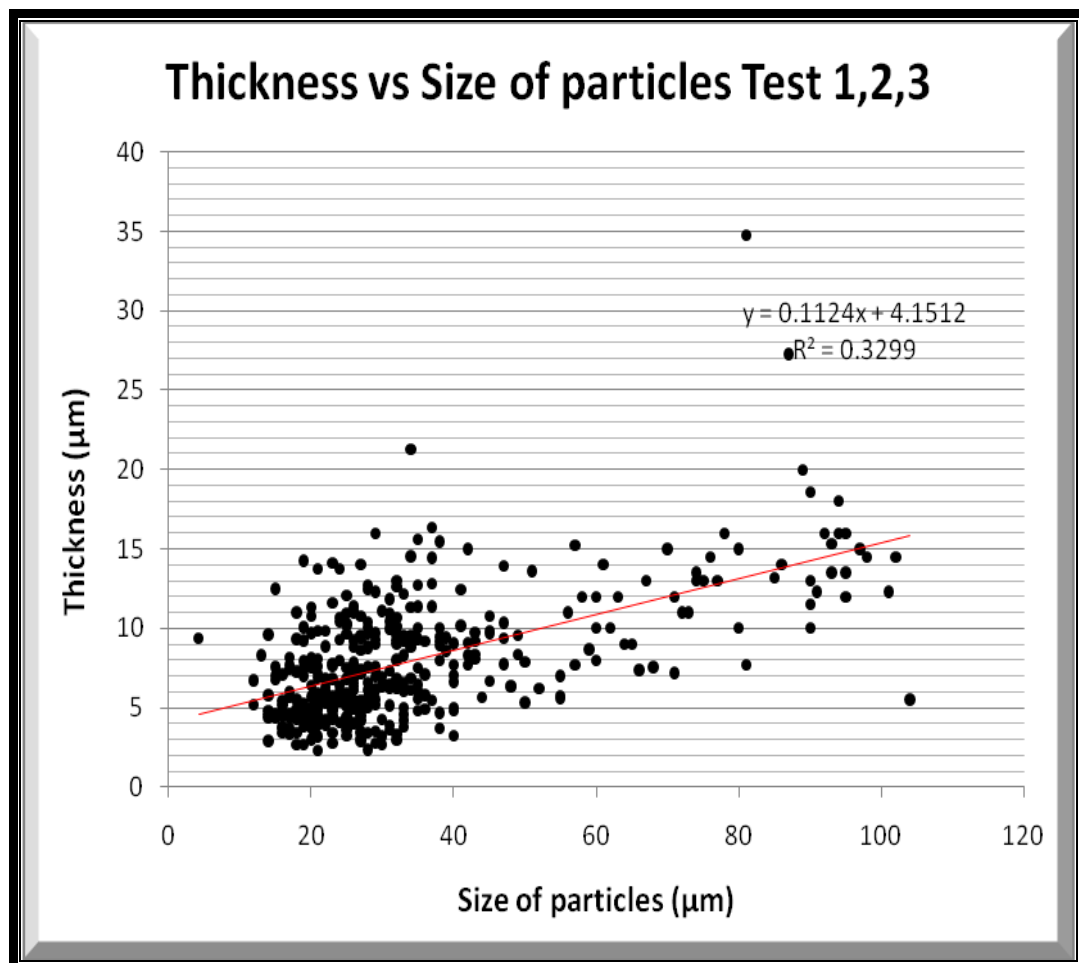


Figure 5-19 : Particle thickness versus size

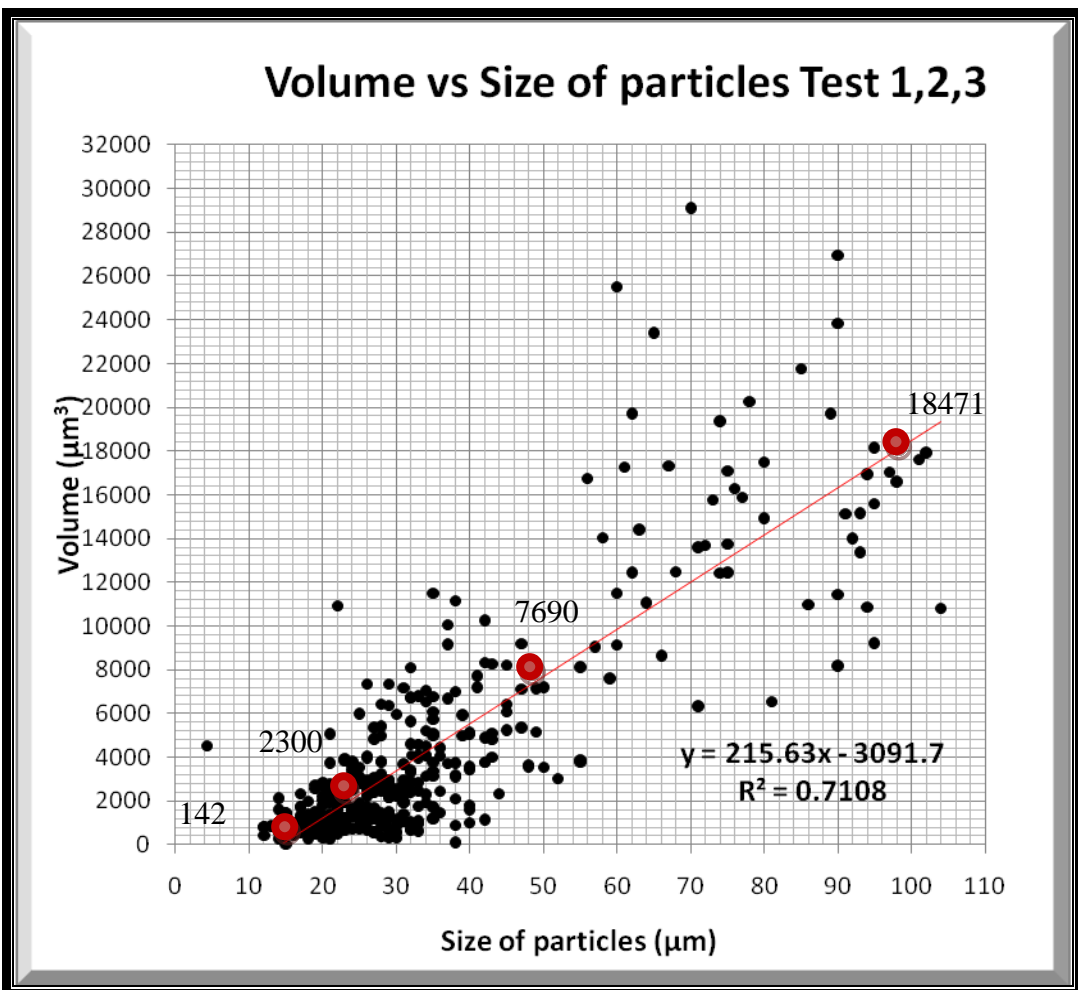


Figure 5-20 : Estimated volume of particles

From Figure 5-20, a volume was estimated for sizes 15, 25, 50 and 100 um using linear correlation and inserted in Table 5-4, which was used to calculate the mass of the particles. Even though the R squared was only 0.7108, it is the closest trend that can be achieved with the data collected. The volumes estimated for the selected sizes were then used to estimate the mass of the particles as shown in Table 5-4.

Table 5-4: Volume and mass of particles on selected sizes test 1, 2 and 3

Sizes	Volume (μm^3)	Steel density (g/cm^3)	Mass (microgram)
100 μm	18471	7.85	0.14500
50 μm	7690	7.85	0.06036
25 μm	2300	7.85	0.01805
15 μm	142	7.85	0.01147

5.4.1 Result of test 1

For test 1, a volume analysis was conducted on samples collected throughout the experiment where approximately 350 images of particles were analyzed to estimate their volume; this follows the method of rectangle area equivalent analysis described in subsection 5.3.2.

The values of the mass of particles in Table 5-4 were multiplied with the particle counts of the respected size and divided by the time taken to produce the amount of debris to yield wear rate. The wear rate of the particles was calculated using equation 9.

$$\text{Wear rate} = (Q \times M) / t_t - t_{t-1} \dots \text{eq. 9}$$

Q: Number of particles counted by PODs

M: Mass for each particle for its designated size

$t_t - t_{t-1}$: time taken for each test

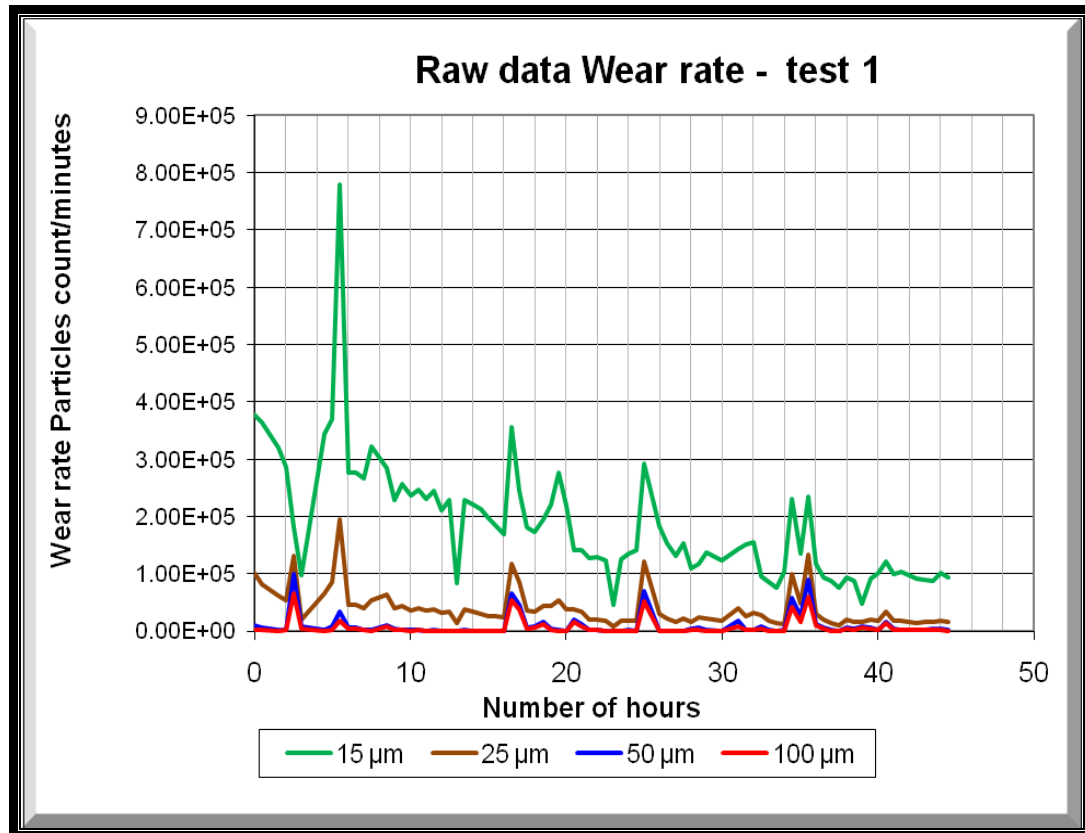


Figure 5-21: Raw data wear rate versus time-test 1

Figure 5-21 represents the wear rate over time using the particle count per minute for test 1. In using direct raw material data particle counts, the wear rates of different sizes were unlikely to cross each other. For example, the particle count of wear debris at 100 μm was very unlikely to exceed the particles count of 15 μm . However, when the amount of metal removed for the gear teeth was taken into consideration as shown in Figure 5-22, at several points the wear rate of 100 μm exceeded the wear rate of 15 μm . This shows that the mass of the metal was more representative in indicating the deteriorating of the gear surfaces.

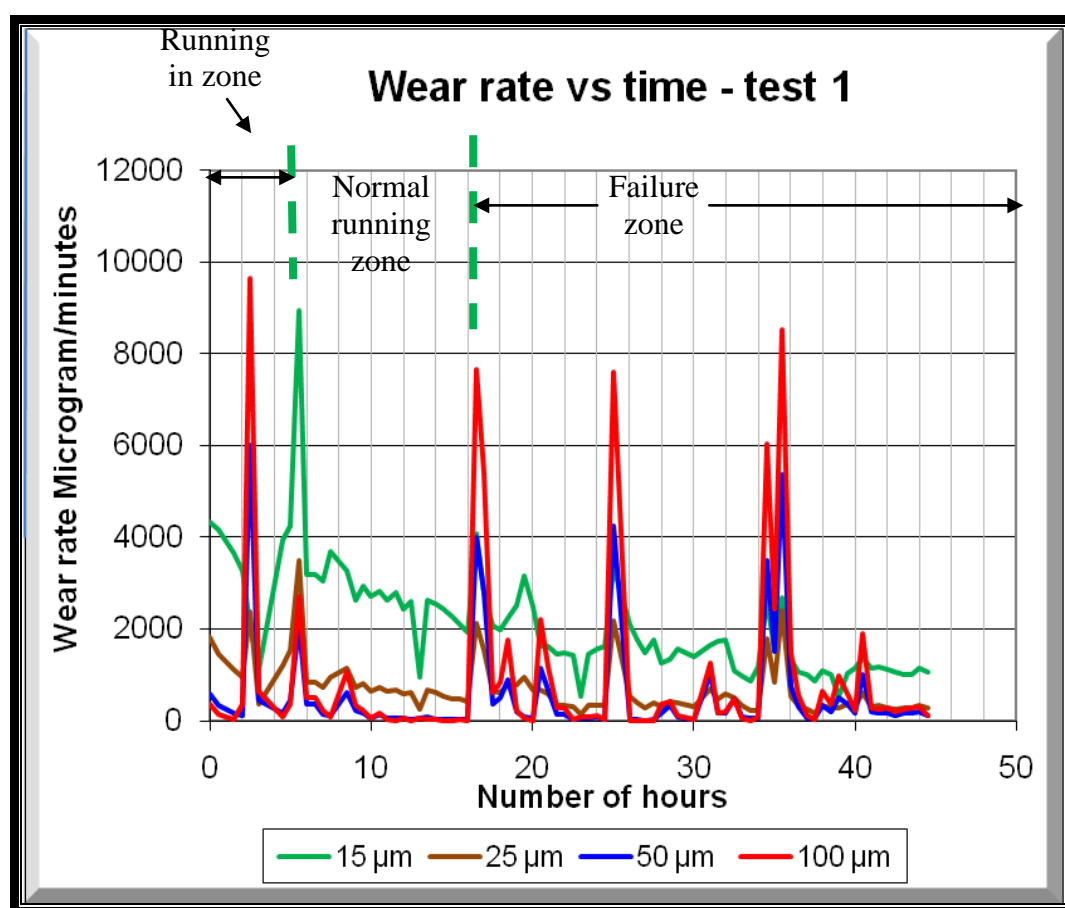


Figure 5-22: Wear rate of mass particles versus time test 1

Figure 5-22 shows the three wear zones, which was one of the main objectives of this research in determining the progress of wear. The running in zone ended at about hour 6 and the wear rate decreased significantly. This

indicates that the surface of the gear teeth was polished and the asperity due to imperfections of manufacturing was removed. After hour 6, the wear rate stabilized and the removal of metals from the gear teeth reduced significantly as the gear experienced normal running conditions. The gear reached the onset of failure after hour 16 as the wear increased significantly to signify that the metal removal has reached its highest level. Once metal broke off from the surface, the surface continued to be polished by the rolling and rubbing action of the mating gears. Then, since the stress applied on the mating surfaces continued to exceed the allowable limit, another break off of material occurred again at hour 26. The same process occurred at approximately hour 36, indicating that the gears were deteriorating. This shows that once the pits on the surfaces were created, more and more metal was removed to create bigger pit. The same explanation also applies for the peaks in Figure 5-23 at approximately hour 26 and hour 36.

In Figure 5-23, in order to project the total wear rate of the debris generated, the wear rate for each size was summed. Even though it is the same trend in comparison to Figure 5-22, from Figure 5-23 we can clearly distinguish the high wear rate and lower wear rate during the experiment. In Figure 5-23, the points on the line which are more than 5000 microgram per minutes were considered to have a higher wear rate and the ones lower than the 5000 microgram per minute were considered to have a low wear rate. The 5000 microgram per minute rate was chosen because it could the higher wear rate from the lower wear rate by analyzing trends.

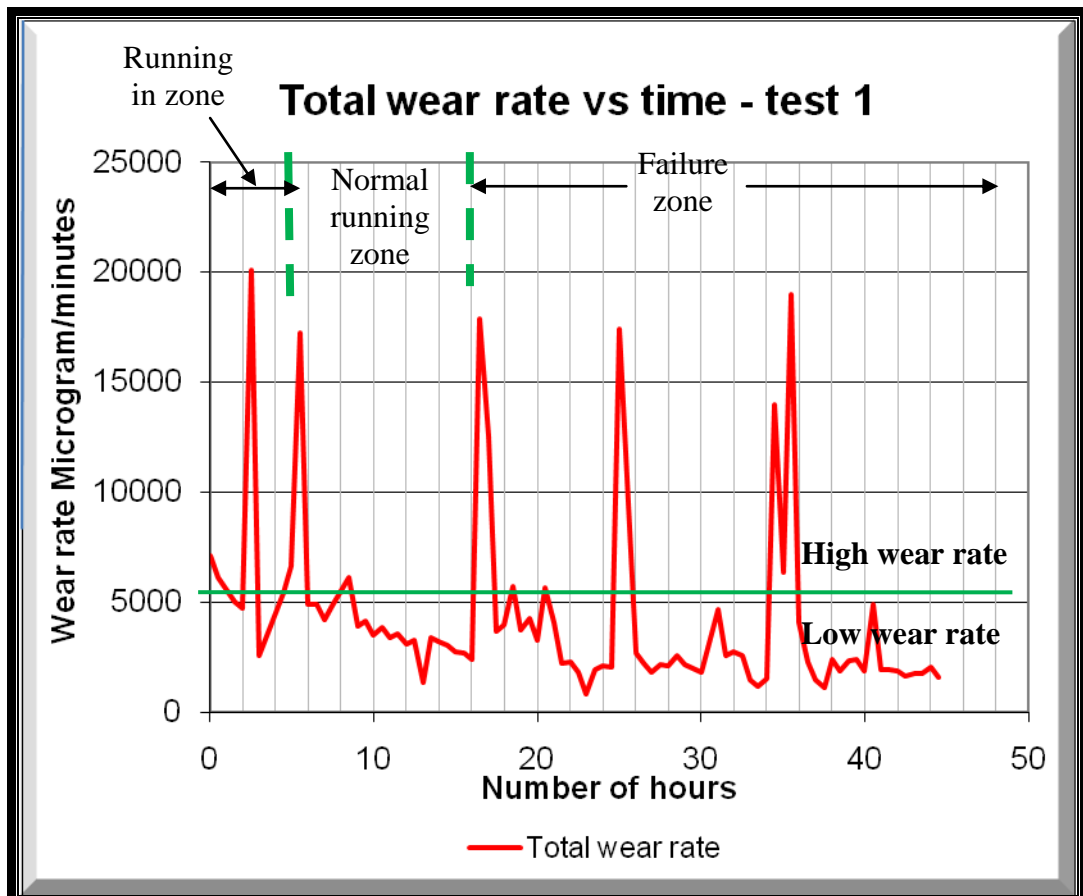


Figure 5-23: Total wear rate mass particles versus time test 1

Pitting is a fatigue failure caused by stress applied on the surface of gears exceeding the surface fatigue limit in the gear material. According to research conducted by Dempsey and Dudley, initial pitting occurs when the pits generated are less than 0.397 mm and cover less than 25 percent of the tooth contact area, whereas destructive pitting refers to pits greater than 0.397 mm diameter that cover more than 25 percent of the contact area [67; 68; 74; 77]. Destructive pitting, if not noticed in time, will cause catastrophic gear failure if the gear teeth crack. In determining the onset of failure for these experiments, these definitions of initial pitting and destructive pitting were considered. Figure 5-24 shows images of the gears undergoing pitting wear where the gears started to have micro pitting as early as hour 6 and then entered the destructive pitting phase at hour 15. At hour 15 the pit diameter reached 2.34 mm wide and the pit extended to 9.76

mm length, which is more than 25 % of the total tooth contact area. This supports the trending graph of Figures 5-22 and 5-23 which show that the onset of failure was after hour 16.

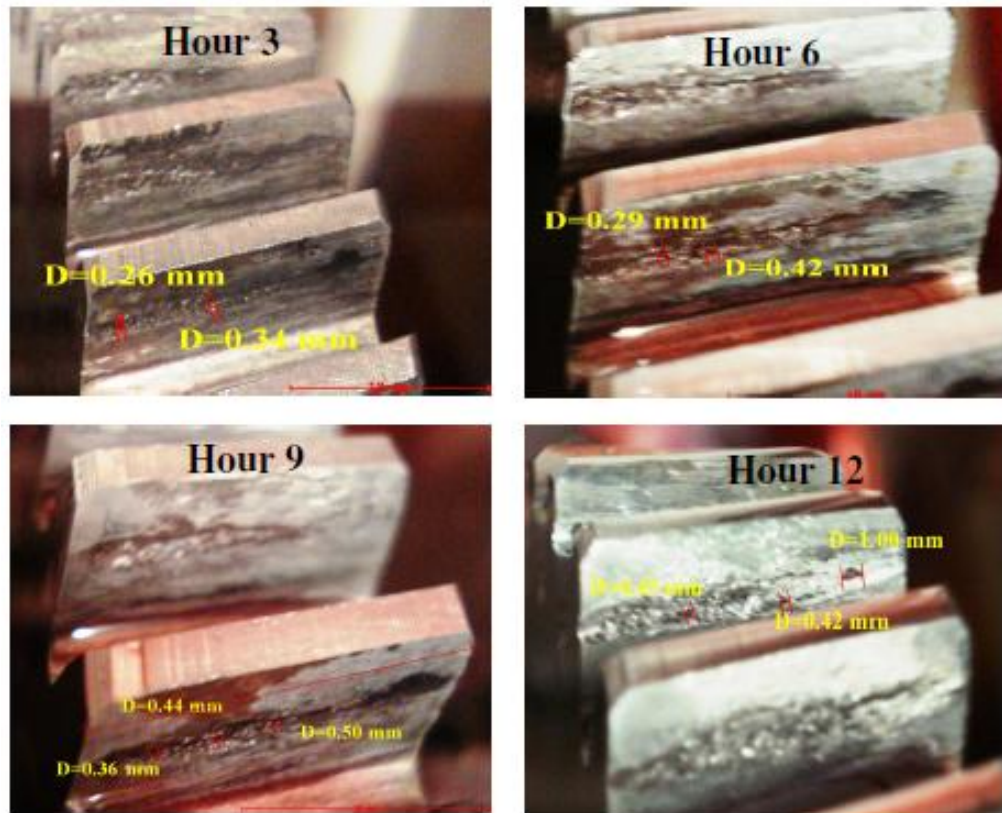




Figure 5-24: Pitting progress on gears - test 1

The pits on the surface of the gear tooth were measured using the infinity camera measurement tool. At every measurement, the tool needed to be calibrated before the actual measurement of the pits was conducted. The width of the tooth was

used as the reference for the calibration as it was known to have a width of 15 mm.

5.4.2 Result of test 2

For test 2, a volume analysis was also conducted on samples collected throughout the experiment where approximately about 300 images of particles were analyzed to estimate their volume; this follows the method of rectangle area equivalent analysis as described in subsection 5.3.2. The volume data and sizes were then used to produce Figure 5-15, which represents the estimated volume of the particles versus their ferret lengths sizes.

Figure 5-25 shows the wear rate in term of the particle counts over time for 15 μm , 25 μm , 50 μm and 100 μm respectively. By only referring to the particle counts, the severity of the damage of the gear surfaces was not alarming in comparison to the quantity of metal removed from the gears.

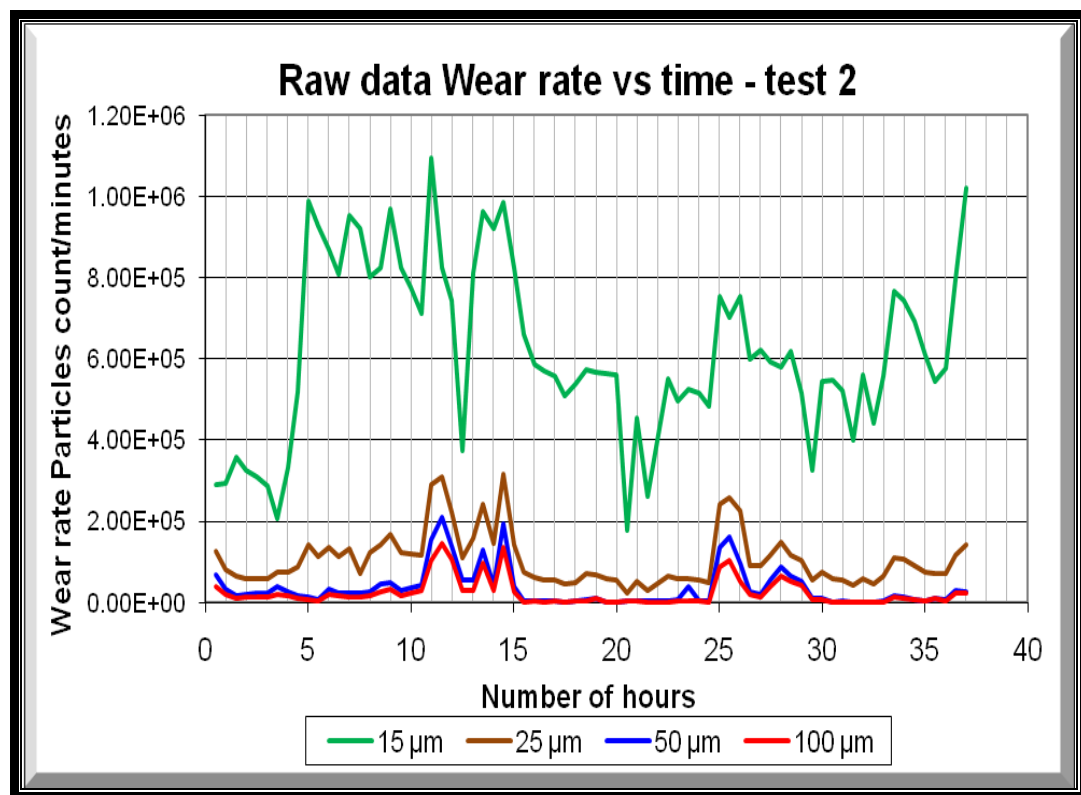


Figure 5-25: Raw data wear rate particle counts versus time-test 2

Figure 5-26 shows the wear rate in mass per unit time, where the 100 μm and 50 μm exceeded the 15 μm particles at hour 11 to hour 15 and hour 25 to hour 26. The high wear rates at these hours indicated high removal of metal from the surfaces of gear teeth, which may have signified the onset of failure. Hour 11.5 recorded the highest wear rate and shows the onset of failure. Hour 13.5 and hour 14.5 were the continuous break off of material from the surface gears and the hours in which the two occurrences are closest to each other. This confirms that the gears entered the failure zones, where maintenance action would be required to address the possibility of complete failures of the gears at a later stage. After these hours, the wear rate decreased until hour 25. This period of low wear rate represents the polishing process on the surface of mating area of the gear mesh. However, as the stresses applied at the mating area continued to exceed the allowable stress of the gear material, cracks were created underneath the surface until a section broke off from the surface of the gear. This occurred at hour 25.5 and hour 27 as a high wear rate was recorded.

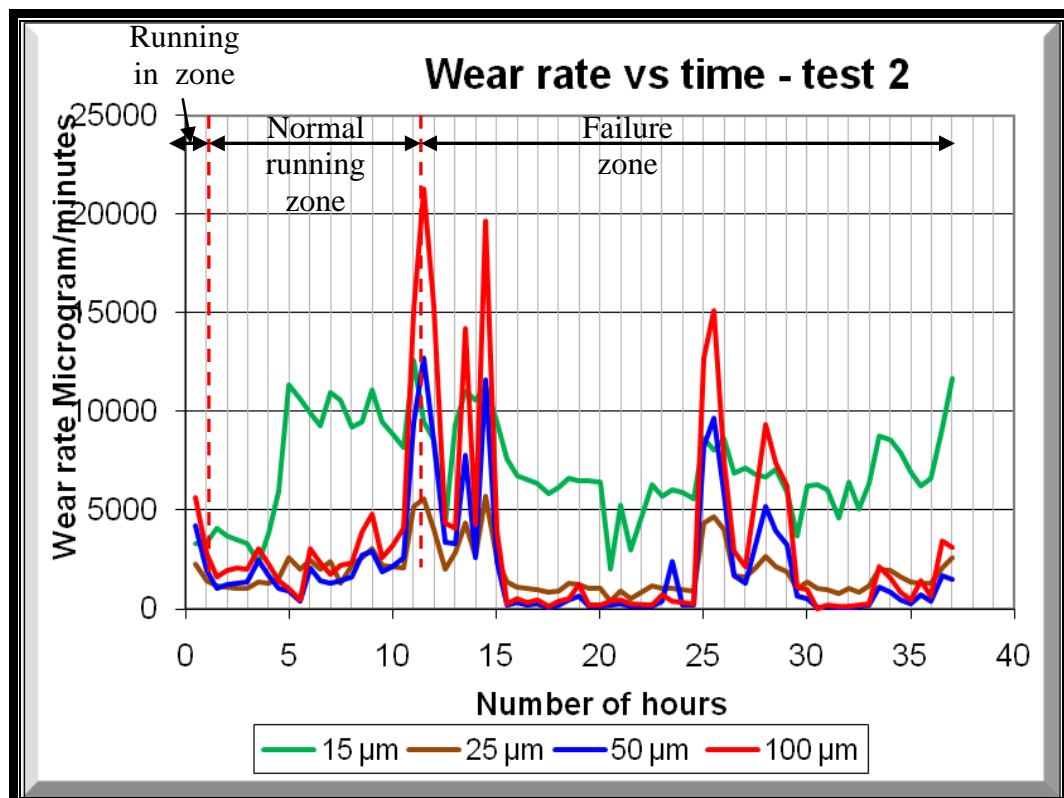


Figure 5-26: Wear rate mass of particles versus time - test 2

Figure 5-27 shows the total of wear rate in mass per unit times for every hour; the red line shows the fluctuation of the wear rate. Even though the summing up of the wear rate did not change the onset of failures as deduced from Figure 5-26, it gives an indication for separating the points of high wear rate and low wear rate. The low wear rate and high wear rate were separated at a wear rate line of 10000 micrograms per minutes.

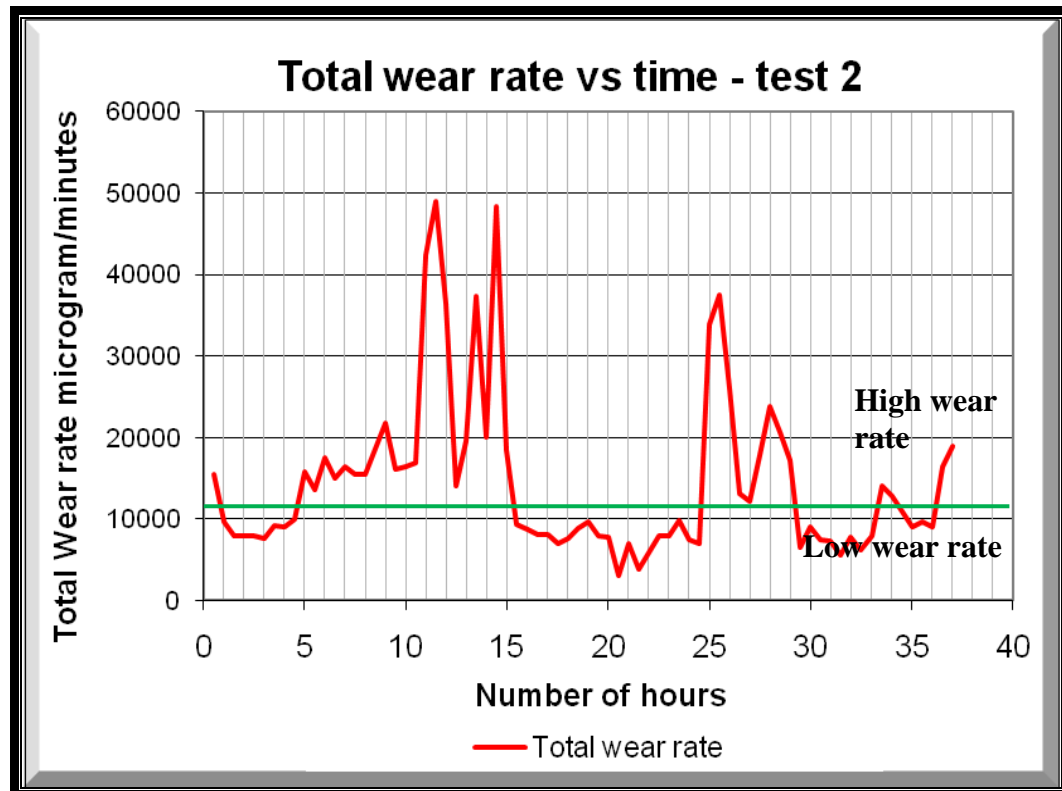


Figure 5-27: Total wear rate versus time - test 2

Figure 5-28 shows images of the gears which experienced pitting damage gradually from the start of the experiment until the end. The initial pitting started as early as hour 6 and the onset of failure can be estimated by looking at the images taken at hour 12, in which the pits covered almost half of the tooth contact area. This supported the determination that the onset of failure started at hour 11.5 of the experiment, as shown in Figure 5-26. The pits on the gear teeth surface continued to enlarge, signifying the deterioration of the gear mesh and showing that catastrophic failure was imminent if no maintenance decision were taken to

address the issue. In order to make a comparison of the gradual deterioration of the gear surface damage, the same tooth damage images were taken at three hourly intervals and analyzed.



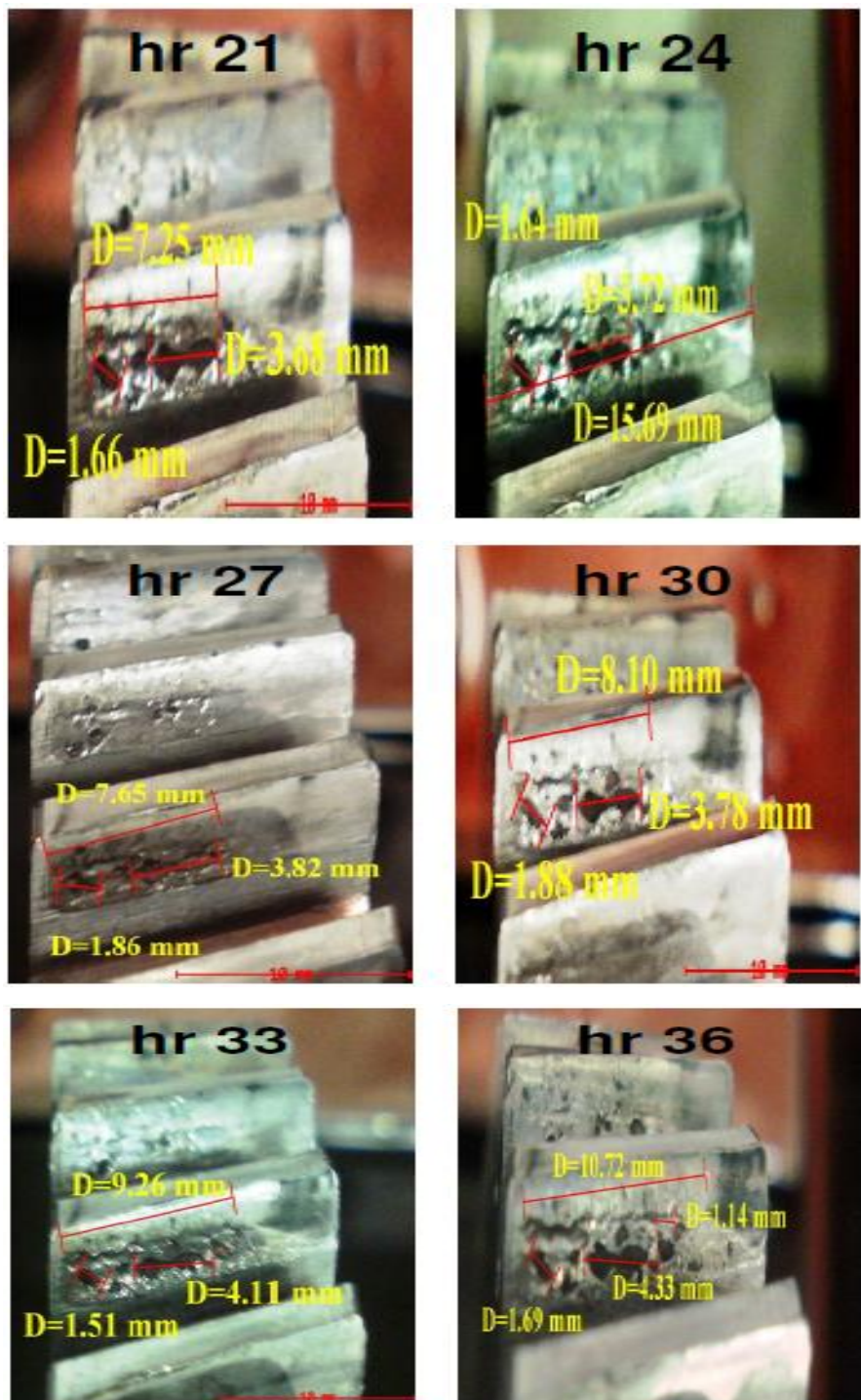


Figure 5-28: Pitting progress on gears - test 2

5.4.3 Result of test 3

In order to confirm that the method described previously as able to detect the onset of failure of the gears under test, another experiment (test 3) was arranged (with the same parameters of loading and speed of the gears) for comparison. The experiment was conducted for 37 hours, similar to test 2, but the particle counts were done continuously and automatically. For test 1 and test 2, the counts were done at half-hour intervals, but for test 3, the particle counting processes were continuous, with an average interval of 6 minutes between each count. The objective of continuous counting was to monitor the behaviour of particle counts when the number of samples was increased. In addition, frequent sampling allowed data to be analyzed earlier in the failure-development period [81].

Figure 5-29 shows the particle counts over time; the counts showed multiple peaks throughout the experiments. As in previous sections, particle counts alone cannot really indicate the severity of the damage of the gears. On the other hand, the removal of metal from the surface of the gears gave a better idea on the deterioration of the gears. Therefore, Figure 5-30 was created to show the high wear rate based on the metal removal rate from the gears surface.

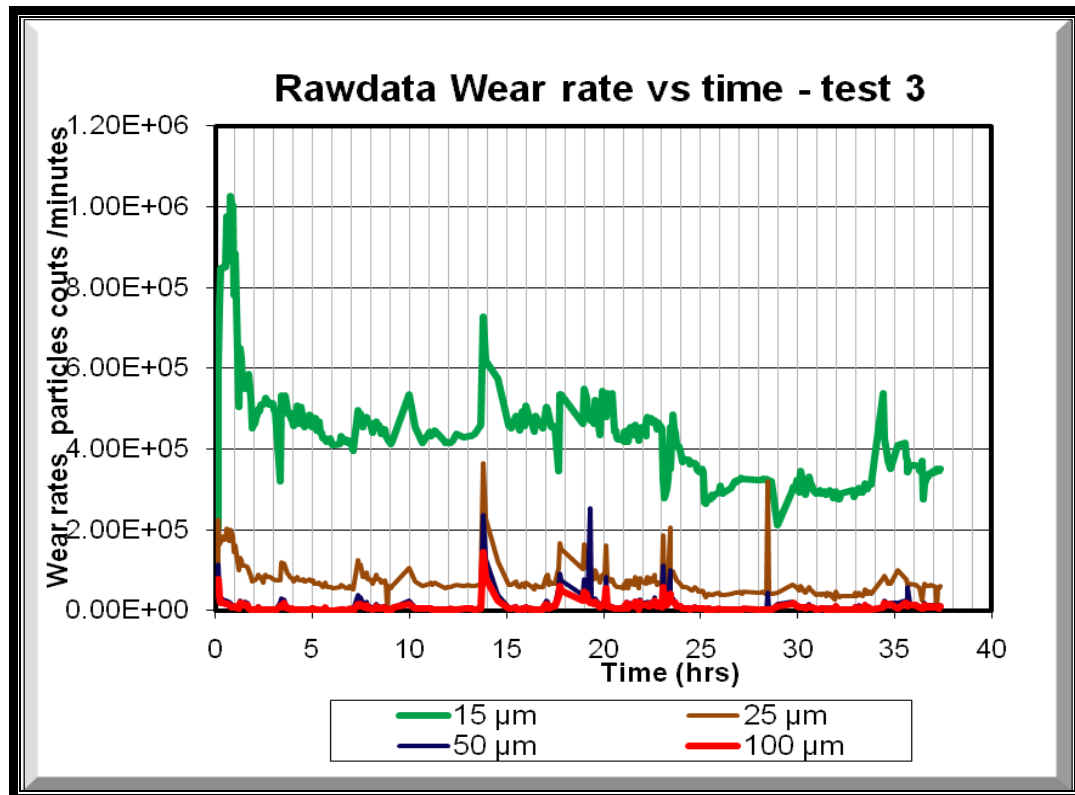


Figure 5-29: Raw data wear rate versus time – test 3

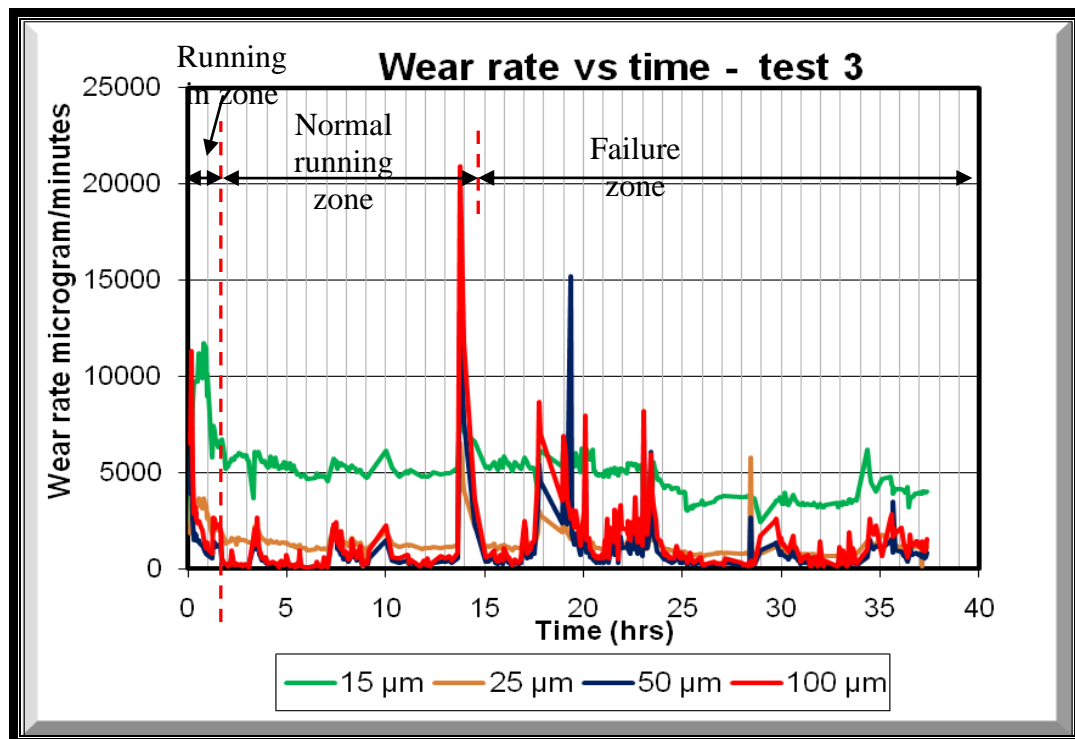


Figure 5-30: Wear rate mass of particles versus time – test 3

Figure 5-30 shows that the running in zone ended at hour 2 and the wear rate reached the lowest count, indicating that surface asperities due to imperfection in the fabrication of the gears had been polished. The gear mesh is entering the steady state or the normal running zone at hour 2 and reaches the onset of failures at hour 14 where the highest wear rate was recorded. The failure zone started after hour 14 and the occurrence of a high wear rate indicated that the gears were in the failure zones.

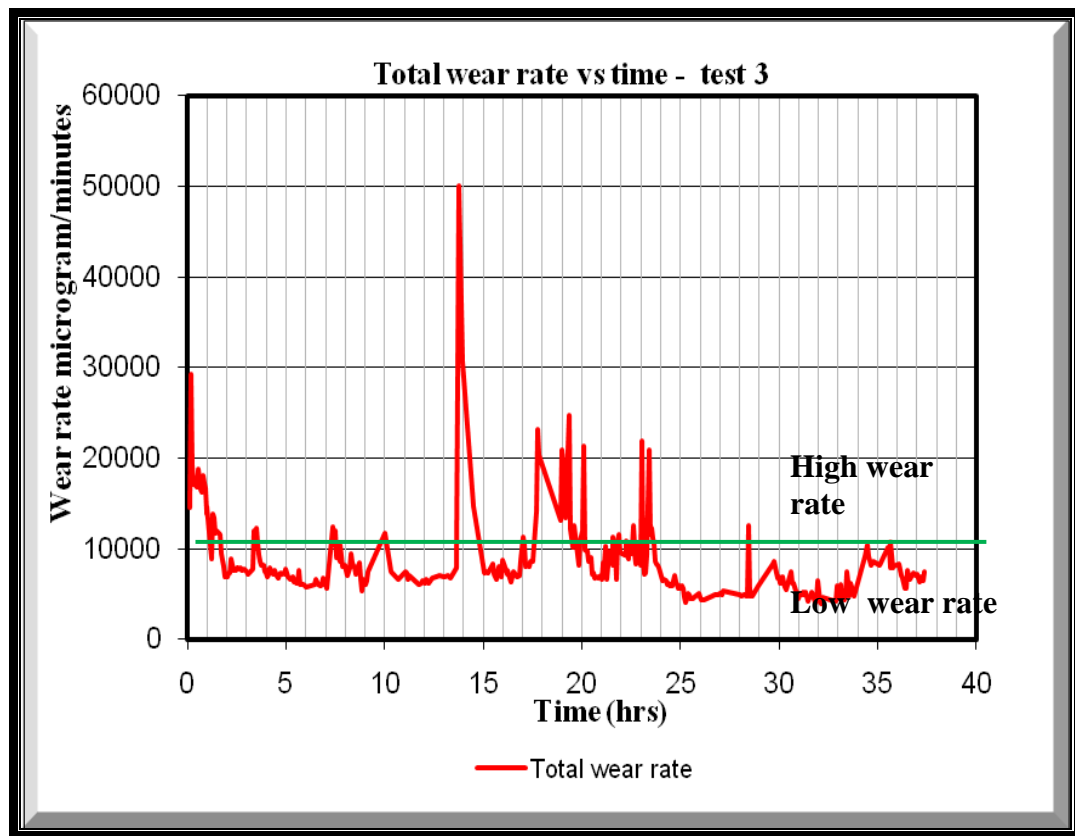
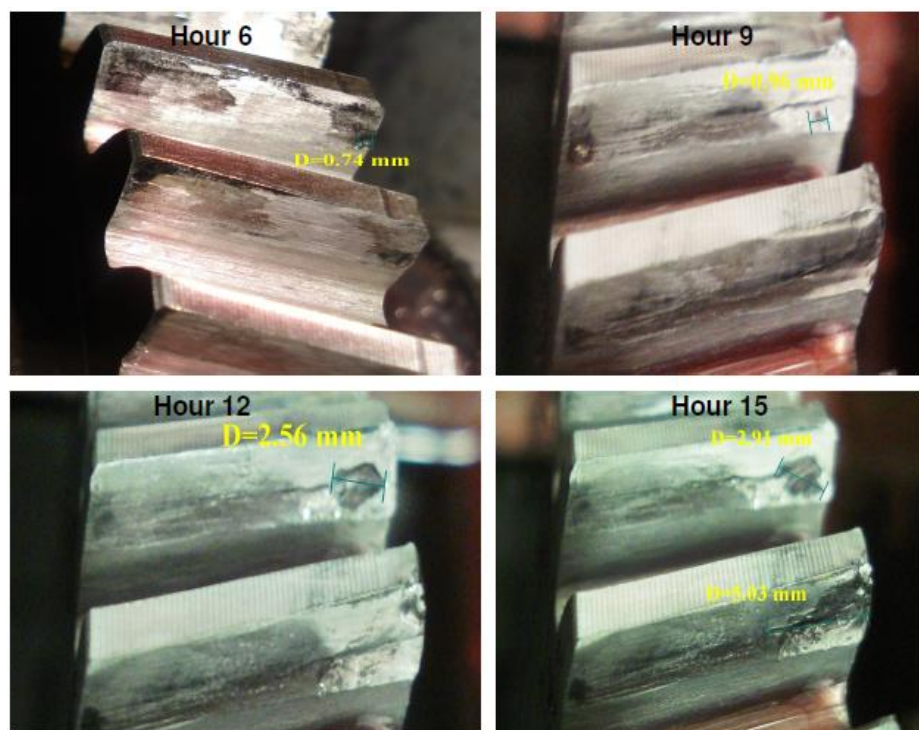


Figure 5-31: Total wear rate mass of particles versus time-test 3.

Figure 5-31 shows the total wear rate of all particle sizes, which reaffirms the wear regimes. This graph clearly shows the high wear rate zone and the low wear rate zones by the 10000 micrograms/minutes line. Even though Figure 5-30 is sufficient to show the demarcation of the regime, this graph separates the high wear rate zone and the lower rate zone according to the wear rate itself. So, in Figure 5-31, once the wear rate touched the line at hour 14, it was actually

reaching the onset of failure. Subsequently, there were many similar occurrences at hour 18 to hour 24, showing that the gear was deteriorating even more and removal of metal from the surfaces was increasing. At the time the line dipped below the separating line of 10,000 microgram/minutes, the gears were expected to be in the polishing process after a big chunk of metal was removed. However, if the stresses on the mating area of the gears continued to exceed the allowable stress, a crack would form from the surface underneath the gear tooth surface which eventually broke the metal off in big particles.



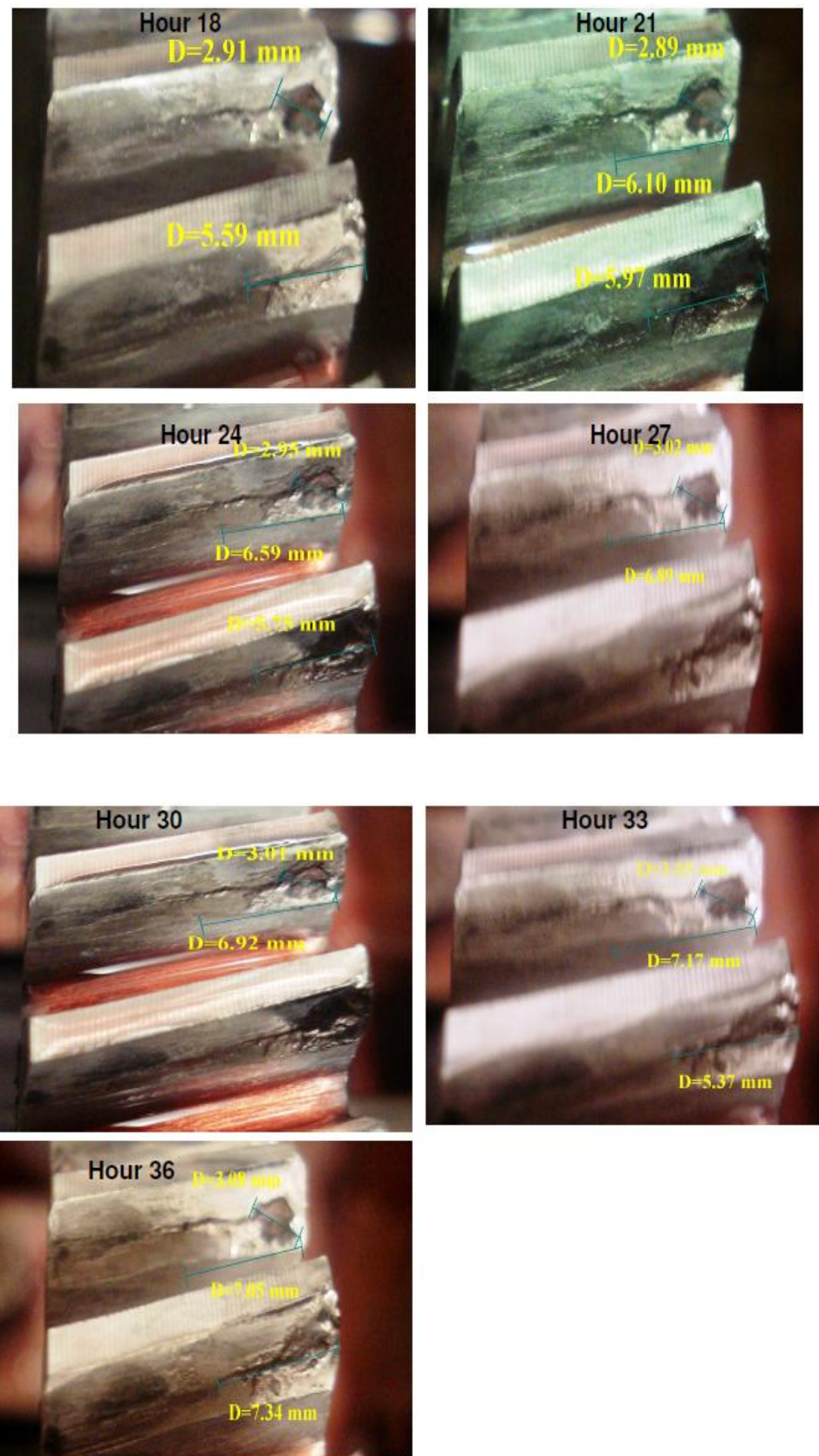


Figure 5-32: Pitting progress on gears - test 3

Figure 5-32 shows images of the same gear which experienced the initial pitting process which started as early as hour 6 and continued to deteriorate throughout the experiment. A big chunk of metal had been removed by hour 9 of the experiment from one flank, which indicated that the wear process was entering into the ‘unhealthy’ zone but had not entered the failure zone. The failure zone started between hour 14 and hour 15, where the damage to a particular flank increased to more than 5 mm or thirty-three percent of the total width of the tooth. This is supported by Figure 5-30.

5.4.4 Summary of results

Table 5-5 summarizes the three zones in which the condition of the gears had deteriorated.

Table 5-5: Summary of result

Test	Speed (rpm)	Load (Newton)	Running in zone (hours)	Normal running (hours)	Failure zone (hours)
Test 1	1000	4350 N	0.0 - 6.0	6.0 - 16.0	16.0 - 45.0
Test 2	1000	4350 N	0.0 - 1.5	1.5 - 12.0	11.5 - 37.0
Test 3	1000	4350 N	0.0-2.0	2.0 - 14.0	14.0 - 37.0

By analyzing the results, a conclusion can be made that if the same speed of gear rotation and load were used in the three experiments, the demarcation of the three phases of the life of the gears, running-in zone, normal working life, and failure zone, are about the same. Indeed, this conclusion is supported by the trend of the wear rate and the actual images of the gear damage.

5.5 Shape analysis of the wear debris particles.

In determining the shape of the particles, simple calculations of aspect ratio (AR), roundness factor (RF), Standard deviation (Rq), Skewness (Rsk) and

Kurtosis (Rku) were used and values in Table 2-6 were used to classify the shape of the particles. Figure 5-33 shows an example of a particle which was analysed and contains information which enables us to determine the actual shape of the particle.

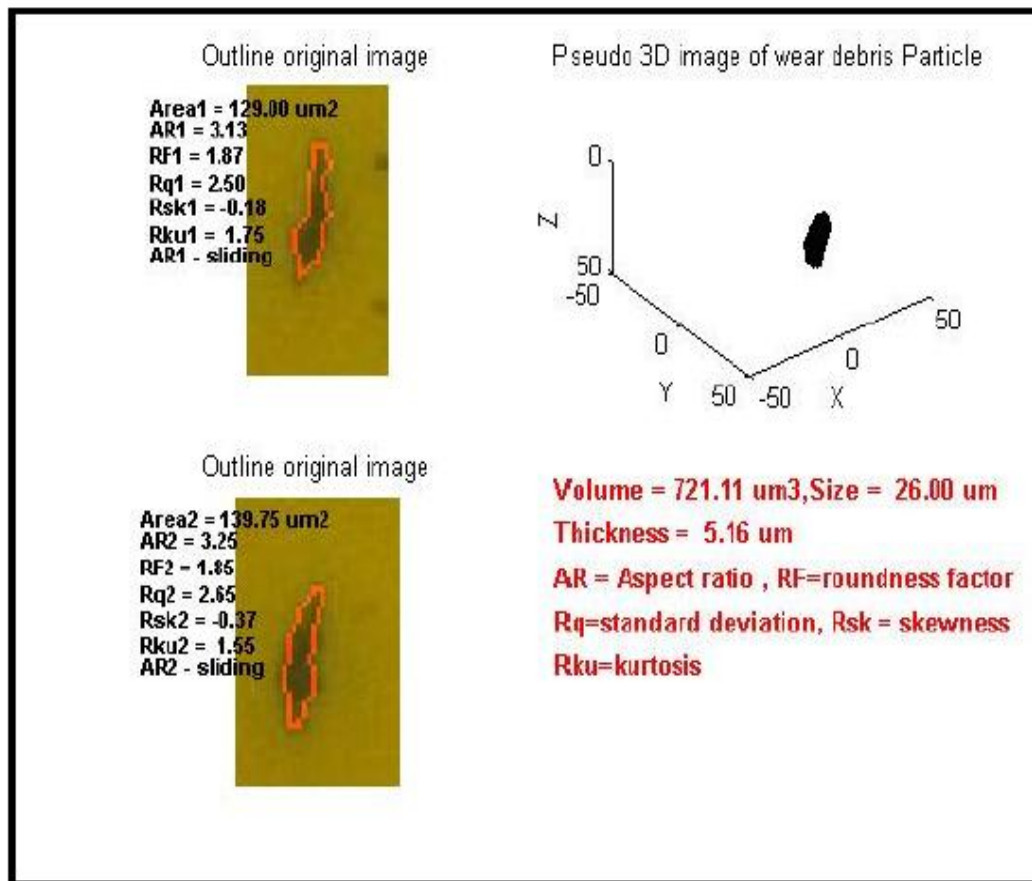


Figure 5-33: Shape results of the particle analysis

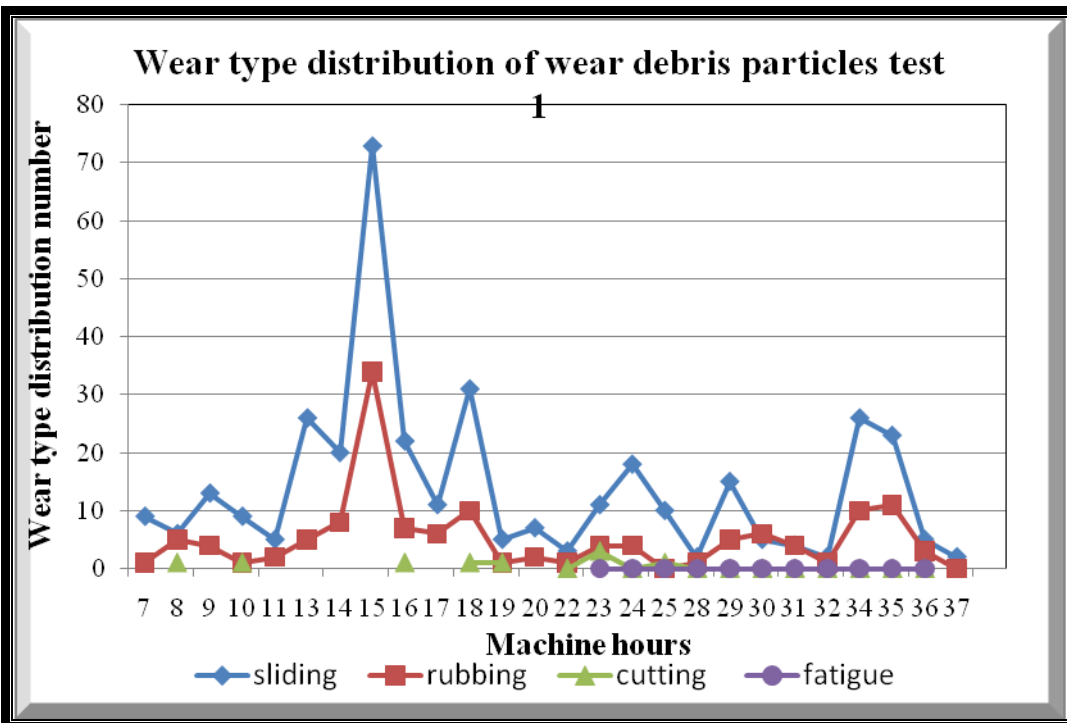


Figure 5-34: Wear type distribution of wear debris particles – test 1

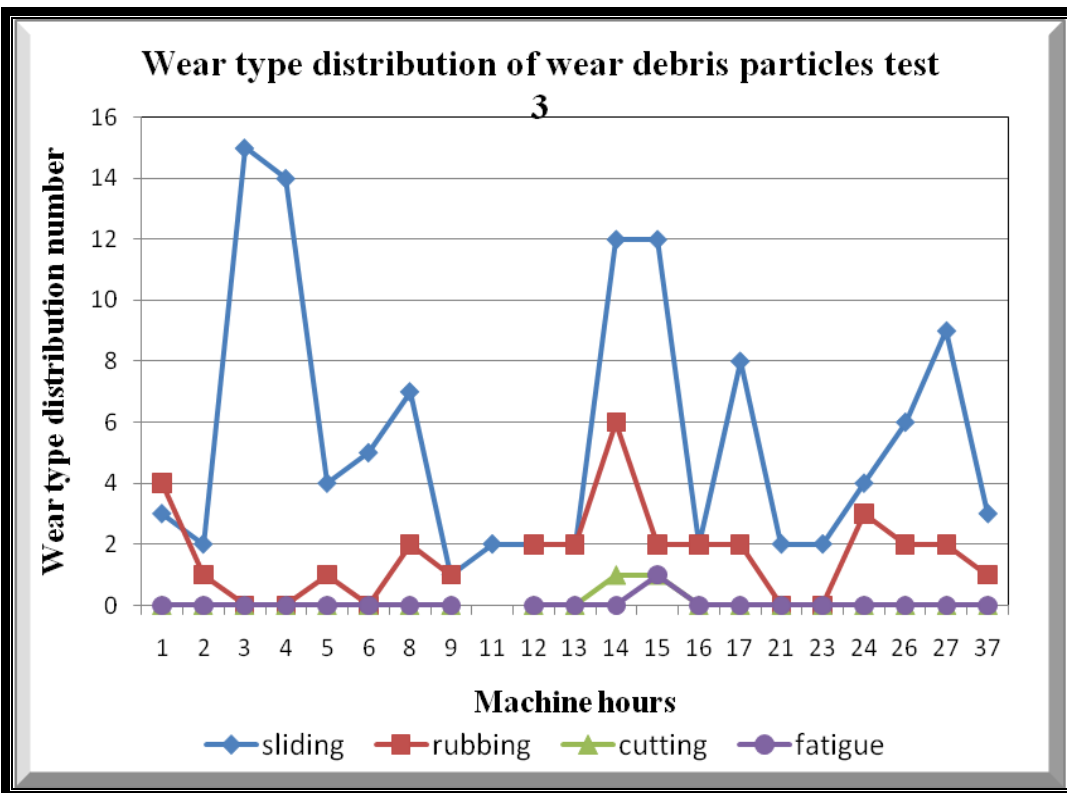


Figure 5-35: Wear type distribution of wear debris particles test 3

Figures 5-34 and 5-35 show the distribution of the wear type of the particles where the majority fall into sliding type particle. Figures 5-32 to 5-34 show the ratio of the major dimension over the thickness of the particle. In particle identification using CASPA, severe sliding normally results in a major dimension over thickness ratio of 11:1 to 20:1, while chunky fatigue gives a major dimension over thickness ratio of 2:1 to 5:1; this includes the majority of particles in tests 1, 2 and 3 [33]. In addition, Table 2-2 in Chapter 2 shows that the combined rolling and sliding wear type particles normally have a major dimension to thickness ratio of 4:1 to 10:1 while a rolling fatigue spall particle has a major dimension to thickness ratio of 10:1.

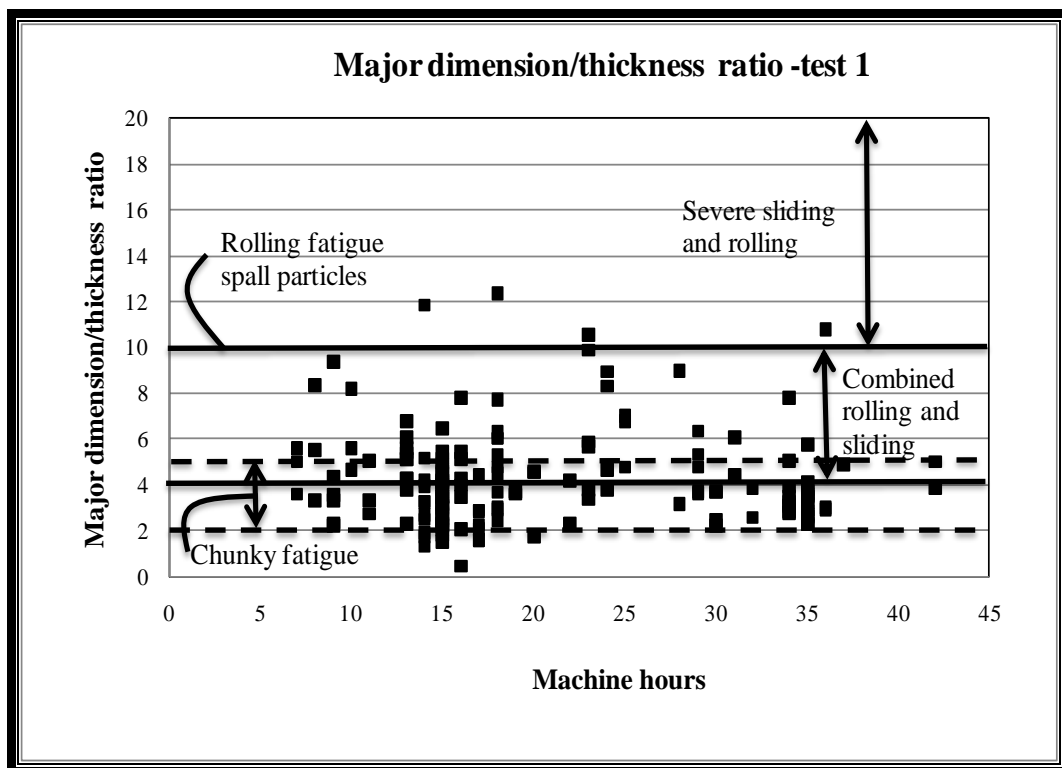


Figure 5-36: Major dimension/thickness ratio-test 1

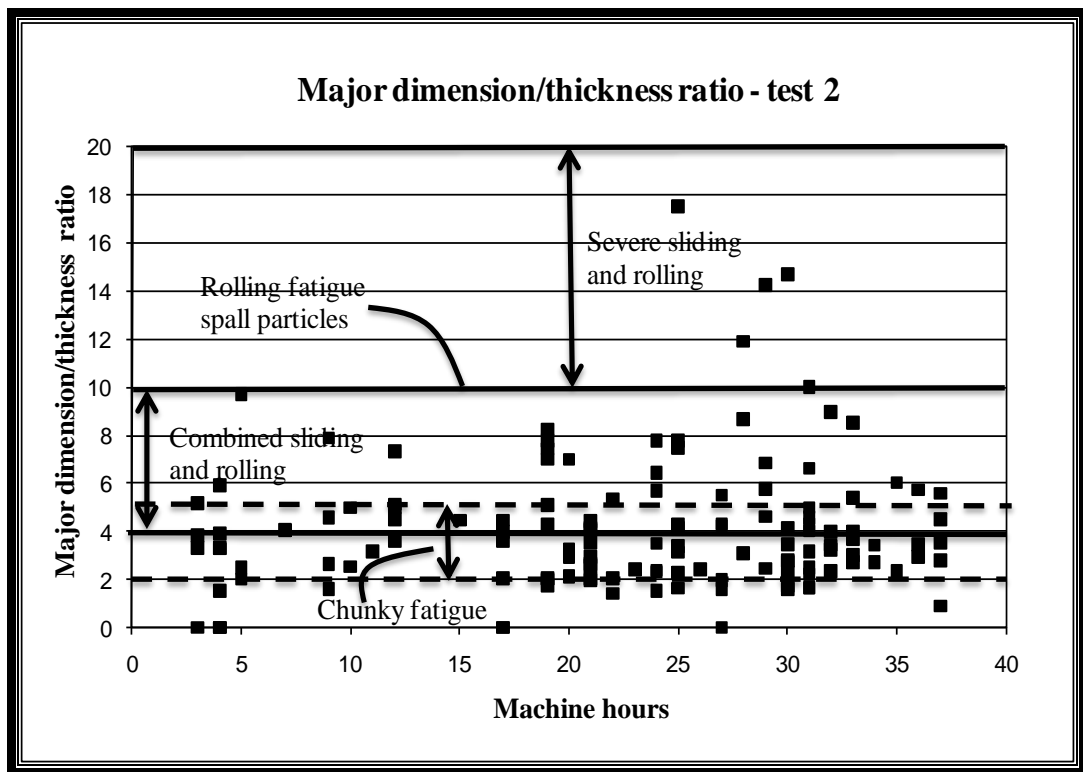


Figure 5-37: Major dimension/thickness ratio - test 2

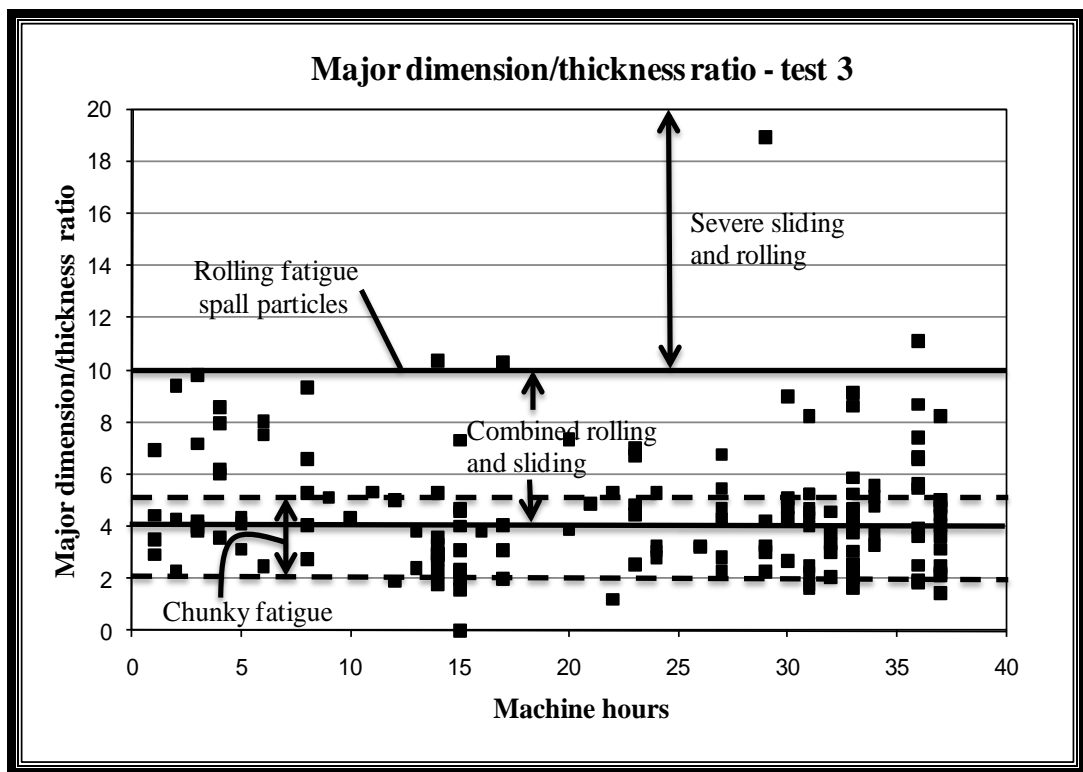


Figure 5-38: Ratio size/thickness versus time - test 3

Figures 5-36 to 5-38 show classification of wear type according to major dimension over thickness ratio method for all three experiments. A majority of the particles fall on the category of chunky fatigue and combine rolling and sliding. However, in Figures 5-36 and 5-38, there are signs that rolling fatigue and severe sliding and rolling wear type began to appear at hour 14 and hour 15, which signifies the deterioration of the gears condition.

5.6 Conclusions

This chapter expanded on the results of the experiments where the onset of failure of the gears was determined by the quantitative analysis of the rate of particles generation, supported by images of the gear damages. It reaffirmed the value and importance of obtaining information on volume and thickness of the particles, which was used to calculate the wear rate of the gears. The method used in identifying the onset of failure was proven effective in all three experiments. Furthermore, information on the thickness of the particles enables the determination of the ratio of major dimension over thickness which assists in classifying the type of the particles generated.

Chapter 6.0 Discussion

6.1 Introduction

This chapter will discuss key areas in the contribution of the research with some of the challenges and weaknesses, the preliminary and final results, and it also contains a critical appraisal of the experimental work and the outcome of the research.

6.2 Contribution

The research has shown that the multi-view images of a particle can provide tools for volume estimations of a particle and provide the amount of wear rate in term of metal removed in a given time. Many techniques are only based on two dimensions which ignore the thickness of the particles or just assign the thickness ratio value. This will assume that the thickness of a group of particles is the same under any conditions without taking into account the individual particle thickness to be evaluated. In this research the individual thickness was taken into account to calculate the volume and a correlation of the volume data was established in order to get the best volume for a particular size particle. The correlation value of R squared ranged from 0.73 to 0.38 with the value of 1.0 being the perfect correlation. The correlation for the test 3 is 0.73 which is quite high for so many uncertainties in the estimation. The volume estimations of 15, 25, 50 and 100 μm for test 1 and test 3 are about the same which shows that the estimations are reliable even though the two experiments were conducted separately.

The use of mass particle wear rate over particle count wear rate enhanced the decision making of the wear regimes. This is due to the fact that metal removal from the gear surfaces is more likely to represent the severity of the damage to the gears rather than particle counts only. The wear rate graphs in Chapter 5 show how the mass of wear debris enhances the determination of the wear regimes. In addition, the summing up of the wear rate of 15, 25, 50 and 100 μm shows that the wear regime demarcation is even clearer and that higher wear

rate and low wear rate zones can be separated. However, the data of particle counts are important to present the total wear rate and demonstrates the trend.

The modification of the peristaltic pump to allow change of flow direction based on time assisted in mechanically rotating the suspended particles. However, the system cannot rotate a particle size of more than 250 μm as the internal height of the flow cell is only 300 μm and smaller particles below 10 μm could hardly be seen rotating.

The suspended particles in the fluid flowing in a direction possessed inertia; once the flow was disturbed and the flow changes in the opposite direction inside the flow cell, the irregular edges and imbalance of the particle itself caused the particle to rotate. Figure 6-1 below shows the flow of the gear oil inside the flow cell which contains a particle. The oil flows from the bottom inlet and is directly guided in the direction of the outlet by the parallel plate. The streamlines flow around the particles because the oil velocity in the flow cell is much higher than the velocity of the particle. The calculation of the velocity of oil and velocity of particles is explained in Chapter 4.

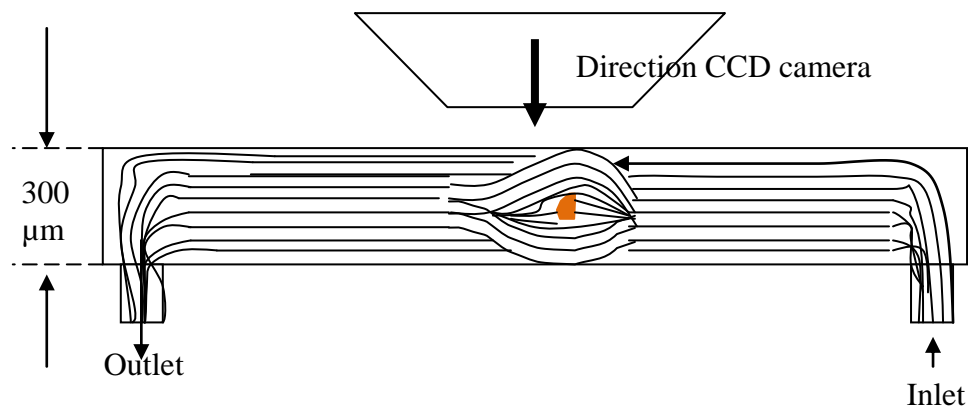


Figure 6-1: Flow pattern of oil around a particle

During the flow some particles, due to their shape, rotate while flowing but some particles do not. Therefore, in order to initiate rotation, the flow needed to be

disturbed by changing direction. Figure 6-2 shows the effect of the flow on a particle which causes it to rotate.

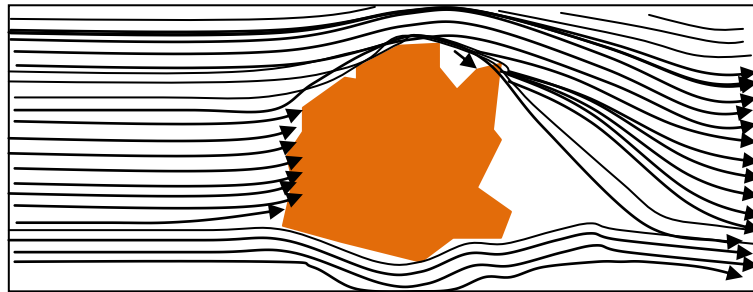


Figure 6-2: Flow pattern (side view) of oil around a particle when the direction of flow is reversed.

There are some issues with the rotation of the particles in which some debris did not rotate on the same axis, making it difficult to reconstruct the pseudo 3D images or even to capture the side view image of a particle. In these cases, that particle sample will not be used for the volume calculation. However, the images that rotate at an angle could still be used by rotating back the image manually using standard image capture software.

The rectangular area used in calculating the volume area recorded two digit errors, especially if the particles were spherical shape or cylindrical in shape. However, for wear in gear, the generation of such shape are quite rare. Spherical shape particles are normally produced during the wear of bearing rather than gears.

6.3 Discussion on preliminary results

The results of the particle count found in the experiments were very difficult to associate with the “bath tub” curve. This was due to the fact that while the end of the running-in zone can be identified easily by examining the change of the trend line from a reducing trend to a constant straight line, the beginning of a failure zone was difficult to determine due to variation of wear rates towards the end of the experiment. Actual pictures taken of the gears at hourly intervals were

meant to substantiate the failure condition. The result of the pitting failure cumulative particle count shows that the estimated running-in zone ended at between hours 5-7 of the experiment and the onset of failure was predicted at about hour 16. The result of the scuffing test shows that the running in zone ended at about hour 5 but the onset of the failure zone was not identified.

The up- and-down trend of the graphs indicates that the gears experienced a healing process, during which the amount of particles generated reduced. Once the metal was removed from a tooth flank, a load redistribution process occurred in which the tooth flanks may have self-healed by smoothing themselves to a certain extent [26]. However, when the pressure on the contact area kept exceeding the surface stress limit, the surface cracked and the pulling and rubbing action when the gears mesh removed particles from the gears, giving a high peak again on the graph.

In constructing the three dimensional images from image capturing, coordinates establishment and 3D reconstruction, as stated in Chapter 3, all of the work was undertaken manually. At the moment, there is not yet any automation in any of these processes. During these procedures, the video images were transformed into many still image frames. The selection of these frames was done manually and two frames (the front view and side view) were analyzed further using the MATLAB program for volume estimations. While the process was manual, it provides a good direction for future work. 3D image construction methods used in the study were an estimate of the actual particle object. Despite this, the 3D image produced is still able to give a general shape of a particle from different views.

6.4 Discussion on the final and validation experimental results

Three experiments were conducted to test and to validate the system that has been developed in this research. For the purpose of comparison, all of the parameters in these experiments were kept the same; the loading was fixed at 4350 N and the speed was fixed at 1000 RPM. The only difference between these three experiments was that the particle counts for test 3 were done continuously

with the objective of monitoring the behaviour of the trend if the number of samples (due to continuous measurement) increased significantly.

The results for all of the three experiments were relatively close, where the onset of failure for test 1 was at 16 hours while the onset of failures for test 2 and test 3 were at hour 11.5 and hour 14 respectively. The decision for determining the onset of failure was assisted by the wear rate graphs; at these hours, the wear rate increased significantly. The theoretical life calculations as shown in Appendix I indicated that the onset of failure will begin at 12.8 hours, which is not far away from the value in the graphs. This confirmed that the wear rate graphs are effective in determining the three phases of the gear life, which are a running-in zone, normal steady running zone and the failure zone. It has been noted that even though the particle counts for test 3 were done continuously, the onset of failure was still clearly indicated at hour 14 which is relatively close to the calculated theoretical value of the gears' life as mentioned in chapter 4 and shown in Appendix 1.

6.5 Critical appraisal of the experimental setup

- **Gear setup** - The setting up of the experimental setup took longer than it should because the driving shaft, under torsion stress, tended to twist slightly during any previous test. This caused difficulty in mounting the new gears onto the shaft. Figure 6-3 shows the section of the shaft that gave the problems. Any new design should use a long shaft to facilitate easy fitting of the gears.
- **Oil reservoir** - The design of the oil reservoir was such that two screws penetrated the floor of the reservoir and oil tended to leak through these screws. Figure 6-3 shows the screws going through a mounting bracket and a steel plate before reaching the Perspex floor of the container. The original design did not provide any means of sealing between these three layers of components, so when the machine was running under load, the vibration caused oil to leak through these joints or layers. A great deal of time was spent fixing the problem by disassembling the components to apply liquid sealant between the layers. The application of sealants needed to be very thin to avoid misaligning the holding bar.

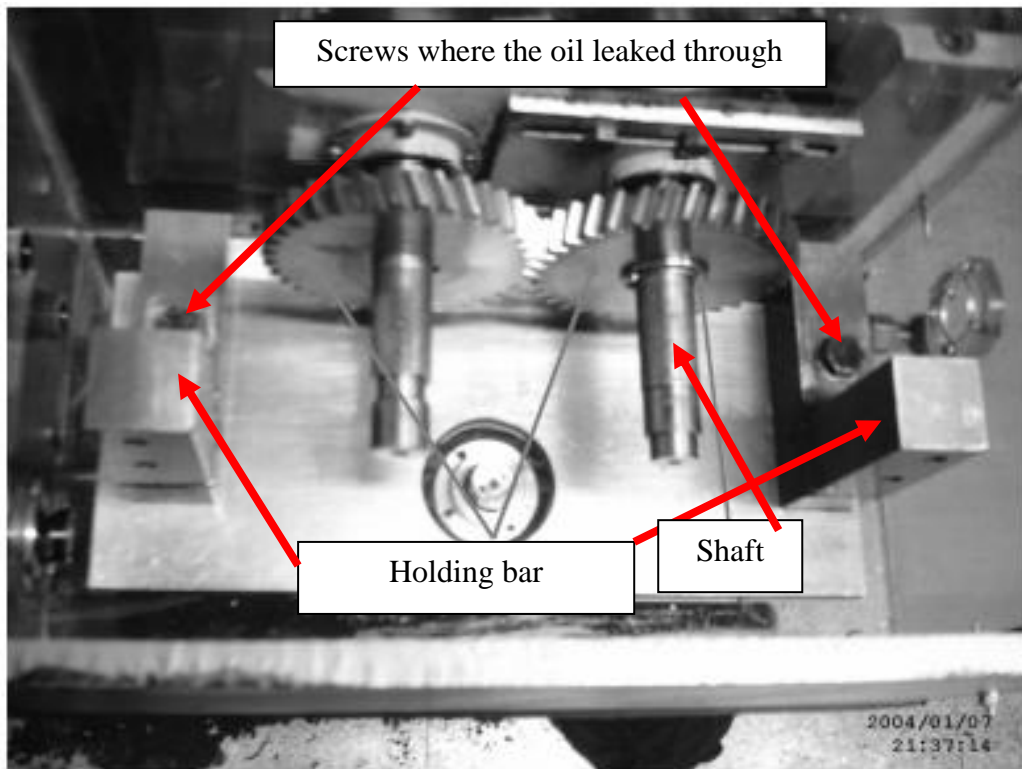


Figure 6-3: gear setup

- **Inspection.** During the experiments, the machine needed to be stopped at three hourly intervals to take images of the condition of the gears. This required opening up the oil sump cover and rotating of the loaded gear manually. If a small-miniaturized camera were installed for the image capturing, all of these steps could be avoided. In experiments conducted by Dempsey, a micro video camera was installed close to the gears to capture images of the damaged gears without having to open the cover of the gearbox [78]. Therefore, images of every damaged tooth of the gear were taken to show the extent of the damage.
- **Testing.** Due to non-continuous testing, the results of the particle counts that were produced at the start of the day showed occasionally high particle counts due to the settling of the particles at the bottom of the reservoir where the tube was placed to draw the sample. Time was needed to ensure the majority of particles were in circulation; this was done by allowing the circulation of oil to start for approximately 15 minutes before the start of the test. This task avoided

the scenario termed “false negative,” in which the samples tested while the machine is at rest would not give the correct density of wear debris generation [76].

6.6 Outcome of the research

The main objective of this research was to explore the possibility of using multi-view and pseudo 3D images to gather information (such as the volume and the thickness) from multiple images of a single particle using online sampling. The developed system has the ability to obtain this type of information which can be used to estimate the wear rate of the gears. In spite of the system being designed not to be fully automatic, it has reduced human intervention in the area of sampling to a minimum level.

Furthermore, the ability of the wear rate graphs to pinpoint the onset of failure of the gears was proven with all of the tests, giving a very close estimate of the beginning of the failure zone. This will provide maintenance personnel with useful information on when to react to the maintenance needs of the gears. In addition, the system provides information about the shape of the particles for classifying the wear type of particles by which the condition of the gears can be predicted.

6.7 Conclusions

Chapter 6 discusses the research contribution, the preliminary and final experiment results. It also contains a critical appraisal of the experimental setup and the overall outcome of the research. The results clearly show the approach was successful in determining the onset of failures, which supported by the actual images of the damage gears and theoretical gear life calculations. The outcome of the research reveals that while the system is not fully automatic, its concept has reduced the human intervention to the minimum, which accomplishes the objectives of the research and provides a new method of wear debris analysis.

Chapter 7.0 Conclusions and future works

7.1 Introduction

The developed system successfully extracts information about the particles and provides the means to determine the onset of failure of the gears. It employed the quantitative and qualitative methodology in analyzing the particles. The achievement of the research and the future works are elaborated in detail in Section 7.2 and Section 7.3 respectively.

7.2 Achievement of objectives

Objective one – Identify the area of novelty in wear debris analysis.

The literature review exercise identified and proposed an online multi-view and pseudo-3D image technique as the novelty area of this research. Throughout the exercise, it was found that there has been no attempt to analyze any particle from two different views. A technique such as LNF, considered a highly automated on-line way of measuring the physical dimensions and shape of particles, only looks at the particle from one view, therefore disregarding their thickness aspect.

Many of the current WDA techniques do not take into account the thickness of particles, and so consequently deprive users from calculating the correct amount of material removed from the gears. The proposed technique allows the estimation of volume and mass of the particles, which yields the wear rate of material removal from gears.

Optical microscopy was chosen to address the issue of online sampling; it does not require sample preparation, as proven in the experiment. Next, the setup also addressed the issue of taking images of a particle at different angles. The introduction of an auto controller RS232, allows the flow of the sample to change direction intermittently (causing the particles to be rotated) and the video images of the rotating particles are captured online. This is also another new area that has been achieved by automatically rotating the particles in the oil while the debris sample is flowing.

The review also revealed that current work undertaken on three-dimensional analysis uses a great deal of expensive equipment, such as SEM and LSCM, which will not be feasible for industry-wide usage due to high up-front costs. The proposed system setup, which is estimated at about £12,400 (as shown in appendix VII), should be a more attractive cost. Considering all of these scenarios, the review has resulted in the focus of the research being on the fields of online sampling, multi-view and pseudo three-dimensional images of wear debris analysis, in determining the onset of failure of the gears.

Objective two – Develop methodology that can minimize human intervention in wear debris analysis.

The system developed in this research employed online sampling, which is free from the risk of contamination and any time consuming sampling preparation. This significantly reduces the human intervention in its analysis work, in comparison with the sampling procedure in the preliminary test or any other offline approach applied in the industry.

In the preliminary experiment, bottle and magnetic plug sampling were used and the following issues proved to be highly significant: amount of time taken to collect the sample at fixed intervals and the length of time they were kept in storage before being analyzed using PODs and image capturing tools. For instance, conducting particle counts for the 75 ml sample required about 10 minutes, and the higher the number of samples to be tested, the more time that needed to be allocated. In addition, the time designated for particle counts and image processing can only be done after the experiment was completed because during the experiment, only the collection of the samples was done. Online sampling used in the research drew the samples directly from the oil reservoir using a soft tube, which eliminated the need for this non-value added procedure, since the particle counts can be done simultaneously during the experiment and images of the particles are captured while they are flowing in the flow cell.

A visit to a service company which has a contract to provide wear debris analysis to the Ministry of Defense in South London in April 2007, confirmed

how intensive an offline wear debris analysis is. Every fortnight a large number of bottles containing samples from military vehicles and ships are sent to the laboratory. A special rack must be provided to arrange the bottles and a proper label was stuck on each bottle. An expert is designated to analyze all of the samples in the bottles individually and these repetitive tasks are part of the procedure of day. The information gathered from the analysis is used to predict the health status of the components under monitoring.

The system as described in this thesis had also enabled the particles, which are suspended in the gear oil, to be mechanically rotated by means of changing flow direction in the flow cell. This task was completed automatically by the introduction of RS232 remote automatic control on the peristaltic pump that receives the instruction from the computer through the HyperTerminal program. The capture of the video images was completed, and the system obviated the need to analyze the actual particles and migrated to only analyze the video images of the particles. This saves a lot time compared to bottling and offline sample procedures, which have been the choice of a majority of users of the WDA technique.

However, the system was not intended to be fully automatic, as some tasks such as 3D image reconstruction still require manual intervention to complete the analysis. All in all, the system had saved time and costs in analyzing the wear debris analysis during the experiments, and would do so in any commercialization effort in the future.

Objective three –Implement the multi-view images and pseudo three-dimensional methodology to extract information from generated particles.

The online sampling data that were collected in terms of video images were converted to still images for the purpose of extracting volume and thickness data and reconstructing pseudo three-dimensional images. Two images of a single particle were used to estimate the volume of a particle using the rectangular equivalent area. The two images were taken at an approximately 90 degree angle

to each other, which represented the facial view and the side view. In order to ease the selection of the images, the largest image was chosen to represent the facial view of the particle, while the smallest image of the particle represented the side view. The area to the facial side was multiplied by the thickness of the side view of the particle to yield volume data. The data were then tabulated and a trend line was drawn and volumes for the 15, 25, 50 and 100 um were estimated using this trend line. These volumes were later converted to mass and then multiplied by the particle counts to produce graphs of wear rate over time. The graphs show and pinpoint the hours which experienced the highest wear rate and metal removal from the gears.

The rectangular equivalent area method is more accurate than the Sphere of Identical Surface Area Diameter (SISAD) in this research, because most of the particles were platelets rather than spheres [10]. The SISAD gives the diameter of a sphere whose surface area is the same as the particle. It is useful if the particle is a sphere, but for platelet type particles, the proposed system reduces error rates.

The pseudo-3D images constructed are not perfect, but they do provide more information in comparison to other techniques, because they analyze two images of a single particle at the same time and provide an estimate of the third dimension. The dynamic study of wear debris particles shows that the rotation is possible for further volume analysis which has never been done before

Objective four – Use extracted information to predict the onset of failure and to assist in maintenance decision making.

This research used the equivalent area rectangle to measure the thickness and subsequently calculate the volume of the particles, which was then converted to mass weight by multiplying with the density of the material that the gears were made from. Subsequently, the particle counts were multiplied by the mass weight of selected size particle counts to produce the wear rate of wear debris generation in terms of microgram per minute. The quality of the volume data in this research is more reliable than the general estimated major dimension to thickness ratio for different types of wear, as mentioned in Table 2-2. The ability to estimate the

thickness of the particle by measuring the side view images replaces the major dimension to thickness ratio.

The onset of failure was determined by the peak of the graphs of wear rate and supported by the images of gear damage and the theoretical gear life calculations. In addition, the shape information may also be acquired from the particle, with the two images, as information from one image substantiates the other image.

The technique of analyzing two images from a single particle has not been attempted in any WDA analysis before, which demonstrates the novelty of this research.

7.3 Future work

This research has proven the importance of employing an online sampling technique to capture multi-view images of a particle to generate its thickness and volume data for further analysis. The following future work is proposed to further improve the developed system for any application.

Proposal 1: Miniaturisation of the hardware for commercial use.

This research has demonstrated modification of equipment on an experimental scale, which was not done by a previous researcher even though the same equipment was used. Since the research was still trying to prove a concept, the size of the equipment used remained the same. The sizes of the apparatuses used in this research are too large to be used in the commercial area or in industry. Therefore, the research proposes the miniaturization of the hardware system as follows:

- The use of a miniaturized pump, which can automatically change the direction and the flow rate of the drawn gear oil sample as required. The size of a miniaturized pump can be 20 times smaller than a peristaltic pump.

- The use of a small web camera, which has the ability to magnify and capture images. There is still no small camera that has the ability to magnify and capture images but as the technology of cell phones fitted with a camera is developing so fast, that magnifying capability shall be soon available. Obviously, this will resolve the size issue of optical microscopes.
- The use of a miniaturized flow cell for video image capturing. The emergence of so many different macro fluid equipment types will support this proposal.
- The use of a smaller off-the-shelf particle count unit to aid in particle counts. This will remove the independence on big size PODs which are not commercially viable to be used at various points in a factory.
- The automatic transfer of the video image file to the analyzing PC using a wireless tool such as Bluetooth. This automation will reduce the task of collecting video images of wear debris samples at different machine running hours.

Proposal 2: Improvement in the software to provide a full automation.

The previous researcher used a two dimensional image, and only one side of the particles was examined. In this study, concentration was focused on multi-view images and near three-dimensional images, which were not considered by previous researchers who used the same hardware. In fact, the previous researchers did not introduce additional control cards which can initiate a time based direction change of the peristaltic pump. However, for future work, development of software is proposed to provide a full automation in:

- Converting the captured video images to still images. Even though converting video images is not a new area of research, with the rotating particle images more work is needed for image selection.
- Calculating the volume and thickness automatically after the still images is analyzed. The selection of images is very important to give good estimation volume and thickness of particles.

- Reconstructing the pseudo-3D images. There is still a lot of room for improvement in the 3D images such as using more images for the construction.

Proposal 3: To improve the pseudo 3D images to full 3D images online

The study has provided the basis for ensuring that particles are able to be rotated for multi-view image capture. This enables a further analysis on the volume of the particles. However, in order to provide a more representative 3D image, further work on manipulating images are proposed.

- Current pseudo-3D images are not a full reflection of the 3D images of the particle and require improvement by using more than two images to reconstruct the 3D image.

REFERENCES

- [1] Starr, A.G. (1997). A structured approach to the selection of the condition based maintenance. 5th International IEE FACTORY Conference, Cambridge.
- [2] Peng, Z.; Kirk, T.B. (1998). "Automatic wear particle classification using neural networks." *Tribology Letter* **5**: 249-257.
- [3] Ebersbach, S.; Peng, Z.; Kessissoglou, N. (2006). "Investigation of the conditions and faults of a spur gearbox using vibration and wear debris analysis techniques." *Wear* **260**: 16-24.
- [4] Peng, Z.; Kessissoglou, N.(2003), "An integrated approach to fault diagnosis of machinery using wear debris and vibration analysis", *Wear* 255 (2003) 1221–1232.
- [5] Lewicki, D.G.; Dempsey, P.J.; Heath, G. F.; Shanthakumaran, P., "Gear Fault Detection Effectiveness As Applied To Tooth Surface Pitting Fatigue Damage", the American Helicopter Society 65th Annual Forum, Grapevine, Texas, May 27–29, 2009.
- [6] Sperring, T.P.; Nowell, T.J. (2005). "SYCLOPS—a qualitative debris classification system developed for RAF early failure detection centres." *Tribology International* **38**: 898-903.
- [7] Bartz, W. J.; Batchelor, A.W. (2000). *Engineering Tribology* 2nd edition. Elsevier Butterworth-Heinemann.
- [8] Myshkin, N.; Markova,L.;Grigoriev, A., Metal-Polymer Research Institute, "Condition Monitoring and Predictive Analysis of Tribosystems by Wear Debris", Practicing Oil Analysis Magazine, Mar 2005.
- [9] Yuan, C. Q.; Peng, Z.; Chou, X.C.; Yan, X.P. (2003). "The characterization of wear transitions in sliding wear process contaminated with silica and iron powder.", *Tribology International* 38 (2005) 129–143.
- [10] Hunt, T. M. (1992). "Handbook of wear debris analysis and particle detection in liquids", Elsevier Science Publisher.
- [11] Khan, M.A.; Starr, A.G. (2006). "Basic principles of wear phenomena, mechanisms and lubrication – a review". Lubmat, Preston UK.
- [12] Moubray, J. (1997), "Reliability Centered Maintenance", Industrial Press Inc

- [13] Dempsey P.J (2001)."Gear damage detection using oil debris analysis", NASA/TM-2001-210936. 14th International Congress and Exhibition on Condition Monitoring and Diagnostics Engineering Management.
- [14] Johnson, Mike (2010). "Strategic oil analysis: Time dependent alarm for extended lubricant lifecycles", Technology and Lubricant Technology.
- [15] Khan, M. A.; Starr A.G. (2006). "Wear debris: basic features and machine health diagnostic." Insight 48(8).
- [16] Roylance, B. J. (2002), "Machine failure and its avoidance-what is tribology's contribution to effective maintenance of critical machinery?" . Proc Instn Mech. Engrs Vol. 217 Part J: J. Engineering Tribology.
- [17] Raadnui, S. "Magnetic Chips detector (MCD) wear particle analysis." The Journal of King Mongkut's Institute of Technology North Bangkok, Vol 14 issue 2 (April-June 2004)
- [18] Edmonds, J. (2000). "Detection of Precursor Wear Debris in Lubrication Systems." IEEE: 73-77.
- [19] Bartz, W. J. (1993). "Lubrication of gearing", Mechanical Engineering Publication, UK.
- [20] Wright, G.J.; Neale, M.J.(1987),"Wear debris analysis as an integral component of machinery condition monitoring.", J. S. Afr. Inst. Min. Metal/.,vol. 87, no. 8. Aug. 1987. pp. 253-260.
- [21] Lange,G.D. (2000). "Failure analysis for gearing." Paper age, September 2000, <http://www.mt-online.com/>[01 July 2007]
- [22] Dudley, D.W. (1994);"Handbook of practical gear design", Technomic publishing company.
- [23] "Gear Pitting and Lubrication", Engineering Edge, http://www.engineersedge.com/gears/gear_pitting_lubrication.htm. [11 Nov 2010]
- [24] "Micropitting and Gear Lubrication", Engineering Edge, http://www.engineersedge.com/gears/gear_pitting_lubrication.htm. [11 Nov 2010]
- [25] Khan, M.A., "Automation of Wear debris analysis for machine health diagnostic", PhD thesis, Department of Mechanical, Aerospace and Civil Engineering, The University of Manchester, (2008).

- [26] BS ISO TR/ 13989-2:2000, Calculation of load scuffing capacity of cylindrical, bevel and hypoid gears.
- [27] "Critical scuffing temperature for gears", Engineering Edge, http://www.engineersedge.com/gears/critical_scuffing_temperature_gears_lubrication.htm. [11 Nov 2010]
- [28] Roylance, B.J. (2005), "Ferrography—then and now", Tribology International 38 (2005) 857–862.
- [29] Kuhnell, B. T. (2004). "Wear in Rolling Element Bearings and Gears- How Age and Contamination Affect them". Machinery Lubrication.
- [30] Raadnui, S. (2005). "Wear particle analysis – utilization of quantitative computer image analysis: A review." Tribology International 38: 871-878.
- [31] Roylance, B.J.; Williams, J.A.; Dwyer-Joyce, R. (2000) "Wear debris and associated wear phenomena-fundamental research and practice" Proceedings of the Institution of Mechanical Engineers, J: Journal of Engineering Tribology, 214 (1). pp. 79-106
- [32] Anderson, D.P. (1982). "Wear Particle Atlas", Naval Air Engineering Centre.
- [33] Roylance, B.J.; Hunt, M. T.(1999)."Wear Debris Analysis: Machine & systems condition monitoring series", Coxmoor publishing company.
- [34] Roylance, B.J.; Raadnui, S. (1994),"The morphological attributes of wear particles - their role in identifying wear mechanism", Wear, 175(1994) 115-121.
- [35] Myshkin, N.K.; a H. Kongb.; A.Ya.; Grigoriev a.; E.-S. Yoon (2001). "The use of colour in wear debris analysis." Wear 251: 1218–1226.
- [36] Laghari, M.S.(2002), "Surface feature recognition of wear debris", Artificial Intelligence , pp 627-637.
- [37] Gebarin S., Noria Corporation, "On-line and In-line Wear Debris Detectors: What's Out There?". *Practicing Oil Analysis Magazine*. September 2003
- [38] Tucker, J. E. ; Reintjes, J. ; Duncan, M. D. ; McClelland, T. L. ; Tankersley, L. L. "LASERNET FINES Optical Oil Debris Monitor"; Naval Research Lab Washington D.C. Laserphysics Section.
- [39] Reintjes, J.; Tucker,J.E.; Sebok, T. J.; Henning, P. F.; DiGiuseppe, T. G., Filicky, D. (2003). "Portable fluid Analyzer." 1-6. US Naval Research Laboratory, Washington, DC 20375; 2 Lockheed.Martin, Akron, OH.

- [40] Eneko, G. (2007). "Lube sensor state of the art :Intelligent sensors, requirement and design", Fundación TEKNIKER.
- [41] Harvey, T. J.; Morris, S.; Wang, L.; Wood, R. J. K.; Powrie, H. E. G." Real-time monitoring of wear debris using electrostatic sensing techniques", Proc. IMechE Vol. 221 Part J: J. Engineering Tribology
- [42] Tasbaz, O.D. ; Wood, R.J.K. ; Browne, M.; Powrie, H.E.G.; Denuault, G., "Electrostatic monitoring of oil lubricated sliding point contacts for early detection of scuffing", Wear 230 (1999). 86–97.
- [43] Khan, M.A.; Starr, A.G.; Cooper, D. (2007). "Academic and commercial efforts in Wear Debris Analysis Automation (WDAA)". Insight 49(12).
- [44] Leavers, V.F.(2007), V41 Particles Ltd., "Classifying Wear Debris Particles with Automatic Image Analysis", Practicing Oil Analysis, <http://www.machinerylubrication.com/Read/806/wear-debris-particles> [15 02 2006]
- [45] Xu K.; Luxmoore, A.R. (1997). "An integrated system for automatic wear particle analysis." Wear 208: 184-193.
- [46] Laghari, M.S.; Boujarwah, A. (1999). "Wear particles texture classification using artificial neural networks." International Journal of Pattern Recognition and Artificial Intelligence 13(3): 415-428.
- [47] Peng, Z. (2001). "Wear-debris analysis in expert systems." Tribology letters 11.3: 177-184.
- [48] Peng, Z.; Goodwin, S., "The development of an expert system for wear debris analysis", DSTO International Conference on Health and Usage Monitoring, Melbourne, February 19-20, 2001
- [49] Peng, Z.; Kirk T. B. (1999). "Wear particle classification in a fuzzy grey system." Wear 225-229: 1238-1247.
- [50] Peng, Z. (2002). "An integrated intelligence system for wear debris analysis." Wear 252: 730-743.
- [51] Memon, Q.A.; Laghari,M.S. (2005). "Self Organising Analysis Platform for wear particle." ENFORMATIKA 6: 122-125.
- [52] Peng, Z. (2002). "An integrated intelligence system for wear debris analysis." Wear 252: 730-743.

- [53] Laghari M.S. (2003). "Recognition of texture types of wear particles" Neural Computer & Application: 18-25.
- [54] Khan M.A (2006). 1st year PhD progression report 2006, Department of Mechanical Aerospace and Civil Engineering, The University of Manchester.
- [55] Radnui, S. (2005), "Machinery health monitoring through low cost maintenance tribology techniques.", The Journal of KMITNB., Vol. 15, No.2, Apr.-Jun.2005.
- [56] Military Sealift Command's Oil Analysis Program: MSCHQ N712E, 202-685-5730
- [57] Davidson, M.W. , Abramowitz, M. (2000), "Optical Microscopy" ,<http://micro.magnet.fsu.edu/primer/pdfs/microscopy.pdf> [20 Jan 2010]
- [58] Heidcamp, William H. "Chapter 1: The microscope introduction", <http://homepages.gac.edu/~cellab/chpts/chpt1/intro1.html> [15 Jan 2011]
- [59] Davidson, M.W. "Resolution", National High Magnetic Field Laboratory <http://www.microscopyu.com/articles/formulas/formulasresolution.html> [15 Jan 2011]
- [60] Mohammed, J.K.; Dwarakadasa, E.S. (1989). "SEM studies of wear debris in Al-Si alloys." Journal of Materials Science Letters 8: 1285-1287.
- [61] Stachowiak, G.W. (1998). "Numerical Characterization of wear particles morphology and angularity of particles and surfaces." Tribology International 31(1-3): 139-157.
- [62] Stachowiak G.W.; Podsiadlo P. (2006). "Towards the development of an automated wear particles classification system." Tribology International 39:1615-1623.
- [63] Podsiadlo, P.; Stachowiak G.W. (1997). "Characterization of surface topography of wear particles by SEM stereoscopy." Wear 206: 39-52.
- [64] Scanning electron microscopy, (19 Nov 2009), <http://www.mos.org/sln/SEM/tour20.html>
- [65] Confocal Microscopy Leica TCS SP5 , http://www.har.mrc.ac.uk/services/bioimaging/confocal_microscopy/index.html, (19 Nov 2009)
- [66] Peng, Z.; Kirk T.B. (1998). "Computer image analysis of wear particles in three-dimensions for machine condition monitoring." Wear 223: 157-167.

- [67] Stachowiak, G.W.; Podsiadlo, P. (1999). "Surface characterization of wear particles." Wear 225–229 (1999). 1171–1185.
- [68] Stachowiak G.W.;Podsiadlo P. (2001). "Characterization and classification of wear particles and surfaces." Wear 249: 194-200.
- [69] Peng, Z.; Kirk, T.B.; Xu, Z.L., "The development of three-dimensional imaging techniques of wear particle analysis", Wear 203-204 (1997) 418-424.
- [70] Huang, J.; Huang, X.; Metaxas, D.; Banerjee, D. (2006). "3D Tumor Shape Reconstruction from 2D Bioluminescence images", Biomedical Imaging: Nano to Macro 3rd IEEE International Symposium, Arlington, Virginia USA.
- [71] Yesilyurt, I., "Gearbox fault detection and severity assessment using vibration analysis in Mechanical", PhD Thesis, Department of Mechanical, Aerospace and Civil Engineering., University of Manchester, 1997.
- [72] Zakarian, J, (2007), DEXRON-III ATF Specification, <http://fileserver.urimarketing.com/LU/CourseCatalog/dexronIII.pdf> [15 Jan 2011]
- [73] Petrocanada TechData GM Dexron III "Approved for H specification" www.petro-canada.de/pdf/IM7804E0308_ENG.PDF [15 Jan 2011]
- [74] ISO BS ISO 6336-2:2006, Calculation of load capacity of spurs and helical gears, part 2 calculation of surface durability (pitting) British standard
- [75] Watson. (2007). "Peristaltic pump manual Watson Marlow pump." from <http://docs-europe.Electro components.com/pdf>. [15 Jan 2010]
- [76] WATSON-MARLOW BREDEL MANUALS
<http://www.watson-marlow.co.uk/pdfs-global/m-323e-s-u-du-gb-06.pdf>
[15 Jan 2010]
- [77] JWF technology, ARTI- PODS (Portable Oil Diagnostic System),
http://www.jwftechnologies.com/argo_hytos/diagnostic/pods.htm.
[03/08/2006]
- [78] Hunt, T.M.; Evans, J.S., (2004). "The Oil Analysis Handbook", Coxmoor Publishing Company's.
- [79] MATLAB tutorial, "What is MATLAB", <http://www.matlabtutorials.com>
[15 Jan 2010]

- [80] Saita, Sandro, (2007). “Standardization versus normalization” Data MiningResearch, <http://www.dataminingblog.com/standardization-versus-normalization/> [15 Jan 2011]
- [81] Fitch, J.(2009), “Virgin particles and weak signals: Finding meaning in wear debris”. Machinery Lubrication magazine, Sep 2009.
- [82] Khan, M.A.; Starr, A.G. (2007) “Theoretical and experimental working life comparison for a helical gear under linear pitting failure”. Applied Mechanic and Material Vols. 7-8(2007) pp95-100.
- [83] MATLAB software –Demo sections/Toolboxes/Image processing/image segmentation/Detecting a cell using image segmentation.
- [84] Beddow JK.; Fong S-T.; Vetter AF (1980). “Morphological analysis of metallic wear debris.” Wear 1980;58 : 201–11.
- [85] Roylance, B.J.; Pocock, G. (1983).” Wear Studies through particle size distribution I: Application of the weibull distribution to ferrography” . Wear, 1983: 90 : pp113 – 136.

APPENDIX

Appendix I

Theoretical life calculation for gear (Pitting experiment) [74;82]

According to BS-ISO 6336-2, the calculation of helical gear pitting failure is based on the contact stresses, σ_H at the pitch point of the meshing gears, or at the inner point of single pair tooth contact. σ_H shall be less than its permissible σ_{HP} for preventing failure and vice versa.

The formula of contact stress for the pinion gear is:

$$Z_B \sigma_{HO} \sqrt{K_A K_V K_{H\beta} K_{Ha}} \leq \sigma_{HP} \dots \dots \dots \text{eq. 10}$$

Where

Table APP I-1: Symbols of parameters

Z_B	pinion single pair tooth contact factor	Z_B (for spur gear) and Z_B (for helical gear) = 1 (ISO 6336-2:2006)
σ_{HO}	nominal contact stress at pitch point	Calculated to be 830.4 N/mm ²
K_A	Application factor (It takes into account the load increment due to externally influenced variations of input or output torque)	K_A - uniform loading for spurs and helical gear = 1
K_V	Dynamic factor (It takes into account load increments due to internal dynamic effects)	K_V (for spur and helical gear) = 1.031
$K_{H\beta}$	Face load factor for contact stress (It takes into account uneven distribution of load over the face width due to mesh misalignment caused by inaccuracies in manufacture or elastic deformations)	$K_{H\beta}$ (for spur and helical gear) = 1.00294
K_{Ha}	Transverse load factor for contact stress (It takes into account uneven load distribution in the transverse direction resulting, for example, from pitch deviation)	K_{Ha} (for spur and helical gear) = 0.8826

In calculating σ_H , the following pre-selected operational and gear physical dimension parameters are used:

Table APP I-2: Pre-selected experimental parameters

Type of gear	Helical
Helix angle	17.75
Pressure angle	20
Centre to centre distance	113 mm
Module of gear	3
Number of teeth on gear	35
Face width	15 mm
Tip diameter	116.25 mm
Pitch diameter (Also selecting as a reference diameter)	110.25 mm
Applied tangential loading (for pitting)	4350 N
Lubricant	DEXRON III Petro Canada
Gear Material	En32, Casehardened
Testing Speed	1000 rpm

In order to calculate σ_H , σ_{HO} need to be determined first,

To calculate σ_{HO} , the following parameters need to be determined:

Determine Z_H Zone factor

$$Z_H = \sqrt{\frac{2\cos\beta_b \cos\alpha_{wt}}{\cos^2\alpha_{at} \sin\alpha_{wt}}} \quad \dots \text{eq.12}$$

β_b : base helix angle :17.75 degrees

α_{wt} : traverse pressure angle at the pitch cylinder : 20.914 degrees

α_t : traverse pressure angle at reference cylinder : 20.914 degrees

$$Z_H = \sqrt{\frac{2 \cos(17.75) \cos(20.914)}{\cos^2(20.0) \sin(20.914)}} = 2.44$$

Determine Z_B

Z_B (for spur gear) and Z_B (for helical gear) = 1 (ISO 6336-2:2006)

Determine Z_E Elasticity factor

Taken from table Z_E = 189.8 (Table 1 pp 14 BS ISO 6336-2:2006)

Determine Z_ε contact ratio factor

Spurs gears

For contact ratio > 1

$$= \sqrt{\frac{4 - 1.47}{3}} = 0.918$$

Helical gears

$$Z\epsilon = \sqrt{\left(\frac{4 - \varepsilon_\alpha}{3}\right)(1 - \varepsilon_\beta)} + \frac{\varepsilon_\beta}{\varepsilon_\alpha} \text{ for } \varepsilon_\beta < 1 \dots \dots \dots \dots \dots \dots \text{ eq. 13}$$

where

Traverse contact ratio:

Traverse base pitch

$$m_t = \frac{m_n}{\cos \beta} = \frac{3}{\cos(17.75)} = 3.149$$

so,

$$P_{bt} = m_t \cos \alpha_t = 3.149 \times 3.142 \times \cos(20.914) = 9.242$$

Length path of contact

$$g_{\alpha} = \frac{1}{2} [\sqrt{d^2_{a1} - d^2_{b1}} \pm \sqrt{d^2_{a2} - d^2_{b2}}] - a \sin \alpha_{wt} \dots \dots \dots \text{eq. 16}$$

$$g_{\alpha} = \frac{1}{2} \left[\sqrt{(116.25)^2 - (102.98)^2} \pm \sqrt{(116.25)^2 - (102.98)^2} \right]$$

$$= 13.56$$

$$\varepsilon_a = \frac{g_a}{P_{bt}} = \frac{13.56}{9.242} = 1.47$$

Overlapped ratio

$$m_n = 3$$

$$\varepsilon_{\beta} = \frac{b \sin \beta}{\Pi m_n} = \frac{15 \sin (17.75)}{3.142 \times 3} = 0.485$$

Use eq. 13

$$Z_\varepsilon = \sqrt{\left(\frac{4-\varepsilon\alpha}{3}\right)\left(1-\varepsilon\beta\right)} + \frac{\varepsilon\beta}{\varepsilon\alpha} \quad \text{for } \varepsilon\beta < 1 \dots \text{eq. 17}$$

$$= \sqrt{\frac{4 - 1.47}{3}}(1 - 0.485) + \frac{0.485}{1.47} \\ \equiv 0.803$$

Determine Z_β

$$Z_\beta = \sqrt{\cos\beta} \quad \dots \dots \dots \text{eq. 18}$$

$$= \sqrt{\cos(17.75)} = 0.9759$$

For spur gears use eq. 11

$$\sigma_{HO} = 2.4344 \times 189.80 \times 0.918 \times$$

$$0.9759 \sqrt{\frac{4350}{110.25 \times 15} \frac{1+1}{1}}$$

$$= 414 \times 2.294$$

$$= 949.7 \text{ N/mm}^2$$

For Helical gears use eq. 11

$$\sigma_{HO} = 2.4344 \times 189.80 \times 0.803 \times 0.9759 \sqrt{\frac{4350}{110.25 \times 15} \frac{1+1}{1}}$$

$$= 362 \times 2.294$$

$$= 830.4 \text{ N/mm}^2$$

K_A - uniform loading for spurs and helical gear = 1
K_V (for spur and helical gear) = 1.031
$K_{H\beta}$ (for spur and helical gear) = 1.00294
K_{Ha} (for spur and helical gear) = 0.8826

For spur gear – use eq. 11

$$\sigma_H = 1 \times 949.7 \sqrt{1 \times 1.031 \times 1.00294 \times 0.8826} = 907 \text{ N/mm}^2$$

For Helical gears – use eq. 11

$$\sigma_{H\text{helical}} = 1 \times 830.4 \sqrt{1 \times 1.031 \times 1.00294 \times 0.8826} = 793.3 \text{ N/mm}^2$$

Using interpolation σ_H

$$\sigma_H = \sigma_{\text{spur}} - \varepsilon_\beta (\sigma_{\text{spur}} - \sigma_{H\text{helical}})$$

$$= 907 - 0.485(907 - 793) = \mathbf{851.9 \text{ N/mm}^2}$$

The following formula is used to calculate the permissible contact stress ' σ_{HP} '

$$\sigma_{HP} = \frac{\sigma_{Hlim} Z_{NT} Z_L Z_V Z_R Z_W Z_X}{S_{Hmin}} \dots \dots \dots \text{eq. 19}$$

σ_{Hlim}	Allowable stress number	420 N/mm ²
Z _{NT}	Life factor for contact stress	1.6
Z _L	Lubrication factor	0.92
Z _V	Velocity factor	0.975
Z _R	Roughness factor	0.99
Z _W	Work Hardening factor	1.211
Z _X	Size factor	1
S _{Hmin}	Safety factor	1.1

Therefore from Eq. 19,

$$\sigma_{\text{HP}} = \frac{\sigma_{\text{Hlim}} Z_{\text{NT}} Z_{\text{L}} Z_{\text{V}} Z_{\text{R}} Z_{\text{W}} Z_{\text{X}}}{S_{\text{Hmin}}}$$

$$= 420(1.6)(0.92)(0.975)(1.211)(1.0) / 1.1$$

$$= 657 \text{ N/mm}^2$$

$$\sigma_H / \sigma_{HP} = 852 / 657 = 1.30$$

So according to BS ISO 6336-2 standard, the theoretical life of the selected helical gear for limited pitting is less than 10^6 load cycles. As the operating speed of the testing rig is 1000 rpm, so the time that is required to complete 10^6 load cycles will be:

$$10^6 \text{ (cycles)} / 1000 \text{ (cycles/min)} = 16.6 \text{ hrs}$$

By performing a very gross assumption, as $\sigma_H = 1.30 \sigma_{HP}$, so the start time of the onset of failure or the useful life of the gears will be $16.6/1.30 = \mathbf{12.8 \text{ hours}}$

APPENDIX II

Table App II-1: Particle counts for scuffing test using valve sampling - preliminary experiment

Running number	Test Date	Test Time	particle size in micrometer							
			1	2	5	10	15	25	50	100
1	5/3/2007	16:13	1.14E+08	8.05E+07	2.26E+07	1.28E+06	1.71E+05	1.87E+04	8.67E+02	4.67E+02
2	5/3/2007	16:20	1.07E+08	7.19E+07	2.15E+07	2.82E+06	8.13E+05	2.41E+05	7.42E+04	4.72E+04
3	5/3/2007	16:31	1.10E+08	7.30E+07	2.10E+07	2.49E+06	6.13E+05	1.87E+05	6.79E+04	3.60E+04
4	5/3/2007	17:29	1.17E+08	7.74E+07	2.11E+07	2.14E+06	4.98E+05	1.15E+05	2.60E+04	8.70E+03
5	5/3/2007	17:38	1.09E+08	7.18E+07	2.04E+07	2.44E+06	6.26E+05	1.85E+05	6.92E+04	4.41E+04
6	5/3/2007	18:08	1.09E+08	6.77E+07	1.53E+07	1.30E+06	3.29E+05	1.09E+05	3.92E+04	1.91E+04
7	5/3/2007	18:16	1.10E+08	6.73E+07	1.43E+07	9.55E+05	1.81E+05	4.72E+04	2.01E+04	9.80E+03
8	5/3/2007	18:22	1.15E+08	7.40E+07	1.78E+07	1.39E+06	2.81E+05	7.53E+04	3.61E+04	2.44E+04
9	6/3/2007	14:06	1.07E+08	6.63E+07	1.59E+07	1.64E+06	4.32E+05	1.37E+05	5.80E+04	3.69E+04
10	6/3/2007	14:51	1.06E+08	6.48E+07	1.52E+07	1.47E+06	3.95E+05	1.30E+05	5.31E+04	3.19E+04
11	6/3/2007	15:08	1.04E+08	6.24E+07	1.38E+07	1.30E+06	3.66E+05	1.21E+05	5.07E+04	3.18E+04
12	7/3/2007	11:14	9.99E+07	6.17E+07	1.67E+07	2.12E+06	5.32E+05	1.53E+05	6.35E+04	3.57E+04
13	7/3/2007	11:25	9.98E+07	6.02E+07	1.49E+07	1.65E+06	4.21E+05	1.26E+05	4.95E+04	3.04E+04
14	7/3/2007	11:35	1.03E+08	6.19E+07	1.44E+07	1.43E+06	3.65E+05	1.10E+05	4.45E+04	2.52E+04
15	7/3/2007	11:44	9.96E+07	5.84E+07	1.31E+07	1.31E+06	3.36E+05	1.06E+05	4.62E+04	2.57E+04
16	7/3/2007	12:04	9.65E+07	5.73E+07	1.40E+07	1.50E+06	3.79E+05	1.13E+05	4.70E+04	2.70E+04
17	7/3/2007	12:16	9.55E+07	5.57E+07	1.29E+07	1.34E+06	3.55E+05	1.25E+05	6.28E+04	3.71E+04
18	7/3/2007	12:25	9.15E+07	5.18E+07	1.17E+07	1.23E+06	3.17E+05	9.91E+04	3.92E+04	2.23E+04
19	7/3/2007	12:34	8.89E+07	5.03E+07	1.15E+07	1.20E+06	3.21E+05	1.11E+05	5.35E+04	3.46E+04
20	7/3/2007	12:42	8.99E+07	5.14E+07	1.20E+07	1.28E+06	3.47E+05	1.13E+05	5.04E+04	3.07E+04
21	7/3/2007	13:02	8.70E+07	4.93E+07	1.16E+07	1.26E+06	3.37E+05	1.10E+05	4.99E+04	3.06E+04

Table App II-2: Particle counts for scuffing test using side magnetic sampling - preliminary experiment

Sample test (machine hour)	Test Date	Test Time	particle size in micrometer							
			1	2	5	10	15	25	50	100
1	3/5/2007	16:27	1.50E+06	1.03E+06	4.64E+05	1.13E+05	4.21E+04	1.66E+04	5.55E+03	2.31E+03
2	3/5/2007	16:37	4.47E+06	3.57E+06	2.04E+06	6.76E+05	2.69E+05	9.67E+04	2.32E+04	5.03E+03
3	3/5/2007	17:34	2.87E+06	2.01E+06	8.77E+05	1.81E+05	5.61E+04	2.10E+04	6.80E+03	3.39E+03
4	3/5/2007	17:42	2.88E+06	2.11E+06	9.99E+05	2.22E+05	7.08E+04	2.47E+04	6.78E+03	3.55E+03
5	3/5/2007	18:13	2.82E+06	1.90E+06	7.58E+05	1.32E+05	3.35E+04	9.70E+03	1.72E+03	2.78E+02
6	3/6/2007	10:40	4.09E+06	2.65E+06	1.05E+06	2.27E+05	7.87E+04	2.84E+04	6.14E+03	2.56E+03
7	3/5/2007	18:26	1.98E+06	1.33E+06	5.40E+05	9.97E+04	2.27E+04	8.04E+03	3.83E+03	2.38E+03
8	3/6/2007	14:08	2.06E+06	1.37E+06	5.40E+05	1.02E+05	2.68E+04	1.23E+04	6.71E+03	4.38E+03
9	3/6/2007	14:53	2.70E+06	1.89E+06	8.04E+05	1.71E+05	5.38E+04	2.13E+04	7.58E+03	4.29E+03
10	3/6/2007	15:15	2.27E+06	1.63E+06	7.54E+05	1.74E+05	5.29E+04	2.01E+04	7.57E+03	4.36E+03
11	3/7/2007	11:17	2.74E+06	2.02E+06	9.51E+05	2.17E+05	7.11E+04	2.79E+04	1.04E+04	5.68E+03
12	3/7/2007	11:28	2.76E+06	2.02E+06	9.30E+05	2.08E+05	6.53E+04	2.66E+04	1.10E+04	6.51E+03
13	3/7/2007	11:38	1.71E+06	1.17E+06	5.13E+05	1.19E+05	3.41E+04	1.40E+04	5.42E+03	3.05E+03
14	3/7/2007	11:47	2.77E+06	1.96E+06	8.60E+05	1.78E+05	4.83E+04	1.30E+04	1.21E+03	1.13E+02
15	3/7/2007	12:09	2.19E+06	1.53E+06	6.55E+05	1.45E+05	4.37E+04	1.77E+04	7.66E+03	4.11E+03
16	3/7/2007	12:20	2.82E+06	2.06E+06	9.62E+05	2.20E+05	6.71E+04	2.63E+04	9.94E+03	5.58E+03
17	3/7/2007	12:29	2.46E+06	1.76E+06	7.98E+05	1.81E+05	5.36E+04	2.05E+04	8.38E+03	4.71E+03
18	3/7/2007	12:38	1.67E+06	1.18E+06	5.48E+05	1.39E+05	4.17E+04	1.80E+04	8.15E+03	4.89E+03
19	3/7/2007	12:46	2.29E+06	1.59E+06	6.97E+05	1.57E+05	4.72E+04	1.93E+04	7.56E+03	4.09E+03
20	3/7/2007	13:05	2.49E+06	1.83E+06	8.84E+05	2.12E+05	6.00E+04	2.12E+04	7.71E+03	4.08E+03
21	3/7/2007	13:13	2.27E+06	1.63E+06	7.55E+05	1.74E+05	5.33E+04	2.19E+04	7.38E+03	2.38E+03

Table App II-3: Particle counts for scuffing test using base magnetic sampling - preliminary experiment

Running number	Test Date	Test		particle size in micrometer						
		Time	1	2	5	10	15	25	50	100
1	3/5/2007	16:22	1.31E+06	8.64E+05	3.51E+05	7.25E+04	2.35E+04	8.45E+03	2.40E+03	9.68E+02
2	3/5/2007	16:39	7.42E+06	6.04E+06	3.41E+06	1.00E+06	2.95E+05	8.12E+04	2.39E+04	7.24E+03
3	3/5/2007	17:36	2.89E+06	2.08E+06	9.53E+05	2.26E+05	8.55E+04	3.60E+04	1.08E+04	5.14E+03
4	3/5/2007	17:41	3.36E+06	2.58E+06	1.35E+06	3.67E+05	1.39E+05	5.50E+04	1.38E+04	6.00E+03
5	3/5/2007	18:11	2.72E+06	1.94E+06	8.83E+05	2.02E+05	6.82E+04	2.57E+04	6.48E+03	2.49E+03
6	3/5/2007	18:20	2.43E+06	1.68E+06	7.01E+05	1.31E+05	3.44E+04	1.41E+04	6.18E+03	3.33E+03
7	3/5/2007	18:24	1.21E+06	8.23E+05	3.59E+05	7.48E+04	1.56E+04	5.60E+03	2.57E+03	1.29E+03
8	3/6/2007	14:04	2.11E+06	1.44E+06	6.25E+05	1.41E+05	4.64E+04	2.07E+04	7.94E+03	4.53E+03
9	3/6/2007	14:56	2.58E+06	1.83E+06	8.34E+05	1.96E+05	6.71E+04	2.95E+04	1.17E+04	6.88E+03
10	3/6/2007	15:06	3.24E+06	1.83E+06	8.38E+05	2.04E+05	7.23E+04	3.22E+04	1.38E+04	7.76E+03
11	3/7/2007	11:20	2.80E+06	2.10E+06	1.04E+06	2.48E+05	8.01E+04	3.10E+04	1.16E+04	5.98E+03
12	3/7/2007	11:30	2.90E+06	2.07E+06	9.27E+05	2.09E+05	6.75E+04	2.52E+04	7.25E+03	3.44E+03
13	3/7/2007	11:40	1.74E+06	1.21E+06	5.44E+05	1.31E+05	4.01E+04	1.53E+04	4.97E+03	1.91E+03
14	3/7/2007	11:57	2.89E+06	2.06E+06	9.24E+05	2.10E+05	6.87E+04	2.58E+04	7.42E+03	3.26E+03
15	3/7/2007	12:12	1.88E+06	1.38E+06	6.69E+05	1.66E+05	5.41E+04	2.39E+04	1.03E+04	5.93E+03
16	3/7/2007	12:21	2.37E+06	1.68E+06	7.55E+05	1.80E+05	5.78E+04	2.27E+04	7.29E+03	3.14E+03
17	3/7/2007	12:31	2.65E+06	1.92E+06	8.89E+05	2.06E+05	6.20E+04	2.18E+04	6.60E+03	2.83E+03
18	3/7/2007	12:39	1.58E+06	1.08E+06	4.91E+05	1.20E+05	3.18E+04	1.29E+04	5.62E+03	2.77E+03
19	3/7/2007	12:49	2.53E+06	1.74E+06	7.65E+05	1.83E+05	5.93E+04	2.26E+04	5.07E+03	1.43E+03
20	3/7/2007	13:09	2.33E+06	1.61E+06	6.86E+05	1.46E+05	4.05E+04	1.70E+04	7.63E+03	4.44E+03
21	3/7/2007	13:15	2.43E+06	1.77E+06	8.45E+05	2.12E+05	7.57E+04	3.41E+04	1.41E+04	7.58E+03

Table App II-4: Particle counts for pitting test using valve sampling - preliminary experiment

Size /hr	1	2	3	4	5	6	7	8	9	10	11	12
1u	1.17E+08	1.03E+08	1.26E+08	1.19E+08	8.92E+07	1.26E+08	1.38E+08	1.23E+08	1.21E+08	1.19E+08	1.32E+08	1.12E+08
2u	7.83E+07	6.34E+07	8.88E+07	9.62E+07	7.09E+07	8.59E+07	1.05E+08	7.86E+07	7.61E+07	7.28E+07	9.43E+07	6.67E+07
5u	2.19E+07	1.56E+07	2.33E+07	3.44E+07	2.38E+07	2.00E+07	3.08E+07	1.56E+07	1.45E+07	1.34E+07	2.20E+07	1.29E+07
10u	2.53E+06	1.65E+06	1.44E+06	1.59E+06	1.17E+06	1.22E+06	1.43E+06	9.88E+05	8.84E+05	8.34E+05	9.50E+05	1.06E+06
15u	6.08E+05	4.23E+05	3.03E+05	2.92E+05	2.77E+05	2.31E+05	2.28E+05	2.12E+05	1.76E+05	1.80E+05	1.49E+05	2.47E+05
25u	1.14E+05	8.99E+04	6.00E+04	9.44E+04	1.43E+05	4.51E+04	2.57E+04	6.11E+04	4.88E+04	5.30E+04	1.70E+04	7.29E+04
50u	1.09E+04	2.77E+03	2.00E+03	5.71E+04	1.00E+05	6.07E+03	7.33E+02	2.82E+04	2.62E+04	2.63E+04	5.33E+02	3.36E+04
100u	2.87E+03	4.00E+02	9.33E+02	3.15E+04	5.58E+04	3.80E+03	1.00E+02	1.85E+04	1.69E+04	1.70E+04	1.00E+02	2.40E+04
size /hr	13	14	15	16	17	18	19	20	21	22	23	24
1u	1.19E+08	9.51E+07	5.27E+07	5.85E+07	4.12E+07	6.37E+07	7.17E+07	6.63E+07	7.23E+07	6.62E+07	7.21E+07	6.95E+07
2u	7.62E+07	4.92E+07	1.57E+07	1.94E+07	1.61E+07	2.08E+07	2.72E+07	2.34E+07	2.84E+07	2.23E+07	2.76E+07	2.60E+07
5u	1.63E+07	8.23E+06	1.31E+06	1.96E+06	2.66E+06	1.50E+06	2.50E+06	1.92E+06	2.89E+06	1.58E+06	2.45E+06	2.46E+06
10u	1.34E+06	8.89E+05	1.07E+05	2.56E+05	4.95E+05	1.10E+05	1.35E+05	9.87E+04	2.05E+05	1.19E+05	1.47E+05	1.74E+05
15u	2.82E+05	2.49E+05	4.41E+04	9.27E+04	2.37E+05	4.76E+04	4.70E+04	4.32E+04	8.51E+04	6.80E+04	7.49E+04	6.84E+04
25u	4.27E+04	7.41E+04	2.78E+04	3.80E+04	1.49E+05	2.72E+04	2.84E+04	3.33E+04	6.01E+04	5.09E+04	5.79E+04	3.91E+04
50u	1.83E+03	2.66E+04	1.69E+04	2.04E+04	9.47E+04	1.73E+04	1.48E+04	2.52E+04	4.15E+04	3.61E+04	4.47E+04	2.21E+04
100u	2.00E+01	1.51E+04	1.06E+04	1.22E+04	5.92E+04	1.14E+04	8.33E+03	1.73E+04	2.89E+04	2.52E+04	3.17E+04	1.20E+04

Table App II-5: Particle counts for pitting test using base magnetic sampling - preliminary experiment

size / hour	1	2	3	4	5	6	7	8	9	10	11	12
1u	6.50E+07	9.91E+07	4.32E+07	4.73E+07	5.49E+07	1.19E+08	4.95E+07	5.36E+07	5.77E+07	3.64E+07	3.76E+07	1.07E+08
2u	4.83E+07	7.40E+07	2.77E+07	2.91E+07	3.33E+07	9.40E+07	3.17E+07	3.43E+07	3.68E+07	2.22E+07	2.33E+07	7.65E+07
5u	2.30E+07	2.78E+07	9.43E+06	8.80E+06	1.06E+07	3.86E+07	1.04E+07	1.10E+07	1.15E+07	6.73E+06	7.37E+06	2.57E+07
10u	5.81E+06	2.66E+06	1.21E+06	9.42E+05	1.71E+06	3.55E+06	1.41E+06	1.42E+06	1.42E+06	9.01E+05	9.04E+05	2.73E+06
15u	2.22E+06	4.92E+05	2.58E+05	1.93E+05	6.22E+05	6.76E+05	4.17E+05	4.18E+05	4.20E+05	2.99E+05	2.13E+05	7.64E+05
25u	6.76E+05	6.13E+04	3.98E+04	2.77E+04	2.61E+05	1.06E+05	1.46E+05	1.50E+05	1.54E+05	1.25E+05	3.61E+04	2.52E+05
50u	6.18E+04	1.10E+03	8.33E+02	6.00E+02	8.35E+04	2.77E+03	5.82E+04	6.38E+04	6.94E+04	6.13E+04	7.33E+02	8.00E+04
100u	3.53E+04	1.00E+02	3.67E+02	1.00E+02	3.21E+04	4.66E+02	3.50E+04	3.87E+04	4.24E+04	3.63E+04	2.00E+02	4.33E+04
size / hour	13	14	15	16	17	18	19	20	21	22	23	24
1u	4.06E+07	3.97E+07	1.37E+07	1.62E+07	1.38E+07	1.10E+07	3.09E+07	2.53E+07	1.75E+07	2.07E+07	2.91E+07	2.51E+07
2u	2.63E+07	2.05E+07	7.61E+06	8.53E+06	7.13E+06	5.60E+06	1.59E+07	1.51E+07	9.42E+06	1.13E+07	1.81E+07	1.63E+07
5u	9.18E+06	5.62E+06	2.42E+06	2.18E+06	2.08E+06	1.46E+06	4.48E+06	4.86E+06	2.51E+06	3.07E+06	6.29E+06	6.28E+06
10u	1.58E+06	9.87E+05	6.85E+05	3.96E+05	4.76E+05	3.23E+05	7.70E+05	9.42E+05	4.45E+05	4.98E+05	1.27E+06	1.29E+06
15u	5.81E+05	3.56E+05	4.04E+05	1.98E+05	2.65E+05	1.94E+05	2.55E+05	4.18E+05	2.25E+05	2.09E+05	5.43E+05	4.88E+05
25u	2.31E+05	1.11E+05	2.60E+05	1.19E+05	1.68E+05	1.37E+05	6.70E+04	2.15E+05	1.46E+05	1.10E+05	2.51E+05	1.77E+05
50u	9.21E+04	8.77E+03	1.37E+05	6.10E+04	9.09E+04	9.87E+04	2.40E+03	8.91E+04	8.47E+04	4.61E+04	9.42E+04	3.23E+04
100u	5.72E+04	9.67E+02	8.07E+04	3.67E+04	5.46E+04	6.87E+04	2.00E+02	4.88E+04	5.35E+04	2.61E+04	5.03E+04	8.23E+03

Table App II- 6: Particle counts for pitting test using side magnetic sampling - preliminary experiment

Size /hr	1	2	3	4	5	6	7	8	9	10	11	12
1u	6.77E+07	1.09E+08	4.25E+07	4.49E+07	4.17E+07	1.20E+08	8.32E+07	4.63E+07	5.35E+07	3.86E+07	4.01E+07	1.20E+08
2u	5.07E+07	8.51E+07	2.75E+07	2.80E+07	2.70E+07	1.00E+08	6.47E+07	2.93E+07	3.44E+07	2.40E+07	2.44E+07	9.79E+07
5u	2.41E+07	3.43E+07	9.40E+06	8.67E+06	9.25E+06	4.91E+07	2.93E+07	9.39E+06	1.09E+07	7.59E+06	7.34E+06	4.58E+07
10u	5.90E+06	2.94E+06	1.16E+06	1.19E+06	1.18E+06	5.68E+06	3.47E+06	1.25E+06	1.25E+06	1.05E+06	9.35E+05	5.31E+06
15u	2.16E+06	4.56E+05	2.55E+05	4.00E+05	2.59E+05	9.82E+05	6.71E+05	3.61E+05	3.45E+05	3.52E+05	2.81E+05	1.08E+06
25u	6.25E+05	5.13E+04	3.78E+04	1.70E+05	3.92E+04	1.33E+05	1.28E+05	1.23E+05	1.23E+05	1.60E+05	1.09E+05	2.07E+05
50u	4.73E+04	6.66E+02	8.33E+02	7.63E+04	1.40E+03	2.40E+03	2.77E+04	5.30E+04	5.38E+04	8.36E+04	5.76E+04	1.06E+04
100u	3.07E+03	1.00E+00	1.00E+00	4.15E+04	3.66E+02	1.00E+02	1.75E+04	3.49E+04	2.98E+04	5.36E+04	3.93E+04	7.33E+02
Size /hr	13	14	15	16	17	18	19	20	21	22	23	24
1u	4.40E+07	1.34E+07	1.64E+07	1.19E+07	1.62E+07	9.23E+06	1.79E+07	2.31E+07	1.36E+07	2.46E+07	2.21E+07	2.81E+07
2u	2.60E+07	7.36E+06	8.80E+06	6.42E+06	8.42E+06	4.97E+06	1.02E+07	1.31E+07	7.07E+06	1.47E+07	1.26E+07	1.71E+07
5u	8.06E+06	2.08E+06	2.22E+06	1.86E+06	2.16E+06	1.33E+06	3.17E+06	3.92E+06	1.64E+06	4.99E+06	3.79E+06	5.73E+06
10u	1.21E+06	4.35E+05	3.60E+05	4.29E+05	4.22E+05	2.24E+05	6.77E+05	7.33E+05	2.04E+05	9.62E+05	7.27E+05	1.13E+06
15u	3.46E+05	2.26E+05	1.77E+05	2.47E+05	2.30E+05	1.04E+05	3.40E+05	3.36E+05	9.16E+04	3.51E+05	3.31E+05	4.91E+05
25u	7.25E+04	1.39E+05	1.07E+05	1.75E+05	1.51E+05	6.13E+04	2.03E+05	1.87E+05	6.23E+04	1.25E+05	1.66E+05	2.32E+05
50u	2.30E+03	7.87E+04	5.47E+04	1.19E+05	9.21E+04	3.61E+04	1.10E+05	9.36E+04	3.59E+04	3.78E+04	5.78E+04	7.37E+04
100u	5.00E+02	4.82E+04	3.14E+04	7.96E+04	6.14E+04	2.35E+04	7.14E+04	5.64E+04	2.10E+04	2.13E+04	2.43E+04	3.46E+04

Appendix III

Simple MATLAB program for capturing images and establishing coordinates [83]

Input	Particles' Image captured by digital camera
Action	Tracing boundary, filter images, establish coordinates
Output	Image with clear boundaries and coordinates

```
% Read the image saved in the file in Jpeg form.
figure;
[fn, path]=uigetfile('*jpg','sasaa');

%Convert the image to black and white in order to prepare for
boundary
%tracing using bwboundaries
I=imread([path fn]);
BW = im2bw(I, graythresh(I));

% remove all objects containing fewer than 30 pixels
BW = bwareaopen(BW,30);

% Fill any gaps
se = strel('disk',5);
BW = imclose(BW,se);

% fill any holes, so that region props can be used to estimate
% the area enclosed by each of the boundaries
BW = imfill (BW,'holes');
imshow (BW)

% Find the boundaries
%Calculate the area, roundness and perimeter and plot original
coordinates
stats = regionprops(L,'Area','Centroid');
for k = 2:length(B)
boundary = B{k};
hold on
plot(boundary(:,2), boundary(:,1), 'b', 'LineWidth', 2)

area = stats(k).Area;
delta_sq = diff(boundary).^2;
perimeter = sum(sqrt(sum(delta_sq,2)));
metric = 4*pi*area/perimeter^2;
metric_string = sprintf('%2.2f %2.2f % 2.2f',area,
perimeter,metric);
text(boundary(1,2)-
70,boundary(1,1)+165,metric_string,'Color','b',...
'FontSize',10,'FontWeight','bold');
xlabel ('AREA PERIMETER ROUNDNESS');
```

%To move image to center of axis and plot

```
m=max(boundary(:,2));
m2=min(boundary(:,2));
widthhave =0.5*(m-m2);
p=boundary(:,2)-widthhave-m2;
plot (p,boundary(:,1), 'b', 'LineWidth', 2)
axis auto
end
hold off;
```

Appendix IV

Simple MATLAB program for reconstructing 3D images by connecting the lines of four edges of two cross images [83]

Input	Two 2D images with clear boundaries and established coordinates
Action	Crossing the two images at a common single axis in the middle of the images and connect the points at four sides at same altitude of z coordinates
Output	A three dimensional images of wear debris particles

```
% Plotting two images on one single axis - Coordinates/data already established

plot3(x,y,z,'red','Linewidth',1)
hold on
plot3(x1,y1,z1,'red','Linewidth',1)
hold on

zmin=min(z1);
zmax=max(z1);

% Loop for Z axis for both images

for k=zmin:zmax

%Loop for first images

l1=1;j=1;
for s=1:zmax
if (z(s)==k)
xcombine1(l1)=x(s);
ycombine1(l1)=y(s);
l1=l1+1;
end

end

x1com_max=max(xcombine1);
x1com_min=min(xcombine1);

y1com_max=max(ycombine1);
y1com_min=min(ycombine1);

% Loop for second image
l1=1;j=1;
for s=1:zmax
```

```

if (z1(s)==k)
    xcombine2(l1)=x1(s);
    ycombine2(l1)=y1(s);
    l1=l1+1;
end
end

%Loop for joining the four edges
x2com_max=max(xcombine2);
x2com_min=min(xcombine2);

y2com_max=max(ycombine2);
y2com_min=min(ycombine2);

xcombine(1)=xcombine1(1);
xcombine(2)=xcombine2(1);
xcombine(3)=xcombine1(2);
xcombine(4)=xcombine2(2);
xcombine(5)=xcombine1(1);

ycombine(1)=ycombine1(1);
ycombine(2)=ycombine2(1);
ycombine(3)=ycombine1(2);
ycombine(4)=ycombine2(2);
ycombine(5)=ycombine1(1);

zcombine(1)=k;
zcombine(2)=k;
zcombine(3)=k;
zcombine(4)=k;
zcombine(5)=k;

plot3(xcombine,ycombine,zcombine,'red','Linewidth',1)

hold on
end

```

Appendix V

MATLAB program for reconstructing 3D images and shape analysis [83].

Input	Two 2D images with clear boundaries and established coordinates
Action	Crossing the two images at a common single axis in the middle of the images and connect the points at four sides at same altitude of z coordinates. Calculate quantitative and qualitative value of images of particle
Output	A pseudo three dimensional image of a wear debris particle together with its size, area, volume, aspect ratio, roundness factor, curvature analysis of standard deviation, kurtosis and skewness.

Step 1: Read Image

```
[fn, path]=uigetfile('*.jpg','*.bmp','jem');
RGB1=imread([path fn]);
[fn, path]=uigetfile('*.jpg','*.bmp','jem');
RGB2=imread([path fn]);
```

Step 2: Convert to Gray image Use rgb2gray function in MATLAB

```
I1=rgb2gray(RGB1);
I2=rgb2gray(RGB2);
```

Step 3: Use Edge detection function 'edge' and imdilate function to detect edge of the image

```
[junk threshold] = edge(I1, 'sobel');
[junk threshold] = edge(I2, 'sobel');
fudgeFactor1 = 0.3;
fudgeFactor2 = 0.5;

BW1s = edge(I1,'sobel', threshold * fudgeFactor1);
BW2s = edge(I2,'sobel', threshold * fudgeFactor2);

se90 = strel('line', 3, 90);
se0 = strel('line', 3, 0);

BWsdill1 = imdilate(BW1s, [se90 se0]);
BWsdil2 = imdilate(BW2s, [se90 se0]);
```

Step 4: Filled the hole in the area using imfill function in the MATLAB

```
BW1dfill1 = imfill(BWsdl1, 'holes');
BW1dfill2 = imfill(BWsdl2, 'holes');

BWdfill1 = bwareaopen(BW1dfill1,30);
BWdfill2 = bwareaopen(BW1dfill2,30);
```

Step 5: Remove any small insignificant area using bwareaopen and clear the border using imclearborder function to smoothen the edges.

```
BWnobord1 = imclearborder(BWdfill1 ,1);
BWnobord2 = imclearborder(BWdfill2 ,1);

seD = strel('diamond',1);
```

Step 6: Erode the image using the imerode function

```
BWfinal1 = imerode(BWnobord1,seD);
BWfinal2 = imerode(BWnobord2,seD);

BWfinal1 = imerode(BWfinal1,seD);
BWfinal2 = imerode(BWfinal2,seD);
```

Step 7: Use bwperim function to get the perimeter of the white area and

```
BWoutline1=bwperim(BWfinal1);
BWoutline2=bwperim(BWfinal2);
```

Step 8: then bring back the original RGB image to compare the outline with the original image

```
Segout1 = RGB1;
Segout2 = RGB2;
```

Step 9: Then use the outline only for the boundary tracing result which will be used in the 3D construction

```
Segout1(BWoutline1) = 255;
Segout2(BWoutline2) = 255;
```

Step 10: Determine the area inside boundary

```
Area1=bwarea(BWfinal1);  
Area2=bwarea(BWfinal2);
```

Step 11: Establish coordinates of both images

```
[B3,L3] = bwboundaries(BWoutline1,'noholes');  
[B4,L4] = bwboundaries(BWoutline2,'noholes');
```

```
for k=1:length(B3)  
    boundary = B3{k};  
  
end  
  
for k=1:length(B4)  
    boundary1 = B4{k};  
  
end  
  
for l=min(boundary1(:,2)): max(boundary1(:,2))  
    for a=1:length(boundary1)  
  
        if boundary1(a,2)==l  
            ll =boundary1(a,1);  
            [l,ll];  
        end  
    end  
end  
  
for l=min(boundary(:,2)): max(boundary(:,2))  
    for b=1:length(boundary)  
  
        if boundary1(b,2)==l  
            ll =boundary1(b,1);  
            [l,ll];  
        end  
    end  
end
```

Step 12: Calculating std deviation, kurtosis & skewness & Aspect Ratio & Roundness factor

```
xbar=mean(boundary(:,2));
```

```

xbar2=mean(boundary1(:,2));
N=length(boundary);
N2=length(boundary1);
x1=0;
x2=0;
x3=0;

for j=1:length(boundary)

    x(j)=boundary(j,2);

    Rq1a(j) = (((x(j)-xbar)^2));
    x1=x1+Rq1a(j);

    Rsk1a(j) = (((x(j)-xbar)^3));
    x2=x2+Rsk1a(j);

    Rkula(j) = (((x(j)-xbar)^4));
    x3= x3+Rkula(j);
end

Rq1=sqrt(x1/(N-1));

Rsk1=x2/(N*(Rq1^3));

Rkul=x3/(N*(Rq1^4));

y1=0;
y2=0;
y3=0;

for j=1:length(boundary1)

    y(j)=boundary1(j,2);

    Rq1a(j) = (((y(j)-xbar)^2));
    y1=y1+Rq1a(j);

    Rsk1a(j) = (((y(j)-xbar)^3));
    y2=y2+Rsk1a(j);

    Rkula(j) = (((y(j)-xbar)^4));
    y3= y3+Rkula(j);
end

Rq2=sqrt(y1/(N2 -1));

```

```

Rsk2=y2/ (N2*(Rq2^3)) ;

Rku2=y3/ (N2*(Rq2^4)) ;

Determine the middle axis of the images. (tt for image 1,
gg for image 2)

tt=(max(boundary(:,2)-min(boundary(:,2)))*0.5)+
min(boundary(:,2));
gg=(max(boundary1(:,2)-min(boundary1(:,2)))*0.5)+
min(boundary1(:,2));

Determine the sizes of the particles [ferret length]

Ymin1=min(boundary(:,1));
Ymax1=max(boundary(:,1));
Xmin1=min(boundary(:,2));
Xmax1=max(boundary(:,2));

Ymin2=min(boundary1(:,1));
Ymax2=max(boundary1(:,1));
Xmin2=min(boundary1(:,2));
Xmax2=max(boundary1(:,2));

size1=Ymax1-Ymin1;
size2=Xmax1-Xmin1;
size3=Ymax2-Ymin2;
size4=Xmax2-Xmin2;

if size1>size2
    size12=size1;
    size22=size2
else
    size12=size2;
    size22=size1
end

if size3 > size4
    size34=size3;
    size44=size4
else
    size34=size4;
    size44=size3
end

```

```

if size12 > size34
    size=size12;
else
    size=size34;
end

Determine the aspect ratio of both images of a particle

AR1=size12/size22;

AR2=size34/size44;

Determine the roundness factor of both images of a particle

RF1= (length(boundary))^2/(4*pi*Area1);
RF2= (length(boundary1))^2/(4*pi*Area2);

Determine the thickness of particle

Thickness=(Area1/(Ymax1-Ymin1));
Thickness;

Determine the volume of particle

Volume=Area2*Thickness;
Volume;

```

Step 13: construction of 3D image

```

subplot (2,2,1),imshow(Segout1),title ('Outline original
image');

metric_string = sprintf('Area1 = %2.2f um2',Area1);
text(-25,2,metric_string,'Color','black','FontSize',
12,'FontWeight','bold');

metric_string = sprintf('AR1 = %2.2f ',AR1);
text(-25,6,metric_string,'Color','black','FontSize',
12 , 'FontWeight','bold');

metric_string = sprintf('RF1 = %2.2f ',RF1);
text(-25,10,metric_string,'Color','black','FontSize',
12 , 'FontWeight','bold');

metric_string = sprintf('Rq1 = %2.2f ',Rq1);

```

```

text(-25,14,metric_string,'Color','black','FontSize',
12,'FontWeight','bold');

metric_string = sprintf('Rsk1 = % 2.2f ',Rsk1);
text(-25,18,metric_string,'Color','black','FontSize',
12,'FontWeight','bold');

metric_string = sprintf('Rkul = % 2.2f ',Rkul);
text(-25,22,metric_string,'Color','black','FontSize',
12,'FontWeight','bold');

if AR1 >= 1.1 && AR1 <=1.2

metric_string = sprintf(' AR1 - rubbing ');
text(- 25,24,metric_string,'Color','black','FontSize',
12,'FontWeight','bold');
hold on

elseif AR1 >= 1.5 && AR1<=4.0

metric_string = sprintf('AR1 - sliding ');
text(-25,24,metric_string,'Color','black','FontSize',
12,'FontWeight','bold');
hold on

elseif AR1 >= 1.5 && AR1 <=2.0

metric_string = sprintf(' AR1 - pitting fatigue ');
text(-25,24,metric_string,'Color','black','FontSize',
12,'FontWeight','bold');
hold on

elseif AR1 >= 3.3 && AR1 <=12.5
metric_string = sprintf(' AR1 - cutting ');
text(-25,24,metric_string,'Color','black','FontSize',
12,'FontWeight','bold');
end

if RF1>=1.5 && RF1<=1.6
metric_string = sprintf(' RF1 - rubbing ');
text(-25,26,metric_string,'Color','black','FontSize',
12,'FontWeight','bold');
hold on

elseif RF1>=2.2 && RF1<=3.6
metric_string = sprintf('RF1 - sliding ');
text(-25,26,metric_string,'Color','black','FontSize',

```

```

12,'FontWeight','bold');
hold on

elseif RF1>=2.6 && RF1<=2.9
metric_string = sprintf(' RF1 - pittig fatigue ');
text(-25,26,metric_string,'Color','black','FontSize',
12,'FontWeight','bold');
hold on

elseif RF1>=6.9 && RF1<=17.0
metric_string = sprintf(' RF1 - cutting ');
text(-25,26,metric_string,'Color','black','FontSize',
12,'FontWeight','bold');

hold on
end

if Rku1>= 4.0 && Rku1<=5.0
metric_string = sprintf(' Rku1 - rubbing ');
text(-25,28,metric_string,'Color','black','FontSize',
12,'FontWeight','bold');
hold on

elseif Rku1>= 4.2 && Rku1<=5.7
metric_string = sprintf('Rku1 - sliding ');
text(-25,28,metric_string,'Color','black','FontSize',
12,'FontWeight','bold');
hold on

elseif Rku1>= 3.4 && Rku1<=4.5
metric_string = sprintf(' Rku1 - pittig fatigue ');
text(-25,28,metric_string,'Color','black','FontSize',
12,'FontWeight','bold');
hold on

elseif Rku1>= 5.9 && Rku1<=6.8
metric_string = sprintf(' Rku1 - cutting ');
text(-25,28,metric_string,'Color','black','FontSize',
12,'FontWeight','bold');

hold on
end

if Rq1>=22 && Rq1<= 24
metric_string = sprintf(' Rq1 - rubbing ');
text(-25,30,metric_string,'Color','black','FontSize',
12,'FontWeight','bold');
hold on

```

```

elseif Rq1>=27 && Rq1<= 32
metric_string = sprintf(' Rq1 - sliding ');
text(-25,30,metric_string,'Color','black','FontSize',
12,'FontWeight','bold');
hold on

elseif Rq1>=40 && Rq1<= 43
metric_string = sprintf(' Rq1 - pitting fatigue ');
text(-25,30,metric_string,'Color','black','FontSize',
12,'FontWeight','bold');
hold on

elseif Rq1>=30 && Rq1<= 35
metric_string = sprintf(' Rq1 - cutting ');
text(-25,30,metric_string,'Color','black','FontSize',
12,'FontWeight','bold');
hold on
end

if Rsk1>=0.00 && Rsk1<=0.6
metric_string = sprintf(' Rsk1 - rubbing ');
text(-25,30,metric_string,'Color','black','FontSize',
12,'FontWeight','bold');
hold on

elseif Rsk1>=0.5 && Rsk1<=1.5
metric_string = sprintf(' Rsk1 - sliding ');
text(-25,30,metric_string,'Color','black','FontSize',
12,'FontWeight','bold');
hold on

elseif Rsk1>=-0.4 && Rsk1<=-0.9
metric_string = sprintf(' Rsk1 - pitting fatigue ');
text(-25,30,metric_string,'Color','black','FontSize',
12,'FontWeight','bold');

elseif Rsk1>=0.7 && Rsk1<=2.5
metric_string = sprintf(' Rsk1 - cutting ');
text(-25,30,metric_string,'Color','black','FontSize',
12,'FontWeight','bold');
hold on
end

subplot (2,2,3),imshow(Segout2),title ('Outline original
image');

```

```

metric_string = sprintf('Area2 = %2.2f um2',Area2);
text(- 25,2,metric_string,'Color','black','FontSize',
12,'FontWeight','bold');

metric_string = sprintf('AR2 = %2.2f ',AR2);
text(-25,6,metric_string,'Color','black','FontSize',
12,'FontWeight','bold');

metric_string = sprintf('RF2 = %2.2f ',RF2);
text(-25,10,metric_string,'Color','black','FontSize',
12,'FontWeight','bold');

metric_string = sprintf('Rq2 = %2.2f ',Rq2);
text(-25,14,metric_string,'Color','black','FontSize',
12,'FontWeight','bold');

metric_string = sprintf('Rsk2 = % 2.2f ',Rsk2);
text(-25,18,metric_string,'Color','black','FontSize',
12,'FontWeight','bold');

metric_string = sprintf('Rku2 = % 2.2f ',Rku2);
text(-25,22,metric_string,'Color','black','FontSize',
12,'FontWeight','bold');

if AR2 >= 1.1 && AR2 <=1.2
metric_string = sprintf(' AR2 - rubbing ');
text(-25,24,metric_string,'Color','black','FontSize',
12,'FontWeight','bold');
hold on

elseif AR2 >= 1.5 && AR2<=4.0
metric_string = sprintf('AR2 - sliding ');
text(-25,24,metric_string,'Color','black','FontSize',
12,'FontWeight','bold');
hold on

elseif AR2 >= 1.5 && AR2 <=2.0
metric_string = sprintf(' AR2 - pittig fatigue ');
text(-25,24,metric_string,'Color','black','FontSize',
12,'FontWeight','bold');
hold on

elseif AR2>= 3.3 && AR2 <=12.5
metric_string = sprintf(' AR2 - cutting ');
text(-25,24,metric_string,'Color','black','FontSize',
12,'FontWeight','bold');
hold on

```

```

end

if RF2>=1.5 && RF2<=1.6
metric_string = sprintf(' RF2 - rubbing ');
text(-25,26,metric_string,'Color','black','FontSize',
12,'FontWeight','bold');
hold on

elseif RF2>=2.2 && RF2<=3.6
metric_string = sprintf('RF2 - sliding ');
text(-25,26,metric_string,'Color','black','FontSize',
12,'FontWeight','bold');
hold on

elseif RF2>=2.6 && RF2<=2.9
metric_string = sprintf(' RF2 - pittig fatigue ');
text(-25,26,metric_string,'Color','black','FontSize',
12,'FontWeight','bold');

elseif RF2>=6.9 && RF2<=17.0
metric_string = sprintf(' RF2 - cutting ');
text(-25,26,metric_string,'Color','black','FontSize',
12,'FontWeight','bold');
hold on
end

if Rku2>= 4.0 && Rku2<=5.0
metric_string = sprintf(' Rku2 - rubbing ');
text(-25,28,metric_string,'Color','black','FontSize',
12,'FontWeight','bold');
hold on

elseif Rku2>= 4.2 && Rku2<=5.7
metric_string = sprintf('Rku2 - sliding ');
text(-25,28,metric_string,'Color','black','FontSize',
12,'FontWeight','bold');
hold on

elseif Rku2>= 3.4 && Rku2<=4.5
metric_string = sprintf(' Rku2 - pittig fatigue ');
text(-25,28,metric_string,'Color','black','FontSize',
12,'FontWeight','bold');
hold on

elseif Rku2>= 5.9 && Rku2<=6.8
metric_string = sprintf(' Rku2 - cutting ');
text(-25,28,metric_string,'Color','black','FontSize',
12,'FontWeight','bold');

```

```

hold on
end

if Rq2>=22 && Rq2<= 24
metric_string = sprintf(' Rq2 - rubbing ');
text(-25,30,metric_string,'Color','black','FontSize',
12,'FontWeight','bold');
hold on

elseif Rq2>=27 && Rq2<= 32
metric_string = sprintf(' Rq2 - sliding ');
text(-25,30,metric_string,'Color','black','FontSize',
12,'FontWeight','bold');
hold on

elseif Rq2>=40 && Rq2<= 43
metric_string = sprintf(' Rq2 - pitting fatigue ');
text(-25,30,metric_string,'Color','black','FontSize',
12,'FontWeight','bold');
hold on

elseif Rq2>=30 && Rq2<= 35
metric_string = sprintf(' Rq2 - cutting ');
text(-25,30,metric_string,'Color','black','FontSize',
12,'FontWeight','bold');
hold on
end

if Rsk2>=0.00 && Rsk2<=0.6
metric_string = sprintf(' Rsk2 - rubbing ');
text(-25,32,metric_string,'Color','black','FontSize',
12,'FontWeight','bold');
hold on

elseif Rsk2>=0.5 && Rsk2<=1.5
metric_string = sprintf(' Rsk2 - sliding ');
text(-25,32,metric_string,'Color','black','FontSize',
12,'FontWeight','bold');
hold on

elseif Rsk2>=-0.4 && Rsk2<=-0.9
metric_string = sprintf(' Rsk2 - pitting fatigue ');
text(-25,32,metric_string,'Color','black','FontSize',
12,'FontWeight','bold');

```

```

elseif Rsk2>=0.7 && Rsk2<=2.5
metric_string = sprintf(' Rsk2 - cutting ');
text(-25,32,metric_string,'Color','black','FontSize',
12,'FontWeight','bold');
hold on
end

Step 14: Constructing 3D

for kkk=min(boundary(:,1)):1:(max(boundary(:,1)))
    for a=1:length(boundary1)
        for b=1:length(boundary)
            if boundary1(a,1)== kkk && boundary(b,1)== kkk
%*****
y3(a)=boundary1(a,2);
z3(a)=boundary1(a,1);
x3(a)=tt;

%*****
y4(a)=boundary1(a,2);
z4(a)=boundary1(a,1);
x4(b)=boundary(b,2);

%*****
y5(a)=gg;
z5(a)=boundary1(a,1);
x5(b)=boundary1(b,2);

%*****
subplot(2,2,2),plot3
(x3(a),y3(a),z3(a),'red','LineStyle','-','LineWidth',3);
hold on

subplot(2,2,2), plot3
(x4(b),y4(a),z4(a),'black','LineStyle','--',
'LineWidth',3);

hold on

subplot(2,2,2),plot3
(x5(b),y5(a),z5(a),'blue','LineStyle','--',
'LineWidth',3);
hold on

axis('ij');

```

```

axis equal;
axis on

xcombine(1)=x3(a);
xcombine(2)=x4(b);
xcombine(3)=x5(b);
xcombine(4)=x3(a);
xcombine(5)=x4(b);
xcombine(6)=x5(b);
xcombine(7)=x4(b);
xcombine(8)=x3(a);

ycombine(1)=y3(a);
ycombine(2)=y4(a);
ycombine(3)=y5(a);
ycombine(4)=y3(a);
ycombine(5)=y4(a);
ycombine(6)=y5(a);
ycombine(7)=y4(a);
ycombine(8)=y3(a);

zcombine(1)=z3(a);
zcombine(2)=z4(a);
zcombine(3)=z5(a);
zcombine(4)=z3(a);
zcombine(5)=z4(a);
zcombine(6)=z5(a);
zcombine(7)=z4(a);
zcombine(8)=z3(a);

hold on

subplot(2,2,2),plot3(xcombine,ycombine,zcombine,'black
','Linewidth',3);

xlabel ('X');
ylabel('Y');
zlabel('Z');
title ('Pseudo 3D image of wear debris
Particle');

hold on
set(gca,'ZDir','reverse')
end
end
end
end

```

```

axis([-50 50 -50 50 0 50]);
metric_string = sprintf('Volume = %2.2f um^3, Size = %2.2f um',
Volume, size);
text(-120,0,100,metric_string,'Color','red',
'FontSize',12,'FontWeight','bold');

metric_string2 = sprintf('Thickness = % 2.2f um',
Thickness);
text(-120,0,120,metric_string2,'Color','red',
'FontSize',12,'FontWeight','bold');

metric_string2 = sprintf('AR = Aspect ratio ,
RF=roundness factor % 2.2f');
text(-120,0,140,metric_string2,'Color','red',
'FontSize', 12,'FontWeight','bold');

metric_string2 = sprintf('Rq=standard deviation, Rsk =
skewness % 2.2f');
text(-120,0,160,metric_string2,'Color','red',
'FontSize',12,'FontWeight','bold');

metric_string2 = sprintf('Rku=kurtosis % 2.2f');
text(-120,0,180,metric_string2,'Color','red',
'FontSize',12,'FontWeight','bold');

hold off

```

Appendix VI

Table App VI-1: Sample of Command codes sent to peristaltic pump and the associated time of every task.

Command codes	Tasks	Time (secs)	Cumulative time (mins)
1GO	Start pump	15	0.25
1SP003	Set pump run at 3 rpm	15	0.50
1RL	Set counter-clockwise Direction- sample flows into the cell	15	0.75
1RS	Show pump information (no change)	15	1.00
1RS	Show pump information (no change)	15	1.25
1RS	Show pump information (no change)	15	1.50
1RS	Show pump information (no change)	15	1.75
1RS	Show pump information (no change)	15	1.75
1RS	Show pump information (no change)	15	2.00
1RR	Set clockwise direction – sample flow in reverse direction.	15	2.25
-----complete one cycle-----		-----	-----
1RL	Set counter-clockwise direction-sample flow into the cell	15	2.50
1RS	Show pump information (no change)	15	2.75
1RS	Show pump information (no change)	15	3.00
1RS	Show pump information (no change)	15	3.25
1RS	Show pump information (no change)	15	3.50
1RS	Show pump information (no change)	15	3.75
1RS	Show pump information (no change)	15	4.00
1RR	Set clockwise Direction – sample flow in reverse direction	15	4.25
-----complete one cycle-----		-----	-----
1RL	Set counter-clockwise Direction-sample flow into the cell	15	4.50
1RS	Show pump information (no change)	15	4.75
1RS	Show pump information (no change)	15	5.00
1RS	Show pump information (no change)	15	5.25
1RS	Show pump information (no change)	15	5.50
1RS	Show pump information (no change)	15	5.75
1RS	Show pump information (no change)	15	6.00
1RS	Show pump information (no change)	15	6.25
1RS	Set clockwise Direction – sample flow in reverse direction	15	6.50
-----complete one cycle-----		-----	-----

Appendix VII

Table VII-1: Estimated cost of current setup of the proposed system

	Items	Cost (£)
1	CCD camera	£ 1,000
2	Microscopy	£ 4,000
3	Flow cell	£ 100
4	Tubes for sample	£ 100
5	Peristaltic pump (2 pumps)	£ 1,400
6	PODs (used)	£ 4,500
7	Flexible lights	£ 500
8	Desktop PCs (2 nos incl. monitors)	£ 800
	Total	£12,400

APPENDIX VIII

	Side view		Front view			Side view		Front view	
1					11			11	
2					12			12	
3					13			13	
4					14			14	
5					15			15	
6					16			16	
7					17			17	
8					18			18	
9					19			19	
10					20			20	

Appendix VIII
Table APP VIII-2 Result of the study of wear debris particles dynamic

	Size (um)	Shape	Movement	Speed of rotation (s/rotation)	RPM
1	57	platelet	Swaying	no	
2	49	platelet	Swaying	no	
3	15	thick platelete	Rolling	11	5.5
4	25	platelet	Rolling	11	5.5
5	37	platelet	Yawing	no	
6	18	curl	Rolling	10	6.0
7	47	platelet	Rolling	24	2.5
8	12	curl	Rolling	12	5.0
9	30	platelet	Rolling	10	6.0
10	23	platelet	Rolling	11	5.5
11	18	thick platelete	Rolling	11	5.5
12	30	thick platelete	Rolling	9	6.7
13	23	thick platelete	Rolling	34	1.8
14	17	thick platelete	Rolling	12	5.0
15	17	thick platelete	Rolling	7	8.6
16	22	thick platelete	Rolling	14	4.3
17	15	thick platelete	Rolling	7	8.6
18	14	platelet	Rolling	12	5.0
19	17	platelet	Rolling	10	6.0
20	18	platelet	Rolling	15	4.0
21	20	platelet	Rolling	35	1.7
22	36	platelet	Rolling	18	3.3
23	22	platelet	Swaying		
24	22	platelet	Swaying		
25	20	platelet	Rolling	18	3.3
26	12	platelet	Rolling	19	3.2
27	12	platelet	Rolling	13	4.6
28	10	platelet	Swaying		5.9
29	9	platelet	Rolling	8	7.5
30	8	platelet	Rolling	10	6.0
31	18	platelet	Rolling	14	4.3
32	8	platelet	Rolling	19	3.2
33	7	platelet	Rolling	15	4.0
34	14	platelet	Rolling	15	4.0
35	18	platelet	Rolling	15	4.0
36	12	platelet	Rolling	13	4.6

37	15	platelet	Rolling	20	3.0
38	10	platelet	Rolling	25	2.4
39	9	platelet	Rolling	15	4.0
40	12	platelet	Rolling	15	4.0
41	16	platelet	Rolling	10	6.0
42	26	platelet	Rolling	28	2.1
43	30	platelet	Swaying		
44	16	platelet	Rolling	5	12.0
45	20	platelet	Rolling	10	6.0
46	21	platelet	Rolling	20	3.0
47	18	platelet	Rolling	8	7.5
48	21	platelet	Rolling	5	12.0
49	26	curl	Rolling	26	2.3
50	11	platelet	Rolling	5	12.0
51	8	platelet	Rolling	6	10.0
52	9	platelet	Rolling	5	12.0
53	7	platelet	Rolling	5	12.0
54	13	platelet	Rolling	8	7.5
55	22	platelet	Yawing		
56	15	platelet	Rolling	14	4.3
57	19	platelet	Yawing		
58	17	platelet	Rolling	9	6.7
59	22	platelet	Rolling	7	8.6
60	14	curl	Rolling	7	8.6
61	17	curl	Rolling	10	6.0
62	26	platelet	Swaying		
63	9	needle	Rolling	13	4.6
64	29	needle	Rolling	13	4.6
65	10	needle	Rolling	12	5.0
66	10	needle	Rolling	14	4.3
67	12	needle	Rolling	14	4.3
68	10	needle	Rolling	18	3.3
69	11	needle	Rolling	24	2.5
70	27	platelet	Swaying		
71	20	thick platelete	Swaying		
72	14	curl	Rolling	17	3.5
73	24	platelet	Rolling	10	6.0
74	12	platelet	Rolling	8	7.5
75	9	platelet	Rolling	6	10.0
76	15	platelet	Rolling	9	6.7
77	20	platelet	Rolling	6	10.0
78	12	platelet	Swaying		

79	9	platelet	Rolling	6	10.0
80	13	platelet	Rolling	6	10.0
81	17	platelet	Swaying		
82	8	platelet	Rolling	8	7.5
83	15	platelet	Rolling	8	7.5
84	12	platelet	Rolling	8	7.5
85	9	platelet	Swaying		
86	29	needle	Rolling	6	10.0
87	15	platelet	Rolling	13	4.6
88	18	platelet	Rolling	13	4.6
89	11	platelet	Rolling	16	3.8
90	21	needle	Swaying		
91	25	platelet	Rolling	8	7.5
92	17	platelet	Rolling	10	6.0
93	19	needle	Rolling	11	5.5
94	14	needle	Rolling	8	7.5
95	12	platelet	Swaying		
96	11	platelet	Rolling	12	5
97	13	platelet	Swaying		
98	13	platelet	Rolling	15	4
99	9	platelet	Swaying		
100	9	platelet	Rolling	5	12
101	13	platelet	Rolling	8	7.5
102	7	platelet	Rolling	5	12
103	13	platelet	Swaying		
104	7	platelet	Rolling	8	7.5
105	10	platelet	Rolling	8	7.5
106	14	platelet	Rolling	10	6
107	24	platelet	Rolling	30	2
108	13	platelet	Rolling	15	4
109	23	platelet	Rolling	16	3.75
110	35	platelet	Rolling	16	3.75
111	26	curl	Rolling	8	7.5
112	10	curl	Rolling	20	3
113	15	curl	Rolling	16	3.75
114	15	platelet	Rolling	13	4.61538
115	10	platelet	Swaying		
116	13	platelet	Swaying		
117	26	platelet	Rolling	17	3.52941
118	40	platelet	Rolling	34	1.76471
119	20	platelet	Rolling	33	1.81818
120	20	platelet	Rolling	16	3.75

END OF THESIS